

ELECTROCHEMICAL PAPER-BASED IMMUNOSENSOR FOR BIOMARKERS DETECTION



A Dissertation Submitted in Partial Fulfillment of the Requirements
for the Degree of Doctor of Philosophy in Chemistry

Department of Chemistry

FACULTY OF SCIENCE

Chulalongkorn University

Academic Year 2020

Copyright of Chulalongkorn University

อิมมูโนเซ็นเซอร์ฐานกระดาษเชิงเคมีไฟฟ้าสำหรับการตรวจวัดตัวบ่งชี้ทางชีวภาพ



วิทยานิพนธ์นี้เป็นส่วนหนึ่งของการศึกษาตามหลักสูตรปริญญาวิทยาศาสตรดุษฎีบัณฑิต

สาขาวิชาเคมี ภาควิชาเคมี

คณะวิทยาศาสตร์ จุฬาลงกรณ์มหาวิทยาลัย

ปีการศึกษา 2563

ลิขสิทธิ์ของจุฬาลงกรณ์มหาวิทยาลัย

Thesis Title ELECTROCHEMICAL PAPER-BASED IMMUNOSENSOR FOR
 BIOMARKERS DETECTION

By Miss Suchanat Boonkaew

Field of Study Chemistry

Thesis Advisor Professor Dr. ORAWON CHAILAPAKUL

Thesis Co Advisor Associate Professor Dr. Weena Siangproh

 Professor Dr. SIRIRAT RENGPIPAT

Accepted by the FACULTY OF SCIENCE, Chulalongkorn University in Partial Fulfillment of the Requirement for the Doctor of Philosophy

..... Dean of the FACULTY OF SCIENCE
(Professor Dr. POLKIT SANGVANICH)

DISSERTATION COMMITTEE

..... Chairman
(Associate Professor Dr. VUDHICHAI PARASUK)

..... Thesis Advisor
(Professor Dr. ORAWON CHAILAPAKUL)

..... Thesis Co-Advisor
(Associate Professor Dr. Weena Siangproh)

..... Thesis Co-Advisor
(Professor Dr. SIRIRAT RENGPIPAT)

..... Examiner
(Dr. JANJIRA PANCHOMPOO)

..... Examiner
(Associate Professor Dr. NATTAYA NGAMROJANAVANICH)

..... External Examiner
(Assistant Professor Dr. Amara Apilux)



จุฬาลงกรณ์มหาวิทยาลัย
CHULALONGKORN UNIVERSITY

สุชานาถ บุญแก้ว : อิมมูโนเซ็นเซอร์ฐานกระดาษเชิงเคมีไฟฟ้าสำหรับการตรวจวัดตัวบ่งชี้ทางชีวภาพ.
(ELECTROCHEMICAL PAPER-BASED IMMUNOSENSOR FOR BIOMARKERS DETECTION) อ.
ที่ปรึกษาหลัก : ศ. ดร.อรวรรณ ชัยลภากุล, อ.ที่ปรึกษาร่วม : รศ. ดร.วีณา เสียงเพราะ, ศ. ดร.ศิริรัตน์
เร้งพิพัฒน์

วิทยานิพนธ์ฉบับนี้มุ่งเน้นการพัฒนาอิมมูโนเซ็นเซอร์ฐานกระดาษสำหรับตรวจวัดตัวบ่งชี้ทางชีวภาพที่สำคัญ โดยใช้วิธีการตรวจวิเคราะห์แบบไม่ใช้สารติดฉลาก วิทยานิพนธ์นี้สามารถแบ่งออกเป็นสี่ส่วนประกอบหลัก ในส่วนแรก อุปกรณ์ฐานกระดาษแบบพับถูกพัฒนาขึ้นเพื่อตรวจวัดซีรีแอกทีฟโปรตีนโดยอุปกรณ์ฐานกระดาษแบบพับถูกออกแบบมาเพื่อรวมขั้นตอนการเตรียมอิมมูโนเซ็นเซอร์และการตรวจวัดบนอุปกรณ์ขึ้นเดียวกัน อนุภาคทองคำระดับนาโนถูกดัดแปรลงบนขั้วไฟฟ้าพิมพ์กรีนคาร์บอนที่ถูกดัดแปรด้วยแกรฟีนเพื่อช่วยเพิ่มความไวในการตรวจวัด เซนเซอร์ที่ถูกพัฒนาขึ้นสามารถนำไปประยุกต์เพื่อตรวจวัดซีรีแอกทีฟโปรตีนในตัวอย่างเซรัมอ้างอิงได้ สำหรับส่วนที่สอง เซนเซอร์ฐานกระดาษเชิงเคมีไฟฟ้าถูกสร้างขึ้นเพื่อตรวจวัดตัวบ่งชี้ทางชีวภาพสำหรับโรคหลอดเลือดและหัวใจทั้งสามตัวพร้อมกัน ประกอบด้วยซีรีแอกทีฟโปรตีน โทโรโปรนินไอและ โพรแคลซิโทนิน เซนเซอร์ฐานกระดาษเชิงเคมีไฟฟ้าที่พัฒนาขึ้นมีเซนเซอร์จับหลายโซน และมีขั้วไฟฟ้าใช้งานหลายขั้ว ซึ่งสามารถใช้ตรวจวัดตัวบ่งชี้ทางชีวภาพทั้งสามตัวพร้อมกันในตัวอย่างซีรัมตัวเดียว โดยให้ค่าความไวในการตรวจวัดและความจำเพาะสูง สำหรับส่วนที่สาม เซนเซอร์ฐานกระดาษเชิงเคมีไฟฟ้าที่ใช้งานง่ายและมีราคาถูกเพื่อตรวจวัดเฟอร์ริตินถูกรายงาน เซนเซอร์ฐานกระดาษเชิงเคมีไฟฟ้าถูกออกแบบลงบนกระดาษกรองเพื่อสร้างเป็นอิมมูโนเซนเซอร์ ขั้วไฟฟ้าใช้งานถูกดัดแปรด้วยแกรฟีนออกไซด์โดยใช้เครื่องพิมพ์เพื่อเพิ่มความสามารถในการทำซ้ำของขั้วไฟฟ้า เซนเซอร์ฐานกระดาษเชิงเคมีไฟฟ้าถูกนำมาใช้ในตัวอย่างจริงโดยให้ผลการทดสอบที่สอดคล้องกับวิธีมาตรฐาน ส่วนสุดท้าย เซนเซอร์ฐานกระดาษเชิงเคมีไฟฟ้าถูกออกแบบอย่างจำเพาะเพื่อตรวจวัดไวรัสตับอักเสบบีและไวรัสตับอักเสบบีไปพร้อมกัน ช่องการไหลแบบเร็วและช่องชะลอการไหลถูกสร้างขึ้นเพื่อควบคุมความเร็วของการไหลบน เซนเซอร์ฐานกระดาษเชิงเคมีไฟฟ้า เพื่อยืนยันการประสิทธิภาพของอิมมูโนเซ็นเซอร์ เซนเซอร์ฐานกระดาษเชิงเคมีไฟฟ้าที่พัฒนาขึ้นถูกนำมาหาปริมาณไวรัสตับอักเสบบีและไวรัสตับอักเสบบีในตัวอย่างเซรัม อิมมูโนเซ็นเซอร์ทั้งหมดที่ได้พัฒนาขึ้น มีประสิทธิภาพสูงสำหรับการวิเคราะห์ตัวอย่างทางชีวภาพและทางคลินิก และได้รับการพัฒนารูปแบบขั้นสูงต่อไป

จุฬาลงกรณ์มหาวิทยาลัย
CHULALONGKORN UNIVERSITY

สาขาวิชา เคมี
ปีการศึกษา 2563

ลายมือชื่อนิสิต
ลายมือชื่อ อ.ที่ปรึกษาหลัก
ลายมือชื่อ อ.ที่ปรึกษาร่วม
ลายมือชื่อ อ.ที่ปรึกษาร่วม

5872107523 : MAJOR CHEMISTRY

KEYWORD: Electrochemical detection, Paper-based analytical device, Biomarker, Immunosensor
 Suchanat Boonkaew : ELECTROCHEMICAL PAPER-BASED IMMUNOSENSOR FOR BIOMARKERS
 DETECTION. Advisor: Prof. Dr. ORAWON CHAILAPAKUL Co-advisor: Assoc. Prof. Dr. Weena
 Siangproh, Prof. Dr. SIRIRAT RENGPIPAT

This dissertation focused on the development of electrochemical paper-based immunosensor for determining essential biomarkers by using a label-free immunoassay. This dissertation can be divided into four main parts. In the first part, an origami paper-based analytical device (oPAD) was developed for c-reactive protein (CRP) detection. oPAD was designed to combine the preparation of immunosensor and detection step into a single device. A gold nanoparticle modified graphene screen-printed carbon electrode (AuNPs/G/SPCE) was utilized to enhance the sensitivity of the electrode. The developed sensor was successfully applied to determine CRP in a certified serum sample. For the second part, an electrochemical paper-based analytical device (ePAD) was created for simultaneous determination of three crucial cardiovascular disease (CVD) biomarkers including CRP, troponin I (cTnl), and procalcitonin (PCT). The proposed ePAD has multiple detection zones and multiple working electrodes, which could enable simultaneous three biomarkers in a single sample with high sensitivity and selectivity. For the third part, a simple and low-cost ePAD immunosensor for ferritin determination was reported. The ePAD was custom designed on the filter paper to successfully fabricate an immunosensor. The working electrode was first modified with graphene oxide (GO) using an inkjet-printing technique to enhance the reproducibility of the electrode. The ePAD was finally applied in a practical sample, giving results that are in agreement with the standard method. Lastly, an ePAD was architecturally designed for simultaneous detection of hepatitis B (HBV) and hepatitis C core antigen (HCV). The fast-flow and delayed channels were created to control the flow velocity on an ePAD device. To validate the sensor performance, the developed immunosensor was applied to measure the known amount of HBV and HCV in the serum samples. All developed immunosensors provided good performances for biological and clinical diagnosis and allowed for further development of an advanced platform.

Field of Study: Chemistry

Student's Signature

Academic Year: 2020

Advisor's Signature

Co-advisor's Signature

Co-advisor's Signature

ACKNOWLEDGEMENTS

This thesis would not have been possible without the support of many people. First and foremost, I would like to thank my advisor Professor Dr. Orawon Chailapakul, Co-advisor Professor Dr. Sirirat Rengpipat, and Associate Professor Dr. Weena Siangproh for believing in me and giving me a chance to contribute to the scientific community. In addition to valuing my research contributions, they invested much of their time towards my personal and professional development. I also thank my committee member (Professor Dr. Vudhichai Parasuk, Associate Professor Dr. Nattaya Ngamrojanavanich, Dr. Janjira Panchompoo, and Assistance Prof Dr. Amara Apilux) for their encouragement and support.

I truly acknowledge the Center of Excellence on Petrochemical and Materials Technology (PETROMAT) through High Performance and Smart Material (HPSM) research program that made my project possible by supporting funding throughout my Ph.D. research.

I would also like to thank Professor Charles S. Henry and Colorado state University for giving me the internship opportunities in Henry's group. I have had the pleasure of knowing Chuck and Henry's member. They always support and help me during I am living in USA for 7 months. It's a good memory to be a part of Henry's member and CSU student.

I would also like to thank EOSCE's lab member for their support, suggestion, and encouragement during my Ph.D. life. It has been a great moment to spend time in this lab through a good and difficult times.

Lastly, I would like to thank my family for their unwavering support of my ambitious, regardless of how they changed over time. I know they don't quite understand what I have been doing these past five years, but they were always there to talk to during both exciting and stressful time. I am extreme lucky to have the best support system that I have with them. Family over everything. I love you, always.

Suchanat Boonkaew

TABLE OF CONTENTS

	Page
ABSTRACT (THAI).....	iii
ABSTRACT (ENGLISH).....	iv
ACKNOWLEDGEMENTS.....	v
TABLE OF CONTENTS.....	vi
LIST OF TABLES.....	xiii
LIST OF FIGURES.....	xiv
LIST OF ABBREVIATIONS.....	xxii
CHAPTER 1.....	1
INTRODUCTION.....	1
1.1 Introduction.....	1
1.2 Objectives of the research.....	5
1.3 Scope of the research.....	6
CHAPTER 2.....	10
THEORY.....	10
2.1 Paper-based analytical devices.....	10
2.1.1 Fabrication of PAD.....	10
2.2 Biosensor.....	12

2.2.1 Electrochemical biosensor.....	14
2.2.2 Applications of an electrochemical biosensor	15
2.3 Immunoassay	16
2.4 Electrochemical detection	20
2.4.1 Faradaic and non-faradaic processes.....	20
2.4.2 Mass transfer modes	21
2.4.2.1 Diffusion	22
2.4.2.2 Convection	22
2.4.2.3 Migration.....	22
2.4.3 Electrochemical technique.....	23
2.4.3.1 Voltammetry	24
2.4.3.2 Cyclic voltammetry (CV).....	25
2.4.3.3 Differential pulse voltammetry (DPV)	27
2.4.3.4 Square wave voltammetry (SWV)	28
2.4.4 Electrochemical impedance spectroscopy (EIS).....	29
2.4.5 Chronoamperometry.....	31
2.4.6 Electrochemical cell.....	32
2.4.6.1 Working electrode (WE).....	33
2.4.6.2 Counter electrode (CE)	35
2.4.6.3 Reference electrode (RE).....	35
CHAPTER 3.....	36
THE DEVELOPMENT OF ELECTROCHEMICAL PAPER-BASED IMMUNOSENSOR FOR THE DETERMINATION OF ESSENTIAL BIOMARKERS	36

3.1 An origami paper-based electrochemical immunoassay for C-reactive protein detection using a screen-printed carbon electrode modified with graphene and gold nanoparticles.....	37
Abstract.....	38
3.1.1 Introduction.....	39
3.1.2 Experimental.....	42
3.1.2.1 Chemicals and materials.....	42
3.1.2.2 Instrumentation.....	43
3.1.2.3 Design and fabrication of oPAD.....	45
3.1.2.4 Preparation of the immunosensor and measurement.....	46
3.1.2.5 Preparation of serum samples.....	48
3.1.3 Results and discussion.....	48
3.1.3.1 Characterization of the modified electrode.....	48
3.1.3.2 Optimization of the experimental conditions.....	56
3.1.3.2.1 The effect of graphene loading.....	57
3.1.3.2.2 The effect of AuNPs concentration and deposition time.....	58
3.1.3.2.3 The effect of the capture anti-CRP.....	59
3.1.3.2.4 The effect of bovine serum albumin (BSA).....	60
3.1.3.2.5 The effect of incubation time.....	61
3.1.3.3 Analytical performance.....	62
3.1.3.4 Selectivity.....	65
3.1.3.5 Stability, reproducibility and repeatability of the CRP immunosensor..	66
3.1.3.6 Detection of CRP in a certified human serum sample.....	68

3.1.4 Conclusion.....	69
PART II.....	70
3.2 Electrochemical paper-based analytical device for multiplexed, point-of-care detection of cardiovascular disease biomarkers.....	70
Abstract.....	71
3.2.1. Introduction.....	72
3.2.2 Experimental.....	75
3.2.2.1 Chemicals and materials.....	75
3.2.2.2 Apparatus and measurements.....	76
3.2.2.3 ePADs fabrication.....	79
3.2.2.4 Electrode modification.....	80
3.2.2.5 Electrochemical detection of CVDs biomarkers.....	81
3.2.2.6 Preparation of serum samples.....	82
3.2.3 Results and discussion.....	82
3.2.3.1 SEM/EDS and Raman spectroscopy characterization of the modified electrode.....	82
3.2.3.2 Electrochemical characterization of the immunosensor.....	87
3.2.3.3 Wetting area vs time.....	90
3.2.3.4 Optimization.....	91
3.2.3.4.1 Measurement parameter of SWV.....	91
3.2.3.4.2 Effect of anodized GO.....	93
3.2.3.4.3 Effect of reduce GO (rGO).....	94
3.2.3.4.4 Effect of washing time.....	95

3.2.3.4.5 Antibody concentration.....	96
3.2.3.4.6 Incubation time	97
3.2.3.5 Electrochemical detection of CVDs biomarkers.....	99
3.2.3.6 Reproducibility, selectivity, and stability of the immunosensor.....	103
3.2.3.7 Sample analysis	105
3.2.4 Conclusion.....	106
PART III	108
3.3 Cost-effective paper-based electrochemical immunosensor using a label-free assay for sensitive detection of ferritin.....	108
Abstract.....	109
3.3.1 Introduction.....	110
3.3.2 Experimental.....	113
3.3.2.1 Chemical and reagents.....	113
3.3.2.2 Apparatus	114
3.3.2.3 Design and fabrication of the electrochemical paper-based analytical device (ePAD)	115
3.3.2.4 Inkjet printing for electrode modification.....	117
3.3.2.5 Preparation of the paper-based electrochemical immunosensor	118
3.3.2.6 Electrochemical measurement and sample analysis	119
3.3.3 Results and discussion.....	120
3.3.3.1 Characterization of GO-modified electrode.....	120
3.3.3.2 Electrochemical detection of ferritin using the developed immunosensor	121

3.3.3.3 Electrochemical characterization of the modified electrode	122
3.3.3.4 Optimization of the variable parameters	126
3.3.3.4.1 Electrochemical condition of DPV.....	126
3.3.3.4.2 Inkjet printing parameters	128
3.3.3.4.3 Influence of antibody concentration.....	131
3.3.3.4.4 Influence of incubation time.....	132
3.3.3.5 Analytical performance	133
3.3.3.6 Reproducibility, selectivity, and stability of the electrochemical paper-based immunosensor.....	136
3.3.3.7 Detection of ferritin in a human serum sample.....	138
3.3.4 Conclusion.....	139
PART IV.....	141
3.4 Dual flow-controlled behaviors on microfluidic fast-flow/delayed channels for an automated and simultaneous electrochemical detection of Hepatitis B virus and Hepatitis C virus core antigen.....	141
Abstract.....	142
3.4.1 Introduction.....	143
3.4.2 Experimental	147
3.4.2.1 Material and reagent.....	147
3.4.2.3 Apparatus	148
3.4.2.3 ePAD fabrication.....	149
3.4.2.4 Electrode modifications.....	149
3.4.2.5 Sample preparation.....	151

3.4.2.6 Detection procedure.....	152
3.4.3 Results and discussion.....	153
3.4.3.1 Design and operation of the immunosensing ePAD.....	153
3.4.3.2 Electrochemical characterization of the immunosensing ePAD	159
3.4.3.3 Optimization of device geometry.....	162
3.4.3.3.1 Effect of channel width of the delayed channel.....	163
3.4.3.3.2 Effect of gap height of the fast-flow channel.....	163
3.4.3.4 Optimization of assay conditions	165
3.4.3.4.1 Effect of the $K_3[FeCN_6]$ concentration	165
3.4.3.4.2 Concentration of antibodies.....	165
3.4.3.4.3 Incubation time.....	166
3.4.3.5 Analytical performance of ePAD device for detection of HBV and HCV	169
3.4.3.6 Real sample analysis.....	173
3.4.4 Conclusion.....	173
CHAPTER 4.....	175
CONCLUSIONS AND FUTURE PERSPECTIVE.....	175
4.1 Conclusion.....	175
4.2 Future perspective.....	178
REFERENCES.....	180
VITA.....	207

LIST OF TABLES

	Page
Table 1. The comparison of analytical performance of the other assays for a label-free CRP detection.....	64
Table 2. Recoveries of the origami paper-based electrochemical immunosensor for CRP detection. The data were averaged with three pieces of sensors.	68
Table 3. The comparison of analytical performance of different immunosensors for CRP, cTnI, and PCT assays.....	101
Table 4. The percent recoveries of simultaneous CRP, cTnI, and PCT detections in serum sample using the ePADs immunosensor (n=3) ^a	106
Table 5. The comparison of different analytical performance for detecting ferritin using different immunoassay methods.	135
Table 6. The comparison of determination results for ferritin in spiked serum samples obtained by the developed system (ePAD) and CLIA as a reference method. All measurements were a mean of three replicates (n=3).....	139
Table 7. The comparison of analytical performance of label-free immunosensors for HBV and HCV assays.....	171
Table 8. The comparison of the determination results by the proposed ePAD and CLIA reference method for HBV and HCV detection in real clinical sera from patients.....	172

LIST OF FIGURES

	Page
Figure 1. The patterned hydrophobic and hydrophilic zones on paper-based substrate and basic step using wax-printing method ³³	12
Figure 2. The components of biosensor ³⁸	13
Figure 3. The components of immunoassay consist of antibody (purple) and antigen (yellow).	17
Figure 4. The four common types of immunoassay ⁴⁴	18
Figure 5. The comparisons of label-free immunoassay and sandwich immunoassay (labelled immunoassay) ⁴⁵	19
Figure 6. Modes of mass transfer, including diffusion, migration, and convection ⁴⁶	22
Figure 7. The family tree of the interfacial electrochemical techniques ⁴⁷	24
Figure 8. (a) the applied potential waveform as a function with time in cyclic voltammetry and (b) a typical cyclic voltammogram (I-E curve) for a reversible process ⁴⁸	26
Figure 9. (a) differential pulse waveform where (t_1) and (t_2) is the sampling before and after pulse, respectively, and differential pulse voltammogram (b) where Δi_p is the difference current between two points ($\Delta i_p = i_1 - i_2$) ⁵⁰	28
Figure 10. (a) square wave waveform where (t_f) and (t_r) is the sampling before and after pulse, respectively, and typical square wave voltammogram (b) where Δi_p is the different current between two points ($\Delta i_p = i_f - (-i_r)$) ⁵⁰	29
Figure 11. AC waveform for an applied potential (E) and the result of current response (I).	30
Figure 12. the Nyquist plot where R_Ω is solution resistance, R_{ct} is charge transfer resistance, Z_{Re} is real resistance while Z_{Im} is the imaginary resistance, ω is the angular frequency, and C_{dl} is interface capacitance.	31

- Figure 13. (a) potential simulation and (b) the current response during the chronoamperometric measurement (chronoamperogram)⁵⁰..... 32
- Figure 14. The three electrodes set up for potentiostat setup..... 33
- Figure 15. (A) The design and component of the oPAD (B) The overall electrode preparation and immobilization step of the immunosensor for CRP determination. . 44
- Figure 16. Photograph of the oPAD device connected with PG30 potentiostat to measure the R_{ct} of electrode surface..... 48
- Figure 17. SEM images of the SPCE (A), G/SPCE (B), AuNP/G/SPCE at 3000 x magnification (C), the photomicrograph (D) and the corresponding EDS spectra (F) of the AuNP-modified on the electrode surface..... 49
- Figure 18. SEM/EDS images of the AuNPs on G/SPCE (A), K line of C atom presented as the composition of the carbon-based ink (B), M line of AuNPs on the G/SPCE surface (C), and the corresponding EDS spectra (D) related to the results tabulated in the table. 50
- Figure 19. The cyclic voltammogram of (a) G/SPCE (green line), and (b) SPCE (blue line) in the presence of 5 mM $[\text{Fe}(\text{CN})_6]^{3-/4-}$ in 0.1 M KNO_3 was performed from -0.8 to 1.0 V vs Ag/AgCl at a scan rate of 100 mV s^{-1} 50
- Figure 20. CV comparison of the SPCE (A and B) and G/SPCE electrodes (C and D) in 5 mM $\text{Fe}(\text{CN})_6^{3-/4-}$ at different scan rates from 20 to 200 mV s^{-1} 52
- Figure 21. (A) The Nyquist plot of AuNPs-modified on G/SPCE (yellow line), G/SPCE (blue line), and SPCE (black line). The EIS technique was used in a frequency range of 100 kHz to 0.01 Hz with 0.1 V of potential and amplitude of 0.01 V using 5 mM $[\text{Fe}(\text{CN})_6]^{3-/4-}$ in 0.1 M KNO_3 as the redox couple. (B) SEM images of the AuNPs-modified on G/SPCE (a) and AuNPs-modified on SPCE (b) with a 500x magnification. 53
- Figure 22. The stepwise of CRP detection using oPAD was characterized by EIS. Nyquist plot of AuNP (a; yellow line), L-cys/EDC-NHS (b; orange line), Anti-CRP (c; grey line), BSA (d; green line), and (e; blue line) 20 $\mu\text{g mL}^{-1}$ CRP was immobilized on the electrode surface in the presence of 5 mM $[\text{Fe}(\text{CN})_6]^{3-/4-}$. Inset picture: equivalent circuit applied

to model EIS data. R_e : the electrolyte solution resistance; C_{dl} : the constant phase angle element; R_t : the interfacial electron transfer resistance; Z_w : the Warburg impedance introduced by the diffusion of ions.....	54
Figure 23. Optimization of the variable parameters: (A) amount of graphene loading, (B) deposition time of AuNPs, (C) concentration of $K[AuCl_4]$, (D) concentration of anti-CRP, (E) the amount of blocking agent (%BSA), and (F) incubation time, using EIS technique in 5.0 mM of $[Fe(CN)_6]^{3-/4-}$ as a redox probe.....	57
Figure 24. SEM images of the AuNPs at various deposition times on the G/SPCE with different magnifications: 100s (A)-(C), 300s (D)-(F), and 500s (G)-(I).	59
Figure 25. The impedance response between the blocked and unblocked surface of anti-CRP/AuNP/G/SPCE in the presence of 20 $\mu\text{g/mL}$ CRP, using EIS technique in 5.0 mM of $Fe(CN)_6^{3-/4-}$	61
Figure 26. (A) EIS response of the oPAD immunosensor for the detection of various concentration of CRP (0.05-100 $\mu\text{g mL}^{-1}$) in the presence of 5 mM $[Fe(CN)_6]^{3-/4-}$ and (B) Variation of the ΔR_{ct} at different concentrations of CRP (ng mL^{-1}). Inset: Calibration plot between logarithm of CRP concentration and ΔR_{ct} . The data points were averaged from 3 pieces of electrodes.....	62
Figure 27. The R_{ct} response in EIS of CRP detection after immobilization with 50 $\mu\text{g mL}^{-1}$ bilirubin, myoglobin, 10 % w/v BSA, and CRP 5 $\mu\text{g mL}^{-1}$ using 50 $\mu\text{g mL}^{-1}$ Anti-CRP, 0.2% BSA, and in presence of 5 mM $[Fe(CN)_6]^{3-/4-}$	65
Figure 28. The storage stability of oPAD for CRP detection.....	66
Figure 29. Design and fabrication of the multiplexed ePAD (A and B). (a), (b), and (c) small holes (4 mm in diameter) made on the transparency film for immobilization of detection antibodies, (d) redox solution inlet (5 mm in diameter), and step-by-step preparation of the electrochemical immunosensor and detection of the antigen/biomarker on the sensor (C). WE = working electrode; CE = counter electrode; and RE = reference electrode.....	78

- Figure 30. SEM images of SPCE (a), G-SPCE (b), GO/G-SPCE (c), and after reducing the excess of GO at -1.4 V for 30s using PBS pH 7.4 (d). 83
- Figure 31. SEM/EDS images of anodized GO on the SPCE (a and b), K line of C atom presented as the composition of graphene in GO solution (c), K line of O and Na represented as the composition of GO and NaOH solution for anodize process (d and e), and the corresponding EDS spectra (f) related to the results tabulated in the table. 85
- Figure 32. Raman spectra of bare G-SPCE (black line) and the GO/G-SPCE electrode (orange line). 86
- Figure 33. CV and EIS characterization of the electrodes at various modification steps using 5 mM of $[\text{Fe}(\text{CN})_6]^{3-/4-}$ containing 0.1 M KNO_3 for C-reactive protein (CRP) (a), troponin I (cTn I) (b), and procalcitonin (PCT) detection (c), respectively. The bare G-SPCE electrode is shown in the dash line, GO modified on the electrode as denoted as GO/G-SPCE (grey line), after anodized GO (green line), after antibodies was immobilized on the electrode (yellow line), after reducing the excess of GO (blue line), BSA was used to block non-specific protein and blocked active site binding (orange line), and after antigen or biomarkers were captured the electrochemical response reduced (red line), respectively. 88
- Figure 34. Normalized wetting area vs time. Symbols and error bars show the average and standard deviation of triplicate experiments, respectively. 90
- Figure 35. Each electrochemical condition of SWV technique including; (a) amplitude, (b) frequency, and (c) step height. The optimal conditions were as follow: an amplitude, frequency, and step height were 150 mV, 5 Hz, and 5 mV. 91
- Figure 36. The effect of anodized potential (a), anodized time (b) and the effect of reduce potential (c), and reduce time (d). 93
- Figure 37. Study of the effect of washing time on the current response. 95
- Figure 38. Optimization of experimental conditions for the proposed ePADs immunosensor: concentration of antibodies (a, b) and incubation time (100 ng mL⁻¹ for

anti-PCT and anti-cTnI, $3 \mu\text{mL}^{-1}$ of anti-CRP, 3mg mL^{-1} of BSA, $0.05 \mu\text{g mL}^{-1}$ of CRP, and 0.1ng mL^{-1} of PCT and cTnI were immobilized on the modified electrode) (c). The Error bars indicate standard deviations calculated from three repetitions ($n = 3$). 96

Figure 39. Left: Square wave voltammograms of simultaneous detection of various concentrations of CRP (a), cTnI (b), and PCT (c), respectively. Right: The quantitative calibration curve plot of the change in current response (ΔI) as a function of logarithm of concentration of biomarkers. ΔI was calculated from $\Delta I = I_{(\text{CVDs biomarkers})} - I_{(\text{BSA})}$; Where $I_{(\text{CVDs biomarkers})}$ is belong to the current response value after the immobilization of CVDs biomarkers (CRP, cTnI, and CRP) onto BSA/rGO/antibody/GO/G-SPCE. The $I_{(\text{BSA})}$ is belong to the current response value of BSA/rGO/antibody/ GO/G-SPCE. Error bars represent the standard deviation calculated from three repetitions ($n=3$)..... 98

Figure 40. The quantitative calibration curve plot of the change in current response (ΔI) as a function of concentration and logarithm of concentration of CRP (a), cTnI (b), and PCT (c), respectively. Error bars represent the standard deviation calculated from three repetitions ($n=3$)..... 99

Figure 41. The change in current response (ΔI) of ePAD detection after immobilization with $0.05 \mu\text{g mL}^{-1}$ of CRP, 0.1ng mL^{-1} of cTnI, 0.1ng mL^{-1} of PCT, and 1mg mL^{-1} of other proteins using $3 \mu\text{g mL}^{-1}$ of anti-CRP, 100ng mL^{-1} of anti-cTnI and anti-PCT, and in the presence of $5 \text{mM} [\text{Fe}(\text{CN})_6]^{3-/4-}$ in 0.1M KNO_3 as a redox solution. 103

Figure 42. The storage stability of the electrochemical paper-based immunosensor. Error bars represent the standard deviation calculated from three repetitions ($n=3$). 105

Figure 43. Schematic illustration of the design and composition of ePAD (a) and the overall preparation and immobilization step of electrochemical paper-based immunosensor for detecting of ferritin (b). 117

Figure 44. SEM images of bare SPGE (a), GO/SPGE (b) and the FTIR spectra of SPGE and GO/SPGE (c)..... 121

Figure 45. (a) the current response of $5 \text{mM} [\text{Fe}(\text{CN})_6]^{3-/4-}$ in the absence and presence of 100ng mL^{-1} of ferritin that were performed by DPV technique and (b) EIS

- characterization of the modified electrode in a step-by-step fashion for 100 ng mL⁻¹ of ferritin detection using ePAD. Inset picture: equivalent circuit of the Randles model modified with Warburg impedance as a model EIS data..... 124
- Figure 46. The cyclic voltammogram of stepwise modification on the modified GO/SPGE electrode was performed in the potential between -0.8 and 0.9 V vs Ag/AgCl at a scan rate of 50 mV s⁻¹..... 126
- Figure 47. Each electrochemical condition of DPV technique including; (a) the modulation amplitude, (b) step potential, (c) standby potential, and (d) modulation time. The optimal conditions were as follow: a modulation amplitude, step potential, standby potential, and modulation time were 150 mV, 10 mV, 0 V, and 75 ms..... 128
- Figure 48. Optimization of the variable parameters: (a) The effect of GO:NMP ratio, (b) number of GO layer modified on the SPGE, (C) the effect of drop spacing, (d) and applied voltage of inkjet printing, using DPV technique in 5.0 mM [Fe(CN)₆]^{3-/4-} as a redox probe..... 131
- Figure 49. The effect of concentration of ferritin antibodies (from 25 to 250 ng mL⁻¹) with 100 ng mL⁻¹ of ferritin (a) and incubation time between 100 ng mL⁻¹ of antibodies and 100 ng mL⁻¹ of ferritin (from 10 to 90 min) (b), using DPV technique and 5 mM of [Fe(CN)₆]^{3-/4-} as a redox solution..... 133
- Figure 50. (a) a current response of ferritin concentration in the range from 1 to 1000 ng mL⁻¹, (b) A linear calibration plot between a ΔI and ferritin concentration (1-1000 ng mL⁻¹) is following to the equation $y = 0.0325x + 10.434$ with a correlation coefficient (R^2) of 0.9932. All measurements were a mean of three replicates (n = 3). 134
- Figure 51. The change of current response in DPV after immobilization with 10000 ng mL⁻¹ of myoglobin, C-reactive protein, homocysteine, bilirubin, creatinine, and 100 ng mL⁻¹ using 100 ng mL⁻¹ of anti-FTH, and in the presence of 5 mM [Fe(CN)₆]^{3-/4-} 136
- Figure 52. The storage stability of the electrochemical paper-based immunosensor. 138

Figure 53. Schematic illustration of components and ePAD device assembly for the simultaneous determination of HBV and HCV.....	148
Figure 54. The step-by-step modification on the modified electrode.....	151
Figure 55. (a) ePAD components and assembly and (b) operation of ePAD: (i) sample loading via a sample inlet, (ii) running buffer loading through the buffer inlet to perform the automated assay, and simultaneous electrochemical measurements.	152
Figure 56. (a) Time-lapse images of ePAD device during flow using a red dye to represent a redox solution in a delayed channel and (b) Time-lapse images after buffer loading by using a green dye representing a sample and a red dye representing a redox solution with gap height at 150 μm and the channel width of the delayed channel at 4.0 mm.....	157
Figure 57. (a) Image showing the flow path after sample loading by using a green dye to represent a sample solution and (b) Image showing the flow path after buffer loading.	158
Figure 58. The flow profile of redox solution using 25 mM $\text{K}_3[\text{Fe}(\text{CN})_6]$ spot on the delayed channel.....	158
Figure 59. CV (i) and EIS (ii) characterization of step-by-step modification in a static system using 5 mM of $\text{Fe}(\text{CN})_6^{3-/4-}$ containing 0.1 M KCl for HBV (a) and HCV (b), respectively.....	159
Figure 60. Optimization of device geometry for simultaneous HBV and HCV detection including (a) effect of channel width on the delayed channel and (b) effect of double-sided adhesive layers (gap height). All results were a mean of three replicated measurements (n=3). Note that HCV core antigen was used as a representative model analyte for the optimization (conditions: 10 $\mu\text{g mL}^{-1}$ of anti-hepatitis C concentration, 3 mg mL ⁻¹ of BSA blocking, and 10 ng mL ⁻¹ of HCV core antigen).....	162
Figure 61. The optimization of assay condition; (a) effect of the $\text{K}_3[\text{Fe}(\text{CN})_6]$ concentration to the velocity (i) and the total time (ii), (b) antibodies concentration of anti-hepatitis	

b (i), anti-hepatitis c (ii), and (c) the suitable incubation time between antibody and antigen. 167

Figure 62. The quantitative calibration plot between the change in charge (Δ charge) and logarithmic concentration of HBV (a) and HCV (b), and its corresponding chronoamperograms (left). Study of the specificity of the ePAD in the presence of common proteins (c). The error bar represents the standard deviation calculated from three replicated measurements (n=3). 168

Figure 63. The storage stability of ePAD device. All measurements were calculated from three replicates (n=3) 172



LIST OF ABBREVIATIONS

A	Electrode surface area
A	Ampere
AE	Auxiliary electrode
Ag/AgCl	Silver-silver chloride electrode
Au	Gold
AuNPs	Gold nanoparticles
BSA	Bovine serum albumin
C	Concentration
C	Carbon
C_1	Capacitance
C_i	Concentration of the species i (mol cm^{-3})
$^{\circ}\text{C}$	Degree Celsius
C_{dl}	interface capacitance
CE	Counter electrode
CRP	C-reactive protein
cTnl	Troponin I
CV	Cyclic Voltammetry
CVDs	Cardiovascular disease biomarkers
D_i	Diffusion coefficient (in cm^2s^{-1})
DPV	Differential pulse voltammetry
E°	Standard reduction potential
E	Apply potential
E_p	Potential
$E_{p,a}$	Anodic peak potential
$E_{p,c}$	Cathodic peak potential
EDC	1-ethyl-3-(3-dimethylaminopropyl) carbodiimide hydrochloride
EDS	Energy dispersive x-ray spectra

ePAD	Electrochemical paper-based analytical device
EIS	Electrochemical impedance spectroscopy
F	Faraday's constant
G	Graphene
G-SPCE	Graphene-modified stencil-printed carbon electrode
G-SPCE	Graphene modified on screen-printed carbon electrode
GO	Graphene oxide
HBV	Hepatitis B virus
Hz	Hertz
HPV	Hepatitis C virus core antigen
i	Current
i_f	Forward pulse
i_r	Reverse pulse
$J_i(x)$	Flux of species i
K_{et}	The electron transfer rate
L	Liter
L-Cys	L-Cysteine
LOD	Limit of detection
LOQ	Limit of quantitation
M	Molar
μL	Microliter
μm	Micrometer
μPAD	Microfluidic paper-based analytical devices
min	Minute
mL	Milliliter

mm	Millimeter
mM	Millimolar
mV	Milivolt
ms	Milisecond
n	Number of electrons
n	Number of repetitions
ng	Nanogram
nm	Nanometer
Na	Sodium
NHS	<i>N</i> -hydroxysulfosuccinimide
PAD	Paper-based analytical device
oPAD	Origami paper-based analytical device
PB	Phosphate buffer
PCT	Procalcitonin
PBS	Phosphate buffer saline
PBST	Phosphate buffer saline containing 0.5% Tween 20
POCT	Point-of-care testing
R	The ideal gas constant ($\text{JK}^{-1} \text{mol}^{-1}$)
R^2	Correlation coefficient
R_s	Electrolyte resistance
R_Ω	Solution resistance
R_s	Resolution
R_{ct}	Charge transfer resistance
RE	Reference electrode
RSD	Relative standard deviation
s	Second

SAM	Self-assembled monolayer
S/cm	Siemens per centimeter
S/N	Signal-to-noise ratio
SD	Standard deviation
SEM	Scanning electron microscope
SPCE	Screen-printed carbon electrode
SPGE	Screen-printed graphene electrode
SWV	Square wave voltammetry
T	Temperature (K)
V	Volt
W	Peak width
W_1	Warburg impedance
WE	Working electrode
Z	Impedance
Z_i	Charge
Z_{Im}	Imaginary resistance
Z_{Re}	Real resistance
α	Transfer coefficient
Ω	Ohm
ν	Scan rate ($V s^{-1}$)
ν	Velocity ($cm s^{-1}$)
ω	Angular frequency
θ	Phase shift





จุฬาลงกรณ์มหาวิทยาลัย
CHULALONGKORN UNIVERSITY

CHAPTER 1

INTRODUCTION

1.1 Introduction

To date, the growing demands of reliable tools to perform the point-of-care testing (POCT) lead to the continuous development of sustainable sensors. The novelty of the development not only provides a new class of sensors which offer rapidity, simplicity, and non-invasive test but also requires a low-cost, portable, sensitive, selective, and easy to use^{1, 2}, which have raised the potential for use in awareness of controlling and monitoring of the various disease globally^{3, 4}. Moreover, the display of new detection platforms is another criterion that mostly focused on the development for analytical applications. Recently, an alternative miniaturized sensor using cellulose as a substrate was proposed and successfully used to fabricate a new platform called paper-based analytical device (PAD). These platforms have become a promising and popular device in a variety of applications owing to its superb properties⁵⁻⁷. These benefit characteristics include disposability and self-pumping ability through capillary force, and it is easy to operate and fabricate using various printing and patterning techniques⁵. Besides, PAD patterns can be easily designed to combine the multiple steps of sensor preparation (i.e., storing, depositing and flowing) into a single device⁸⁻¹⁰. Due to the mentioned outstanding properties, PAD has been then applied for several applications including chemical^{11, 12}, environmental^{10, 13}, biological¹⁴, and clinical diagnosis¹⁵. In addition, there are several detection methods (i.e., colorimetric

detection, fluorescence detection, chemiluminescence detection, and spectrometry detection)^{14, 16} can be friendly combined to PAD depending on their applications. However, the previous methods often require a relatively expensive instrumentation, large sample volume requirement, and complicated pumping mechanisms that can increase the cost and lead to the limitation for portability of the POCT device¹⁷. Moreover, most of the previous works have introduced PAD platforms for a single analyte determination which limits the performance of device. Thus, the development of PAD with an additional function is necessary to achieve a better performance and to allow multiplex analysis using a single PAD device¹⁸. An electrochemical technique is a powerful and versatile method, which provides the advantages in terms of portability, simplicity, fast response time, and minimal instrumentation^{1, 2}. As these unique properties, it has led to the emergence of a new class of PAD device, which is the integration between the electrochemical technique and PAD. It is known as “electrochemical paper-based analytical devices (ePADs)”³. ePAD offers high sensitivity, selectivity, and allows multiplex measurement while maintaining a simple procedure and portability⁴. As mentioned earlier, PAD is applied extensively in numerous vital areas; nonetheless, in this research, its applications in clinical diagnosis were only focused.

In general, proteins or biomarkers cannot be directly detected by only using ePAD; therefore, to make it detectable, the electrode modification is normally required. Several nanomaterials, including carbon nanomaterials (i.e. graphene,

graphene oxide (GO)) and metal nanoparticles (i.e. gold nanoparticles (AuNPs)) were extensively employed to modify sensor surface to enhance the detection sensitivity and electroactive surface area, and also to provide more anchoring sites of an capturing element on the modified sensor surface (biomolecule, antibody)⁵⁻⁷.

Herein, simple, low-cost, sensitive, and selective electrochemical immunosensors for multiplex biomarker detections were developed to provide the alternative platforms used for clinical analysis.

For the first part, the three important biomarkers which responsible for high-risk cardiovascular disease (CVD), inflammation, and sepsis; C-reactive protein (CRP), troponin I (cTnI), and procalcitonin (PCT), were examined using the developed electrochemical immunosensing platforms. These biomarkers have been recognized to be the major cause of CVD which is one of the diseases that cause people death globally (around 18 million people die each year)^{8, 9}. According to statistical reports, several lifestyles or conditions, such as high blood pressure, high cholesterol, excessive alcohol use, diabetes, overweight and physical inactivity, can lead people to a high-risk situation of CVD development⁹⁻¹¹. Hence, to reduce the molarity rate of people globally, the early detection of this disease is tremendously needed. In recent times, several detection approaches, such as colorimetric detection, lateral-flow immunoassay (LFIA), electrochemiluminescence (ECL) and mass-spectroscopy have been continually developed for the investigation of CVD biomarkers^{12, 13}. Nevertheless,

these techniques mentioned above provide low sensitivity and specificity as well as false-positive result in the presence of other biomarkers¹⁴. The most importance is that they require an expensive and bulky instrument, long-time analysis, and skilled expertise¹⁵. To overcome these limitations, this research therefore developed an origami paper-based analytical device (oPAD) immunosensor for the detection of CRP. Furthermore, to expand capacity of the proposed design, simultaneous detection of three important CVD biomarkers using a single ePAD was also proposed. The motivation and details of the developed electrochemical sensors and platforms are intensively described in Chapter III, part I, and part II, respectively.

For the second work, the ePAD sensor for iron deficiency anemia marker detection, named ferritin, was created. Ferritin is a crucial biomarker that is used to estimate the risk assessment of iron deficiency anemia (IDA) and responsible for the metallic process of iron stored in a cell¹⁶. It has been reported by the World Health Organization (WHO) that a typical concentration of ferritin within the range of 30 – 300 ng mL⁻¹ and 15 – 200 ng mL⁻¹ for men and women, respectively¹⁷. The lower amount of ferritin in women is caused by losses of iron during menstruation and childbirth. In addition, a smaller or higher amount of ferritin in the blood can cause several health problems, including IDA, infection, hyperthyroidism, and cancer^{18, 19}. In clinical laboratories, ferritin is tested by electrochemiluminescence (ECL), chemiluminescent microparticle immunoassay (CMIA), and immunonephelometric or immunoturbidimetric methods²⁰. These approaches are expensive, time-consuming,

require expertise, advanced instrumentation, and multistep sample preparation. Therefore, a sensitive, selective, and simple POCT device for ferritin detection is required with rapid turn-around time. Therefore, to overcome this challenge, ePAD immunosensor was developed for investigation of trace ferritin levels in the serum sample. The device operation, fabrication, and the detection are demonstrated in part III of chapter III.

Lastly, the ePAD immunosensor was developed to be an automated paper-based platform for the simultaneous determination of hepatitis B (HBV) and hepatitis C core antigen (HCV). HBV and HCV are a chronic viral disease that are an essential global healthcare concern^{21, 22}. A high-level presence of both HBV and HCV can be identified as chronic hepatitis, cirrhosis, and liver cancer.^{23, 24} Over the past few decades, several techniques such as radioimmunoassay, enzyme-link immunoassay (ELISA), and chemiluminescence immunoassay (CMIA) have been reported; however, these techniques are not suitable for point-of-care detection.²⁵ Therefore, a new assay that is highly sensitive, selective, easy to use, and low-cost, is still in great demand. Hence, the report on an ePAD for the simultaneous detection of HBV and HCV using a single device is the aim of this part. The detail of the construction, operation, and application of this proposed immunosensor is provided in part IV of Chapter III.

1.2 Objectives of the research

This research consists of two main developing goals:

1. To develop a novel electrochemical paper-based immunosensor for the determination of essential biomarkers such as CRP, cTnI, PCT, ferritin, HBV, and HCV core antigen.

2. To apply the proposed electrochemical immunosensor for analysis of target analytes in biological samples.

1.3 Scope of the research

To achieve the research objectives, the scope of this research was set as follows:

1. An origami paper-based analytical device (oPAD) was developed for CRP detection using a label-free immunoassay. This immunosensor was created to integrate the electrode preparation and detection using a single PADs device. A graphene-modified screen-printed carbon electrode (G/SPCE) was utilized to improve sensitivity of the electrode system. Gold nanoparticles (AuNPs) were first deposited onto the G/SPCE, followed by a self-assembled monolayer of L-Cysteine. The monoclonal antibody was next immobilized on the modified electrode. The amount of CRP was quantified by detecting the change of charge transfer resistance of the redox mediator ($\text{Fe}(\text{CN})_6^{3-/4-}$) using electrochemical impedance spectroscopy (EIS). The optimization of the assay conditions was investigated and discussed. Moreover, the analytical performance was investigated. Finally, to evaluate the applicability of the oPAD sensor, the certified serum sample with known amount of CRP was used to test.

2. An electrochemical paper-based device (ePAD) for multiplexed, point-of-care detection of cardiovascular disease based on a label-free assay was reported. The ePAD was designed for the simultaneous determination of three essential CVD biomarkers, including CRP, cTnI, and PCT. To create a fluidic channel, an ePAD was fabricated by stacking a wax paper, transparency film, and double-sided adhesive tape. In addition, to detection CVD biomarkers at their optimal conditions, an ePAD has multiple detection zones. Based on a label-free assay, specific antibodies to the target analytes were immobilized on graphene-oxide (GO)-modified carbon electrodes stencil-printed. The determination of target analytes was conducted by measuring the electrochemical current response of redox solution ($\text{Fe}(\text{CN})_6^{3-/4-}$) using square wave voltammetry (SWV). Analytical performances, such as sensitivity, selectivity, and reproducibility, were investigated. Finally, this developed sensing platform was applied to determine CRP, cTnI, and PCT in certified serum sample.

3. A simple and cost-effective ePAD immunosensor based on a label-free format for the determination of ferritin was fabricated. The ePAD device was custom designed on the filter paper to successfully fabricate an immunosensor. The screen-printed graphene electrode (SPGE) was first modified with GO using an inkjet-printing technique. After all, anti-ferritin antibodies were assigned to covalently anchor onto the surface of modified electrode. The present amount of ferritin was then monitored by using differential pulse voltammetry (DPV). Under the optimal conditions, the sensitivity, specificity, and reproducibility of the proposed immunosensor were

carefully examined. This proposed platform was eventually applied to quantify the amount of ferritin in the serum samples.

4. An electrochemical paper-based analytical device (ePAD) for simultaneous detection of hepatitis B (HBV) and hepatitis C core antigen (HCV) using a label-free immunoassay format was developed. The ePAD was created using a wax paper, transparency film, and double-sided adhesive tape to create fluid channels. The components of ePAD consist of a sample and buffer inlets, fast-flow channel, delayed channel, electrode layer, and fan-shape reservoirs, respectively. In this proposed platform, the advantages of fast-flow velocity were taken to create a fast-flow channel for the washing steps of the immunoassay process. Once buffer was loaded, the buffer will automatically flow through the fast-flow channel, delayed channel, and waste reservoirs without the need of an external pump. As proof of concept, the HBV and HCV were used as a model analyte. The optimization of assay conditions and device designs were clearly studied and discussed. The presence of target analytes was examined by using chronoamperometry. To validate the sensor performance, the developed immunosensor was applied to measure the known amount of HBV and HCV in the serum samples.

In summary, there are four chapters in this dissertation. Chapter I is the introduction. Chapter II is the theory arranged into topics as follows: paper-based analytical device, electrochemical detection, electrochemical biosensor, and immunoassay. Next, chapter III demonstrates the development of electrochemical

immunosensing platforms for the detection of some important biomarkers. Lastly, chapter IV is the conclusions and future perspectives.



CHAPTER 2

THEORY

2.1 Paper-based analytical devices

Paper-based analytical devices (PADs) have witnessed explosive growth in the past decade²⁶. A paper-based analytical platform, a material manufactured in thin sheets from the pulp of the fibrous substances, has many unique advantages including; (i) use small sample and less reagent consumption, (ii) fluid transport via a capillary action, (iii) easy to modify and operate to provide high surface area to volume ratio which could improve the limit of detection for various applications, and (iv) the ability to store reagent through its fiber network, and it can be chemically modified through the hydroxyl group (-OH) to introduce a variety of functional properties. Because of these outstanding properties, PAD has been then applied as a simple platform for several analysis applications including chemical, biological, environmental, and clinical diagnosis²⁷⁻²⁹. In this work, the filter paper is used to create the PAD device owing to it provides low cost, uniform thickness and wicking properties as well as superior adsorption.

2.1.1 Fabrication of PAD

Sever fabrication methods, such as microcontact printing, plasma oxidation, photolithography, wax screen printing and dipping as well as laser printing techniques, have been extensively employed to define hydrophobic and hydrophilic zones on the

PAD devices³⁰⁻³². Among these fabrication methods, the wax printing has received considerable interest and broadly used in a wide range of applications as it offers high throughput production and requires only a commercial printer. Hence, this fabrication method is employed to fabricate the PAD device in this dissertation.

2.1.1.1 Wax printing

Wax printing is one of the most popular methods for PAD fabrication owing to its simplicity, high throughput, speed, cost-effectiveness, high resolution, and use common office equipment³³. From these reasons, the wax printing method is suitable for fabrication the PAD device in this research. This method consists of two steps; first, a wax pattern is printed on the paper substrate via a commercial wax-printer. Second, the printed wax pattern was then melt using hot plate or oven to create hydrophobic and hydrophilic zones. For the hydrophobic zone, the melted wax will penetrate through a fiber paper to define a barrier. At the same time, the hydrophilic zone will also be created, generating the fluid channel for detection. Thus, this fabrication technique has gained tremendous attention in use in analytical chemistry as it possesses straightforward method for PADs design with particular application. The patterned hydrophobic and hydrophilic zones on a paper-based substrate and basic step using wax-printing method are shown in Figure 1.

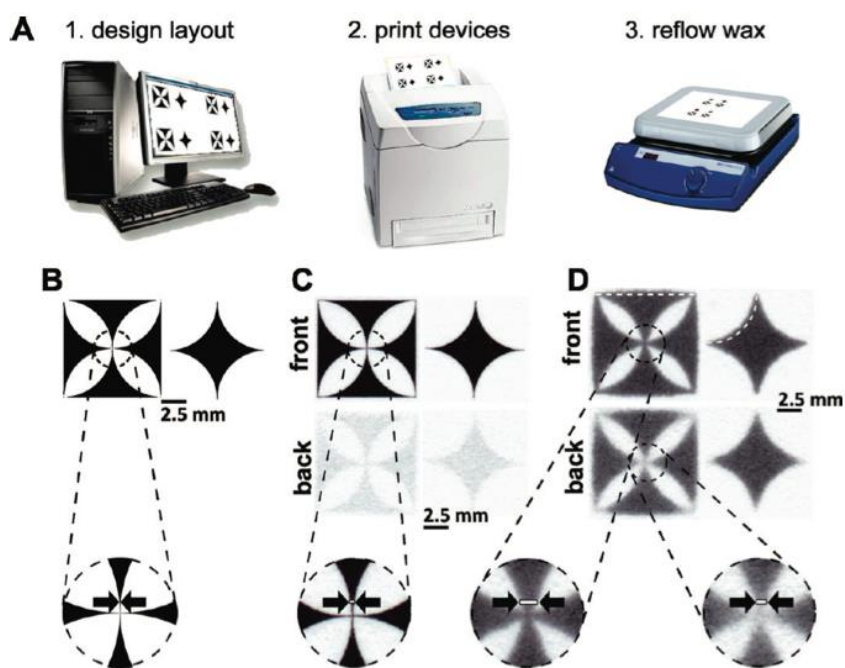
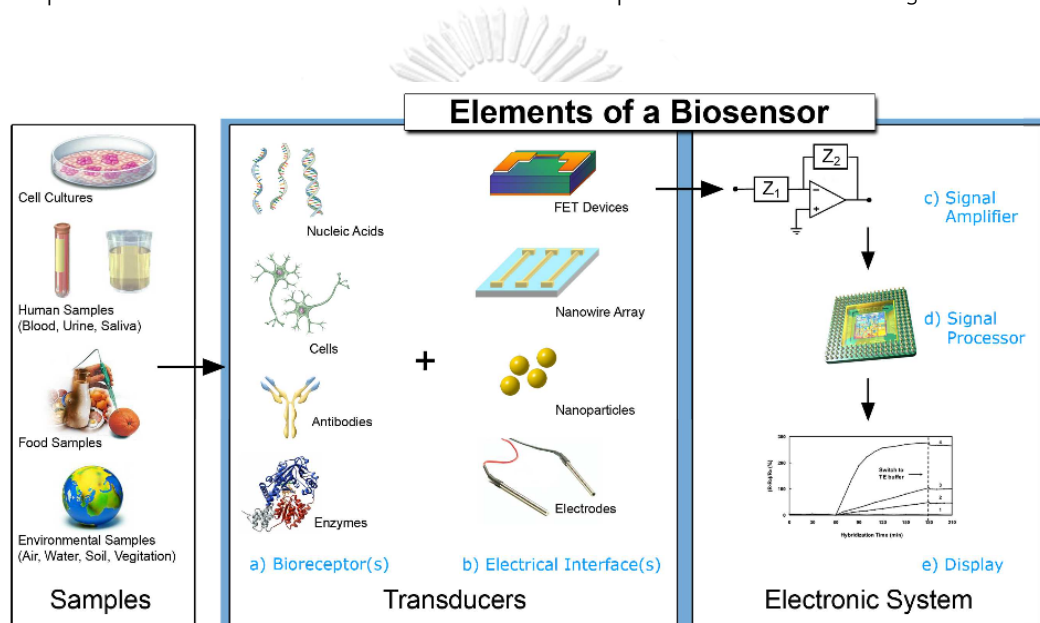


Figure 1. The patterned hydrophobic and hydrophilic zones on paper-based substrate and basic step using wax-printing method³³

2.2 Biosensor

In the past few decades, the interest in a biosensor has experienced explosive growth due to it provides high sensitivity, accuracy, selectivity, and simplicity while maintaining low cost and rapidity³⁴. Typically, a biosensor is defined as an analytical tool which converts a biological response into a quantifiable and processable signal. The compositions of the biosensor are composed of three main parts^{35, 36}. First, bioreceptors such as nucleic acids, enzymes, antibodies, tissues, etc., are elements that specifically bind with target analyte and could induce a chemical reaction to occur. The second part of a biosensor is a transducer element, which generally applied to convert a biological interaction into an electronic signal³⁷. This used transducer was

subsequently amplified by a detector circuit using a proper reference. After the amplification process, the signal will be sent to the third part of the biosensor, which is a computer or software. For the final step, the signal will be processed into a user-friendly way to end-users. Indeed, these characteristics make biosensor applicable in a wide range of samples such as biological fluid, food, cell cultures, and environmental samples³⁸. The summarization of biosensor components is shown in Figure 2.



CHULALONGKORN UNIVERSITY

Figure 2. The components of biosensor³⁸

Although numerous bioreceptors are used in biological sensing, among them, antibody is broadly used with biosensor applications due to it provides high specificity because it can bind only a single position on antigen or analyte. Moreover, it is available in the commercial market, high sensitivity, and also high reproducibility. As aforementioned the advantages of antibody, it is suitable to be developed and

employed as a bioreceptor in our system and coupled with a portable electrochemical sensing technique.

2.2.1 Electrochemical biosensor

An electrochemical biosensor is a sensor that utilizes an electrochemical technique as a detector^{39, 40}. This sensor is considered to be a chemically modified electrode since electronic conducting, semi-conducting, or ionic conducting material is coated with a biochemical film⁴¹. Electrochemical biosensors mostly rely on the enzymatic or redox reaction, which produces electrons in the system. In this platform, electrode systems are commonly used to serve as a transducer, and consist of the reference electrode (RE), the counter or auxiliary electrode (CE/AE), and the working electrode (WE)⁴². Once the target analyte was captured on the WE, the redox reaction may cause the electron transfer across the electrode surface, resulting in change of the detected potential or current response (rate of flow of electrons is proportional to the concentration of target analyte)⁴³.

To create an electrochemical biosensor, the bioreceptor is immobilized on the electrode surface (transducer in electrochemical biosensor). Once the bioreceptor interacts with the target analyte, the change in physical or chemical property on the electrode surface will be obtained. This altered property is then converted into an electric signal, followed by amplifying and exhibiting process. The signal is preferably

converted into several forms, such as current, potential, and charge, etc., which related to the concentration of target analyte in the sample.

For this work, we prefer to convert the obtained signal onto the electrochemical platform since this technique offers high sensitivity and high selectivity, portability, low cost, simplicity, ease to operation and also fast analysis time. It is due to the biological sample, such as serum and blood sample, contains many interferences; therefore, to avoid the matrix in the real sample, high selectivity and sensitivity technique are widely integrated with the biosensor application.

2.2.2 Applications of an electrochemical biosensor

Electrochemical biosensors have received tremendous attention from a research community, with a variety of publications in different areas. The applications of electrochemical biosensor can be summarized as follows:

Biological and clinical diagnosis: It is the most commonly used platform for the determination of various essential biomarkers.

Environment: The biosensor is employed to investigate the heavy metal, organic molecule, inorganic molecule in air, pollution, water, particulate matter, etc.

Food safety and food control: The biosensor is performed to evaluate the food colorants in food dye, water quality, protein in meat, vegetable, etc.

Industry: The biosensor is used to identify the products from organic synthesis process.

Drug development: The biosensor is used to verify the amount of drug in the sample, to detect a certain amount of target molecule in the drug delivery process.

2.3 Immunoassay

An immunoassay is a bioanalytical method, which is used to quantify and detect a specific substance or target analyte using a reaction between the antigen (target analyte) and antibody. Basically, this method is based on the specific binding between an antibody and target antigen. An antibody is used as a reagent that is fixed on the substrate to detect an antigen of interest. Once reagents are mixed and incubated, the target analyte is captured by the antibody, forming an immunocomplex (antigen-antibody complex). For biological applications, depending on the principle of detection, the capture antibody can be either monoclonal or polyclonal. In the development of immunoassay, the monoclonal antibody is more popular over the polyclonal due to its high specificity and high affinity with the target antigen. These unique abilities allow a monoclonal antibody to specifically identify and quantify substances by combining with a variety of detection methods.

Based on the advantages aforementioned above, immunoassay method has been then widely applied in various applications, including pharmaceutical analysis,

foodborne pathogen testing, food industry, allergen testing, and clinical-biological diagnosis. The common components of immunoassay are displayed in Figure 3.

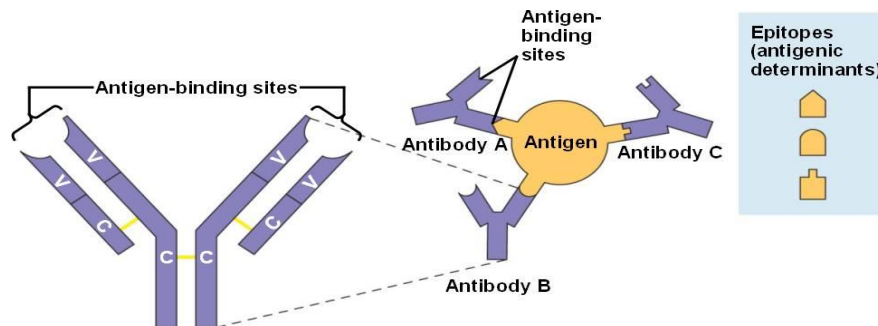


Figure 3. The components of immunoassay consist of antibody (purple) and antigen (yellow).

However, according to the detection platforms, immunoassay systems can be divided into four categories: direct immunoassay, indirect immunoassay, sandwich immunoassay, and competitive immunoassay.

A direct immunoassay, also known as the simplest type of immunoassay, measures the number of antigens or target analytes using a matched pair of antibodies.

An indirect immunoassay, a primary antibody is incubated with an antigen, followed by adding a secondary labelling antibody that recognizes as the primary antibodies.

A sandwich immunoassay typically requires the matched pair of antibodies, one for analyte capture on a solid substrate and one for detection which is a secondary

antibody. This type is the popular immunoassay approach in clinical and biological diagnostics.

The competitive immunoassay relies on the competition between the target antigen and the constant amount of labeling antigen at the same free binding site of the antibody. This method uses the labelling antigen or the labeling antibody for detecting analytes.

The four common types of immunoassay are shown in Figure 4.

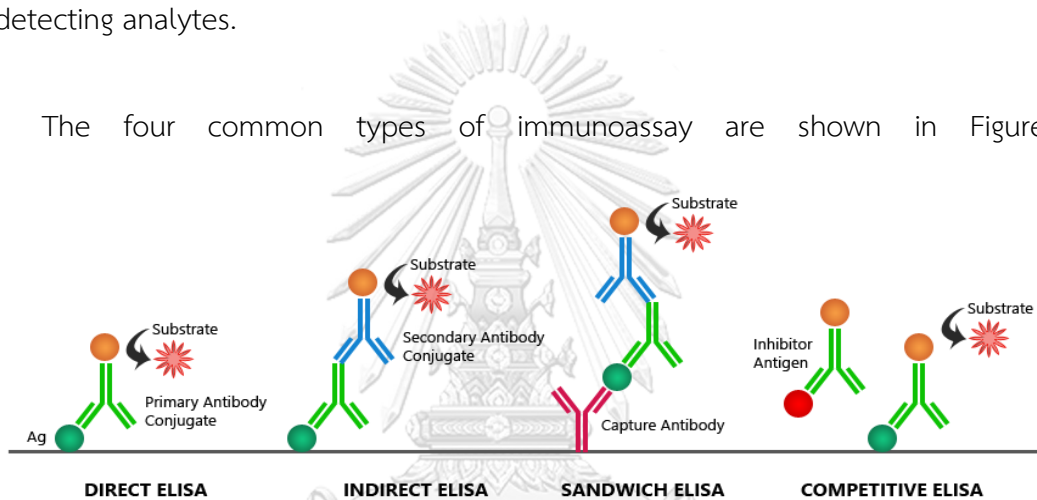


Figure 4. The four common types of immunoassay⁴⁴

As aforementioned, several types of sandwich immunoassay require a labeling molecule or signaling antibody in which a labeling step is needed. This makes the analysis more sophisticated and multiple processes. To circumvent this limitation, a label-free immunoassay has therefore been developed.

2.3.1 Label-free immunoassay

To enable ease of use, an alternative approach called “label-free immunoassay” was developed. This system allows direct conjugation between the

capture antibody and target molecules without any secondary antibody labels needed. By eliminating the requirement of labelling material, the label-free system can potentially operate with minimal or no user intervention, allowing an examination of the binding affinity and kinetic reaction of a biomolecule. Also, this system is cost-effective as it requires only one antibody and uncomplicated step, providing direct information with high throughput. The response signal from this approach can be detected in terms of a mechanical, optical and electrical signal.

Nowadays, electrochemical techniques, such as electrochemical impedance spectroscopy (EIS), square wave voltammetry (SWV), and differential pulse voltammetry (DPV), are implemented for monitoring the changed signal in order to examine the amount of biomolecule/biomarker using the label-free immunoassay system. The comparisons of label-free immunoassay and sandwich immunoassay (labelled immunoassay) are exhibited in Figure 5.

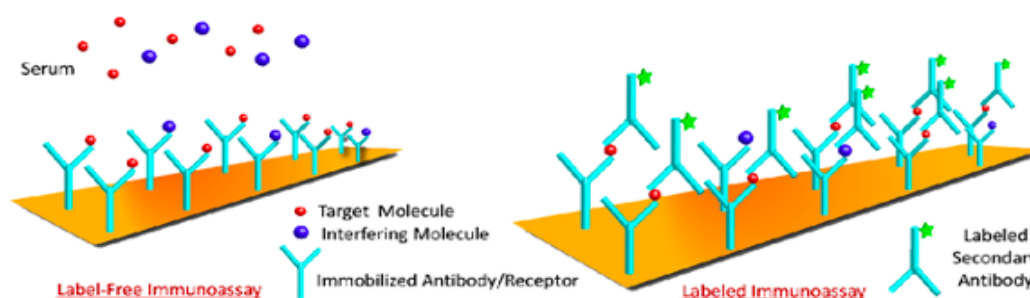


Figure 5. The comparisons of label-free immunoassay and sandwich immunoassay (labelled immunoassay)⁴⁵

2.4 Electrochemical detection

Electrochemical detection is a powerful tool widely applied in various applications; chemical, biological, industrial, food control, environmental, and clinical diagnosis. This detection offers many advantages including high sensitivity, selectivity, simplicity and fast response time, and has the potential to perform simultaneous detection of multiple target analytes in a single device. Therefore, electrochemical detection was miniaturized to create a POCT device for real-time monitoring of the biomarkers or biomolecules in clinical samples. The electrochemical detection can be implemented to study the redox reactions, which are the oxidation and reduction processes of the target analyte at the electrode surface. These redox reactions could occur when electron transfer takes place on the electrode surface. This technique examines electrical changes and transforms them into potential, current and charge, depending on the used transducer. By using this methodology, we can achieve the information from this circumstance, for instance, the concentration, reaction mechanism, kinetic reaction, and the other behavior of analyte species in the solution.

2.4.1 Faradaic and non-faradaic processes

In electrochemical detection, there are two types of processes which can possibly take place on the electrode surface, called “faradaic and non-faradaic processes”. For the faradaic process, the electrons are transferred across the metal-solution interface, which results in oxidation and reduction reactions of electroactive

species. These processes are achieved from the change in the oxidation state of the electroactive species from Faraday's law, which can be explained as follows: when the potential is applied to the electrode system, normally higher than the potential of electroactive species, the reduction reaction will occur at the working electrode. Both the electroactive species and the reduction products then diffuse from bulk solution to the electrode surface. As a consequence, the flow of the current response is proportional to the rate of an electrochemical reaction. Thus, the study of these charge transfer reaction is the goal of the most techniques in analytical electrochemistry.

On the other hand, non-faradaic process, the absence of electron transfer, or charge transfer at the metal-solution interface. Some conditions, such as adsorption and desorption, could occur at the electrode surface without charge transfer. As a result of adsorption or desorption at the electrode surface, the changing of the potential or electrode area, would occur.

2.4.2 Mass transfer modes

The mass transfer process is one of the main fundamental electrochemistry to demonstrate the charge transfer through the electrode surface. The definition of mass transfer is the transition of material or substance in a solution from one location to another location, resulting in a change of chemical potential or electrical property. There are different modes of mass transfer, as shown in Figure 6.

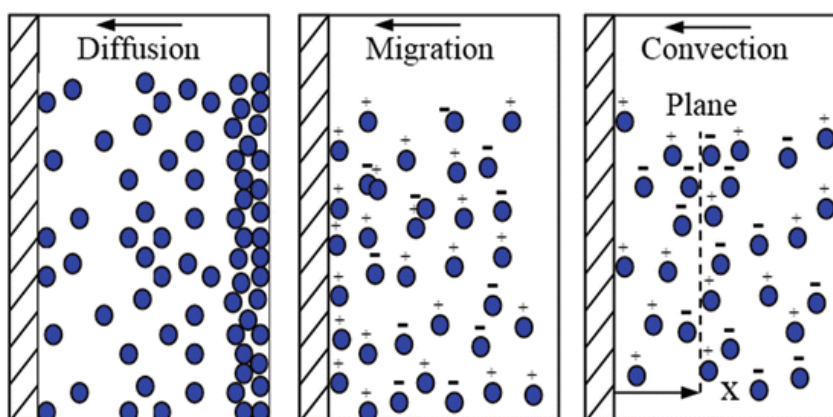


Figure 6. Modes of mass transfer, including diffusion, migration, and convection⁴⁶.

2.4.2.1 Diffusion

Diffusion is the process by which molecules, ions, or other small particles spontaneously mix, or move from one region of relatively high concentration to the other areas of low concentration.

2.4.2.2 Convection

Convection occurs when stirring or hydrodynamic transporting is applied in the detection system. Typically, the natural convection and forced convection occur when fluid flows in the system which is caused by density gradient and may be characterized by stagnant regions, laminar flow, and turbulent flow.

2.4.2.3 Migration

Migration is the movement of charged species under the effect of an electrical field (gradient of electrical potential). The opposite charge of ions could migrate through another opposite side of the electrode. This result consequently

creates the migration in the focused system. In the electrochemical cell, the migration should be addressed by adding a high concentration of supporting electrolyte.

Mass transfer generated on the electrode surface is explained by using a Nernst-Planck equation as following,

$$J_i(x) = -D_i \frac{\partial C_i}{\partial x} - \frac{Z_i F}{RT} D_i C_i \frac{\partial \phi(x)}{\partial x} + C_i v(x)$$

Where $J_i(x)$ is the flux of species i ($\text{mol s}^{-1} \text{cm}^{-2}$) at distance x from the electrode surface.

D_i is a diffusion coefficient ($\text{cm}^2 \text{s}^{-1}$)

$\partial C_i(x)/\partial(x)$ is the concentration gradient at distance x

$\partial \phi(x)/\partial(x)$ is the potential gradient

Z_i is the charge (dimensionless)

C_i is the concentration of the species i (mol cm^{-3})

$v(x)$ is the velocity (cm s^{-1}) in which a volume in electrolyte solution moves along the axis. The three terms on the right-hand side represent the diffusion, migration, and convection, respectively, to the flux.

2.4.3 Electrochemical technique

The electrochemical techniques can be divided into several categories based upon the aspects of the cell that are controlled and measured. Normally, there are

composed of four main types, which are potentiometry, voltammetry, amperometry, and coulometry (Figure 7). In this research, the voltammetry and chronoamperometry are implemented as an electrochemical method. Hence, the electrochemical measurements based on controlled-potential techniques are discussed in this chapter.

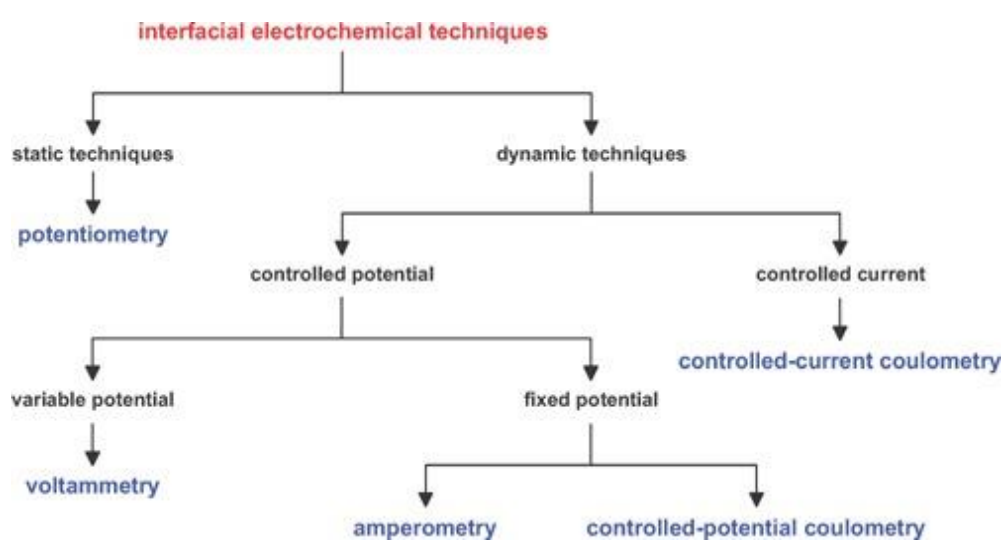


Figure 7. The family tree of the interfacial electrochemical techniques ⁴⁷.

2.4.3.1 Voltammetry

Voltammetry refers to the electrochemical methods in which the current response is investigated as a function of applied voltage or potential to a working electrode (WE). The result from this technique (current vs potential plot) is called voltammogram. These methods are now widely used as they are simple and sensitive. A crucial consideration in voltammetry is the process in which species in electrolyte solution move forward to the electrode surface, where if electroactive, they can be oxidized or reduced depending on the direction of the applied potential. When the

potential is applied to a more positive direction, it becomes more strongly oxidizing. The oxidation reaction is then produced. Contrarily, the electroactive species becomes more reducing during the positive potential is applied to the electrode surface, and the reduction reaction will be forced, respectively. There are a variety of voltammetry employed depending on the applied potential waveforms such as cyclic voltammetry, polarography, anodic stripping voltammetry, linear sweep voltammetry, staircase voltammetry, normal pulse voltammetry, differential pulse voltammetry, square wave voltammetry, anodic stripping voltammetry, cathodic stripping voltammetry, as well as adsorptive stripping voltammetry. In this research, the electrochemical measurement based on controlled-potential techniques are discussed.

2.4.3.2 Cyclic voltammetry (CV)

Cyclic voltammetry (CV) is the most common and popular technique employed in electrochemical detection, which is typically used to investigate the redox reaction process (oxidation-reduction reaction) of target analytes. CV is also employed to study the electrochemical properties, characterization, and electron transfer-initiated chemical reaction of interesting analytes. A triangular potential waveform (Figure 8a) is applied to an electrolyte solution that consists of an electroactive species. In short, the potential is scanned from a negative direction to enforce a reduction reaction of an electroactive species, and the cathodic peak will then be created. Contrarily, if potential is scanned back to a positive direction, the

oxidation reaction will occur at the WE surface. This redox reaction is then detected by a potentiostat as shown in Fig 14. The results from CV technique are called cyclic voltammogram, and the voltammograms are plotted between the current response (i) and potential (E) as exhibited in Figure 8b.

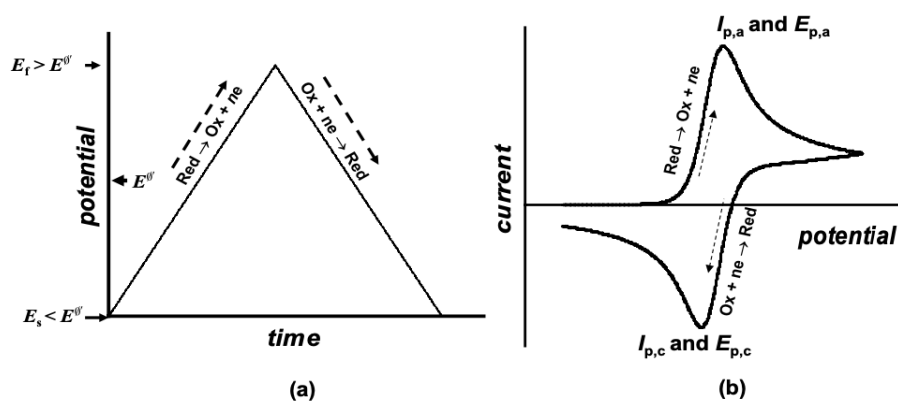


Figure 8. (a) the applied potential waveform as a function with time in cyclic voltammetry and (b) a typical cyclic voltammogram (I-E curve) for a reversible process⁴⁸

For reversible system, at 25°C, the generated peak current (I_p) from CV is proportional to the concentration of target analyte, which can be described by the Randles-Sevcik equation as followed⁴⁹:

$$I_p = (2.69 \times 10^5) n^3 A F C D^{\frac{1}{2}} \nu^{\frac{1}{2}}$$

Where n is the number of electrons, A is the effective electrode area (cm^2), F is a faraday constant (C mol^{-1}), C is the concentration (mol cm^{-3}), D is diffusion coefficient ($\text{cm}^2 \text{s}^{-1}$), and ν is the scan rate (V s^{-1}). The peak position on the potential

axis (E_p) is related to the formal of the redox process. In the reversible system, the formal potential is centered between $E_{p,a}$ and $E_{p,c}$.

$$E^\circ = \frac{E_{p,c} + E_{p,a}}{2}$$

The peak separation (E_p , mV) between the peak potential is given by

$$\Delta E_p = E_{p,a} - E_{p,c} = \frac{59}{n}$$

According to this equation, the number of electrons transferred in the reduction-oxidation reaction can be measured using the separation of cathodic and anodic peak potential. Nevertheless, CV technique is normally used for the qualitative determination of electroactive species due to its low sensitivity.

2.4.3.3 Differential pulse voltammetry (DPV)

Differential-pulse voltammetry (DPV) is one of sub-class techniques in voltammetry substantially implemented to measure trace levels of organic and inorganic species. DPV is often used to study an electrochemical behavior of the target analytes owing to the advantages of 1) the effect of the charging current is decreased; hence, high sensitivity is obtained, 2) only the faradaic current is extracted, consequent, the interpretation of reaction occurs on the electrode is more accurate. The voltammogram from DPV shows that the peak height is directly proportional to the concentration of target analytes, thus, this technique can be used as an alternative approach to precisely quantify an interested analyte.

Generally, in DPV, the applied potential is swept with a series of a pulse (Figure 9a), and the current response is measured at two-point. First, current (i_1) is measured before applying the pulse at position 1 (t_1). The current (i_2) is then measured again at the end of the pulse when the charging current has been decayed (t_2). The difference of the current response between the two points ($\Delta i = i_1 - i_2$) are plotted against the applied potential as presented in Figure 9b.

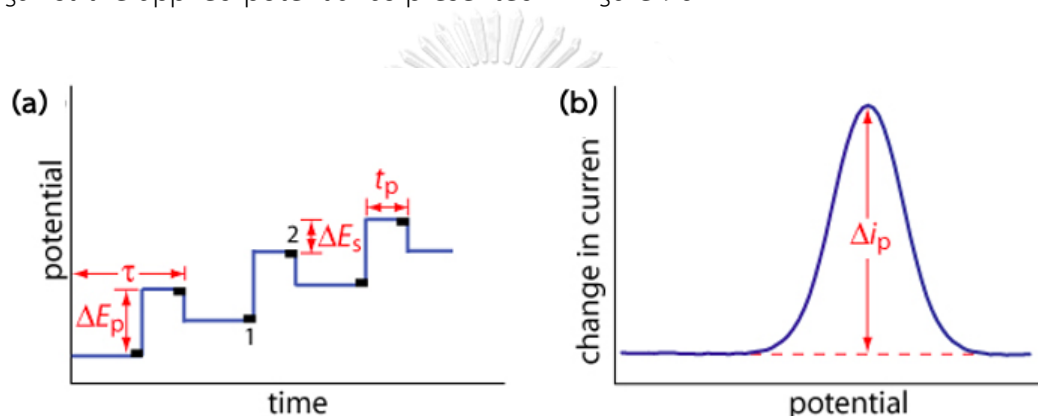


Figure 9. (a) differential pulse waveform where (t_1) and (t_2) is the sampling before and after pulse, respectively, and differential pulse voltammogram (b) where Δi_p is the difference current between two points ($\Delta i_p = i_1 - i_2$)⁵⁰.

2.4.3.4 Square wave voltammetry (SWV)

Square wave voltammetry (SWV) is one of the most powerful voltammetric techniques for determination of trace heavy metals or inorganic compounds. SWV integrates the best features of various pulse techniques such as the background suppression (high signal-to-noise ratio) or sensitivity improvement. The applied potential to the WE is scanned with a series of a pulse (Figure 10a). The current

response is determined two times per cycle, which are at the end of the forward pulse (i_f) and at the end of the reverse pulse (i_r). SWV distinguishes charging current by interrupting the current measurement at the end of pulse. Then, the current response between forward (i_f) and reverse scan (i_r) is calculated. The voltammogram plot between the change in current response ($\Delta i_p = i_f - (-i_r)$) and potential is schemed in Figure 10b. A peak height achieved from SWV is proportional to the concentration of target analyte.

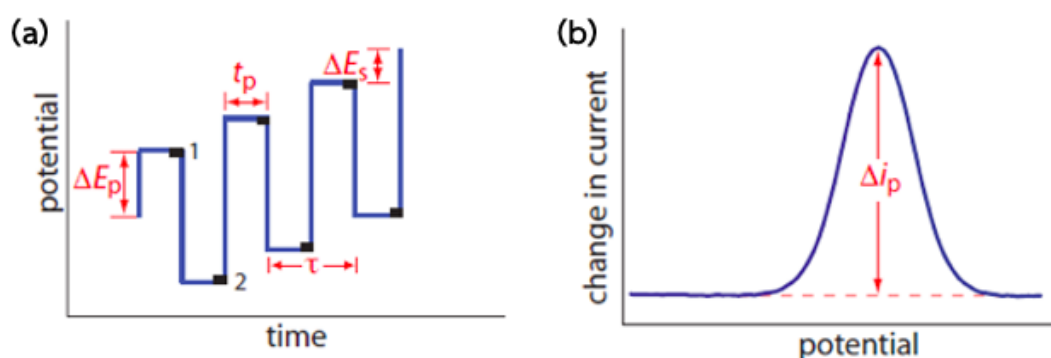


Figure 10. (a) square wave waveform where (t_f) and (t_r) is the sampling before and after pulse, respectively, and typical square wave voltammogram (b) where Δi_p is the different current between two points ($\Delta i_p = i_f - (-i_r)$)⁵⁰.

2.4.4 Electrochemical impedance spectroscopy (EIS)

Basically, electrochemical impedance spectroscopy (EIS) is employed to determine the charge transfer resistance (R_{ct}) between the redox solution and the electrode surface by applying an alternating current (AC) to the electrochemical system. It can be assumed that the excitation of potential or current is applied in term

of sinusoidal potential (Figure 11). The response to this potential is evaluated by using an AC current signal. According to Ohm's law, the impedance or the resistance of the system (Z) is equal to,

$$Z = \frac{E(t)}{I(t)} = \frac{|E|\sin(\omega t)}{|I|\sin(\omega t + \theta)} = |Z| \frac{\sin(\omega t)}{\sin(\omega t + \theta)}$$

Where Z is the impedance of the system

I is the current signal

E is the applied potential

θ is a phase shift

ω is the angular frequency

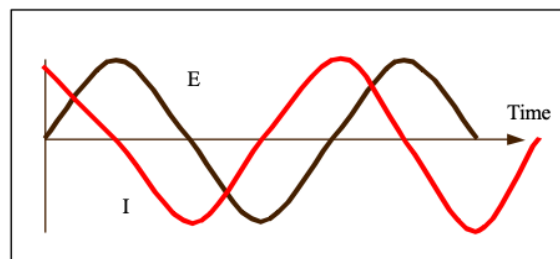


Figure 11. AC waveform for an applied potential (E) and the result of current response

(I).

In recent years, EIS has been extensively applied in various applications such as surface treatment (corrosion and coating) and biosensor applications. The format of EIS results is mostly presented in term of Nyquist plots. Each point of the Nyquist plot stands for an impedance of one frequency scanned from high to low frequency. The

size of the semicircle reflects the resistance of the electrode system. Big semicircle indicates high resistance of the system. The Nyquist plot is exhibited in Figure 12.

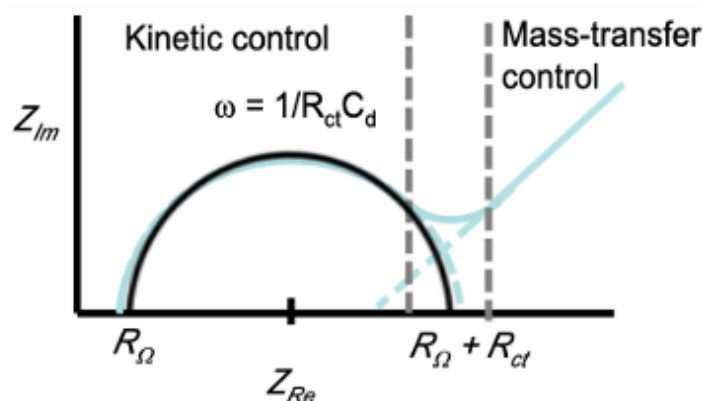


Figure 12. the Nyquist plot where R_{Ω} is solution resistance, R_{ct} is charge transfer resistance, Z_{Re} is real resistance while Z_{im} is the imaginary resistance, ω is the angular frequency, and C_{dl} is interface capacitance.

2.4.5 Chronoamperometry

Chronoamperometry (CA) is another electrochemical method in which step potential is applied for measurement. For this method, the current response is recorded as a function of time as seen in Figure 13a. The applied potential of a working electrode is held at E_1 position at the initial step of the transient experiment. After that ($t \geq 0$), the potential is immediately changed to another position (E_2). The corresponding current which is timely dependent ($i-t$ curve), is recorded, as demonstrated in Figure 13b.

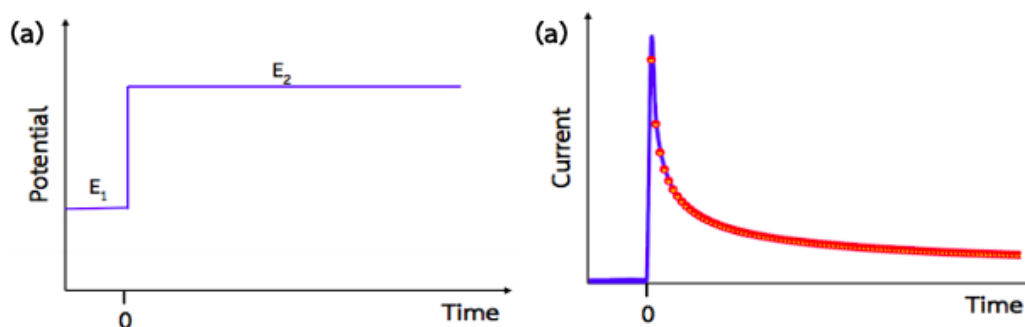


Figure 13. (a) potential simulation and (b) the current response during the chronoamperometric measurement (chronoamperogram)⁵⁰.

2.4.6 Electrochemical cell

An electrochemical cell is a device which produces an electrochemical current from the energy released by spontaneous-redox reaction (reduction-oxidation reaction). The electrochemical cell can be divided into two types: the galvanic and electrolysis cell. An electrochemical cell contains two conductive electrodes, called anode and cathode. The Anode is defined as the electrode where the oxidation occurs, while the cathode is defined as the electrode where the reduction generates. However, in the two electrodes system, the current only flows between two electrodes, and there is no potential is fixed during applying to the electrode. Therefore, an auxiliary electrode known as counter electrode is necessary in order to complete the circuit and to carry current in the system. In this research, three electrodes system was employed. The components of this system consist of the WE, CE, and RE. These electrodes are immersed in an electrolyte solution because an electrochemical

reaction occurs in a medium solution, usually a solvent containing dissolved ions (often called the supporting electrolyte). The properties of supporting electrolyte should provide good solvating power, low viscosity, and rapid transportation of the reactant and products from the electrode reaction. In addition, supporting media should exhibit low resistance, and inert to target analytes as well as electrode. The potentiostat is an electronic device utilized to control and measure the potential difference between WE and RE. For electrochemical measurement, this instrument measures the current flow between WE and CE. The three electrodes set up for potentiostat is sketched in Figure 14.

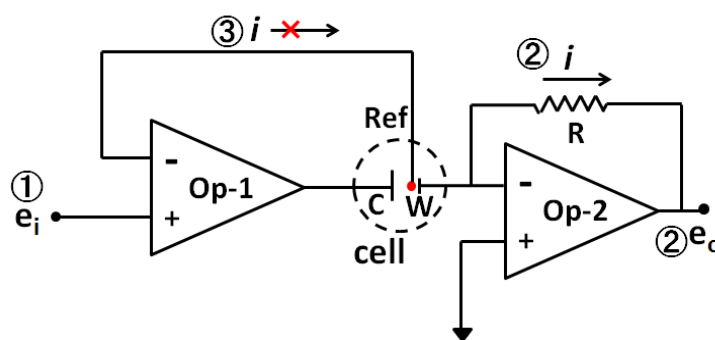


Figure 14. The three electrodes set up for potentiostat setup.

2.4.6.1 Working electrode (WE)

The working electrode (WE) is the most crucial component of an electrochemical cell. The redox reaction and electron transfer of target analytes occur at the interface of this electrode. The WE should be made from the inert materials (i.e., platinum, gold, carbon, and mercury) for long-term stability, good electrochemical inertness, and robustness. In addition, the WE material could provide a well-defined

peak of the target analyte, and reproducible without electrode fouling. The selection of WE material is critical to experimental success. Type, size and shape of materials used to fabricate WE are varied and depended on their applications. In this research, two types of WE which are screen-printed carbon electrode (SPCE) and screen-printed graphene electrode (SPGE), are employed to improve the performance of PAD.

2.4.6.1.1 The screen-printed carbon-based electrode

With the advent of nanotechnology, various nanomaterials, such as carbon-based nanomaterial (i.e., graphene, carbon dots, multiwall carbon nanotube, fullerenes, and single wall carbon nanotube) have been utilized to fabrication of the working electrode for an electrochemical sensor. The outstanding properties of the carbon nanomaterials, for instance, include large surface area, and fast electron transfer. Normally, it provides high electrical conductivity ($\sim 10\text{-}12 \text{ S cm}^{-1}$). In the absence of hydrogen or oxygen, the conductivity of carbon material could increase over ten times compared to the presence of oxygen and hydrogen. Hence, from the outstanding properties, carbon-based material has become a popular material that is extensively applied in an electrochemical sensor. In this research, we fabricated the screen-printed carbon electrode (SPCE) using an in-house screen-printing method. For the construction of SPCE, first, the carbon-based ink was screened on various substrates, for example, paper, polymer sheet, and ceramic. To date, the SPCE has become a popular platform to serve as WE owing to its ease of fabrication, accuracy,

and reproducibility for detection, also it is inherently portable for POCT analysis. Additionally, screen-printed graphene electrode (SPGE) is also popular to serves as an alternative working material. The SPGE was fabrication through a screen-printed method by using a graphene conductive ink. Besides, graphene provides a unique property in term of fast electron transport rate, high thermal conductivity, excellent mechanical flexibility and good biocompatibility. Therefore, it has then extensively employed on extensive applicability in an electrochemical biosensor.

2.4.6.2 Counter electrode (CE)

The counter electrode (CE) or auxiliary electrode (AE), is an electrode which is used to complete the current circuit in the electrochemical cell. Hence, it does not participate in the electrochemical reaction. Commonly, this electrode is made from the inert materials, such as platinum, gold nanoparticle, graphite, glassy carbon, and etc. The surface area of CE should be larger than that of WE as CE could take part as a source of an electron, and it will not limit the kinetic of an electrochemical process during electrochemical measurement.

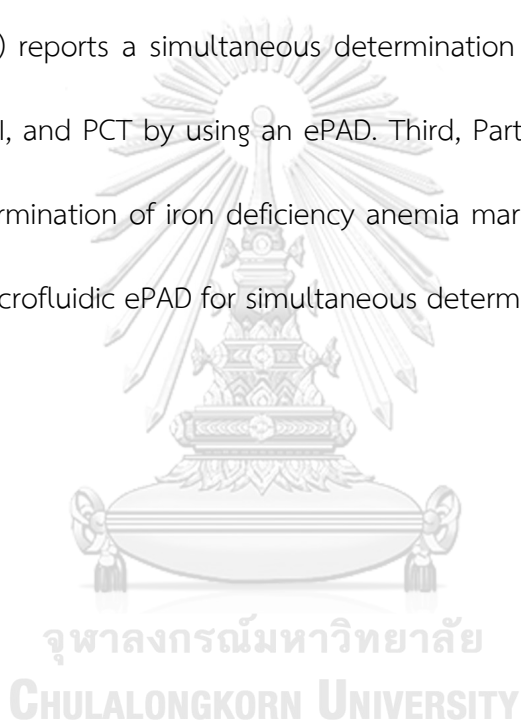
2.4.6.3 Reference electrode (RE)

The reference electrode (RE) is used to measure the potential of WE without passing a current through the electrochemical cell. To be highlighted, the RE could provide a stable, known, and well-defined electrochemical potential. In this research, Ag/AgCl was selected to serve as the RE in an electrochemical cell.

CHAPTER 3

THE DEVELOPMENT OF ELECTROCHEMICAL PAPER-BASED IMMUNOSENSOR FOR THE DETERMINATION OF ESSENTIAL BIOMARKERS

This chapter comprises of four parts. First, Part I (section 3.1) describes the origami paper-based electrochemical immunosensor for C-reactive protein detection using a gold nanoparticles and graphene modified screen-printed carbon electrode. Second, Part II (section 3.2) reports a simultaneous determination of three CVDs biomarkers including CRP, cTnI, and PCT by using an ePAD. Third, Part III (section 3.3) reports an ePAD for the determination of iron deficiency anemia marker. Lastly, Part IV (section 3.4) describes a microfluidic ePAD for simultaneous determination of HBV and HCV.



PART I

3.1 An origami paper-based electrochemical immunoassay for C-reactive protein detection using a screen-printed carbon electrode modified with graphene and gold nanoparticles

(Microchimica Acta)

Suchanat Boonkaew¹, Sudkate Chaiyo¹, Sakda Jampasa², Sirirat Rengpipat³, WeenaSiangproh^{4*}, Orawon Chailapakul^{1,5**}

¹*Electrochemistry and Optical Spectroscopy Center of Excellence (EOSCE), Department of Chemistry, Chulalongkorn University, Pathumwan, Bangkok, 10330, Thailand*

²*Metallurgy and Materials Science Research Institute, Chulalongkorn University, Bangkok, Thailand*

³*Department of Microbiology, Faculty of Science, Chulalongkorn University, Pathumwan, Bangkok, 10330, Thailand*

⁴*Department of Chemistry, Faculty of Science, Srinakharinwirot University, Wattana, Bangkok, 10110, Thailand*

⁵*Center of Excellence on Petrochemical and Materials Technology, Chulalongkorn University, Pathumwan, Bangkok, 10330, Thailand*

**Corresponding author at: Electrochemistry and Optical Spectroscopy Center of Excellence (EOSCE), Department of Chemistry, Chulalongkorn University, Pathumwan, Bangkok, 10330, Thailand. E-mail: corawon@chula.ac.th

*Corresponding author at: Department of Chemistry, Faculty of Science, Srinakharinwirot University, Wattana, Bangkok, 10110, Thailand. E-mail: weenasi@hotmail.com

Abstract

An origami paper-based electrochemical immunoassay for C-reactive protein (CRP) detection is described. The assay integrates multiple steps of electrode modification into a single device. A graphene-modified screen-printed carbon electrode (G/SPCE) was employed to enhance sensitivity. Gold nanoparticles (AuNPs) were first electrodeposited onto the G/SPCE, followed by a self-assembled monolayer (SAM) of L-cysteine. The capture anti-CRP was then covalently immobilized on the modified electrode. CRP was quantified by measuring the changes in the charge-transfer resistance (R_{ct}) of the electrode by using hexacyanoferrate as the redox probe. Cyclic voltammetry (CV) and scanning electron microscopy (SEM) were also applied to verify the successful modification of the electrode. Under optimal conditions, impedance increase in the 0.05-100 $\mu\text{g mL}^{-1}$ CRP concentration range, and the limit of detection (LOD) is 15 ng mL^{-1} (at $S/N = 3$). The immunoassay was successfully applied to the determination of CRP in a certified human serum sample. This method is simple, low-cost, portable and disposable.

Keywords: C-reactive protein, paper-based analytical devices, Graphene, Screen-printed carbon electrode, Electrochemical impedance spectroscopy

3.1.1 Introduction

C-reactive protein (CRP) is an acute-phase protein synthesized by the liver which can be found in human serum. In clinical diagnosis, CRP is commonly used as a biomarker of an infection or inflammatory process in our body. Normally, the CRP level is less than $3 \mu\text{g mL}^{-1}$ in the blood of healthy humans^{51, 52}. However, the CRP level can significantly increase 1000-fold over the normal range within 24-48 h in the presence of inflammation. This leads to a risk of cardiovascular disease or heart attack^{51, 53, 54}. Thus, a method to detect CRP levels in the blood to use to verify a risk factor assessment for these diseases is needed. In the past few decades, several techniques have been developed for CRP detection, such as radial immunodiffusion, radioimmunoassay, luminometric assay, nephelometry, and turbidimetry, as well as enzyme-linked immunosorbent assay (ELISA)^{55, 56}. However, the aforementioned techniques have some limitations. In particular, these techniques require expensive and complicated instrumentation, as well as a large sample volume. In addition, limit of detection of these techniques are inadequate to detect a trace level of CRP in human serum (less than $3 \mu\text{g mL}^{-1}$)^{55, 57}. Therefore, a detection method that offers a short analysis time, a simple and low-cost process, high sensitivity and selectivity is still in demand and important for CRP detection.

Electrochemical techniques have attracted considerable interest to be employed as an alternative method in various applications of immunoassays since it provides high sensitivity, fast analysis time, and requires inexpensive equipment.

Moreover, the detection part of this technique can be reduced leading to use a small volume of sample. These advantages make electrochemical detection especially suitable as a tool for diagnostic applications^{54, 58}. In addition, the screen-printing technique has been developed to enable the mass production of an electrochemical sensor platform onto a disposable, combustible and low-cost substrate^{59, 60}. The combination of these two techniques means that the electrochemical sensor has received more interest in use and makes the sensor become more cost-effective, to be applied in various applications.

Previously, various nanomaterials such as gold nanoparticles (AuNPs)^{61, 62}, copper nanoparticles (CuNPs)⁶³, nitrogen-doped graphene quantum dots (N-GQDs) supported by surfactant-free AuPdCu ternary nanoparticles (AuPdCu/NGQDs)⁶⁴, and quantum dots (QDs)⁵⁶ have been applied for labeling materials of CRP detection. In our previous work⁶⁵, the electrochemical immunosensor based on anthraquinone (AQ)-labelled antibody for CRP detection was proposed, and a good limit of detection was also achieved. Nevertheless, in the previous work requires a labeling step which makes the preparation more sophisticated and time consuming. In another study⁶², an immunochromatographic test was developed for simultaneous determination of CRP, cardiac troponin I, and fatty acid binding protein. The AuNPs and Enzyme-linked immunoassay (ELISA) were operated in this system. The color change is proportional to the concentration of presented biomarker. Although, the immunochromatographic assay provides simple and rapid measurement but it still has some drawback, such as

false positive from other biomarkers, low sensitivity, and time consuming. To overcome this limitation, a label-free immunoassay has therefore been developed. The label-free immunoassay allows direct conjugation between the capture antibody and target molecules. Since it provides simple and rapid detection without the requirement of a labeling step, it has therefore received great interest to be employed as a platform for various biomarker detections.

The first microfluidic paper-based analytical device (μ PADs) was proposed by Whitesides' group⁶⁶. This platform has gained more attention in use because of its natural abundance, inexpensiveness, flexibility, disposability and low sample-reagent usage^{58, 67, 68}. These relevant properties make μ PADs attractive and simple platforms for point-of-care monitoring (POCT). Based on these platforms, the origami paper-based system was developed. Origami is the art of paper folding, which originated from Japan⁶⁹. Moreover, the flexibility of the μ PADs was fabricated by folding into a desired configuration⁷⁰. As a consequence, versatile origami paper-based analytical devices (oPAD) have been reported for various cancer marker detections⁷¹⁻⁷³. In addition, the oPAD can be designed to integrate the electrode modifications and analytical measurements in a single device⁷⁴.

Simplifying the detection even further, we present a label-free electrochemical immunosensor coupled with oPAD for CRP detection. A specific pattern of oPAD was designed to integrate the multiple steps of electrode modification into a single device. The presence of CRP was monitored by measuring the changes of charge transfer

efficiency between electrode and the redox couple $[\text{Fe}(\text{CN})_6]^{3-/4-}$ employed using electrochemical impedance spectroscopy (EIS). The influences of variable parameters that affect the sensitivity of detection were evaluated. Furthermore, analytical performances, such as the sensitivity, specificity, repeatability, and reproducibility of the immunosensors, were also examined. This immunosensor was eventually applied to determine CRP in certified human serum samples to evaluate the applicability of this sensor in determining CRP levels. The results exhibited that this immunosensor provides a high sensitivity, stability, and high selectivity for CRP detection without any interference effect from the commonly three proteins tested (bilirubin, bovine serum albumin, and myoglobin).

3.1.2 Experimental

3.1.2.1 Chemicals and materials

All reagents used are analytical reagent grade and used without further purification. CRP in Human serum (Certified Reference Material ERM-DA474/IFCC, Lot: 081M1600V, <https://crm.jrc.ec.europa.eu>) was purchased from Sigma-Aldrich (St. Louis, USA, www.sigmaaldrich.com). The amount of CRP in the sample was measured by immunonephelometric and immunoturbidimetric assays using ERM-DA470 as calibrant. Anti-CRP, Bovine serum albumin (BSA), L-cysteine, sodium chloride (NaCl), potassium chloride (KCl), potassium dihydrogen phosphate (KH_2PO_4), disodium hydrogen phosphate (Na_2HPO_4), sulfuric acid (H_2SO_4) and potassium hexacyanoferrate (III)

($K_3[Fe(CN)_6]$), 1-ethyl-3-(3-dimethylaminopropyl) carbodiimide hydrochloride (EDC), N-hydroxysuccinimide (NHS) were purchased from Sigma–Aldrich (St. Louis, USA, www.sigmaaldrich.com). Potassium tetrachloroaurate(III) ($K[AuCl_4]$) was purchased from Wako Chemicals (Japan, <https://www.wako-chemicals.de>).

Carbon and silver/silver chloride (Ag/AgCl) inks were obtained from Gwent Group (Torfaen, United Kingdom, <http://www.gwent.org>). Industrial-quality graphene powder was purchased from ACS material, LLC (Pasadena, USA, <https://www.acsmaterial.com>). Filter paper grade no.1 (size, 46x57 cm²) was purchased from Whatman international Ltd. (St. Louis, USA, www.sigmaaldrich.com). The screen-printed templates were designed using Adobe Illustrator and made by the Chaiyaboon Co. Ltd., (Bangkok, Thailand, <http://www.chaiyaboon.com>). All aqueous solutions were prepared in ultra-purified Milli-Q water (MQ) ($R \geq 18.2 M\Omega\text{ cm}$) obtained from a water purification system of Merck Millipore (USA).

3.1.2.2 Instrumentation

Field emission scanning electron microscopy (FESEM) (JSM-7001F at 5 kV) and energy dispersive x-ray spectroscopy (EDS) (INCA penta FETx3 model, <https://www.jeol.co.jp/en>) were applied to verify the successful modification of the electrode. A Xerox Color Qube 8570 series wax printer (Xerox, Japan, <http://www.office.xerox.com>) was used to fabricate the oPAD devices. All electrochemical and electrochemical impedance spectroscopy (EIS) measurements

were carried out on a PGSTAT 30 Potentiostat (Metrohm Siam Company Ltd., Switzerland, <http://www.metrohm-autolab.com>) and controlled with the General-Purpose Electrochemical System (GPES) software. In all cases, EIS and cyclic voltammetry (CV) were performed at room temperature ($25 \pm 2 \text{ }^\circ\text{C}$). EIS was measured under the optimal conditions which are in a frequency range of 100 kHz to 0.01 Hz with potential at 0.1 V and perturbation amplitude of 0.01 V using 5 mM $[\text{Fe}(\text{CN})_6]^{3-/4-}$ in 0.1 M KNO_3 as a redox couple. All of the measurements were carried out in triplicate.

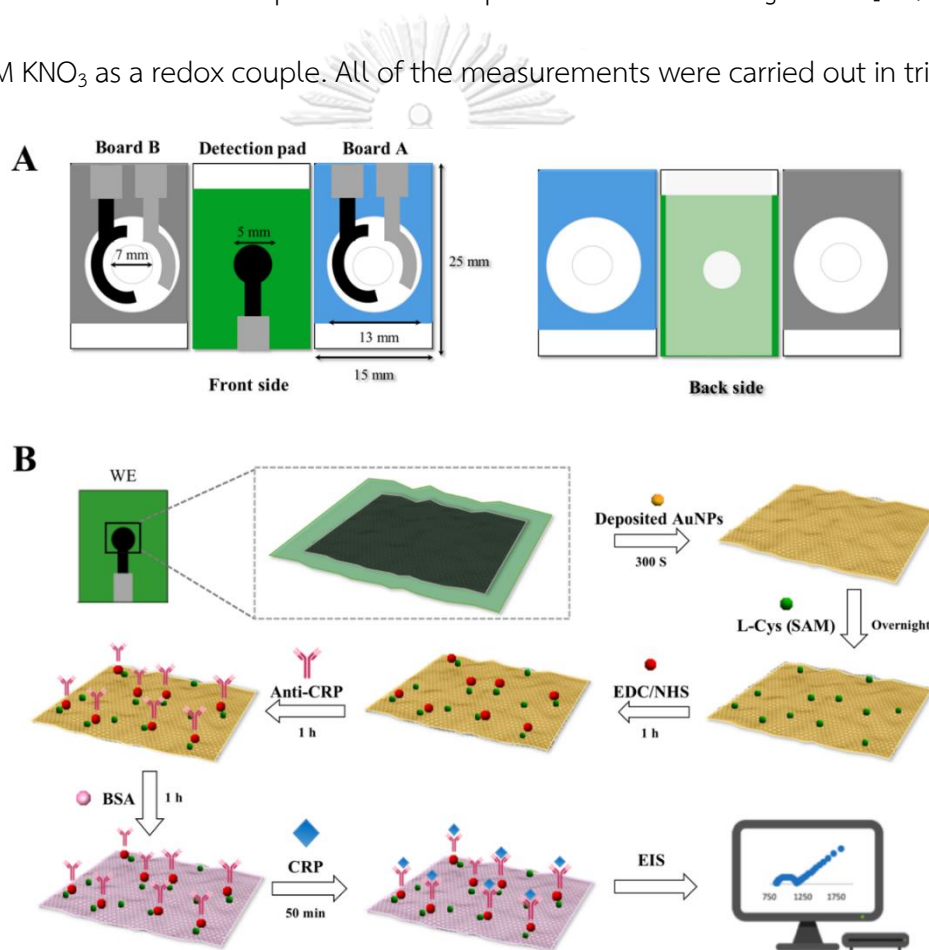


Figure 15. (A) The design and component of the oPAD (B) The overall electrode preparation and immobilization step of the immunosensor for CRP determination.

3.1.2.3 Design and fabrication of oPAD

The wax printing method and filter paper (Whatman No. 1) were selected for the construction of the devices. The pattern of oPAD was designed using Adobe Illustrator CS6. The component of the oPAD consisted of three parts (Fig. 15A): board A, B for counter and reference electrode and detection pad for working electrode. Each part is 25 mm × 15 mm in size. Counter (CE) and reference electrodes (RE) were similarly printed onto both board A and board B to serve as the different functions in modification and detection steps, respectively. The working electrode (WE) was separately designed to avoid the contamination on CE and RE during the modification step. For the fabrication of oPAD, the designed pattern was printed onto the filter paper substrate using a wax printer (Xerox ColorQube 8570, Japan). The printed PADs were subsequently placed on a hot plate for 50 s at 170 °C for melting the printed wax. The wax will penetrate through the filter paper from the top to the bottom layer of the paper to form both the hydrophobic and hydrophilic patterns. After achieving the patterned paper, a conductive carbon-based ink was subsequently screened. The G/SPCE and SPCE were fabricated using an in-house screen-printing method. The composition of G/SPCE ink consisted of graphene and carbon ink at a ratio of 0.001:1 (w/w). The carbon-based ink was screened onto the patterned paper to form both the working (WE) (5 mm of diameter) and counter electrode (CE), followed by screening of Ag/AgCl ink to form both the reference electrode (RE) and the conductive pads. The finished electrodes were baked at 55 °C for 1 h to dry and remove all of the solvent.

After drying the electrodes, the middle of board A and B was then punched to generate sample reservoirs area (7 mm of diameter). Finally, the transparent tape was attached onto the backside of the detection pad to prevent the leakage of solutions once the detection was performed.

3.1.2.4 Preparation of the immunosensor and measurement

A direct conjugation between antibody and antigen was assigned in this system. The immobilization step was then performed as previously described⁶⁵. Briefly, board A was first folded onto the detection pad, and subsequent electrodeposition of AuNPs (5 mM $K[AuCl_4]$ solution in 0.5 M H_2SO_4) onto the electrode's surface was induced by applying a constant potential of -0.5 V for 300 s. The AuNPs-modified G/SPCE (AuNP/G/SPCE) electrode was then thoroughly washed with MQ to remove any physically adsorbed substances on the electrode. The AuNP/G/SPCE was treated with 5 μ L of 10 mM L-Cysteine (L-cys) and left overnight at 4 °C. The electrode consisting of self-assembled monolayer (SAM) of L-cys was thoroughly washed with phosphate buffered saline (PBS) pH 7.4 and was then activated by dropping 5 μ L of EDC/NHS (30 mM) and incubation for 1 h. After this step, the carboxyl group was converted to the amine-reactive sulfo-NHS ester. This electrode was denoted as EDC-NHS/L-cys/AuNP/G/SPCE. After the preparation of the EDC-NHS/L-cys/AuNP/G/SPCE, the immobilization was introduced. A 5 μ L solution of the anti-CRP (50 μ g mL^{-1}) was directly dropped onto an EDC-NHS-activated surface and left for 1 h.

The electrodes were then thoroughly washed with PBS to remove any nonspecifically adsorbed antibody on the electrode's surface. Then, a 0.2%w/v of BSA solution was applied to block the nonspecific active sites on the modified electrode for 1 h, followed by washing with PBS. The modified SPCE electrode was stored in the refrigerator at 4 °C when not in use. For the measurement of CRP protein, 5 µL of standard and sample solution containing various concentrations of CRP were dropped onto the modified SPCE electrode and incubated for 50 min at 4 °C, followed by washing with PBS. For the detection part, board B was then folded to the detection pad, followed by the addition 100 µL of a 5 mM $[\text{Fe}(\text{CN})_6]^{3-/4-}$ (Fig. 16). After this step, the system became ready for electrochemical detection using the EIS technique, in a frequency range of 100 kHz to 0.01 Hz and amplitude of 0.01 V using 5 mM $[\text{Fe}(\text{CN})_6]^{3-/4-}$ in 0.1 M KNO_3 as the redox couple. This technique determines the change of charge transfer efficiency between electrode and redox couple $[\text{Fe}(\text{CN})_6]^{3-/4-}$. The obtained results will give a semicircle diameter. The preparation and electrochemical detection of the CRP immunosensor is shown in Fig. 15B.

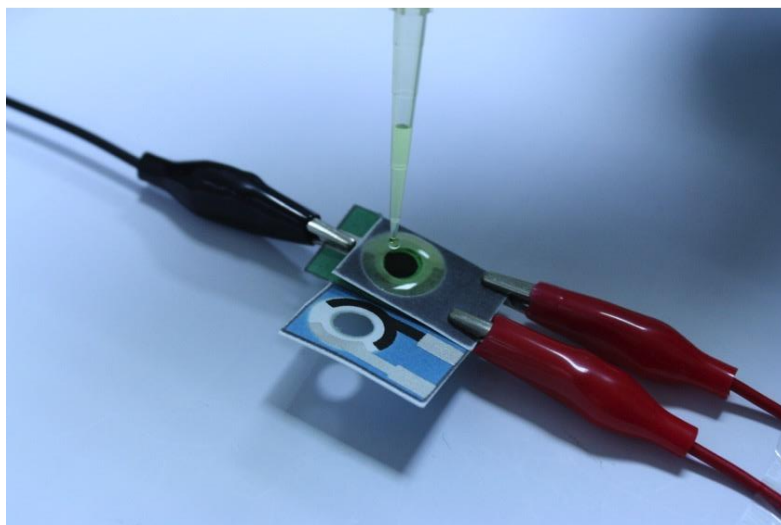


Figure 16. Photograph of the oPAD device connected with PG30 potentiostat to measure the R_{ct} of electrode surface.

3.1.2.5 Preparation of serum samples

The certified reference materials were purchased from the JRC, Directorate for Health, Consumers & Reference Materials (Belgium). The standard or certified CRP in serum samples ($41.2 \mu\text{g mL}^{-1}$) were diluted with PBS buffer (pH 7.4) to the designated concentrations (from 5 to $40 \mu\text{g mL}^{-1}$). The dilutions were kept in the refrigerator until use.

3.1.3 Results and discussion

3.1.3.1 Characterization of the modified electrode

The surface morphologies of the modified and unmodified SPCE were characterized using SEM. As seen in Fig. 17, the graphene-modified SPCE (Fig. 17B) exhibited a rough surface and a stack of graphene layers compared to the unmodified

electrode (Fig. 17A). After the electrodeposition of AuNPs was introduced, the homogenous distribution and size of AuNPs were observed on electrode surface is shown in Fig. 17C. Furthermore, a SEM/EDS analysis of AuNPs was also performed, is shown in Fig. 17D, 17F, and Fig. 18. The EDS spectrum shown the presence of gold (Au), which verifies the successful modification of AuNPs onto the electrode surface. The diameter of AuNPs is approximately 50-70 nm. The uniform distribution of AuNPs on the electrode surface increase the surface area and also affects the number of biomolecule anchoring sites. This ultimately, amplifies the electrochemical signal ⁷⁵. In Fig. 18F, carbon (C) is also present, which can be attributed to the carbon and graphene composition of the carbon-based ink.

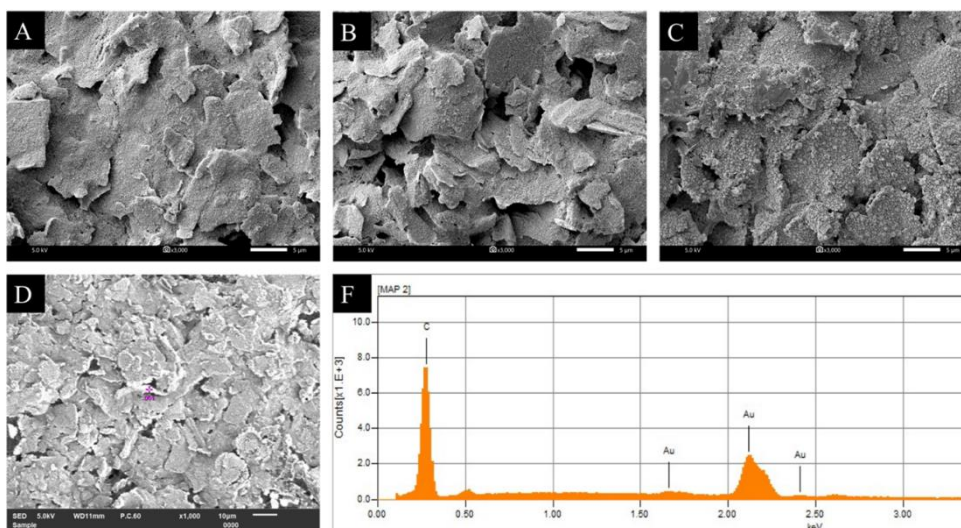


Figure 17. SEM images of the SPCE (A), G/SPCE (B), AuNP/G/SPCE at 3000 x magnification (C), the photomicrograph (D) and the corresponding EDS spectra (F) of the AuNP-modified on the electrode surface.

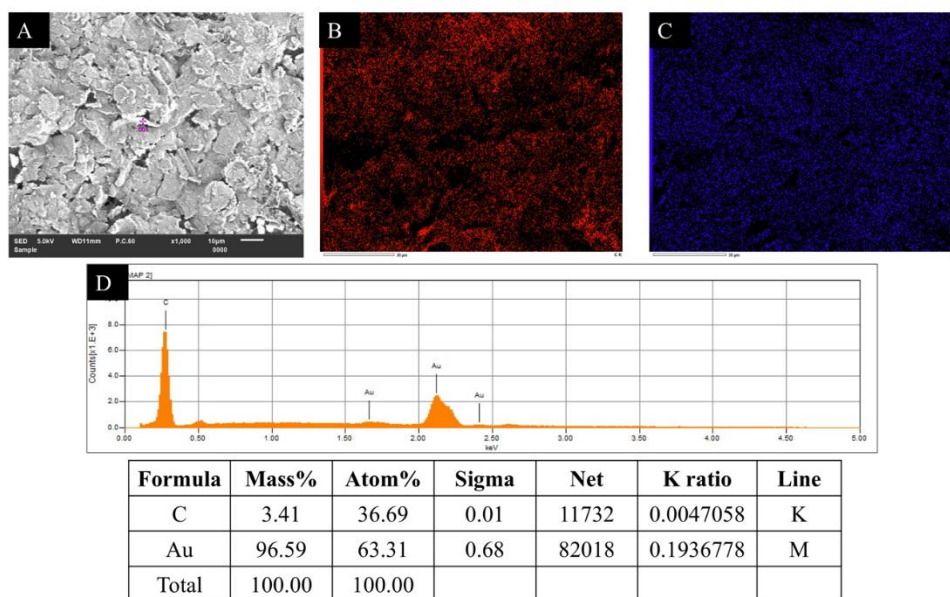


Figure 18. SEM/EDS images of the AuNPs on G/SPCE (A), K line of C atom presented as the composition of the carbon-based ink (B), M line of AuNPs on the G/SPCE surface (C), and the corresponding EDS spectra (D) related to the results tabulated in the table.

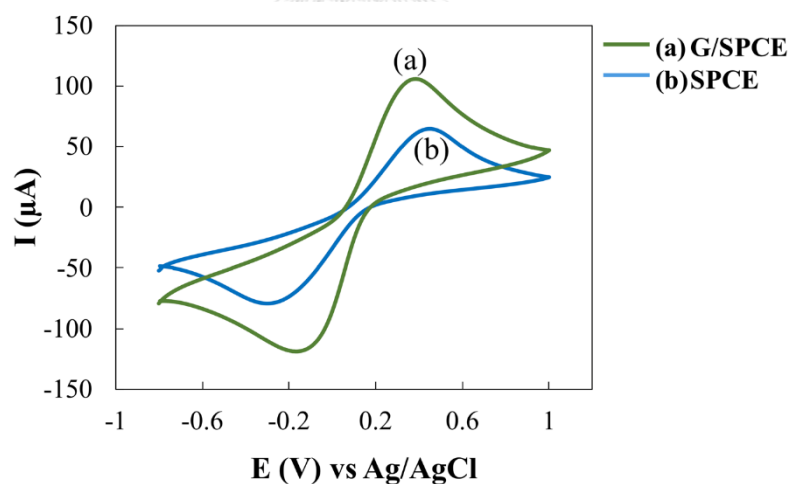


Figure 19. The cyclic voltammogram of (a) G/SPCE (green line), and (b) SPCE (blue line) in the presence of 5 mM $[\text{Fe}(\text{CN})_6]^{3-/4-}$ in 0.1 M KNO_3 was performed from -0.8 to 1.0 V vs Ag/AgCl at a scan rate of 100 mV s^{-1} .

The electrochemical behaviors of the unmodified and modified electrodes were investigated by CV and EIS techniques. The cyclic voltammogram of 5 mM $[\text{Fe}(\text{CN})_6]^{3-/4-}$ in 0.1 M KNO_3 was recorded in the range of -0.8 to 1.0 V. This potential range was selected to provide symmetry redox peak of $[\text{Fe}(\text{CN})_6]^{3-/4-}$ employed. As shown in Fig. 19, the electrochemical signal of 5 mM $[\text{Fe}(\text{CN})_6]^{3-/4-}$ was enhanced approximately 2-fold using the graphene-modified electrode (Fig. 19, curve a) in comparison to the SPCE (Fig. 19, curve b). The increase in current verified that the presence of graphene on the SPCE can enhance the electrochemical sensitivity⁷⁶. Additionally, to confirm that the G/SPCE could improve the surface area, the electroactive surface area (A) was investigated using a 5 mM $[\text{Fe}(\text{CN})_6]^{3-/4-}$ in 0.1 M KNO_3 via CV. The Randles-Sevcik equation according to equation 3.1 was employed to calculate the electroactive surface area^{60,77}:

$$i_p = (2.69 \times 10^5) AD^{1/2} n^{3/2} \nu^{1/2} C \quad (\text{equation 3.1})$$

where i_p is the peak current of the G/SPCE or SPCE (amps), D is the diffusion coefficient of $[\text{Fe}(\text{CN})_6]^{3-/4-}$ ($\text{cm}^2 \text{s}^{-1}$), ν is the scan rate (V s^{-1}), and C is the concentration of $[\text{Fe}(\text{CN})_6]^{3-/4-}$ (M). From the calculation, the electroactive surface areas of 0.056 cm^2 and 0.101 cm^2 were calculated for SPCE and G/SPCE, respectively. The increased area for G/SPCE was found to be 2-times higher than that of SPCE. This increase in electrochemical sensitivity was caused by the use of graphene as the component of

the sensor. The calculation of electroactive surface area of SPCE and G/SPCE are shown in Fig. 20.

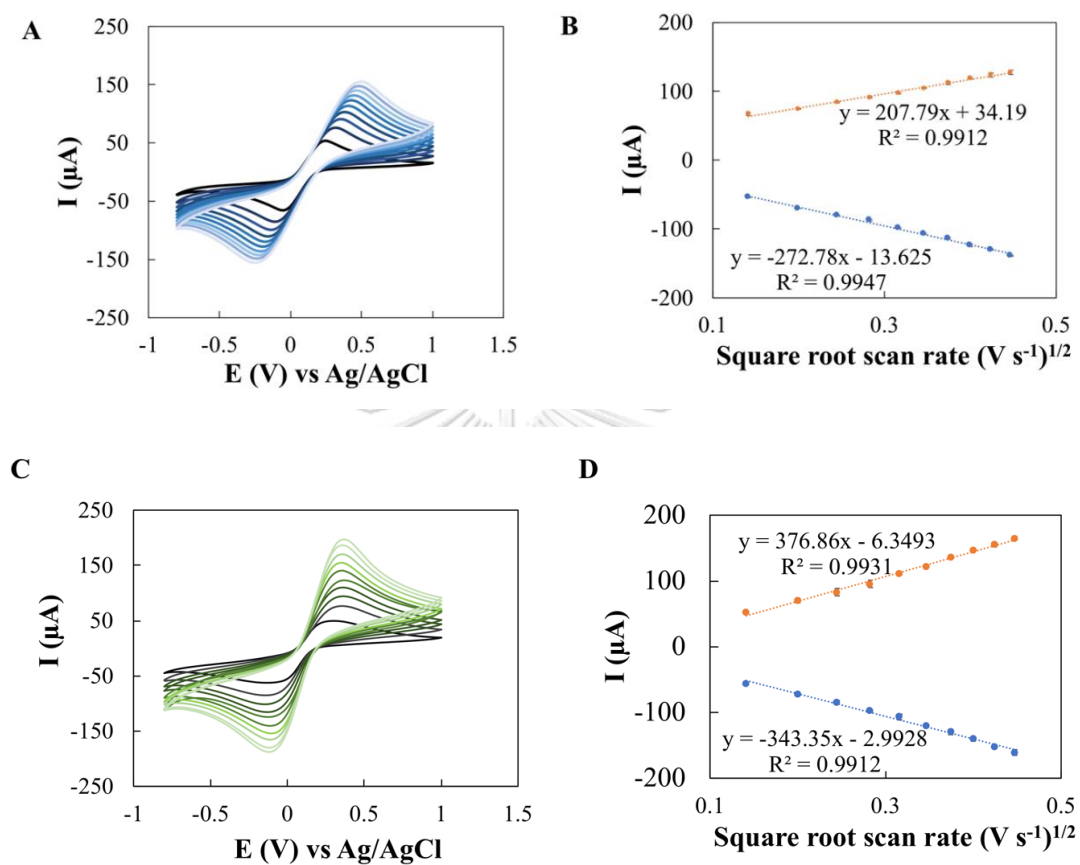


Figure 20. CV comparison of the SPCE (A and B) and G/SPCE electrodes (C and D) in 5 mM $\text{Fe}(\text{CN})_6^{3-/4-}$ at different scan rates from 20 to 200 mV s^{-1}

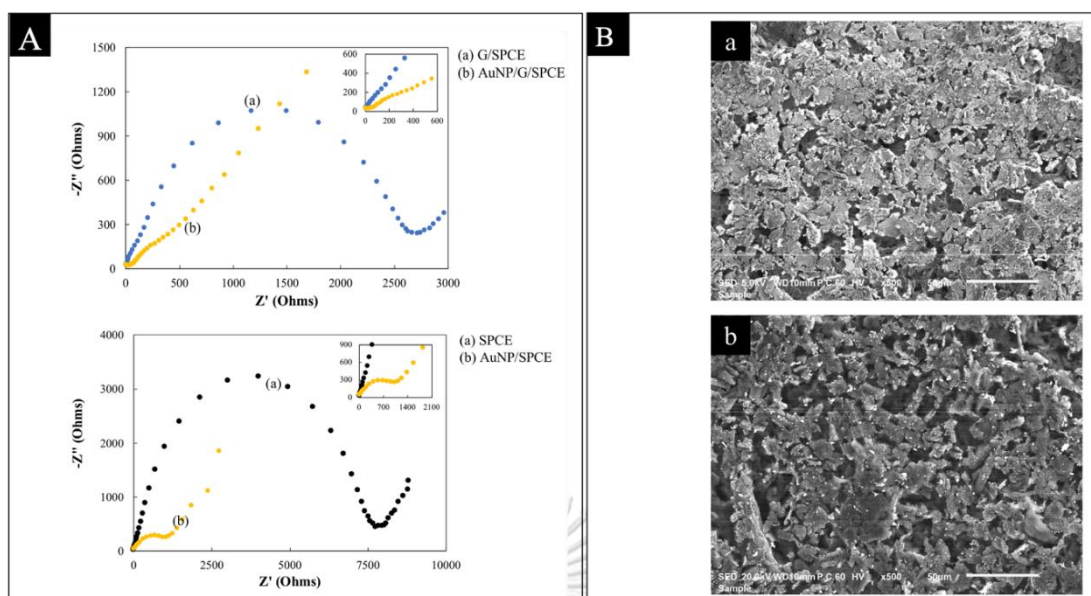


Figure 21. (A) The Nyquist plot of AuNPs-modified on G/SPCE (yellow line), G/SPCE (blue line), and SPCE (black line). The EIS technique was used in a frequency range of 100 kHz to 0.01 Hz with 0.1 V of potential and amplitude of 0.01 V using 5 mM $[\text{Fe}(\text{CN})_6]^{3-/4-}$ in 0.1 M KNO_3 as the redox couple. (B) SEM images of the AuNPs-modified on G/SPCE (a) and AuNPs-modified on SPCE (b) with a 500x magnification.

EIS technique determines the electron-transfer resistance (R_{ct}) between the redox couple $[\text{Fe}(\text{CN})_6]^{3-/4-}$ employed and the electrode surface. The EIS was selected as the detection method due to its simplicity, sensitivity, and rapidness. The format of EIS results is presented in terms of Nyquist plots. Each point of the Nyquist plot stands for an impedance of one frequency scanned from high to low frequency⁷⁸⁻⁸⁰. Semicircle diameters in the high-frequency region reflect the R_{ct} , which controls the electron-transfer kinetics of the redox probe employed 5 mM $[\text{Fe}(\text{CN})_6]^{3-/4-}$ at the electrode interface. As shown in Fig. 21 (A), the R_{ct} values of $[\text{Fe}(\text{CN})_6]^{3-/4-}$ on the

AuNP/G/SPCE and AuNP/SPCE with three sensors ($n=3$) were found to be $19.2 (\pm 3.5)$ ohms and $1019 (\pm 19.1)$ ohms, respectively. From the SEM results are shown in Fig. 21(B), it is clearly demonstrated that the AuNPs modified on both G/SPCE and SPCE electrodes uniformly distributed (approximately 50-70 nm in size) onto the whole electrode surface. However, growing number of AuNPs was deposited and also distributed onto the G/SPCE electrode surface in comparison to the AuNPs deposited onto the SPCE. This is due to stack of graphene layer presented on the G/SPCE electrode surface. The obtained results suggest that the electroactive surface area of the G/SPCE was higher than that of the SPCE, which leads to the uniformity of AuNPs distribution and deposition on the electrode surface.

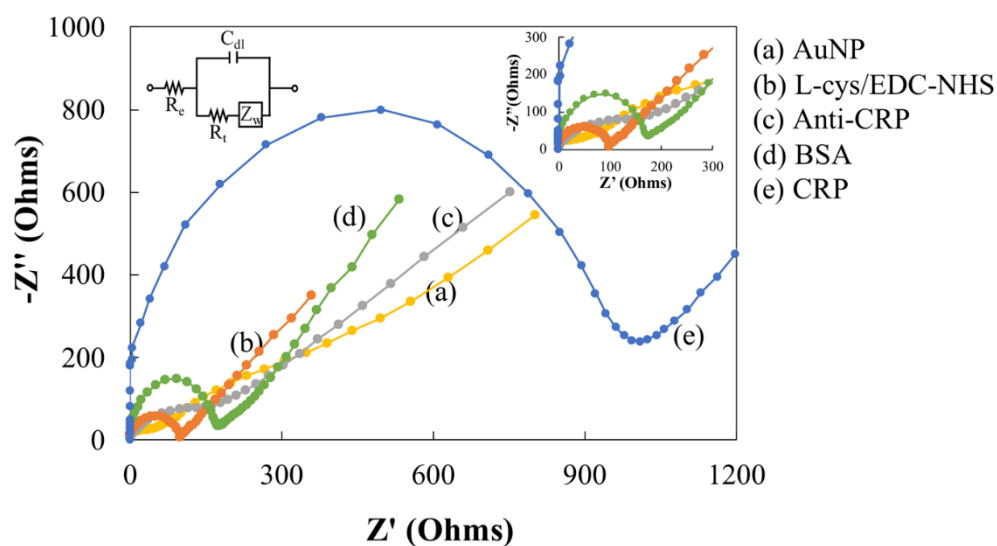


Figure 22. The stepwise of CRP detection using oPAD was characterized by EIS. Nyquist plot of AuNP (a; yellow line), L-cys/EDC-NHS (b; orange line), Anti-CRP (c; grey line), BSA (d; green line), and (e; blue line) $20 \mu\text{g mL}^{-1}$ CRP was immobilized on the electrode surface in the presence of $5 \text{ mM } [\text{Fe}(\text{CN})_6]^{3-/4-}$. Inset picture: equivalent circuit applied

to model EIS data. R_e : the electrolyte solution resistance; C_{dl} : the constant phase angle element; R_t : the interfacial electron transfer resistance; Z_w : the Warburg impedance introduced by the diffusion of ions.

According to the results obtained, the G/SPCE was therefore suitable as a transducer for further electrochemical detection of CRP. Therefore, to obtain a lower detection limit, the G/SPCE was chosen⁶⁵. To verify the successful modification of the oPAD step by step, the EIS technique was implemented. As shown in Fig. 22 (yellow line), the small R_{ct} value of AuNP/G/SPCE at high frequency was observed. This demonstrates a good conductivity and superior electron transfer of AuNPs. After the immobilization was performed, 139.8 (± 11.5) ohms (gray line, Fig. 22) increase in R_{ct} was observed. The increment of R_{ct} suggests that the accessibility of the $[\text{Fe}(\text{CN})_6]^{3-/4-}$ redox probe to the electrode surface was obstructed, resulting in a lower electron transfer rate. The results confirm the successful immobilization of anti-CRP on the surface of the electrode. After the blocking and capturing step, the R_{ct} further increased to 189.6 (± 8.0) ohms (green line, Fig. 22). In the presence of $20 \mu\text{g mL}^{-1}$ CRP, the R_{ct} increased 5-fold to 1024.5 (± 23.5) ohms (blue line, Fig. 22). The R_{ct} value increased after the capturing step due to the conjugation of antibody-antigen complexes formed on the electrode's surface. The R_{ct} increment can be explained by shielding effect of the immunocomplexes because of the negative charge of carbonaceous nanomaterials including graphene. Additionally, these complexes blocked the electron transfer of

redox probe on the electrode surface^{65, 81}. Evidence here therefore confirms the successful modification of the electrode's surface.

3.1.3.2 Optimization of the experimental conditions

To achieve the optimal condition for CRP detection, variable parameters include the amount of graphene loading, the concentration of AuNPs, the deposition time of AuNPs, the amount of blocking agent, the concentration of immobilized antibody and the incubation time, were optimized. The discussions of the optimal conditions are as follows:



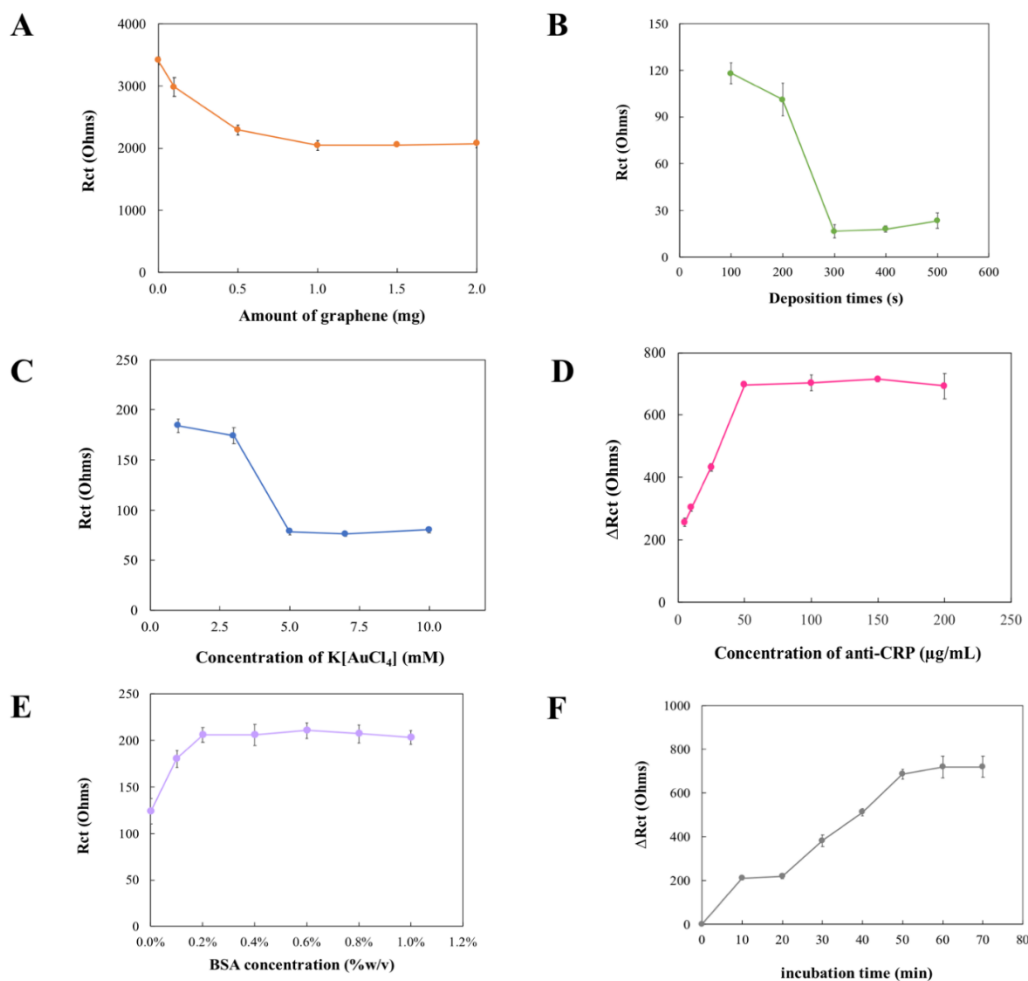


Figure 23. Optimization of the variable parameters: (A) amount of graphene loading, (B) deposition time of AuNPs, (C) concentration of K[AuCl₄], (D) concentration of anti-CRP, (E) the amount of blocking agent (%BSA), and (F) incubation time, using EIS technique in 5.0 mM of [Fe(CN)₆]^{3-/4-} as a redox probe.

3.1.3.2.1 The effect of graphene loading

In this present work, a G powder was used to improve sensitivity of detection. Thus, an appropriate amount of G loading was optimized. The effect of G loading was investigated in the range from 0.0 to 2.0 mg using EIS technique. As shown in Fig. 23 (A), a gradual decrease in G loading results in remarkable decrease in the R_{ct}.

This evidence here proved that G can enhance the electron transfer rate and electrode surface area. However, the R_{ct} of redox probe gradually decrease and reach a plateau signal after the G amount of 1 mg was applied. These results could be due to the agglomeration of graphene at a high concentration⁸². Therefore, a 1.00 mg of graphene was selected as the optimal value for the next studied.

3.1.3.2.2 The effect of AuNPs concentration and deposition time

The electrodeposition method was adopted for the preparation of AuNPs on the electrode surface. First, AuNPs was electrodeposited onto the electrode surface by varying the concentration and deposition time. The deposition time was investigated in the time range from 100 to 500 s. As shown in Fig. 23 (B), the R_{ct} of redox probe decrease with increasing of deposition time, and the signal then reach a plateau. The shorter deposition times may not be sufficient to produce AuNPs, while long deposition times might allow too many AuNPs nanoparticles to be deposited on the electrode surface⁸³. This behavior may due to the formation of particle clusters, leading to the increment of surface thickness which limits the electron transfer ability. The result was confirmed by the SEM image in Fig. 24. Therefore, 300 s of the deposition time was chosen as the optimal condition since it provided the highest sensitivity. Furthermore, the effect of $K[AuCl_4]$ concentration was investigated in the range of 1 to 10 mM as shown in Fig. 23 (C), the R_{ct} of redox probe tends to decrease with increasing of $K[AuCl_4]$ concentration. The lowest R_{ct} was observed with $K[AuCl_4]$ concentration of 5 mM. After this concentration, the R_{ct} becomes stable. This

phenomenon arises from the agglomeration of excess AuNPs on electrode surface, causing a decrease in surface area and electron transfer rate. Hence, 5 mM of $K[AuCl_4]$ concentration was selected for further experiment.

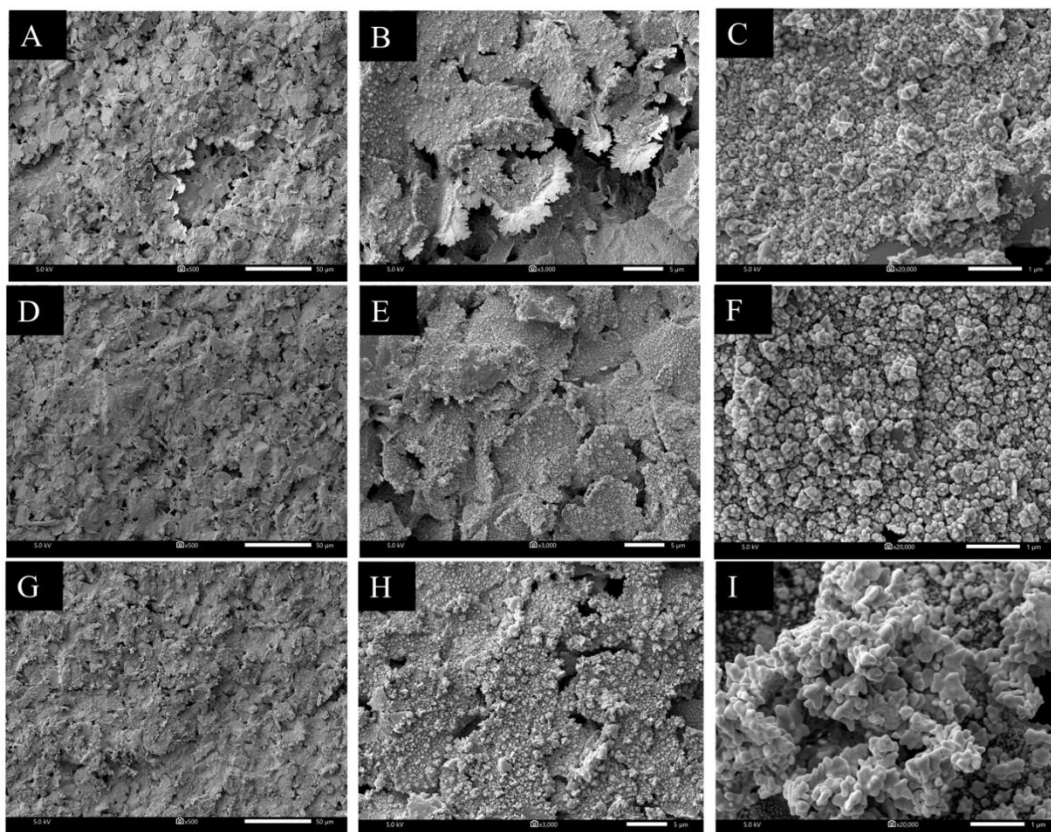


Figure 24. SEM images of the AuNPs at various deposition times on the G/SPCE with different magnifications: 100s (A)-(C), 300s (D)-(F), and 500s (G)-(I).

3.1.3.2.3 The effect of the capture anti-CRP

The concentration of anti-CRP was optimized in the range from 5 to 200 $\mu\text{g mL}^{-1}$ using 20 $\mu\text{g mL}^{-1}$ CRP, 0.2 %w/v BSA and 60 min for the incubation time. The result exhibited that the anti-CRP concentration affected the impedance response. The

R_{ct} was reported in term of the changed R_{ct} (ΔR_{ct}), which calculated from the following equation ⁸⁴.

$$\Delta R_{ct} = R_{ct (CRP-Anti-CRP)} - R_{ct (BSA)}$$

Where $R_{ct (CRP-Anti-CRP)}$ is belong to the R_{ct} value after the immobilization of CRP onto BSA/anti-CRP/EDC-NHS/L-cys/AuNP/G/SPCE. The $R_{ct (BSA)}$ represents the R_{ct} value of BSA/anti-CRP/EDC-NHS/L-cys/AuNP/G/SPCE. As shown in Fig. 23 (D), the ΔR_{ct} gradually increases with increasing the concentration of anti-CRP from 5 to 200 $\mu\text{g mL}^{-1}$. The ΔR_{ct} then reached a plateau after further increasing the anti-CRP concentration, and an anti-CRP of 50 $\mu\text{g mL}^{-1}$ was therefore selected. The obtained results suggested that the active binding between anti-CRP and CRP could be saturated and therefore limited the concentration of anti-CRP⁸⁵.

3.1.3.2.4 The effect of bovine serum albumin (BSA)

BSA was used as a blocking reagent to avoid the non-specific adsorption on the electrode surface. The amount of BSA was investigated in the interval range of 0.1% to 1.0 % w/v using the condition as follows: 50 $\mu\text{g mL}^{-1}$ anti-CRP, and 60 min for incubation time. As can be seen in Fig. 23 (E), the R_{ct} response gradually increased depending on the amount of the applied BSA concentration and the R_{ct} then reached the maximum value at a 0.2% w/v of BSA concentration. At a high concentration of BSA, the R_{ct} value increases due to the increasing of BSA surface density which blocked the surface accessibility of redox probe employed. Moreover, the impedance response

between the blocked and unblocked surface of anti-CRP/AuNP/G/SPCE in the presence of CRP was also compared (Fig. 25). The results revealed that the unblocked surface exhibits almost unchanged signal, while the blocked surface displays the increase in R_{ct} signal. The results obtained can be explained by the non-specific adsorption of antibody-antigen complex on the modified electrode surface. On the other hands, the R_{ct} of the blocked surface was enhanced. It indicated that BSA was successfully blocked the bare region and non-specific adsorption of antibody-antigen complex on the modified electrode surface⁸⁶. Consequently, 0.2 %w/v of BSA was selected as the optimal condition.

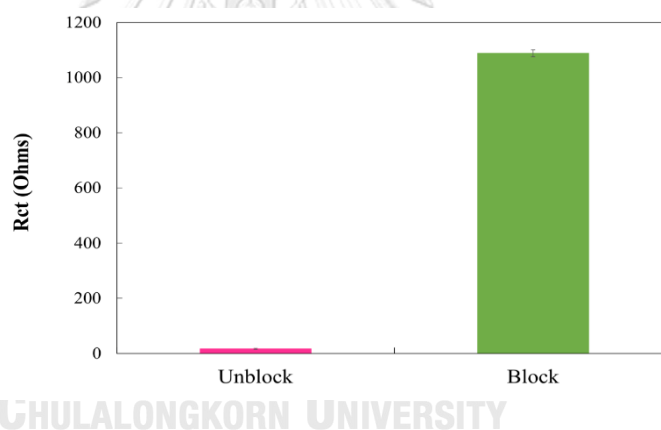


Figure 25. The impedance response between the blocked and unblocked surface of anti-CRP/AuNP/G/SPCE in the presence of 20 $\mu\text{g/mL}$ CRP, using EIS technique in 5.0 mM of $\text{Fe}(\text{CN})_6^{3-/4-}$.

3.1.3.2.5 The effect of incubation time

The influence of incubation time was varied within the range of 10 to 70 min (Fig. 23 (F)). The ΔR_{ct} slightly increases with increasing incubation time and

saturated at 50 min. After that, the ΔR_{ct} value turns to a plateau signal when $20 \mu\text{g mL}^{-1}$ CRP was applied. This indicates that the increasing of incubation time affected the binding efficiency of anti-CRP/CRP complexes. It could be explained by the saturated state between anti-CRP/CRP complexes that could be formed on the electrode surface. As a result, the incubation time of 50 min was selected as a suitable condition for generation of anti-CRP/CRP complexes.

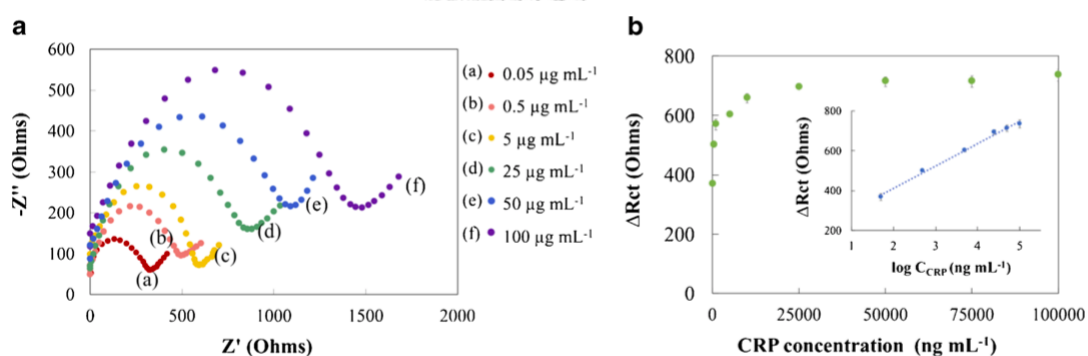


Figure 26. (A) EIS response of the oPAD immunosensor for the detection of various concentration of CRP ($0.05\text{-}100 \mu\text{g mL}^{-1}$) in the presence of $5 \text{ mM } [\text{Fe}(\text{CN})_6]^{3-/4-}$ and (B) Variation of the ΔR_{ct} at different concentrations of CRP (ng mL^{-1}). Inset: Calibration plot between logarithm of CRP concentration and ΔR_{ct} . The data points were averaged from 3 pieces of electrodes.

3.1.3.3 Analytical performance

To evaluate analytical performance of the developed immunosensor, various concentrations of CRP were determined using EIS. As shown in Fig. 26 (A), the EIS response gradually increases with increasing CRP concentration. The value of ΔR_{ct} was

linearity related to the logarithm of CRP concentration from 50 to 100000 ng mL⁻¹ with a limit of detection of 15.0 ng mL⁻¹ (LOD = 3S/N) was obtained ($\Delta R_{ct} = 345.42 \log C_{CRP}$ (ng mL⁻¹) + 171.98, R²= 0.990). The calibration plot is shown in Fig. 26(B). Furthermore, the analytical performance obtained was compared to the previous report^{54, 78, 84, 87, 88}. The summarized data are tabulated in Table 1. The developed immunosensor shows the first-time report of a label-free electrochemical immunosensor on oPAD for CRP detection. Moreover, the substrate used on this device is of low cost and natural abundance. Although the other methods provided a lower detection limit compared to our method, nevertheless it requires a complicated preparation and a modification step. However, the detection limit obtained using this developed sensor sufficiently detects the amount of CRP in a real sample. The CRP level in serum should be below 1 µg mL⁻¹ for the low-risk limit according to the American Heart Association^{65, 89}. Therefore, this immunosensor has a potential to be used as an inexpensive and disposable tool for monitoring CRP levels.

Table 1. The comparison of analytical performance of the other assays for a label-free CRP detection.

Electrode platform	substrate	Measurement principle	LOD ($\mu\text{g mL}^{-1}$)	Linear range ($\mu\text{g mL}^{-1}$)	Incubation time (min)	Ref
VACHFs ^a	silicon wafer	EIS	0.011	0.125 - 5.0	75	87
ssDNA ^b /Au electrode	PDMS ^c	EIS	3.125	3.125-25	10	78
PEG ^d -thiol/Au disk electrode	Au disk electrode	EIS	2.15×10^{-5}	0.061-61.1	60	54
rGO ^e -NP ^f /ITO ^g	glass	EIS	8.0×10^{-5}	0.001-1.0	-	90
3DOM ^h gold film electrode	quartz wafer	EIS	0.0001	0.0001-0.02	60	84
AuNP ⁱ /GI/SPCE ^k	paper	EIS	0.015	0.05-100	50	This work

^a Vertically aligned Carbon nanofiber

^b Single-strand DNA

^c Polydimethylsiloxane

^d Polyethylene glycol

^e Reduced graphene oxide

^f Nanoparticles

^g Indium tin oxide

^h Three-dimensional ordered mesoporous

ⁱ Gold nanoparticles

^j Graphene

^k Screen-printed carbon electrode

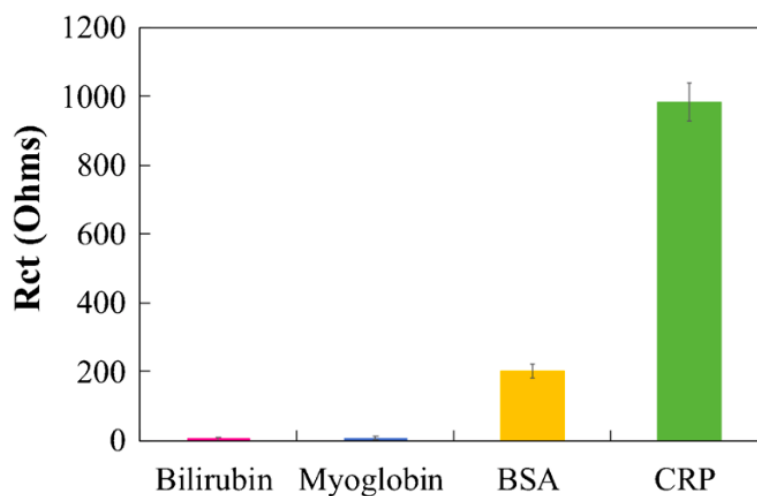


Figure 27. The R_{ct} response in EIS of CRP detection after immobilization with $50 \mu\text{g mL}^{-1}$ bilirubin, myoglobin, 10% w/v BSA, and CRP $5 \mu\text{g mL}^{-1}$ using $50 \mu\text{g mL}^{-1}$ Anti-CRP, 0.2% BSA, and in presence of $5 \text{ mM } [\text{Fe}(\text{CN})_6]^{3-/4-}$.

3.1.3.4 Selectivity

To investigate the selectivity of the CRP immunosensor, the possible interferences that can be found in the real sample, such as myoglobin, bilirubin and BSA were then tested. As seen in Fig. 27, the results show that the changed R_{ct} was obtained in the presence of $5 \mu\text{g mL}^{-1}$ CRP, $50 \mu\text{g mL}^{-1}$ myoglobin, bilirubin, and BSA. However, the largest change in R_{ct} was only achieved in the presence of CRP, whereas the R_{ct} had no change in the presence of 10-fold greater concentrations of myoglobin and bilirubin compared to CRP. A negligible change in R_{ct} for BSA testing was also achieved. This change in R_{ct} possibly is affected by the BSA content in the serum sample which is lower than 3.9 g dL^{-1} or 3.9% w/v⁹¹. Nevertheless, this value was

acceptable. These results suggest that the developed label-free immunosensor provided excellent selectivity for CRP detection.

3.1.3.5 Stability, reproducibility and repeatability of the CRP immunosensor

To investigate the storage stability of the CRP immunosensor, the BSA/anti-CRP/EDC-NHS/L-cys/AuNP/G/SPCE was prepared and stored in a refrigerator at 4°C for 3 weeks until use. The result revealed that a 97.54±0.02% preservation in ΔR_{ct} value was obtained within 15 days compared to the initial ΔR_{ct} value (Fig. 28). After 15 days, the ΔR_{ct} gradually decreased, indicating the loss of anti-CRP activity. According to the achieved result, it can be therefore concluded that the developed CRP immunosensor has good stability for up to 15 days.

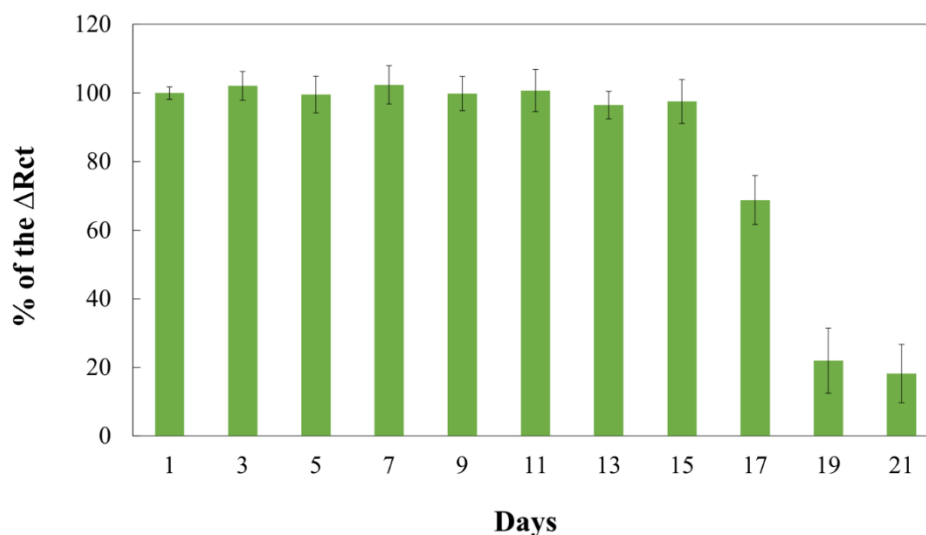


Figure 28. The storage stability of oPAD for CRP detection.

Furthermore, the reproducibility of the immunosensor in repetitive measurement ($n = 3$) of each concentration within intra-assay was studied. These immunosensors were prepared using the same experimental conditions. The variation coefficient (presented in terms of %RSD) for CRP concentration in the range from 0.05 -10 $\mu\text{g mL}^{-1}$ were found in the range of 2.19 to 3.39 (data not shown). To investigate the repeatability, the R_{ct} value on the same immunosensor was examined. The %RSD was found to be less than 1.54% with 10 $\mu\text{g mL}^{-1}$ CRP, which are lower than 5%. This result indicated that the CRP immunosensor offers acceptable reproducibility and repeatability.



Table 2. Recoveries of the origami paper-based electrochemical immunosensor for CRP detection. The data were averaged with three pieces of sensors.

Sample	CRP concentration ($\mu\text{g mL}^{-1}$)	Measured concentration	% Recovery	% RSD
1	5.0	4.9 ± 0.1	97.9	2.3
2	10.0	9.9 ± 0.3	99.2	3.5
3	20.0	20.8 ± 1.9	103.9	4.9
4	40.0	39.2 ± 1.0	98.0	2.6

3.1.3.6 Detection of CRP in a certified human serum sample

To evaluate the applicability of the developed immunosensor for CRP detection, the certified human serum sample was used. After this step, the serum sample was dropped on the immunosensor and incubated for 50 min. The electrochemical detection was performed using the EIS technique, in a frequency range of 100 kHz to 0.01 Hz with 0.1 V of potential and amplitude of 0.01 V. The amount of CRP in the certified sample was determined using an external standard method. As shown in Table 2., the %recovery and relative standard deviation (RSD) with three sensors were found in the range from 98.0% to 103.9% and from 2.3% to 4.9%, respectively.

In addition, a paired t-test at a 95% confidence interval was obtained from certified sample analysis. The results obtained by this method were not significantly

different between the developed and standard methods. Therefore, it can be concluded that the method can be applied to measure CRP in human serum.

3.1.4 Conclusion

A label-free origami paper-based electrochemical immunoassay for CRP detection was successfully developed for the first time. This label-free system offers advantages over widely used electroactive indicators, or labels, since it eliminates the labeling step. The oPAD was custom-designed to combine the multiple steps of electrode modification and detection into a single device. The capture anti-CRP was covalently attached onto the electrode's surface via EDC/NHS coupling. The presence and absence of CRP was monitored by the EIS technique. In the presence of CRP, the R_{ct} signal significantly increased in a concentration-dependent manner, but no signal change was detected with the absence CRP. Under optimal conditions, this immunosensor exhibited a good selectivity against bilirubin, myoglobin and BSA. The advantages of this immunosensor include the ease of preparation and the nonrequirement of labeling step. In addition, the electrode is portable and inexpensively prepared. Finally, the immunosensor was successfully applied to detect CRP in a certified human serum sample with a satisfactory result. Thus, this immunosensor appears to have the potential to be applied to detect several other biomarkers in the future, which can possibly be used as an alternative method for point-of-care monitoring.

PART II

**3.2 Electrochemical paper-based analytical device for multiplexed,
point-of-care detection of cardiovascular disease biomarkers**

(Sensor and Actuator B)

Suchanat Boonkaew,¹ Ilhoon Jang,^{2,3} Eka Noviana,^{2,4} Weena Siangproh,⁵ OrawonChailapakul,^{1,6*} Charles S. Henry^{2**}

¹ Electrochemistry and Optical Spectroscopy Center of Excellence (EOSCE), Department of Chemistry, Chulalongkorn University, Pathumwan, Bangkok, 10330, Thailand

² Department of Chemistry, Colorado State University, Fort Collins, Colorado 80523, USA

³ Institute of Nano Science and Technology, Hanyang University, Seoul 04763, South Korea

⁴ Department of Pharmaceutical Chemistry, Faculty of Pharmacy, Universitas Gadjah Mada, Yogyakarta 55281, Indonesia

⁵ Department of Chemistry, Faculty of Science, Srinakharinwirot University, Wattana, Bangkok, 10110, Thailand

⁶ Center of Excellence on Petrochemical and Materials Technology, Chulalongkorn University, Pathumwan, Bangkok, 10330, Thailand

*Corresponding author at: Electrochemistry and Optical Spectroscopy Center of Excellence (EOSCE), Department of Chemistry, Chulalongkorn University, Pathumwan, Bangkok, 10330, Thailand. E-mail: corawon@chula.ac.th

**Corresponding author at: Department of Chemistry, Colorado State University, Fort Collins, Colorado, 80523, USA. E-mail: Chuck.henry@colostate.edu

Abstract

Cardiovascular diseases (CVDs) are the number one cause of death globally. Therefore, a sensitive and affordable point-of-care sensing device is needed for the diagnosis and monitoring of diseases. Herein, we demonstrated an electrochemical paper-based analytical device (ePAD) coupled with a label-free immunoassay for simultaneous determination of three important CVDs biomarkers including C-reactive protein (CRP), troponin I (cTnI), and procalcitonin (PCT). The ePAD was created by stacking a wax-patterned paper and a transparency film using laser-cut double-sided adhesive to define the sample inlet, three separate detection zones for each analyte, and fluidic channels that connect the inlet and detection zones. Antibodies to the target biomarkers were immobilized on graphene oxide (GO)-modified carbon electrodes stencil-printed on the ePAD. Concentrations of the CVDs biomarkers were determined by square wave voltammetry (SWV). A significant decrease in current response in a concentration-dependent manner was observed in the presence of the cardiac biomarkers while there was no observable change in current response in the absence of the biomarkers. Good linearity ($R^2 > 0.99$), low detection limits (0.38 ng mL^{-1} , 0.16 pg mL^{-1} , and 0.27 pg mL^{-1} for CRP, cTnI, and PCT, respectively), and good reproducibility ($RSD < 5\%$) were achieved for the quantifications. Furthermore, the immunosensor has been applied to simultaneously detect the three biomarkers in serum samples with satisfactory results. The proposed immunosensor can be a great alternative for the early detection of cardiovascular diseases at the point-of-care.

Keywords: Paper-based analytical devices, Point-of-care detection, Multiplexed electrochemical detection, Cardiovascular disease biomarkers

3.2.1. Introduction

Cardiovascular diseases (CVDs) are the leading cause of death globally, and the prevalence of CVDs has continuously grown due to the aging of the world population^{92, 93}. Several physiological/pathological conditions and lifestyles such as high blood pressure, diabetes, obesity, physical inactivity, smoking, and excessive alcohol use can increase the risk for CVDs^{94, 95}. Early detection of CVDs can improve patients' prognosis, and survival as medical treatments can be given sooner to avoid further complications. Detection of CVDs is often done by measuring biomarkers related to the disease. A biomarker is a substance that can be measured in a biological system as an indicator of exposure and susceptibility of the disease and can indicate physiological stage and pathological processes⁹⁶. Also, a biomarker can be used to monitor patients' conditions after medical interventions or administration of therapeutics^{97, 98}. However, the use of a single biomarker for the CVDs diagnosis has some drawbacks such as limited accuracy because a single biomarker can be associated with multiple diseases. Thus, the simultaneous determination of multiple CVDs biomarkers is a more reliable and selective way for diagnosis⁹⁹⁻¹⁰¹. Simultaneous detection of multiple biomarkers can improve the specificity, analysis time, diagnosis cost, and confirm the risk of CVDs sooner⁹⁹.

Several biomarkers, including C-reactive protein (CRP), troponin I (cTnI), and procalcitonin (PCT) are considered as the golden standards and have been widely used in the early detection of CVDs^{102, 103}. CRP is an acute inflammatory protein which was

produced by the liver during inflammation, and injury occurs in the body, tissue damage, and high risk of CVDs^{65, 104}. cTnI is one type of cardiac marker for an acute myocardial infarction (AMI), which is one of the most serious CVDs that related to heart attack and blood vessel injury¹⁰⁵. PCT is an anti-inflammatory, endogenous, and nonsteroidal molecule with composed of 116 amino acids. It is a specific marker for severe sepsis caused by bacterial infection¹⁰⁶. The World Health Organization (WHO) has provided a normal level of CRP within the range of 1-3 mg mL⁻¹ in serum samples¹⁰⁷. PCT and cTnI levels are usually lower than 0.2 ng mL⁻¹ in the serum sample of healthy persons^{108, 109}. While abnormal levels of CRP (> 3 mg mL⁻¹), cTnI, and PCT (> 0.2 ng mL⁻¹) may result in increased risk for future serious heart events¹⁰⁵. Therefore, the measurement of these biomarkers can be used for early diagnosis of myocardial cell damage, assessing patients' response to antibiotic therapy, monitoring sepsis development, and evaluating the effectiveness of the treatment. Various techniques have been reported for CVDs biomarker detection, such as surface plasmon resonance (SPR)^{110, 111}, electrochemiluminescence immunoassay (ECLIA)¹¹², electrochemiluminescence (ECL)^{113, 114}, enzyme-linked immunosorbent assay (ELISA)^{103, 115, 116}, and matrix-assisted laser desorption/ionization mass spectrometry (MALDI-MS)¹¹⁷. Although these methods provide high sensitivity, they still have some limitations, such as being time-consuming and requiring expensive instrumentations and a large sample volume.

The development of proficient point-of-care (POC) diagnosis using an electrochemical paper-based analytical device (ePAD) can potentially pave the way to rapid cardiac disease management. The main advantages of ePADs including fast analysis time, high sensitivity, simplicity, portability, as well as low-cost ¹¹⁸⁻¹²². Combining ePADs with immunoassay specifically can improve assay specificity and offer portable testing devices for point-of-care monitoring. Since proteins cannot be directly detected in ePADs, chemical labels are frequently used for sensitive quantification. Several labeling materials including single-walled carbon nanohorns (SWCNHs)/hollow Pt chains (HPtCs) complex ¹²³, quantum dot (QD) ^{106, 124, 125}, gold nanoparticles (AuNPs) ¹²⁶⁻¹²⁹, gold nanospike (AuNS) ¹³⁰, and anthraquinone (AQ) ⁶⁵ have been previously reported for the electrochemical immunoassays of CVDs biomarkers. Although the use of these labeling materials enhances the sensitivity of the electrochemical measurement, these labeled immunoassays often require expensive reagents and involve time-consuming, and labor-intensive labeling process. Therefore, a label-free immunoassay can significantly simplify the assay platform and reduce the fabrication cost as this approach allows direct detection of the antigen/biomarker-antibody complex ^{131, 132}.

Herein, we demonstrated an ePAD coupled with a label-free immunoassay that simultaneously detected CRP, cTnI, and PCT in serum samples using a single device. The proposed ePAD has multiple detection zones, enabling the detection of CVDs biomarkers at their optimal conditions. A graphene-modified stencil-printed carbon

electrode (G-SPCE) was utilized on the ePAD owing to their low cost, ease of fabrication, and disposability. Graphite was mixed with a carbon ink to improve the sensitivity, then printed through a stencil onto a paper and transparency film substrate. The SPCEs were treated with graphene oxide (GO) and further oxidized to covalently attach the antibodies to the biomarkers onto the surface of the electrodes. The presence of CRP, cTnI, and PCT was detected by measuring the change in electrochemical current response due to the binding of analytes to their immobilized antibodies. The stepwise modifications of the electrodes were characterized using electrochemical impedance spectroscopy and cyclic voltammetry. The influences of various parameters which can affect the sensitivity of detection, including a concentration of immobilized antibodies and incubation time, were also investigated. The optimized sensor was then applied to determine CRP, cTnI, and PCT in artificial serum samples to demonstrate the capability of the proposed ePAD.

3.2.2 Experimental

3.2.2.1 Chemicals and materials

All reagents used were analytical reagent grade and used without further purification. C-reactive protein (CRP) and C-reactive protein monoclonal antibody (anti-CRP) were purchased from Fitzgerald (Massachusetts, USA). Procalcitonin (PCT), procalcitonin monoclonal antibody (anti-PCT), and *N*-hydroxysulfosuccinimide (sulfo-NHS) were purchased from Thermo Fisher Scientific (New jersey, USA). Troponin I (cTnI)

and anti-cardiac Troponin I antibody (anti-cTnI) were purchased from Abcam (Massachusetts, USA). Graphene oxide powder was purchased from Cheptubes (Vermont, USA). Bovine serum albumin (BSA), potassium hexacyanoferrate (III) ($K_3[Fe(CN)_6]$), sodium hydroxide (NaOH), 1-ethyl-3-(3-dimethylaminopropyl) carbodiimide hydrochloride (EDC), myoglobin, glycine, homocysteine, L-cysteine, creatinine, albumin, hemoglobin, and Tween 20 were purchased from Sigma-Aldrich (New Jersey, USA). Artificial serum level I and II were purchased from Pointe Scientific (Michigan, USA). Phosphate buffer saline (PBS) pack pH 7.2 was obtained from Pierce (Texas, USA). Commercial carbon paste (E3178) was purchased from Ercon Incorporated (Massachusetts, USA). Graphite (MG-1599) was obtained from Great Lakes Graphite (Ontario, Canada). Silver/silver chloride (Ag/AgCl) ink was obtained from Gwent Group (Torfean, UK). Whatman 1 filter paper and double-sided adhesive tape were purchased from GE healthcare (Illinois, USA) and 3M (Minnesota, USA), respectively. All aqueous solutions were prepared in ultra-purified water ($18.2 M\Omega\text{ cm}^{-1}$).

3.2.2.2 Apparatus and measurements

All electrochemical measurements were performed on CHI 660B potentiostat (CH Instruments, Inc., USA). The measurements were performed in triplicates at room temperature ($22 \pm 2^\circ\text{C}$). All of the experiments were performed using a three-electrode system with graphene modified stencil-printed carbon electrodes (G-SPCEs) as the working electrode (WE) (3 mm in diameter) and counter electrode (CE), and screen-

printed Ag/AgCl as the reference electrode (RE). A 5 mM $[\text{Fe}(\text{CN})_6]^{3-/4-}$ in 0.1 M KNO_3 solution was used as the redox solution for all electrochemical experiments. The quantification of biomarkers was done by square wave voltammetry (SWV). A potential sweep between -0.3 to +0.5 V was applied for the SWV with 150 mV pulse amplitude, 5 Hz frequency, and 5 mV step potential (more details are provided in the section 3.2.3.4.1). For cyclic voltammetry (CV) measurement, the potential was scanned from -0.7 to 0.8 V with a scan rate of 50 mV s^{-1} . For electrochemical impedance spectroscopy (EIS), the impedance spectra were recorded within a frequency range of 100 kHz to 0.1 Hz with perturbation amplitude of 0.01 V.

A Xerox ColorQube 8870 series wax printer (Xerox, Connecticut) was used to fabricate the paper devices. The stencil-printed carbon electrode (SPCEs) templates were designed using CorelDRAW software (Ontario, Canada) and cut by a laser cutter (Epilog Zing CO_2 , Colorado, USA). Field emission scanning electron microscopy (FE-SEM) (JSM-7001F, Tokyo, Japan) at 5 kV, energy dispersive x-ray spectroscopy (EDS) (INCA penta FETx3 model, Tokyo, Japan), and Raman spectroscopy (Perkin Elmer, Massachusetts, USA) were applied to verify the successful modification of the electrodes.

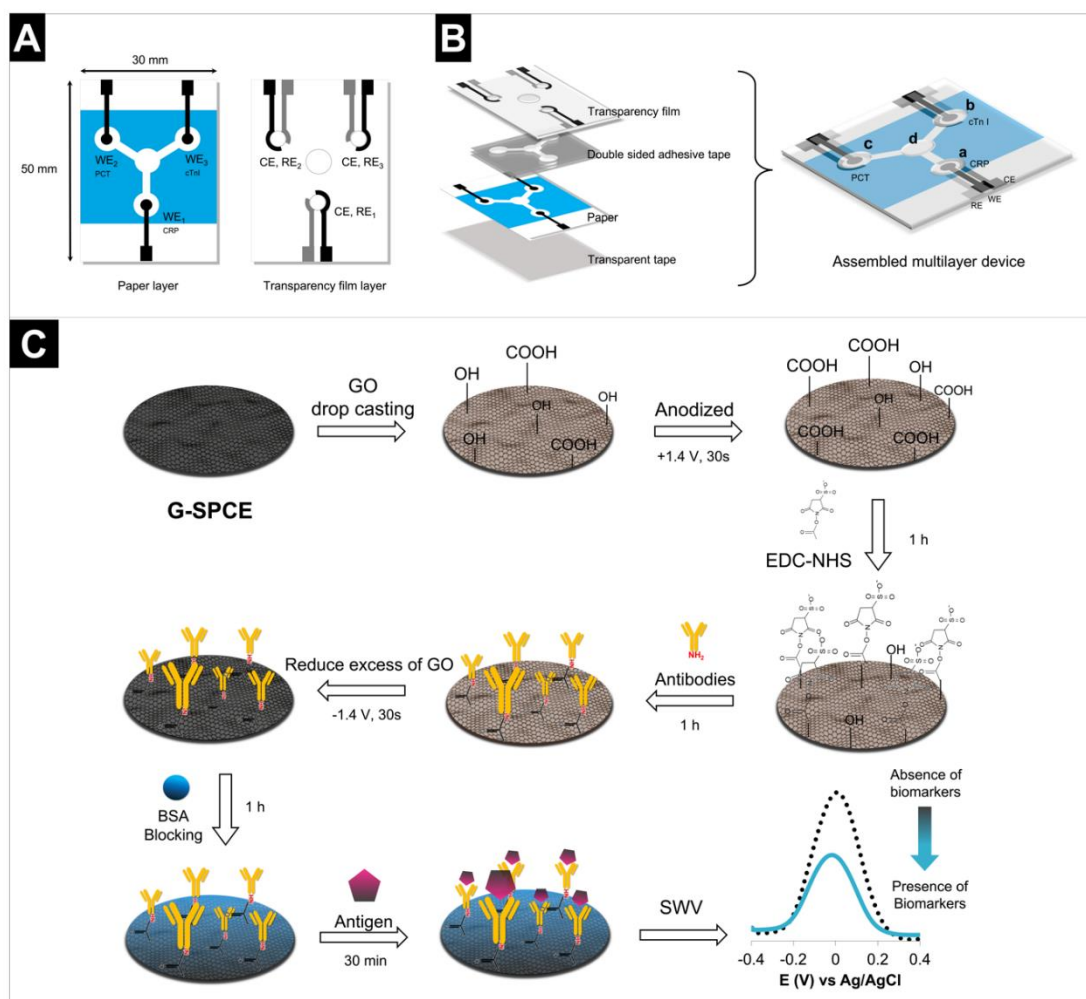


Figure 29. Design and fabrication of the multiplexed ePAD (A and B). (a), (b), and (c) small holes (4 mm in diameter) made on the transparency film for immobilization of detection antibodies, (d) redox solution inlet (5 mm in diameter), and step-by-step preparation of the electrochemical immunosensor and detection of the antigen/biomarker on the sensor (C). WE = working electrode; CE = counter electrode; and RE = reference electrode.

3.2.2.3 ePADs fabrication

Fig. 29 shows the fabrication of the multi-layered ePAD for simultaneous detection of three biomarkers in a single device and rapid sample delivery from the inlet to each detection zone. The developed device has three detection zones for CRP, cTnI, and PCT, which are connected to a single inlet in the center through fast-flow paper/transparency film-based channels. The channels were fabricated by laminating paper, transparency film, double-sided adhesive tape, and transparent tape.¹³³ Wax printing method was employed to construct the paper-based channel. First, the ePAD pattern was wax printed on Whatman 1 filter paper, followed by melting the wax on a hot plate at 170 °C for 90 s to form hydrophobic barriers surrounding the defined inlet, fluidic channels, and detection zones. The backside of ePADs was sealed with a transparent tape to prevent solution leaking during measurements. Three layers of double-sided adhesive tape were used to form a hollow gap with ~245 μm height between the paper and transparency film layers. We made holes on the transparency film for adding and removing solutions during the multi-step immunoassay and electrode modifications.

Before assembling the multilayered device, the electrodes were stencil-printed on the paper and transparency film using previously described methods^{134, 135}. Briefly, a carbon paste was prepared by mixing graphite (MG-1599) and a commercial carbon ink at a ratio of 0.6:1 (w/w) to increase the conductivity of the electrodes and sensitivity of the measurements. The carbon paste was stencil printed on the paper and

transparency sheet to form the WEs (3 mm of diameter), CEs and REs, respectively. These electrodes were denoted as G-SPCE. Ag/AgCl ink was then painted on the REs. After that, electrodes were cured in the oven at 60 °C for 30 min to evaporate solvents from the ink.

3.2.2.4 Electrode modification

The immobilization of detection antibodies onto the working electrodes (WEs) and the washing steps of the preparation of the immunosensor were performed through small holes (4 mm in diameter) made on the transparency film at the detection zones (a, b, and c position in Fig. 29B). Antibodies to the target analytes were immobilized on the WEs surface via direct conjugation. First, a 4 μL of 1.5 mg mL^{-1} GO dispersed in water was separately drop casted on each WE through a small hole of the transparency film layer (a, b, and c position in Fig. 29B), followed by baking in the oven at 60 °C for 10 min to remove the solvent. These electrodes were denoted as GO/G-SPCEs. To increase the number of carboxyl functional groups on the GO sheets, GO/G-SPCEs were then pretreated using 90 μL of 0.5 M NaOH at 1.4 V for 30 s, followed by washing twice with 50 μL of water. In this step, the solutions were directly dropped through a center inlet of the transparency film (d position in Fig. 29B). A 4 μL of EDC/sulfo-NHS (10 mM: 30 mM) solution was added onto each WE through a small hole of the transparency film layer to activate the carboxyl groups for 1 h at room temperature. The WEs were then washed twice (Fig. 37) with 10 μL of PBST (phosphate

buffered saline containing 0.5% Tween 20) via a small hole of the transparency film layer. A 4 μL of the capture monoclonal antibodies (100 ng mL^{-1} of anti-cTnI and anti-PCT, and $3 \mu\text{g mL}^{-1}$ of anti-CRP) were dropped on the WEs and incubated for 1 h at 2°C , followed by subsequent washing with 10 μL of PBST twice through a small hole of the transparency film layer. The capture antibodies were covalently immobilized on the GO-modified electrodes through a direct conjugation between the amine ($-\text{NH}_2$) groups of the antibodies and amine-reactive sulfo-NHS ester groups on the WEs to form amide ($-\text{CO}-\text{NH}-$) bonds between the two¹³⁶. The unreacted carboxyl groups on the modified electrodes were then reduced at -1.4 V for 30 s using 90 μL of PBS pH 7.4, followed by washing twice with 50 μL of water (More detailed information are provided in section 3.2.3.4.2 - 3.2.3.4.4). In this reduction step, PBS solution was added through a center inlet of the transparency film (d position in Fig. 29B). Next, to reduce/eliminate non-specific binding on the electrodes, 4 μL of 3 mg mL^{-1} BSA was added onto the WEs and left for 1 h at 2°C , followed by washing twice with 10 μL of PBST via a small hole of the transparency film layer. The modified electrodes were kept at 2°C if not immediately used. The design, details of the fabrication procedures and the step-by-step electrode modifications are shown in Fig. 29A-C.

3.2.2.5 Electrochemical detection of CVDs biomarkers

To calibrate the sensors, the antibody-modified electrodes were incubated with different concentrations of 4 μL of CRP ($0.001 - 100 \mu\text{g mL}^{-1}$), 4 μL of cTnI ($0.001 - 250$

ng mL⁻¹), and 4 μL of PCT (0.0005 – 250 ng mL⁻¹) for 30 min, followed by washing twice with 10 μL of PBST via a small hole of the transparency film (a, b, and c position in Fig. 29). Subsequently, a 90 μL of 5 mM [Fe(CN)₆]^{3-/4-} was introduced to the center inlet of the transparency film (d position in Fig. 29B). Once the redox solution reached the detection zones (more details are provided in the section 3.2.3.3 and Fig. 34), the electrochemical measurement was then performed.

3.2.2.6 Preparation of serum samples

Applicability of the immunosensors was demonstrated by detecting the CVD biomarkers in serum samples. First, an artificial serum was prepared with PBS pH 7.4 at the 1:1 ratio. After that, the prepared serum was spiked with various concentrations of CRP (1 – 7 μg mL⁻¹), cTnl (1 – 7 ng mL⁻¹), and PCT (1 – 7 ng mL⁻¹). Finally, the recovery percentages of the biomarkers were calculated based on the measured values and the known added concentrations.

3.2.3 Results and discussion

3.2.3.1 SEM/EDS and Raman spectroscopy characterization of the modified electrode

To characterize the electrode surface of bare SPCE, G-SPCE, GO/G-SPCEs, and after reducing the excess of GO, FE-SEM, SEM/EDS, and Raman spectroscopy were performed. First, the surface morphologies were examined using FE-SEM. The bare SPCE exhibited in Fig. 30a. After modified graphene on the SPCE (Fig. 30b) shows a

rough and stack of the graphitic surface layer compared to the bare SPCE. After drop casting GO on the electrode surface, an irregular thin sheet of GO covering the entire surface of the G-SPCE electrode was observed (Fig. 30c). The roughness of the electrode surface increased after the GO layer was reduced (Fig. 30d), which led to an increase in the effective surface on the electrode and improvement in the conductivity of the modified electrode.

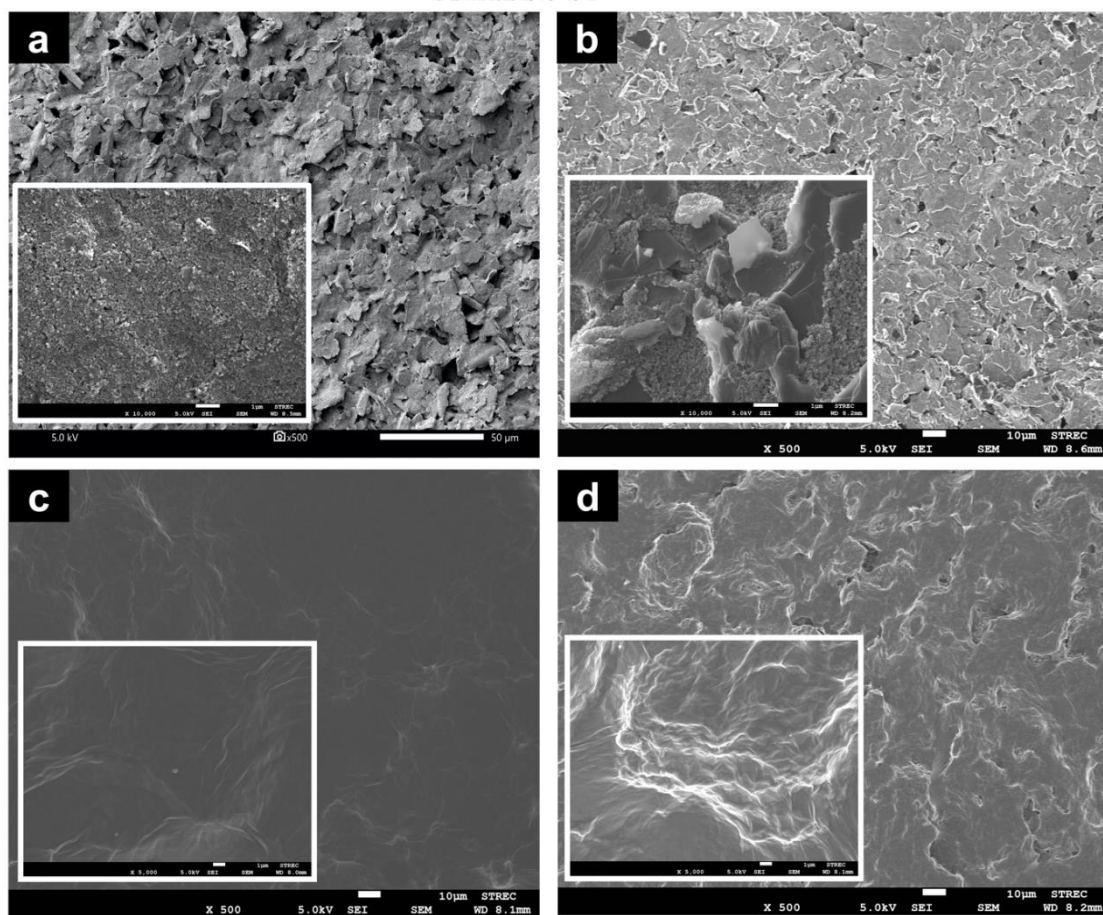


Figure 30. SEM images of SPCE (a), G-SPCE (b), GO/G-SPCE (c), and after reducing the excess of GO at -1.4 V for 30s using PBS pH 7.4 (d).

We then performed SEM/EDS analysis of the oxidized GO/G-SPCE (Fig. 31). The EDS spectra showed a significant presence of oxygen (O, ~30%), which verified the successful modification of GO on the electrode. In Fig. 31f, carbon (C), is also present, that can attribute to the carbon and graphene composition of the GO solution. Sodium (Na) was also present (approximately 5%), which could be attributed to the NaOH solution used in the oxidation of GO.



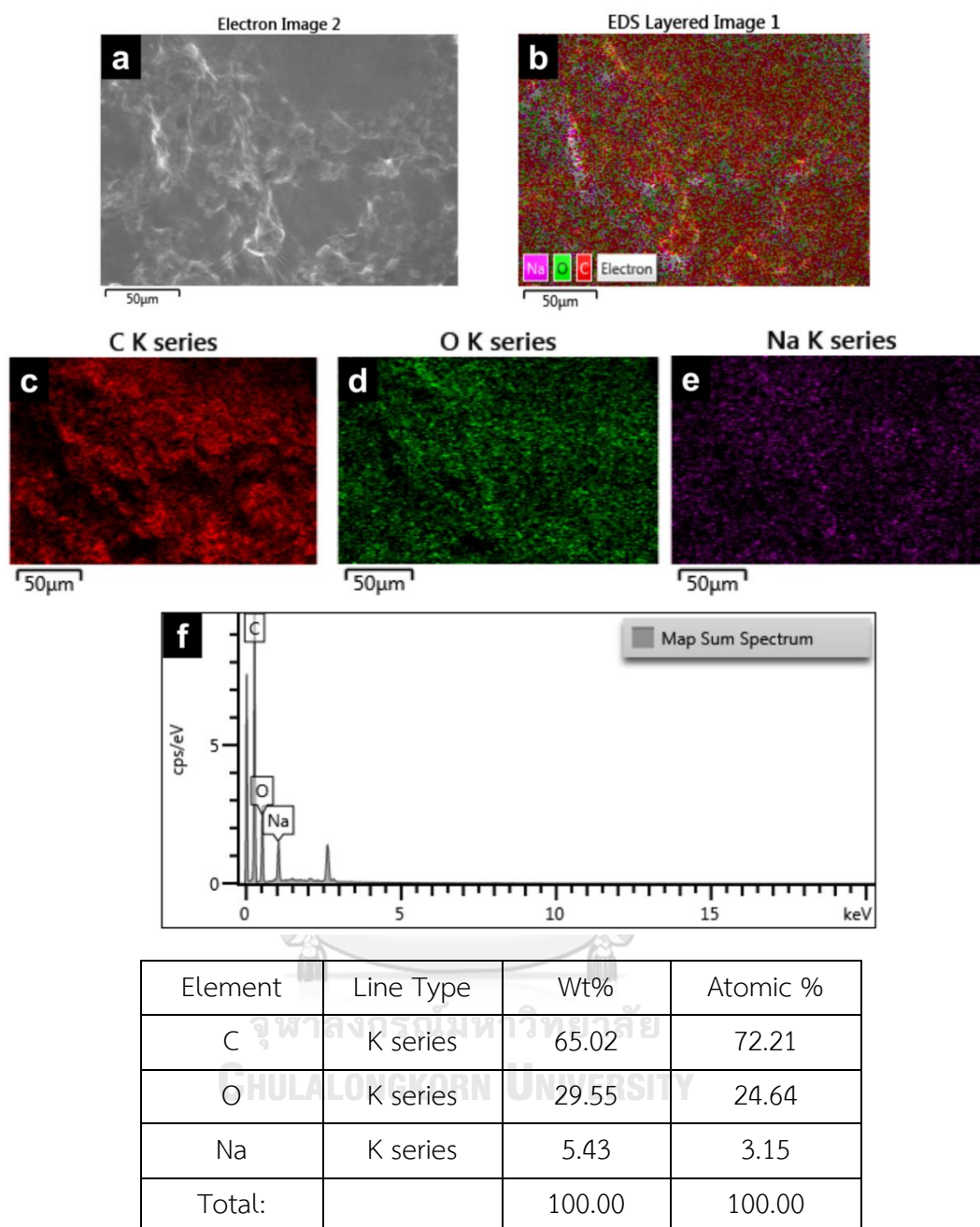


Figure 31. SEM/EDS images of anodized GO on the SPCE (a and b), K line of C atom presented as the composition of graphene in GO solution (c), K line of O and Na represented as the composition of GO and NaOH solution for anodize process (d and e), and the corresponding EDS spectra (f) related to the results tabulated in the table.

Raman spectroscopy was also used to confirm the presence of GO on the electrode surface. As shown in the Fig. 32, Raman spectra of the unmodified electrode (black line) exhibited a small D at $\sim 1300\text{ cm}^{-1}$ and G band at $\sim 1600\text{ cm}^{-1}$, corresponding to the symmetry A_{1g} mode and the E_{2g} mode of sp^2 carbon atom, respectively¹³⁷⁻¹³⁹. Raman spectra of the GO-modified SPCE (orange line) has similar peak positions to the unmodified electrode. However, both G and D bands ($\sim 1300\text{ cm}^{-1}$ and $\sim 1600\text{ cm}^{-1}$) of GO-SPCE had higher intensities than that of bare G-SPCE. An increased in D/G intensity ratio showing the reduction in average size of sp^2 domains, which is due to the oxidation process of GO.¹⁴⁰ Therefore, we can confirm that the modified electrode was covered by GO and readily for further immunoassay step.

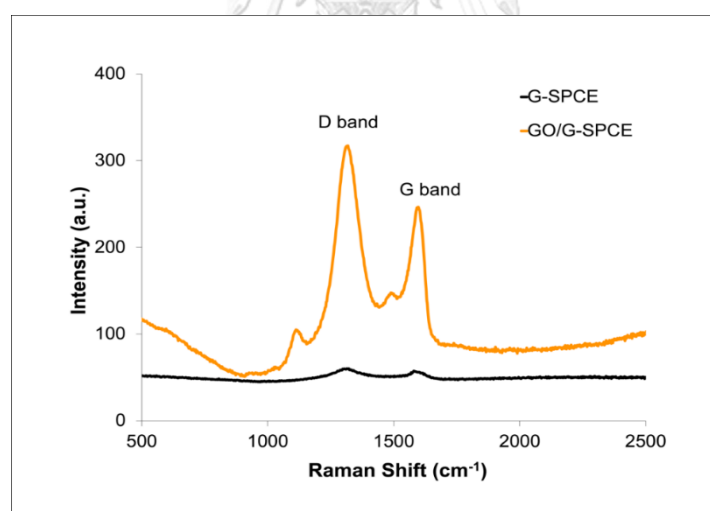


Figure 32. Raman spectra of bare G-SPCE (black line) and the GO/G-SPCE electrode (orange line).

3.2.3.2 Electrochemical characterization of the immunosensor

To confirm the modification steps of each biomarker, the electrochemical behavior at the electrode surface was studied using CV. As shown in Fig. 33, the current response of GO/G-SPCEs (grey line) decreased compared with the bare G-SPCE electrode (dash line). The decreased in current response might have been caused by the insulating property of GO solution cast on the G-SPCE surface. Next, the current response was increased after the anodized process (green line). It is due to this pretreatment process can remove the organic ink constituents or contaminants on the electrode surface and increase surface roughness or functionalities¹⁴¹. Subsequently, the current response was further decreased after antibodies immobilize on the GO/G-SPCEs (yellow line), indicating the successful immobilization of antibodies on the electrode surface. After reducing the unreacted carboxyl group on the GO (blue line), the current response increase due to the unreacted carboxyl group on GO was changed to graphene and tended to increase in electroactive surface area and conductivity. After blocking (orange line) and adding the CVDs biomarker (red line), a decrease in the current response was detected. This result can be explained by the immunocomplex between antigen and antibodies will block the electron transfer of redox solution from electrode surface and the effect of carbonaceous material can block the electron transfer and act as barrier^{14, 142, 143}.

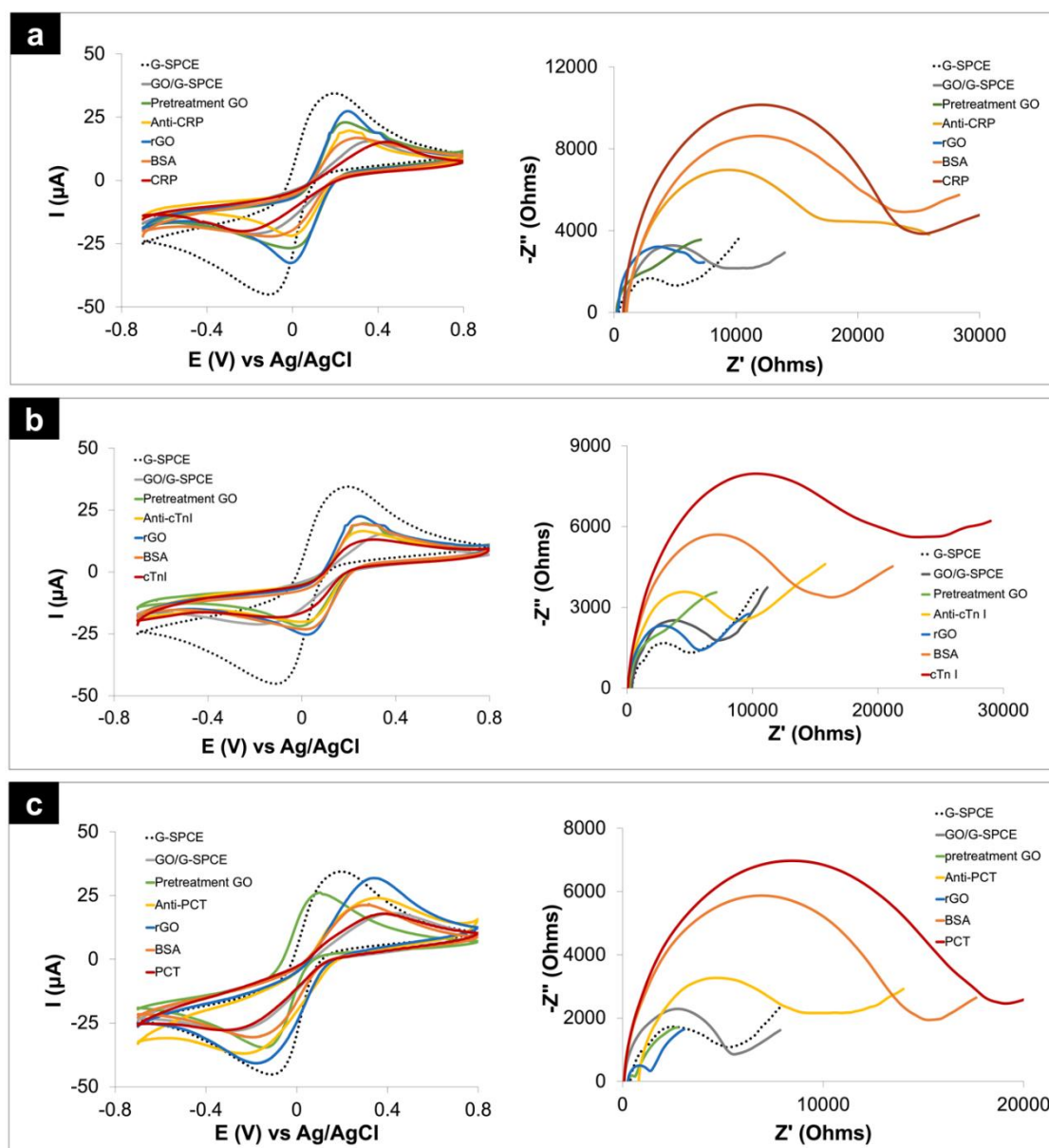


Figure 33. CV and EIS characterization of the electrodes at various modification steps using 5 mM of $[\text{Fe}(\text{CN})_6]^{3-/4-}$ containing 0.1 M KNO_3 for C-reactive protein (CRP) (a), troponin I (cTn I) (b), and procalcitonin (PCT) detection (c), respectively. The bare G-SPCE electrode is shown in the dash line, GO modified on the electrode as denoted as GO/G-SPCE (grey line), after anodized GO (green line), after antibodies was immobilized on the electrode (yellow line), after reducing the excess of GO (blue line),

BSA was used to block non-specific protein and blocked active site binding (orange line), and after antigen or biomarkers were captured the electrochemical response reduced (red line), respectively.

In addition, EIS was used to confirm the electrode modifications. In the Nyquist plots (Fig. 33, right graphs), the straight lines represent the mass transfer, and the semicircles represent the charge transfer resistance (R_{ct}) of the electrochemical cell. The results obtained after GO modification (grey line) on the electrode surface, the R_{ct} was significantly increased as compared to the bare G-SPCE electrode (dash line) due to the existence of GO on the electrode surface that might hinder the electron transfer through the electrode surface. After anodized GO process (green line), the R_{ct} decreased caused by the pretreatment process can remove contaminants or organic contaminations on the electrode surface. After the immobilization of antibodies (yellow line), a higher increase in R_{ct} value was observed due to the antibodies acting as a barrier between the redox solution and the electrode. The reduction of GO to graphene (blue line) decreased the R_{ct} markedly due to the improved electrochemical activity of graphene over GO. Subsequently, the addition of BSA blocking (orange line) and the target biomarkers (red line) increased the R_{ct} value by providing additional barriers to the electrochemical reaction. These results were consistent with the CV study, suggesting a change in the electrode surface.

3.2.3.3 Wetting area vs time

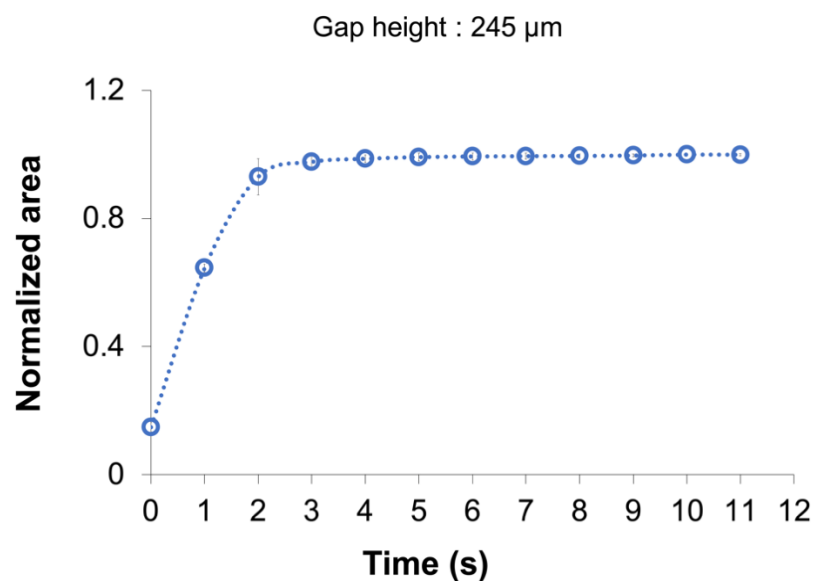


Figure 34. Normalized wetting area vs time. Symbols and error bars show the average and standard deviation of triplicate experiments, respectively.

To confirm the rapid sample delivery in ePADs, we measured the variation of the wetting area over time. Since the ePAD has a transparent top layer, we could record fluid flow from the top of the device using a smartphone after we injected 90 μL of dye solution at the inlet. The wetting area was measured every second by analyzing the color difference in the channel through the Matlab software. To indicate the time required to fill inside the channel completely, the measured area was normalized by dividing the measured area to the total area of the entire channel. Fig. 34 shows the normalized area over time. The normalized area value of 1 indicates that the fluid filled the entire channel. As a result, we can confirm that injected fluid can be delivered from the inlet to all detection zones within ~ 3 s.

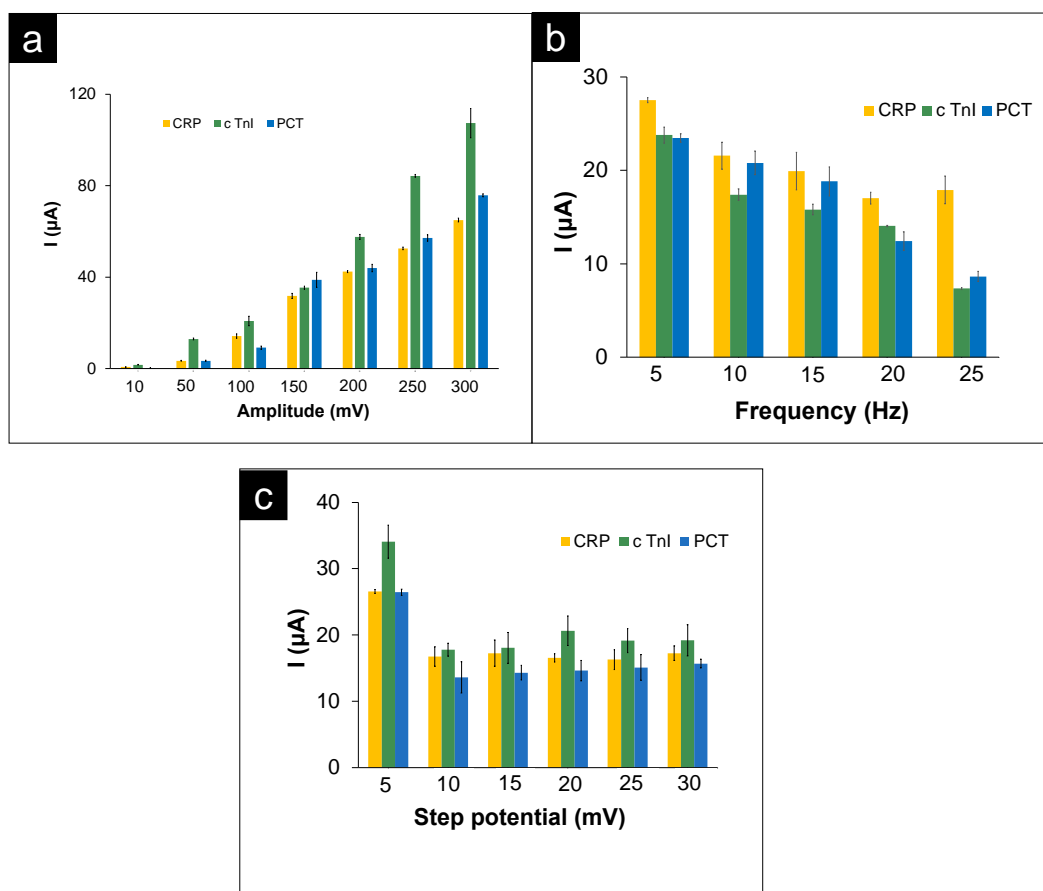


Figure 35. Each electrochemical condition of SWV technique including; (a) amplitude, (b) frequency, and (c) step height. The optimal conditions were as follow: an amplitude, frequency, and step height were 150 mV, 5 Hz, and 5 mV.

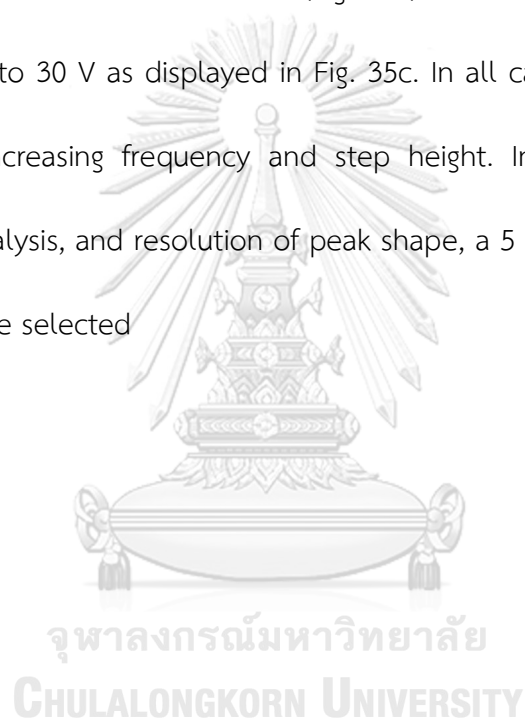
3.2.3.4 Optimization

3.2.3.4.1 Measurement parameter of SWV

To achieve the optimal condition for biomarker detection, various parameter of SWV condition include amplitude, frequency, and step height were optimized. The discussion of the optimal conditions are as follows:

The effect of amplitude was varied in the range from 10 to 300 mV and keep other parameters constant (Fig. 35a). It was observed that the current response gradually increases with increasing amplitude until 300 mV. However, the resolution of peak shape decreased consequently. Therefore, a 150 mV of amplitude was chosen.

Afterwards, the effect of frequency and step height were studied. The frequency was evaluated from 5 to 25 Hz (Fig. 35b). For the step height was studied in the range from 5 to 30 V as displayed in Fig. 35c. In all cases, the current response decreases with increasing frequency and step height. In order to obtain a high sensitivity, fast analysis, and resolution of peak shape, a 5 Hz of frequency and 5 mV of step height were selected



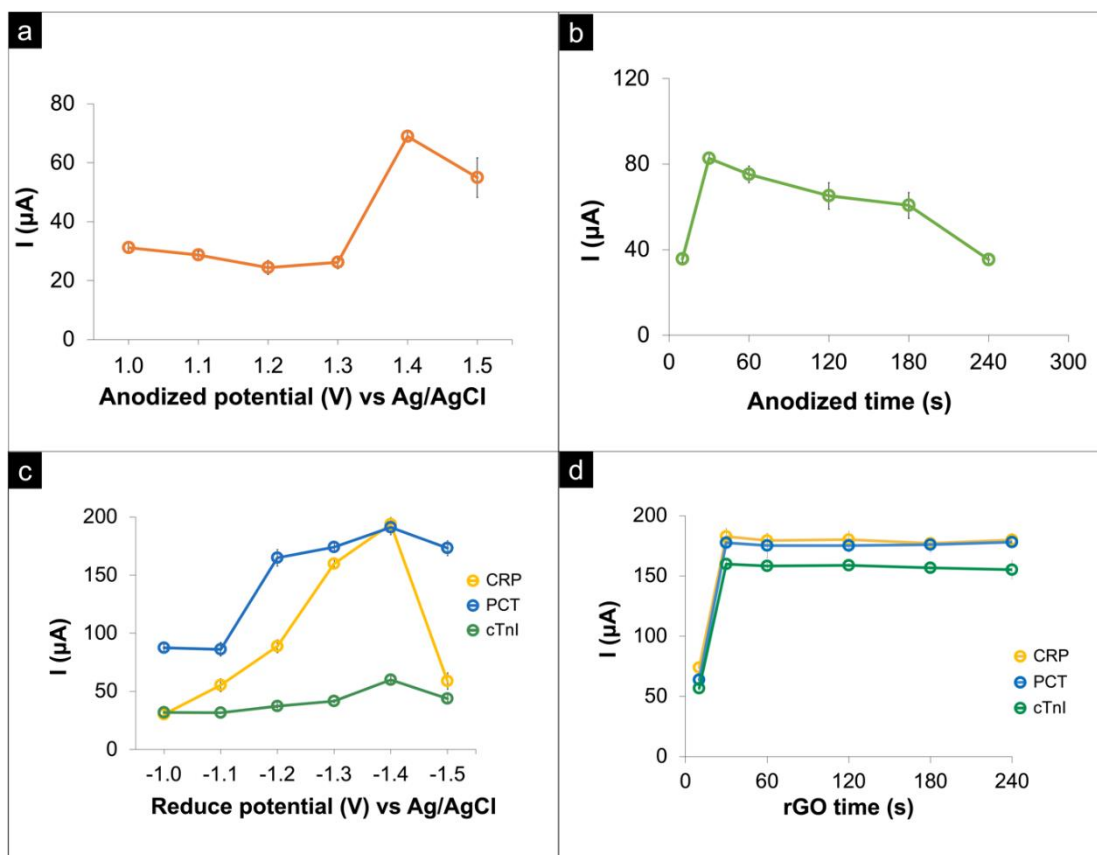


Figure 36. The effect of anodized potential (a), anodized time (b) and the effect of reduce potential (c), and reduce time (d).

3.2.3.4.2 Effect of anodized GO

3.2.3.4.2.1 Anodized potential and time

The anodization was adopted for enlarge the amount of carboxylic group on the GO sheet. The anodized potential was studied in the range of +1.0 to +1.5 V. As can be seen in Fig. 36a, the current response quite stable with increasing of anodize potential from +1.0 to +1.3 V, after that the current response increased at potential +1.4 V. It is because higher potential can increase the rate of

oxidation process. Therefore, +1.4 V was selected as a suitable anodized potential for all biomarkers.

As shown in Fig. 36b, it was observed that the current response increased with prolonger of anodized time and tend to level off after 30 s. So, the anodized time at 30 s was chosen for next experiment. If prolonger much anodized potential and time, the oxidation of water in this system will occur and produce oxygen. The oxygen will be taking place and could affect to the current response ¹⁴⁴.

3.2.3.4.3 Effect of reduce GO (rGO)

3.2.3.4.3.1 rGO potential and time

The rGO process was used to reduce the excess of GO which is uncaptured with antibodies on the electrode surface. This process could affect to the sensitivity of the immunosensor. Therefore, a rGO potential and time were investigated. The rGO potential was varied in the range of -1.0 to -1.5 V. As can be seen in Fig. 36c, the current response slightly increases with increasing the potential from -1.0 to -1.4 V, then the current response decreased at -1.5 V. It is due to more potential will increase the reduction rate of GO. However, if more negative could produce hydrogen gas bubble from the reduction reaction of water ¹⁴⁵. Hence, a -1.4 V of reduce potential was used for next studies.

The rGO time is the period that we applied to the working electrode in the negative direction to reduce the excess of GO to graphene. The reduced time was studied in the range from 10 to 240 s as shown in Fig. 36d. In all

cases, the current response increase, and the signal reach then a plateau after 30 s. The short reduce time may not be sufficient to reduce the excess of GO on the electrode surface, while longer reduce time might allow to completely conversion of GO to graphene. Therefore, 30 s of reduced time was chosen as optimal condition.

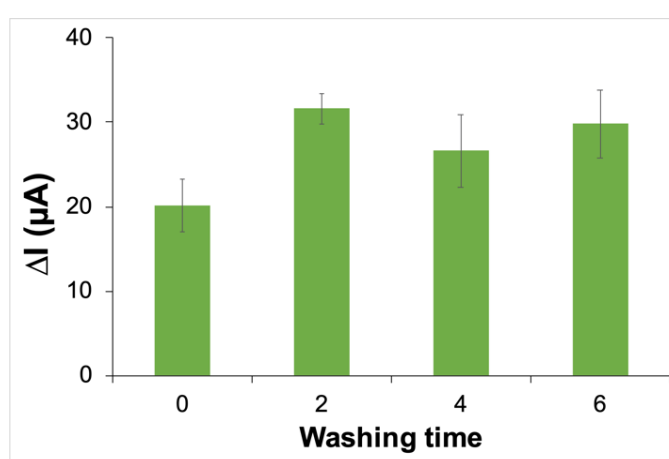


Figure 37. Study of the effect of washing time on the current response.

3.2.3.4.4 Effect of washing time

The effect of washing time on the current response signal was therefore investigated (Fig. 37). The washing time was studied from 0 (without washing) to 6 times. The results exhibited that washing two times provide high sensitivity over the others, and then the current response becomes stable. From the results, if we added the target analyte without any washing step, the non-specific binding on the electrode surface would be increased. This effect could decrease the affinity on the active site of the antibody to bind with target analyte and tend to decrease in the current response. Thus, two times was selected for all of the washing steps.

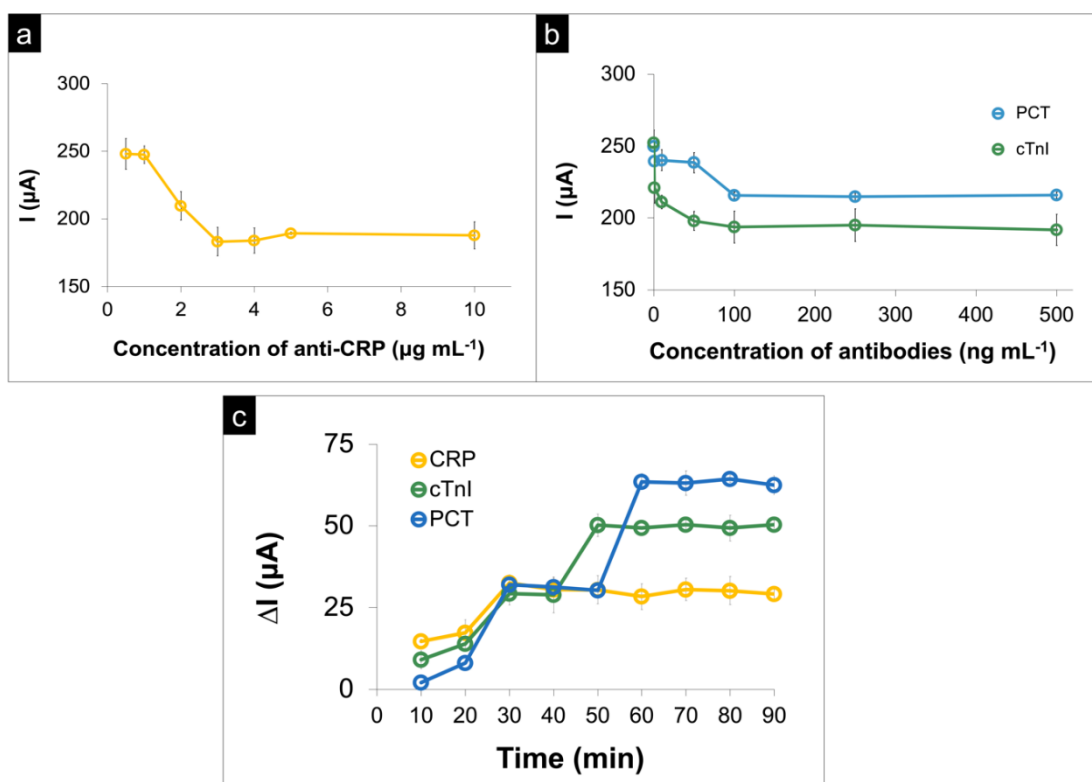


Figure 38. Optimization of experimental conditions for the proposed ePADs immunosensor: concentration of antibodies (a, b) and incubation time (100 ng mL^{-1} for anti-PCT and anti-cTnI, 3 μmL^{-1} of anti-CRP, 3 mg mL^{-1} of BSA, 0.05 $\mu\text{g mL}^{-1}$ of CRP, and 0.1 ng mL^{-1} of PCT and cTnI were immobilized on the modified electrode) (c). The Error bars indicate standard deviations calculated from three repetitions ($n = 3$).

3.2.3.4.5 Antibody concentration

To achieve the best performance of the immunosensor, the concentration of the immobilized antibody was optimized. The concentration of anti-CRP was studied in the range of 0.5 to 10 $\mu\text{g mL}^{-1}$. Anti-cTnI and anti-PCT were investigated in the interval range of 0.1 to 500 ng mL^{-1} . As shown in Fig. 38a and b, the current response (i.e. peak current from SWV) decreased with increasing concentrations

of antibodies. These obtained results can be explained by the steric hindrance of the antibodies which impeded accessibility of the redox solution toward the electrode surface, resulting in a reduction in the current response ¹⁴⁶. This current response reached a plateau at $3 \mu\text{g mL}^{-1}$ of anti-CRP, 100 ng mL^{-1} of anti-cTnI, and 100 ng mL^{-1} of anti-PCT, indicating surface saturation. Hence, these concentrations of antibodies were selected as optimal concentrations for further studies.

3.2.3.4.6 Incubation time

The incubation time of the analyte on the sensor was evaluated in the range from 10 to 90 min. As shown in Fig. 38c, the change of current response increased with increasing of incubation time of antigen with antibodies up to 30 min. Although, a prolonged time can enhance the affinity of antigen-antibody binding, however, to keep in short incubation time and in the real experiment for simultaneous detection of three biomarkers at the same time were measured. Hence, a 30 min binding time was selected for the next studies of all biomarkers.

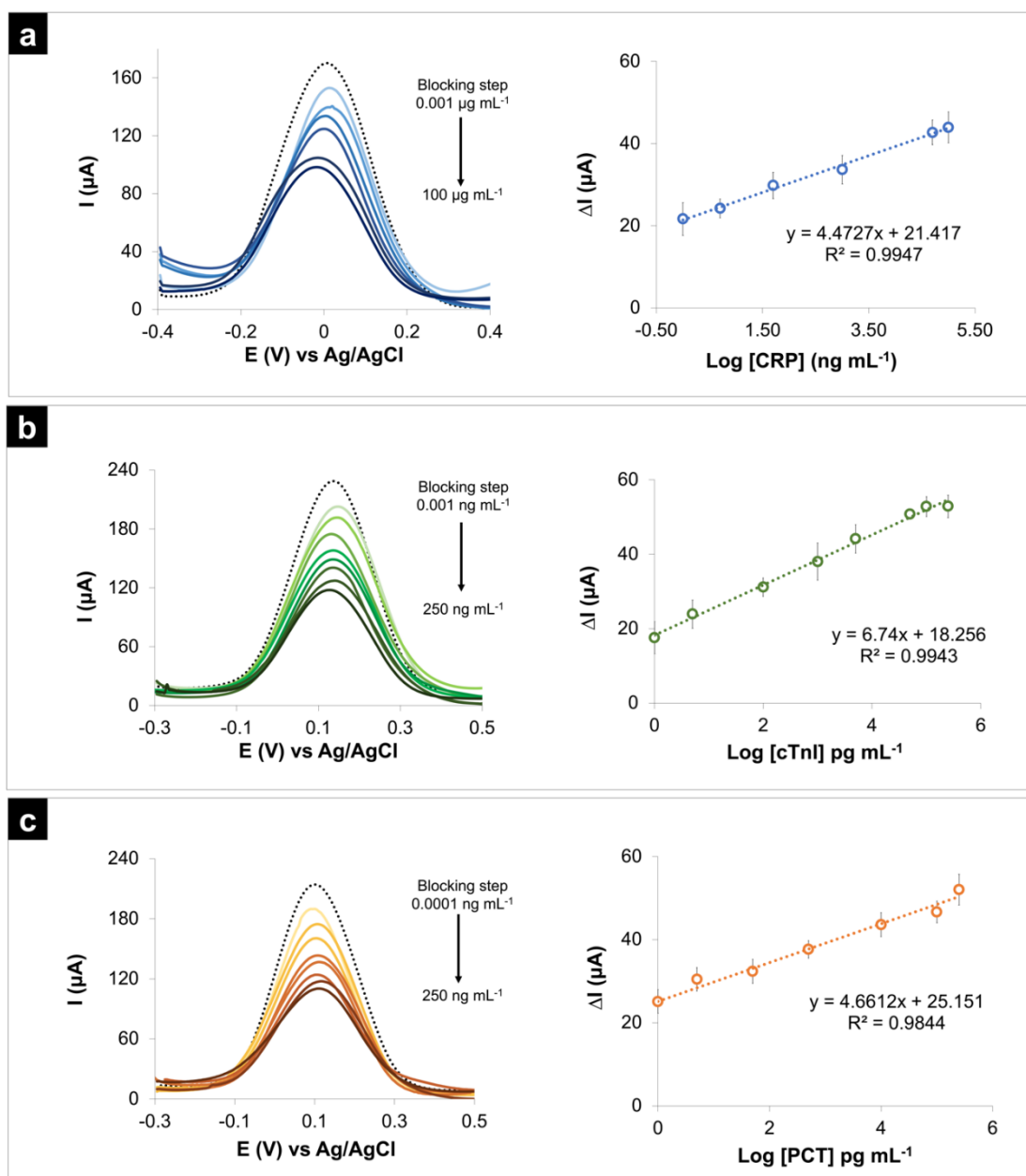


Figure 39. Left: Square wave voltammograms of simultaneous detection of various concentrations of CRP (a), cTnI (b), and PCT (c), respectively. Right: The quantitative calibration curve plot of the change in current response (ΔI) as a function of logarithm of concentration of biomarkers. ΔI was calculated from $\Delta I = I_{(\text{CVDs biomarkers})} - I_{(\text{BSA})}$; Where $I_{(\text{CVDs biomarkers})}$ is belong to the current response value after the immobilization of CVDs

biomarkers (CRP, cTnI, and CRP) onto BSA/rGO/antibody/GO/G-SPCE. The $I_{(BSA)}$ is belong to the current response value of BSA/rGO/antibody/ GO/G-SPCE. Error bars represent the standard deviation calculated from three repetitions (n=3).

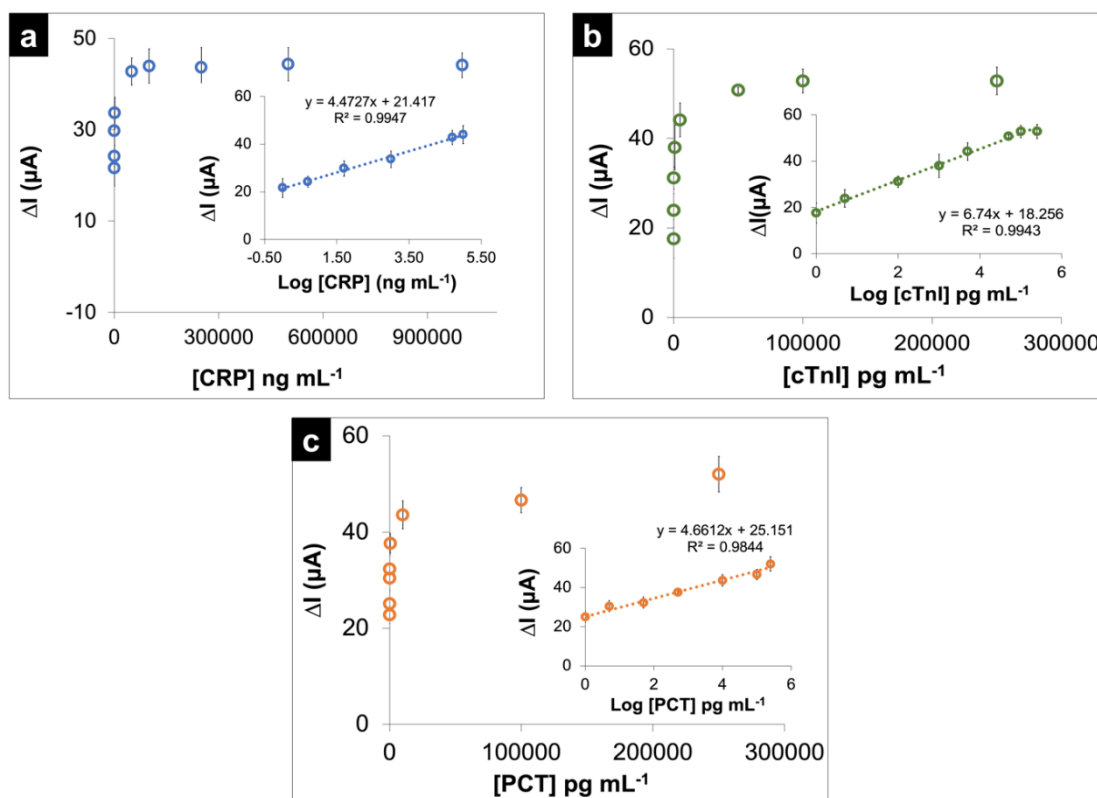


Figure 40. The quantitative calibration curve plot of the change in current response (ΔI) as a function of concentration and logarithm of concentration of CRP (a), cTnI (b), and PCT (c), respectively. Error bars represent the standard deviation calculated from three repetitions (n=3).

3.2.3.5 Electrochemical detection of CVDs biomarkers

After obtaining the optimized condition, the analytical performance of the immunosensor was evaluated by SWV. The voltammograms at various concentrations

of CRP, cTnI, and PCT are shown in Fig. 39. As shown in the left graphs of Fig. 39, the electrochemical response decreased in the presence of CVDs biomarkers. This decreased signal indicates the formation of immunocomplexes (antigen-antibody) barrier on the electrode surface, which reduces the rate of electron transfer of the redox solution towards the electrode surface¹⁴⁷.

The changes in current response (ΔI) with various concentrations of CRP, cTnI, and PCT are shown in Fig. 39 and Fig. 40. The ΔI gradually increased as the concentration of biomarkers increased. The value of ΔI was linearly proportional to the logarithm of CRP concentration (Fig. 39a and 40a) in the range of 0.001 to 100 $\mu\text{g mL}^{-1}$ ($\Delta I = 4.47 \log C_{\text{CRP}} (\text{ng mL}^{-1}) + 21.4$, $R^2 = 0.995$) with a limit of detection (LOD) of 0.38 ng mL^{-1} (LOD = 3 x standard deviation of blank/slope). For cTnI (Fig. 39b and 40b), the calibration curve showed a linear response in the range of 0.001 to 250 ng mL^{-1} ($\Delta I = 6.74 \log C_{\text{cTnI}} (\text{ng mL}^{-1}) + 18.3$, $R^2 = 0.994$) with a limit of detection of 0.16 pg mL^{-1} . For PCT (Fig. 39c and 40c), the calibration curve showed a linear response in the range of 0.5 pg mL^{-1} to 250 ng mL^{-1} ($\Delta I = 4.66 \log C_{\text{PCT}} (\text{ng mL}^{-1}) + 25.2$, $R^2 = 0.984$) with a limit of detection of 0.27 pg mL^{-1} . The comparison of analytical performance of the developed immunosensor with other previously reported methods for CRP, cTnI, and PCT detection are summarized in Table. 3. Among the methods, the developed immunosensor had a relatively wider detection range, easy operation, lower LODs, and higher sensitivity. Thus, immunosensor fabricated in this work could provide an alternative platform for the early diagnosis of cardiovascular diseases.

Table 3. The comparison of analytical performance of different immunosensors for CRP, cTnI, and PCT assays.

Biomarkers	Material	Substrates	Technique	Limit of detection (ng mL ⁻¹)	Linear range (ng mL ⁻¹)	Labelling approach	Ref.
PCT	rGO ^a /Au nanocomposite film	GCE ^b	DPV	0.00043	0.0001 - 20	SWCNH/HPTc ^q	123
PCT	ITO ^c	Glass	CV	0.21	1 - 10000	CdSeZn QD ^r	106
PCT	rGO/AuNPs ^d composite	GCE	Amperometry	0.0001	0.05-100	AuNPs-T ^s	126
PCT	AuNPs	GCE	DPV	0.00003	0.0001 - 36	CuMn-CeO ₂ ^t	148
cTnI	G3/PAMAM/Den/TMB /SAM ^e	Au electrode	EIS ^f	1.58	0.001 - 1000	Label-free	109
cTnI	Lumino/AuNPs	Au electrode	ECL ^g	0.060	0.1-1000	Label-free	149
cTnI	AuNPs	CPE ^h	EIS	0.2	0.2 - 12.5	Label-free	150
cTnI	AuNPs	Ti foil ⁱ	DPV	0.08	0.45 - 490	Label-free	151
CRP	AuNP/SPCE ^j	PADs	EIS	15	50-10000	Label-free	14
CRP	PMPC-SH/SAM/AuNPs/SPCE ^k	PADs	DPV	1.6	5 - 5000	Label-free	152
CRP	APTES/Glu ^l	BB-MZIs ^m	SPR ⁿ	2.1	5-100	Label-free	153
CRP	ssDNA ^o /Au electrode	PDMS ^p	EIS	3125	3125-25000	Label-free	78
CRP				0.38	1 - 100000		
cTnI	GO/G-SPCE	PADs	SWV	0.00016	0.001-250	Label-free	This work
PCT				0.00027	0.0005-250		

^a Reduced graphene oxide

^b Glassy carbon electrode

^c Indium tin oxide

^d Gold nanoparticles

^e Carboxylic acid-functionalized third generation poly(amidoamine) dendrimer on the 3,3',5,5' tetramethyl benzidine modified 6-mercaptohexanoic acid self-assembled monolayer

- ^f Electrochemical impedance spectroscopy
- ^g Electrochemiluminescence
- ^h Carbon paste electrode
- ⁱ Titanium foil
- ^j Electrodeposition of gold nanoparticles on the screen-printed carbon electrode
- ^k Self-assembled monolayer of thiol-terminated poly (2-methacryloyloxyethyl phosphorylcholine) on gold nanoparticle screen-printed carbon electrode
- ^l (3-aminopropyl) triethoxysilane modified with glutaraldehyde
- ^m Silicon broad-band Mach-Zehnder interferometers
- ⁿ Surface plasmon resonance
- ^o Single strand DNA
- ^p Polydimethyl siloxane
- ^q single-walled carbon nanohorns/hollow platinum chains complex
- ^r zinc sulfide capped cadmium selenide quantum dots
- ^s gold nanoparticle-enhanced tyramine
- ^t Copper manganese double-doped cerium oxide nanocomposite

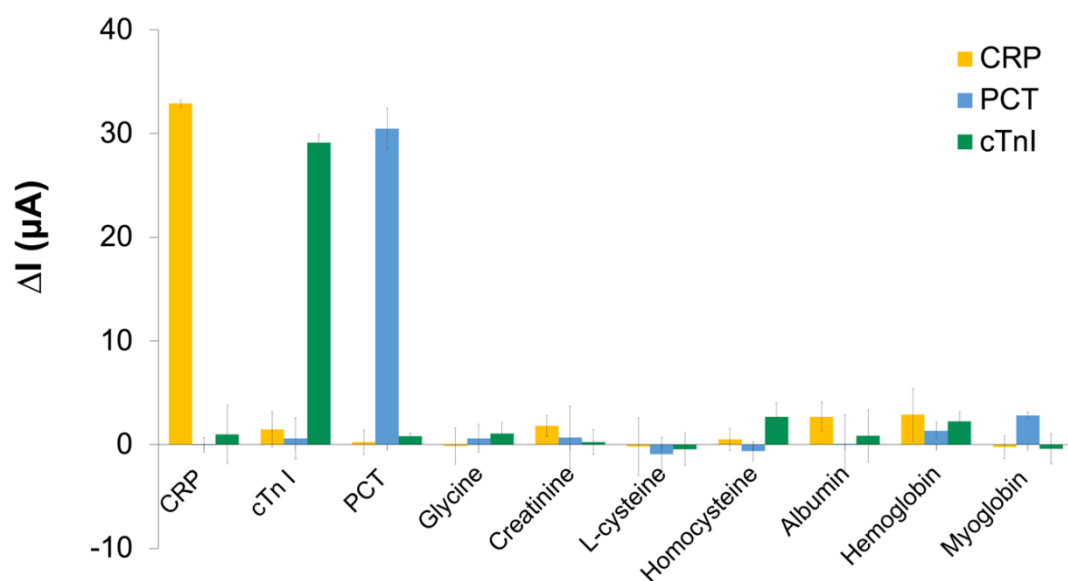


Figure 41. The change in current response (ΔI) of ePAD detection after immobilization with $0.05 \mu\text{g mL}^{-1}$ of CRP, 0.1 ng mL^{-1} of cTnI, 0.1 ng mL^{-1} of PCT, and 1 mg mL^{-1} of other proteins using $3 \mu\text{g mL}^{-1}$ of anti-CRP, 100 ng mL^{-1} of anti-cTnI and anti-PCT, and in the presence of $5 \text{ mM } [\text{Fe}(\text{CN})_6]^{3-/4-}$ in 0.1 M KNO_3 as a redox solution.

3.2.3.6 Reproducibility, selectivity, and stability of the immunosensor

To assess the reproducibility of the immunosensor, different concentrations of CRP (0.05 , 75 , and $250 \mu\text{g mL}^{-1}$), cTnI (0.001 , 0.5 , and 50 ng mL^{-1}), and PCT (0.01 , 0.1 , and 50 ng mL^{-1}) were measured in triplicate in separate of ePADs. The relative standard deviations (RSDs) were achieved in the range of 2.79 – 4.33% for CRP, 2.70 – 4.77% for cTnI, and 1.16 – 4.62% for PCT. The RSDs were less than 5% , which indicates good reproducibility of the developed immunosensor.

Glycine, creatinine, L-cysteine, homocysteine, albumin, hemoglobin, and myoglobin were used as interference substances to examine the selectivity of the immunosensor. A 1 mg mL^{-1} of all of the interferences were prepared and measured on the immunosensor via SWV. As shown in Fig. 41, significant changes in the current responses (ΔI) were only observed in the presence of $0.05 \text{ }\mu\text{g mL}^{-1}$ of CRP, 0.1 ng mL^{-1} of cTnI, and 0.1 ng mL^{-1} of PCT while ΔI in the presence of other interferences were less than 5%, showing great selectivity of the immunosensor toward their designated target analytes.

The stability of the proposed immunosensor was evaluated by keeping the ePADs at $2 \text{ }^\circ\text{C}$ and then measured the sensors weekly for four weeks. As can be seen in Fig. 42, the normalized current of the immunosensor after four weeks of storage decreased by $8.6 \pm 2.1 \%$ for CRP, $7.8 \pm 0.86 \%$ for cTnI, and $9.2 \pm 0.94 \%$ for PCT with %RSD less than 5 %, implying to the developed immunosensor had acceptable stability for up to four weeks¹⁴⁸. The decrease in normalized current due to the loss of antibody activity. As a result, it can be concluded that the developed sensor has good stability for up to one month. Therefore, the ePADs immunosensor could be used to simultaneous detection of three biomarkers in a real sample.

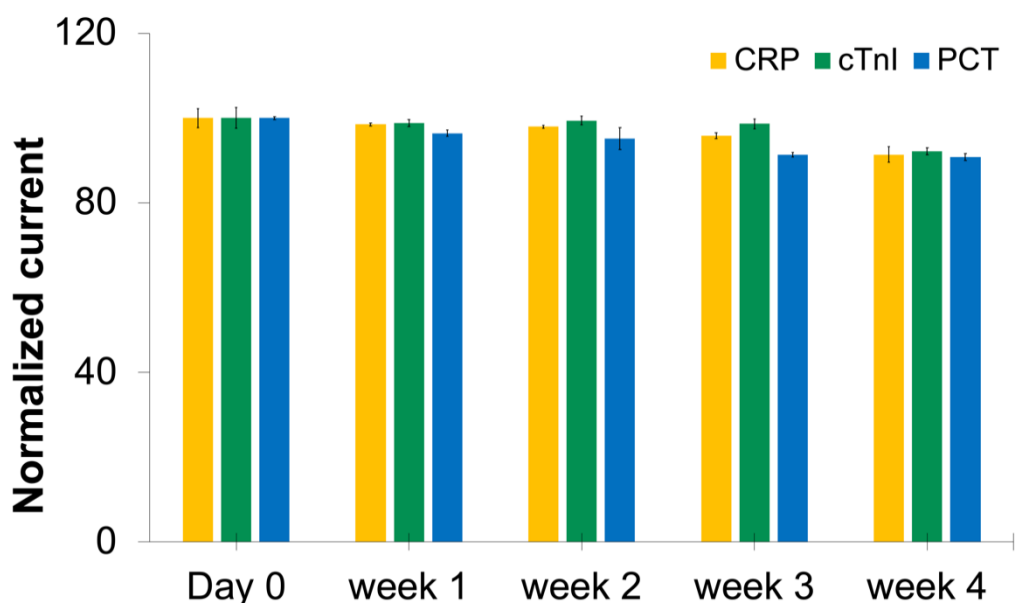


Figure 42. The storage stability of the electrochemical paper-based immunosensor.

Error bars represent the standard deviation calculated from three repetitions ($n=3$).

3.2.3.7 Sample analysis

The practical application of the immunosensor was evaluated in a control serum sample by using the standard addition method. A standard CRP, cTnI, and PCT solution with various concentrations ($1, 3, 7 \mu\text{g mL}^{-1}$ for CRP, $1, 3, 7 \text{ng mL}^{-1}$ for cTnI and PCT) were spiked to control serum and then detected by the developed immunosensor. As summarized in Table. 4, the %recoveries and %RSDs of CRP, cTnI, and PCT in control serum were determined in the range of 98.73% to 103.0% and 0.76% to 4.42%, respectively. This result can confirm that the ePADs immunosensor has favorable application prospects in CRP, cTnI, and PCT detection. Additionally, our

proposed sensor can be used as a new alternative device for detect other biomarkers in a real clinical sample.

Table 4. The percent recoveries of simultaneous CRP, cTnI, and PCT detections in serum sample using the ePADs immunosensor (n=3)^a.

Sample	Added			Found			% Recovery ^b			%RSD		
	CRP ($\mu\text{g mL}^{-1}$)	cTnI (ng mL^{-1})	PCT (ng mL^{-1})	CRP ($\mu\text{g mL}^{-1}$)	cTnI (ng mL^{-1})	PCT (ng mL^{-1})	CRP	cTnI	PCT	CRP	cTnI	PCT
Control serum level I	0	0	0	0.0005 ± 0.0005	0.0001 ± 0.0004	0.0005 ± 0.0005	-	-	-	0.92	4.30	1.04
	1	1	1	0.99 ± 0.02	1.00 ± 0.04	0.99 ± 0.04	99.09	100.5	98.93	2.35	4.02	4.07
	3	3	3	2.96 ± 0.08	3.00 ± 0.07	3.00 ± 0.07	98.73	99.97	99.95	2.86	2.48	2.27
	7	7	7	7.04 ± 0.09	7.09 ± 0.20	7.01 ± 0.07	100.6	101.3	100.2	1.21	2.85	1.06
Control serum level II	0	0	0	0.0005 ± 0.01	0.0003 ± 0.02	0.0003 ± 0.01	-	-	-	2.62	0.76	4.29
	1	1	1	1.01 ± 0.03	1.00 ± 0.02	1.03 ± 0.04	101.0	99.64	102.7	2.60	1.66	3.99
	3	3	3	3.03 ± 0.11	3.06 ± 0.12	3.00 ± 0.08	101.1	102.0	100.1	3.58	3.82	2.72
	7	7	7	7.08 ± 0.22	7.21 ± 0.32	7.20 ± 0.10	101.2	103.0	102.8	3.11	4.42	1.40

^aValues expressed as mean value ± SD.

^bRecovery = (concentration of CVDs biomarker found – concentration of CVDs biomarker in the sample) / concentration of CVDs biomarker added × 100%

3.2.4 Conclusion

A simultaneous electrochemical immunosensing of CRP, cTnI, and PCT on paper-based analytical devices was demonstrated here for the first time. The paper-based device was fabricated by wax-printing technique while the three-electrode system was fabricated by stencil-printed carbon electrode on the paper/transparency

film substrate. This proposed ePAD has multiple detection zones and multiple working electrodes, which could enable simultaneous detection of three CVDs biomarker in a single sample with high selectivity and sensitivity. In the presence of CVDs biomarkers, the changes in current response were proportional to the concentration of biomarkers. The ePADs immunosensor can successfully measure the wide range of 1-1000 ng mL⁻¹, 0.001-250 ng mL⁻¹, and 0.0005-250 ng mL⁻¹ for CRP, cTnI, and PCT, respectively. The proposed immunosensor obtained LODs of 0.38 ng mL⁻¹, 0.16 pg mL⁻¹, and 0.27 pg mL⁻¹ for CRP, cTnI, and PCT, respectively. The detection limit obtained using the proposed sensor sufficiently detects the amount of CRP, cTnI, and PCT in a serum sample according to WHO level. Moreover, this immunosensor provide a high specificity, reproducibility and long-term storage stability for up to 1 month. Finally, the device was then applied for CRP, cTnI, and PCT detection in a certified serum. As a result, this proposed device could open up new possibilities and further extend to a range of point-of-care (POC) testing devices.

PART III

3.3 Cost-effective paper-based electrochemical immunosensor using a label-free assay for sensitive detection of ferritin

(Analyst)

Suchanat Boonkaew,^a Prinjaporn Teengam,^a Sakda Jampasa,^b Sirirat Rengpipat,^cWeena Siangproh,^{d*} and Orawon Chailapakul^{a,e**}

^a*Electrochemistry and Optical Spectroscopy Center of Excellence (EOSCE), Department of Chemistry, Chulalongkorn University, Pathumwan, Bangkok, 10330, Thailand*

^b*Institute of Biotechnology and Genetic Engineering, Chulalongkorn University, Pathumwan, Bangkok 10330, Thailand*

^c*Department of Microbiology, Faculty of Science, Chulalongkorn University, Pathumwan, Bangkok, 10330, Thailand*

^d*Department of Chemistry, Faculty of Science, Srinakharinwirot University, Wattana, Bangkok, 10110, Thailand*

^e*Center of Excellence on Petrochemical and Materials Technology, Chulalongkorn University, Pathumwan, Bangkok, 10330, Thailand*

****Corresponding author at:** Electrochemistry and Optical Spectroscopy Center of Excellence (EOSCE), Department of Chemistry, Chulalongkorn University, Pathumwan, Bangkok, 10330, Thailand. E-mail: corawon@chula.ac.th

***Corresponding author at:** Department of Chemistry, Faculty of Science, Srinakharinwirot University, Wattana, Bangkok, 10110, Thailand. E-mail: weenasi@hotmail.com

Abstract

Ferritin, a blood cell protein containing iron, is a crucial biomarker that is used to estimate the risk assessment of iron deficiency anemia. For point-of-care analysis, a reliable, cost-effective, selective, sensitive, and portable tool is extremely necessary. In this study, a label-free electrochemical immunosensor for detecting ferritin using a paper-based analytical device (ePAD) was created. The device pattern was custom designed onto filter paper to successfully fabricate a deliverable immunosensor. Graphene oxide was first modified onto the working electrode using an inkjet printing technique. An activation step of the electrode surface was then performed using standard 1-ethyl-3-(3-dimethylaminopropyl) carbodiimide (EDC)/N-hydroxysulfosuccinimide (sulfo-NHS) chemistry. Anti-ferritin antibodies were covalently immobilized onto the amine-reactive ester surface. The amount of ferritin was monitored by observing the electrochemical signal of the selected redox couple by differential pulse voltammetry (DPV). In the presence of ferritin, the sensor showed a considerable decrease in electrochemical response in a concentration-dependent manner. In contrast, there was no observable change in current response detected in the absence of ferritin. The current response provided a good correlation with ferritin concentrations in the range of 1 to 1000 ng mL⁻¹, and the limit of detection (3SD/slope) was found to be 0.19 ng mL⁻¹. This fabricated immunosensor offered good selectivity, reproducibility, and long-term storage stability. In addition, this proposed immunosensor was successfully applied to detect ferritin in human serum with satisfactory results. The promising results suggested that this handmade paper-based immunosensor may be an alternative device for the diagnosis of iron deficiency anemia.

Keywords: Ferritin, Paper-based analytical device, Graphene, Label-free, Differential pulse voltammetry, screen-printed graphene electrode

3.3.1 Introduction

Iron, a crucial mineral in our body, plays a vital role in the function of various organ system functions, such as metabolism system, circulation, and the immune system. It has been reported by The World Health Organization (WHO) that iron deficiency is a crucial global health problem caused by numerous factors, such as the frequency of donations, accidents, surgeries, pregnancy, and menstruation ¹⁵⁴. However, one of the most important risks that induces iron deficiency and iron deficiency anemia is receiving blood from donors. Hence, to ensure that the blood that recipients are receiving from blood donors is safe, a screening test is incredibly important and necessary.

Hemoglobin, which is an iron containing-protein in the blood, has long been used as an indicator to certify the safety and quality of blood prior to donation ^{155, 156}. Nonetheless, the estimation of hemoglobin may not be adequate and accurate for early stage detection of iron deficiency anemia because it is not a commonly used biomarker in clinical diagnosis ¹⁵⁷. Furthermore, its sensitivity is very low, implying that the use of this biomarker is insufficient to identify anemia ¹⁵⁸. As a result, detection of other biomarkers related to the iron level in regular blood donors for preclinical diagnosis is vital.

Ferritin is a special type of metalloprotein that is responsible for the metabolic process of iron stored in a cell ^{159, 160}. The WHO has prescribed a normal concentration of ferritin within the range of 30–300 ng mL⁻¹ and 15–200 ng mL⁻¹ for males and

females, respectively ¹⁶¹. The lower levels of ferritin in women are caused by losses of iron during menstruation and childbirth. A smaller or higher amount of ferritin in the blood can lead to several medical issues, including iron deficiency anemia, fatigue, infection, nephritis, hyperthyroidism, hemochromatosis, and cancer ¹⁶². Over the past decades, various detection methods were carried out for ferritin detection, such as electrochemiluminescence, chemiluminescent microparticle immunoassay, radioimmunoassay, and mass spectrometry ^{163, 164}. However, these methods are labor-intensive and require expensive instruments, sophisticated and multiple-step sample preparation, and a large amount of sample, thereby prohibiting quick, on-line, and real-time analysis. In addition, these limitations are missing from the criteria of "ASSURED" in the framework of point-of-care devices.

To circumvent these disadvantages, an electrochemical technique has been developed for ferritin detection. The main advantages of electrochemical techniques are their inherently high sensitivity, rapidity, portability, and the ability to perform real-time analysis ¹⁶⁵. Moreover, the electrode used in these techniques can be miniaturized, leading to a user-friendly device because of the small sample volume requirement. Generally, a sandwich immunoassay, called the "two-sites" assay, has been widely used in many research areas owing to its high sensitivity, selectivity, and robustness. In recent decades, electrochemical detection of important biomarkers based on a sandwich-type format using various labeling with nano- and/or bio-materials has been extensively reported. ¹⁶⁵⁻¹⁶⁷. Labeling materials, including gold

nanorods ¹⁶⁸, quantum dots ^{169, 170}, enzymes ¹⁷¹, and metal oxides ¹⁴⁸, have been reported. The use of these labeling materials has been claimed to improve the sensitivity of detection ¹⁷². In 2017, Song and co-workers enhanced the sensitivity of ferritin detection by using a gold nanorod reporter probe ¹⁶⁸. Although, the labeled materials can improve the sensitivity and feasibility for chemical modification, it still has some limitations, such as requiring expensive materials and labelling step preparations which make more sophisticated and time consuming¹⁴. To eradicate these limitations, it is more desirable to develop a novel label-free immunoassay that allows direct conjugation of antibody and antigen immunocomplexes. This format of assay results in fast multiple steps of antibody preparation and significantly reduces the analysis time. Hence, a label-free immunosensor based on agarose hydrogel was applied for ferritin detection in 2006 (Zhang and co-workers), and the linearity was found to be in the range of 50–500 ng mL⁻¹. Nonetheless, this immunosensor used a large-scale electrode, which precludes mass production and miniaturization of the electrochemical immunosensor. This limitation has led to the widespread use of a disposable, portable, and miniaturized paper-based analytical device (PAD) as an immunosensing platform. The first PAD was originally described by the Whiteside group in 2007. After this introduction, PADs have been widely adopted as a device in various applications, such as for health diagnosis ^{173, 174}, biochemical analysis ¹⁷⁵, forensic science ¹⁷⁶ and food quality control ¹⁷⁷⁻¹⁷⁹. A significant benefit of the PAD is the inherent disposability, portability, low cost, and incinerate after use. In addition, a

pattern on a PAD can be easily designed and constructed¹⁸⁰⁻¹⁸². These properties made PADs are useful as simple, portable, and low-cost platform for various purposes especially for medical diagnosis.

Herein, our aim was to develop a label-free electrochemical immunosensor for the determination of ferritin using a paper-based analytical device for the first time. Unlike normal electrochemical sensor, this proposed ePAD is inexpensive and disposable, which can be incinerated easily and safety after use. The pattern of the paper-based device was specifically designed to avoid the contamination on the counter and reference electrode during modification step. Graphene oxide (GO) was casted onto a screen-printed graphene electrode (SPGE) using an inkjet printing technique to improve the reproducibility. Influencing parameters that could affect the sensor performance, such as other proteins that might be presence in the real sample, incubation time, and antibody concentration, were systematically investigated. In addition, the analytical performance of this immunosensor was also evaluated. The fabricated immunosensor was then applied for screening and monitoring of ferritin in the preliminary stage of iron deficiency anemia and hemochromatosis.

3.3.2 Experimental

3.3.2.1 Chemical and reagents

All reagents used are analytical reagent grade and used as received. Natural human ferritin protein (ab96514) and Anti-ferritin antibody (ab75973) were purchased

from Abcam (Cambridge, United Kingdom). The stock standard solutions of ferritin were prepared with phosphate buffer saline (PBS 0.01 M, pH 7.4) and then stored at 4 °C until use. Albumin from human serum (A9511) was purchased from Sigma-Aldrich (St. Louis, USA). Myoglobin, Bilirubin, homocysteine, bovine serum albumin (BSA), creatinine, alpha-fetoprotein (AFP), C-reactive protein (CRP), potassium hexacyanoferrate (III) ($K_3[Fe(CN)_6]$), 1-ethyl-3-(3-dimethylaminopropyl) carbodiimide hydrochloride (EDC), and N-hydroxysulfosuccinimide (sulfo-NHS) were purchased from Sigma-Aldrich (St. Louis, USA). Trichloroacetic acid (TCA) was obtained from Merck (Darmstadt, Germany).

Graphene and silver/silver chloride (Ag/AgCl) inks were obtained from Gwent Group (Torfaen, United Kingdom). Nano graphene Oxide platelets (GO) was purchased from Angstrommaterials (Dayton, USA). Filter paper grade no.1 (size, 46×57 cm²) was purchased from Whatman international Ltd. (St. Louis, USA, www.sigmaaldrich.com). The screen-printed templates were designed using Adobe Illustrator and made by the Chaiyaboon Co. Ltd., (Bangkok, Thailand, <http://www.chaiyaboon.com>). All aqueous solutions were prepared in ultra-purified Milli-Q water (MQ) ($R \geq 18.2 M\Omega \text{ cm}^{-1}$) that obtained from a water purification system of Merck Millipore (USA).

3.3.2.2 Apparatus

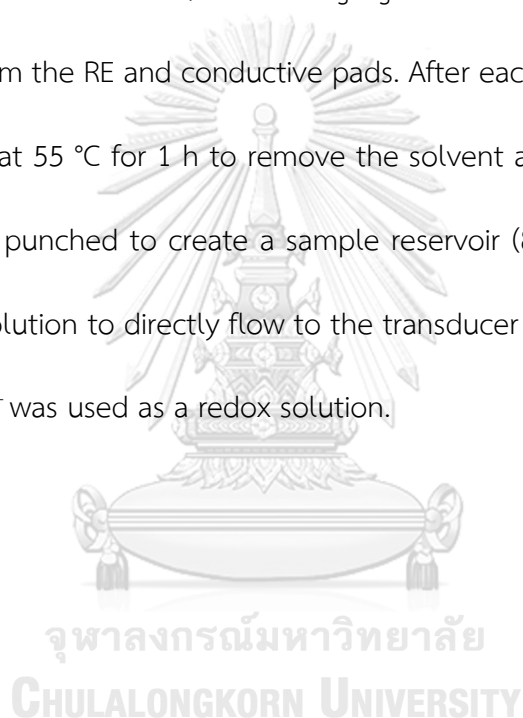
Field emission scanning electron microscopy (FE-SEM) (JSM-7001F at 5 kV) was implemented to verify the successful modification of the electrode. A Xerox Color

Qube 8570 series wax printer was used to create the hydrophobic and hydrophilic areas on the PAD. The Dimatix™ material printer (DMF-2800, FUJIFILM Dimatix, Inc., Santa Clara, USA) was employed for the electrode modification. All electrochemical measurements were carried out by a PGSTAT 30 Potentiostat (Metrohm Siam Company Ltd., Switzerland) and controlled with the General-Purpose Electrochemical System (GPES) software. In all cases, differential pulse voltammetry (DPV) and cyclic voltammetry (CV) were performed at room temperature (25 ± 2 °C) with the adjusted experiments: 150 mV of amplitude, 75 ms of modulation time and 0 V of standby potential (Fig. 47). The potential range was scanned from -0.2 to +0.4 V. All of the experiments were performed in three replications using 5 mM $[\text{Fe}(\text{CN})_6]^{3-/4-}$ in 0.1 M KNO_3 as a redox solution.

3.3.2.3 Design and fabrication of the electrochemical paper-based analytical device (ePAD)

In this study, an ePAD was specifically designed to facilitate the preparation step of immunosensor. The ePAD pattern, which was designed using Adobe Illustrator CS6, is displayed in Fig. 43a. The ePAD components consisted of two main parts: board A as the counter electrode (CE), a reference electrode (RE), and board B as the working electrode (WE) (1.8 cm × 1.9 cm in size). The main benefit of this design was separately designed to prevent the contamination on the CE and RE during the modification step. For construction of the ePAD, the device pattern was first printed onto filter paper (Whatman No.1) using a wax printing technique, followed by placing the printed device

onto a hot plate at 175 °C for 50 s to melt the wax to define hydrophobic and hydrophilic areas. The back side of board B was taped with transparent tape to prevent leaking of the redox solution during the measurements. A three-electrode system on the patterned paper was fabricated using an in-house screen-printing method. Graphene inks were screened onto the hydrophilic area of board A and board B to form the WE (4 mm of diameter) and CE. Ag/AgCl inks were screened onto board A and board B to form the RE and conductive pads. After each screen-printing layer, the ePAD was heated at 55 °C for 1 h to remove the solvent and dry electrode. Board A was subsequently punched to create a sample reservoir (8 mm of diameter) and to allow the redox solution to directly flow to the transducer surface. In this work, the 5 mM of $[\text{Fe}(\text{CN})_6]^{3-/4-}$ was used as a redox solution.



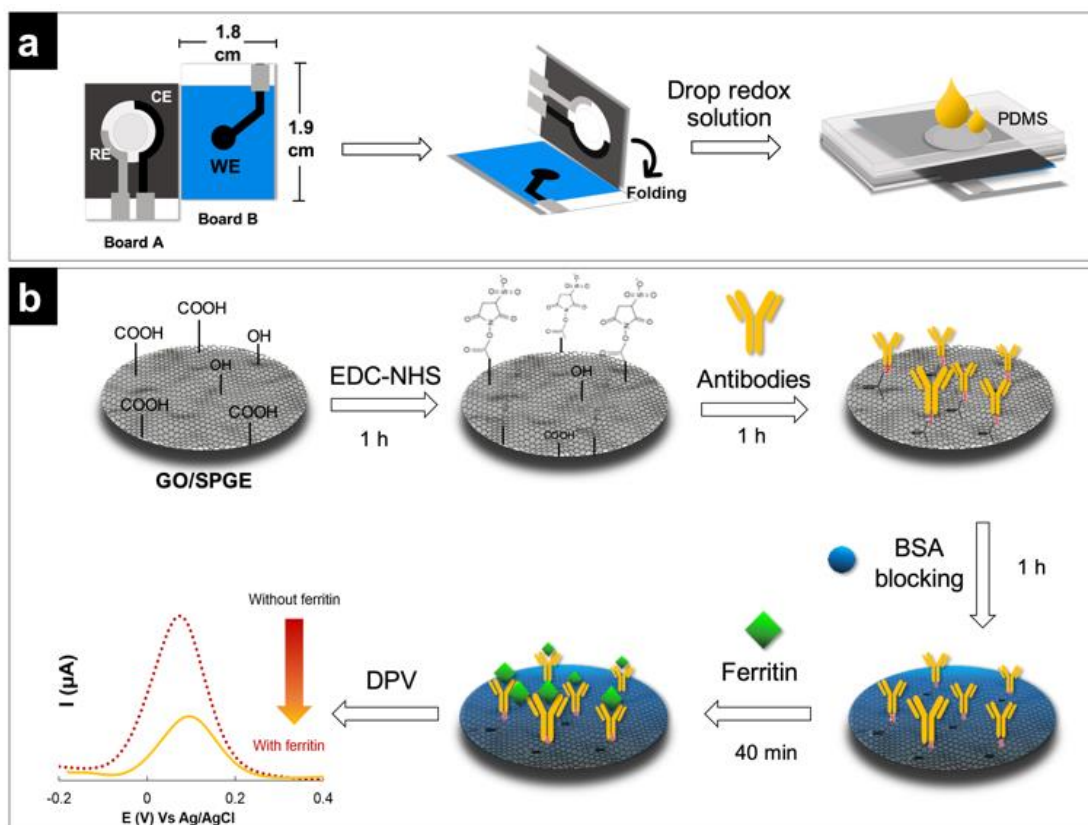


Figure 43. Schematic illustration of the design and composition of ePAD (a) and the overall preparation and immobilization step of electrochemical paper-based immunosensor for detecting of ferritin (b).

3.3.2.4 Inkjet printing for electrode modification

To receive the highest reproducibility, an inkjet printing technique was employed for drop-casting of the GO solution onto the electrode surface. A tiny droplet of GO modifier in the picoliter range was achieved using this technique¹⁸³⁻¹⁸⁵. This technique also generated less material waste due to the small amount of modifier required for each modification step.

Prior to electrode modification, GO was dispersed in N-methyl-2-pyrrolidone (NMP) (7:3 %v/v) and sonicated for 1 h at room temperature (25 ± 2 °C). Subsequently, the GO solution was centrifuged at 6000 rpm for 1 h and filtered through a 0.45- μ m PTFE filter membrane. The GO solution was loaded into a cartridge and printed onto the WE area of the ePAD using a DimatixTM material printer (DMP-2800, FUJIFILM Dimatix, Inc., Santa Clara, USA). The optimal conditions of inkjet printing were as follows: a temperature of 30 °C, 40 V for the jetting voltage, 25 μ M of drop spacing, and two layers of GO printing. These modified electrodes were then baked at 60 °C for 15 min to eliminate the residue solvent for the final step. More explanations of the optimized results can be found in the Sections 3.3.3.4.

3.3.2.5 Preparation of the paper-based electrochemical immunosensor

In this system, direct conjugation between the antibody and target antigen was assigned. The immobilization of the capture antibody was performed as previously described¹⁴. First, 2 μ L of solution containing EDC/NHS (10 mM: 30 mM) was dropped onto the modified WE surface and allowed the activation for 1 h, followed by extensively washing with PBS at pH 7.4. A 2 μ L of the capture monoclonal antibodies (100 ng mL⁻¹ of anti-FTH) were subsequently dropped on the GO-modified SPGE and left for 1 h. The capture antibody was covalently attached onto the GO-modified electrode through direct conjugation between a carboxylic group (-COOH) of GO and the primary amine groups (-NH₂) on the antibodies^{186, 187}. Next, 2.0 mg mL⁻¹ of bovine

serum albumin (BSA) was dropped onto the modified electrode to block the remaining sites on the surface and incubated for 1 h, followed by washing with PBS. The modified immunosensor was stored in the refrigerator at 4 °C until use. The preparation steps for the ePAD immunosensor are summarized in Fig. 43b.

3.3.2.6 Electrochemical measurement and sample analysis

For detection, the prepared immunosensor was first incubated with different concentrations of 2 μL of ferritin (1–1000 ng mL^{-1}) for 40 min, followed by thoroughly washing twice with PBS. After the folding step of boards A and B (Fig. 43a), the ePAD was then sandwiched with polydimethylsiloxane (PDMS) lid to hold two layers (board A and board B) together as well as to avoid the leakage of the solution. Subsequently, 50 μL of 5 mM $[\text{Fe}(\text{CN})_6]^{3-/4-}$ was introduced into the center of PDMS through the hole in the sample reservoirs; subsequently, the electrochemical measurement was performed. For the measurement of ferritin in biological samples, lyophilized human serum was prepared in PBS buffer at pH 7.4. These prepared samples were spiked with various concentrations (10–100 ng mL^{-1}) of ferritin. Finally, the recoveries of these spiked ferritin concentrations were thoroughly calculated.

3.3.3 Results and discussion

3.3.3.1 Characterization of GO-modified electrode

FE-SEM was first implemented to observe the surface morphologies of the modified and unmodified electrodes. Fig. 44 shows the SEM images of SPGE before and after modification of the electrode surface. As shown in Fig. 44b, after casting GO onto the electrode surface, a thin GO sheet was clearly observed, while the unmodified SPGE electrode exhibited a rough surface and stack of graphene layers (Fig. 44a). This result confirmed the successful modification of the electrode surface.

To confirm the existence of GO, Fourier-transform infrared spectroscopy was performed. As shown in Fig. 44c, the characteristic bands of GO, including O-H stretching band at 3350 cm^{-1} , C=O stretching at 1651 cm^{-1} , and C-O stretching at 1025 cm^{-1} , were observed. The IR characteristic bands of the GO-modified SPGE were similar to the bare SPGE electrode, except that the characteristic peak owing to C=O stretching at 1651 cm^{-1} remarkably increased. This clearly confirmed the existence and successful modification of GO on the electrode surface¹⁸⁸.

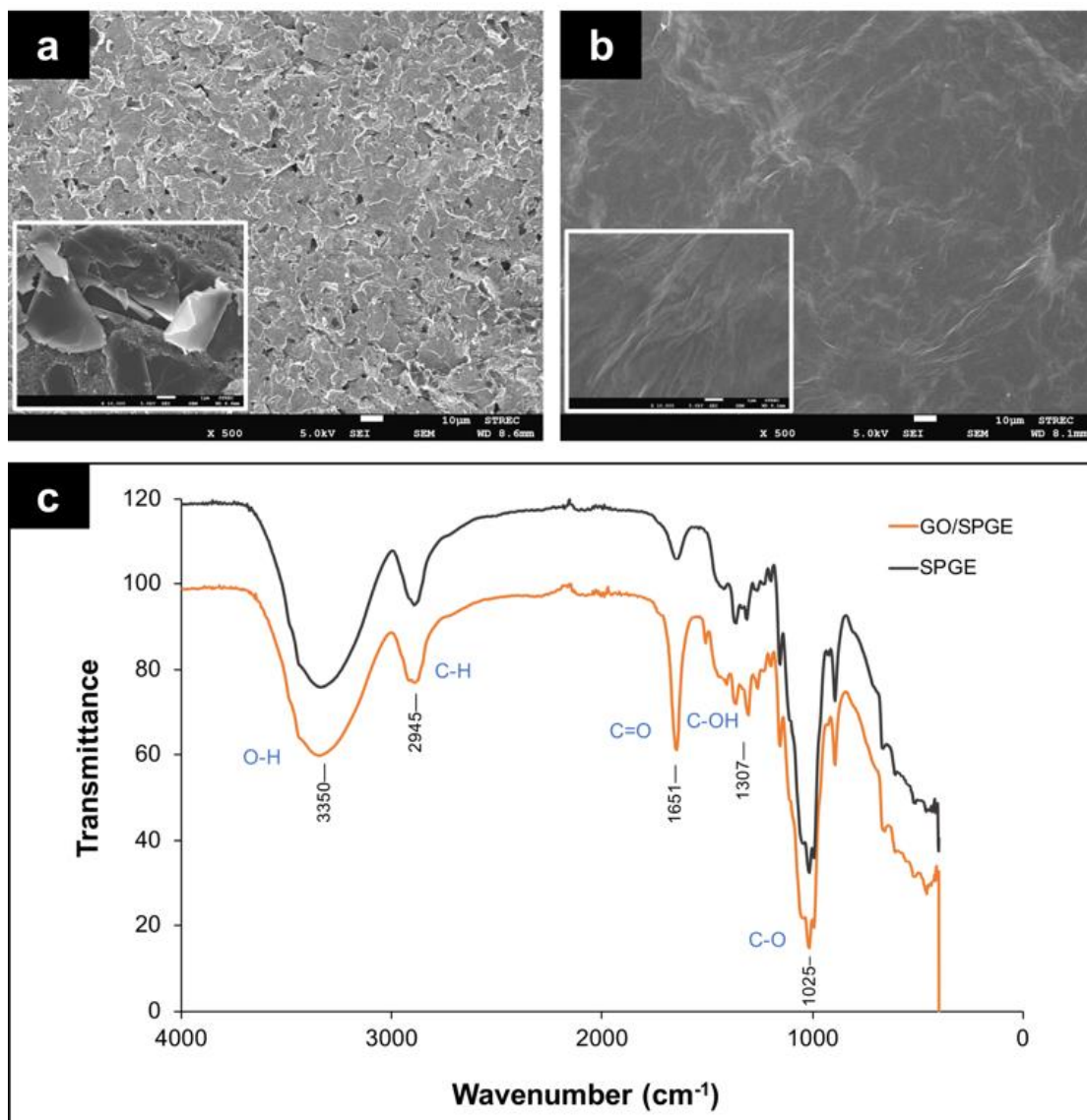


Figure 44. SEM images of bare SPGE (a), GO/SPGE (b) and the FTIR spectra of SPGE and GO/SPGE (c).

3.3.3.2 Electrochemical detection of ferritin using the developed immunosensor

To confirm the proposed concept, the electrochemical signal responses of the modified BSA/Anti-FTH/GO/SPGE with and without ferritin were evaluated. As displayed in Fig. 45a, the presence of ferritin decreased the electrochemical signal response

compared to when there was an absence of ferritin. This decreased signal indicates the formation of an immunocomplexes (antigen–antibody) barrier on the electrode surface, which hinders the diffusion of the redox probe towards the electrode surface¹⁶³. All results confirmed that the process of capturing the biomolecule was accomplished on the immunosensor surface. The results suggested that the developed immunosensor was successfully applied for detection of ferritin.

3.3.3.3 Electrochemical characterization of the modified electrode

The electrochemical impedance spectroscopy (EIS) technique was used to study the electrical property changes at the electrode interface after each modification step. This technique measures the resistance in terms of the charge transfer resistance (R_{ct}). All the impedance spectra include a straight line and a semicircle part controlled by the diffusion process and kinetics-controlled region, respectively. The impedance spectra of 5 mM $[\text{Fe}(\text{CN})_6]^{3-/4-}$ in 0.1 M KNO_3 were recorded in the frequency range of 100 kHz to 0.01 Hz and at an amplitude of 0.1 V. The Nyquist plot of the stepwise modification of each electrode is shown in Fig. 45b. The obtained R_{ct} values were $5.1 \pm 0.3 \text{ k}\Omega$ (curve a, black line), $44 \pm 3.6 \text{ k}\Omega$ (curve b, orange line), $54 \pm 2.5 \text{ k}\Omega$ (curve c, yellow line), $59 \pm 1.9 \text{ k}\Omega$ (curve d, green line), and $80 \pm 1.1 \text{ k}\Omega$ (curve e, blue line) for SPGE, GO/SPGE, Anti-FTH/EDC-NHS/GO/SPGE, BSA/Anti-FTH/EDC-NHS/GO/SPGE, and ferritin/BSA/Anti-FTH/EDC-NHS/GO/SPGE, respectively. The increase in R_{ct} values after each step modification can be explained by the inherent semiconductor GO being cast

onto the electrode surface and the shielding effect of immunocomplexes on the surface^{189, 190}. In addition, the NMP solvent which presence in the preparation of GO can increase the semiconductor properties of the modified electrode. This evidence obviously showed that modification of the immunosensor was successful. Additionally, to confirm the improvement on the R_{ct} value from semiconductor properties of GO and the shielding effect of immunocomplexes on the electrode surface. The relationship between the R_{ct} and the heterogeneous electron-transfer constant (K_{et}) according to the equation (3.3.1) was employed to calculate the K_{et} value^{191, 192}.

$$K_{et} = \frac{RT}{n^2 F^2 R_{ct} A C_{redox}} \quad (\text{equation 3.3.1})$$

Where R is ideal gas constant ($J K^{-1} mol^{-1}$), T is temperature (K), n is a number of electron transfer, F is the faraday constant, R_{ct} value is obtained from the Nyquist plot, A is the geometrical area of the electrode surface (cm^2), and C_{redox} is the concentration of $[Fe(CN)_6]^{3-/4-}$ redox solution (5×10^{-3} M). From the calculation, the K_{et} values of $2.80 \times 10^{-4} cm s^{-1}$, $3.26 \times 10^{-5} cm s^{-1}$, $2.62 \times 10^{-5} cm s^{-1}$, $2.42 \times 10^{-5} cm s^{-1}$, and $1.79 \times 10^{-5} cm s^{-1}$ were calculated for the bare SPGE, GO/SPGE, Anti-FTH/EDC-NHS/GO/SPGE, BSA/Anti-FTH/EDC-NHS/GO/SPGE, and ferritin/BSA/Anti-FTH/EDC-NHS/GO/SPGE, respectively. The decrease in K_{et} value was caused by the shielding effect of immunocomplex on the electrode surface. The evidence here indicates that the successful modification of antibody and antigen complex on the electrode surface.

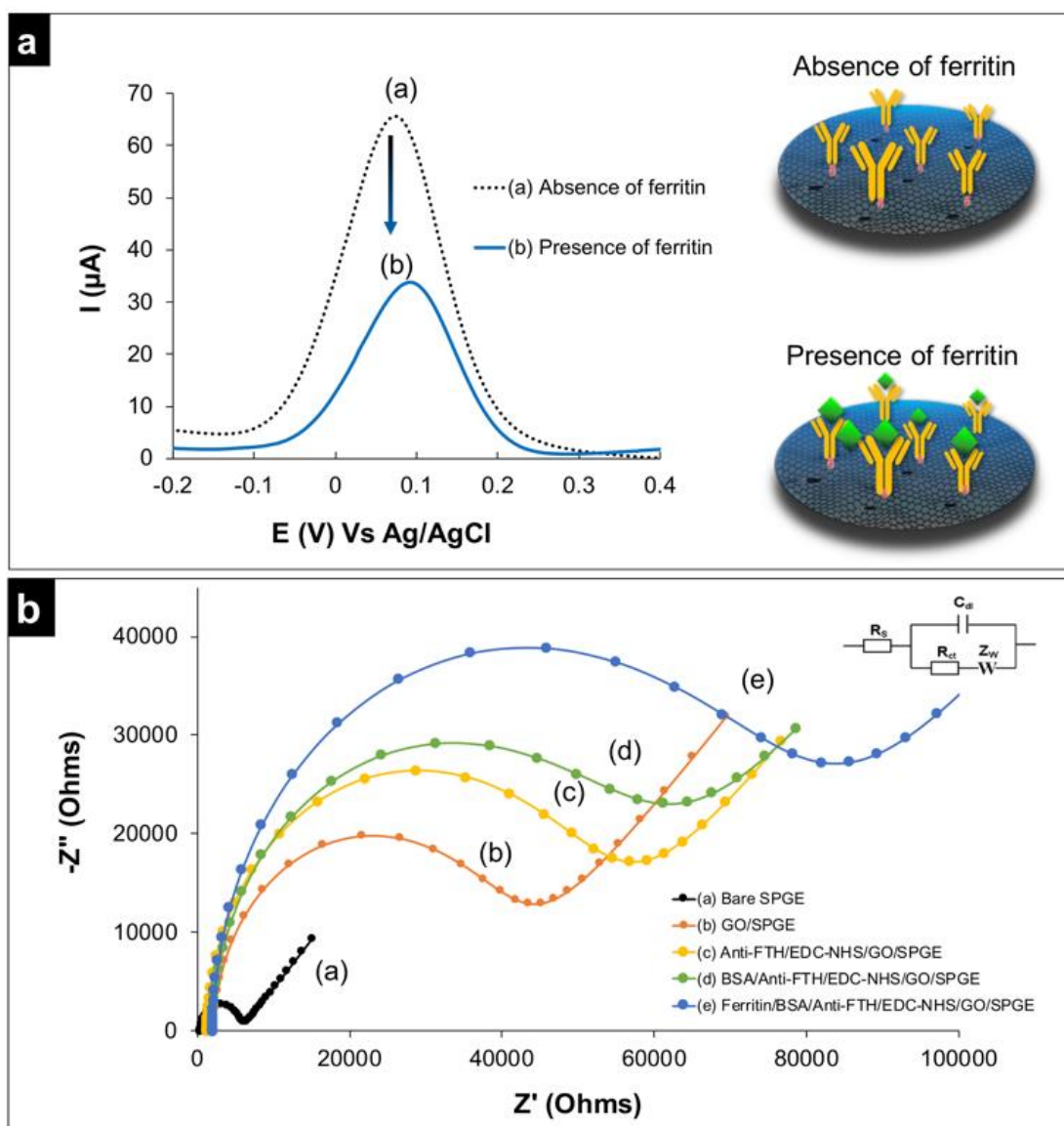


Figure 45. (a) the current response of 5 mM $[\text{Fe}(\text{CN})_6]^{3-/4-}$ in the absence and presence of 100 ng mL⁻¹ of ferritin that were performed by DPV technique and (b) EIS characterization of the modified electrode in a step-by-step fashion for 100 ng mL⁻¹ of ferritin detection using ePAD. Inset picture: equivalent circuit of the Randles model modified with Warburg impedance as a model EIS data.

In addition, the modified electrodes were electrochemically characterized using the cyclic voltammetry technique. As shown in Fig. 46, the current response of the GO/SPGE (curve b, orange line) decreased compared with the unmodified SPGE (curve a, black line). This decreased current response might have been caused by the insulating property of the GO material casted on the electrode surface. The importance of using GO in this work is to create a carboxylic group (-COOH) on the electrode surface before antibody immobilization. Afterwards, the current response was further decreased for Anti-FTH/GO/SPGE (curve c, yellow line), indicating the successful immobilization of antibodies onto the altered surface. After blocking (curve d, green line) and adding the target ferritin (curve e, blue line), a considerable decrease in the current response was detected. This result can be explained by the shielding barrier of the immunocomplexes on the electrode surface, which obstructed electron transfer of the $[\text{Fe}(\text{CN})_6]^{3-/4-}$ redox couple. These results were consistent with the EIS study, suggesting a change in the electrode surface chemistry.

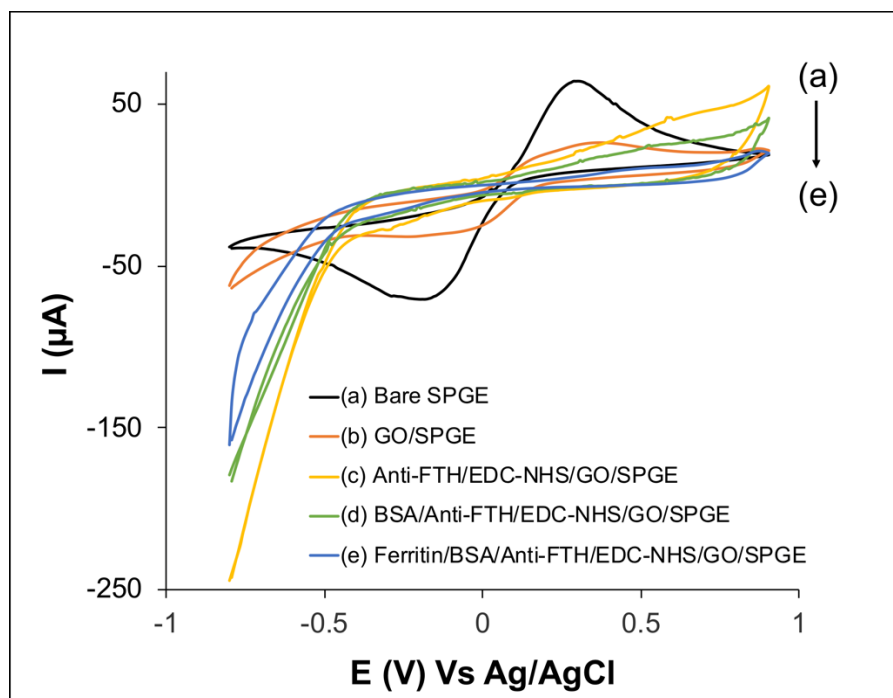


Figure 46. The cyclic voltammogram of stepwise modification on the modified GO/SPGE electrode was performed in the potential between -0.8 and 0.9 V vs Ag/AgCl at a scan rate of 50 mV s^{-1} .

3.3.3.4 Optimization of the variable parameters

3.3.3.4.1 Electrochemical condition of DPV

To achieve the optimal condition for ferritin detection, various parameter of DPV condition include modulation amplitude, modulation time, step potential, and standby potential were optimized. The discussion of the optimal conditions are as follows:

The effect of modulation amplitude was varied in the range from 10 to 250 mV and keep other parameters constant (Fig. 47a). It was observed that the current response gradually increases with increasing amplitude until 250 mV. However, the

resolution of peak shape decreased consequently. Therefore, a 150 mV of modulation amplitude was chosen. Afterwards, the effect of step and standby potential were studied. The step potential was evaluated from 10 to 100 mV (Fig. 47b). For the standby potential was studied in the range from 0 to 7 V as displayed in Fig. 47c. In all cases, the current response decreases with increasing step and standby potential. In order to obtain a high sensitivity and resolution of peak shape, a 10 mV of step potential and 0 V of standby potential was selected. Additionally, the modulation time was studied in the range from 10 to 100 ms as can be seen in Fig. 47d. The similar trend was achieved from modulation time. The current response increase with increasing the modulation time until 100 ms. The results showed that the modulation time at 75 ms was the best condition in term of current response and resolution of peak. Hence, a 75 ms of modulation time were chosen for further studied.

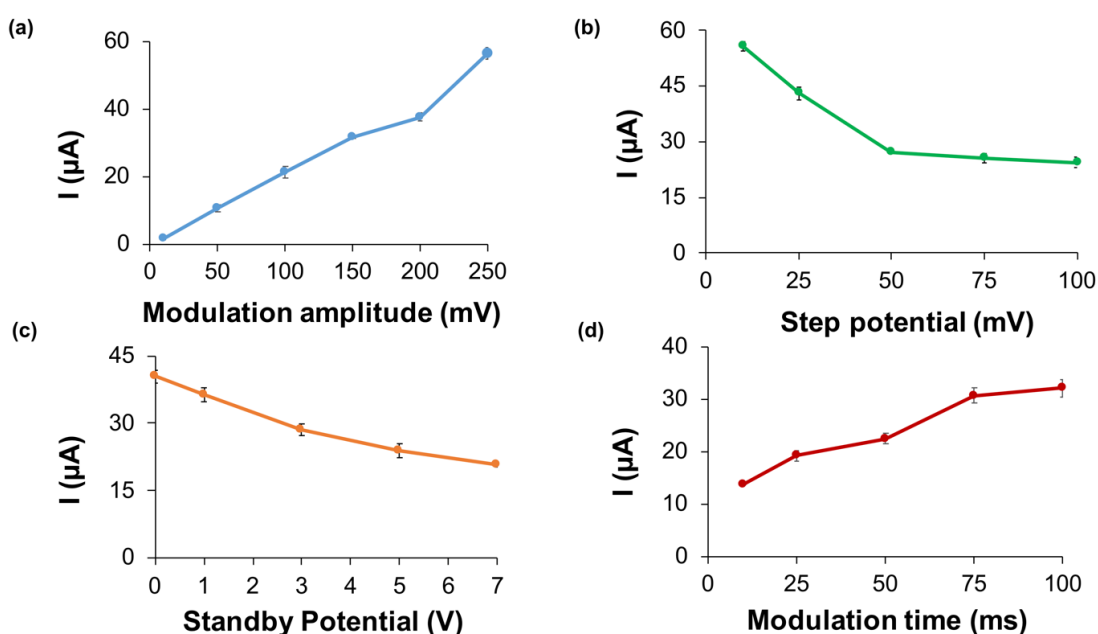


Figure 47. Each electrochemical condition of DPV technique including; (a) the modulation amplitude, (b) step potential, (c) standby potential, and (d) modulation time. The optimal conditions were as follow: a modulation amplitude, step potential, standby potential, and modulation time were 150 mV, 10 mV, 0 V, and 75 ms.

3.3.3.4.2 Inkjet printing parameters

3.3.3.4.2.1 The effect of GO:NMP ratio and number of GO

layer

The effect of GO:NMP ratio on the electrochemical response of the modified electrode was investigated¹⁹³. Briefly, GO was prepared by sonicating the mixture of GO and NMP at different ratio. A 5 mM $[\text{Fe}(\text{CN})_6]^{3-/4-}$ in 0.1 M KNO_3 was used as a redox solution. The current response of redox solution was obtained as shown in Fig. 48a. It can be seen that the current responses increased with increasing of GO:NMP

ratio from 5:5 to 7:3 %v/v and decreased when the ratio of GO: NMP was over 7:3 %v/v. Above 7:3 %v/v of GO: NMP ratio, the current response exhibited poor anodic, cathodic peak currents and also provided high capacitive current. It is due to the agglomeration of graphene within GO solution and a thicker GO films decelerated electron transfer at the electrode surface^{194, 195}. Therefore, an optimal ratio of GO: NMP was found to be 7:3 %v/v.

The number of GO printing layer is another key parameter which affects a loading amount of antibody and an electrochemical behavior of the immunosensor. As illustrated in Fig. 48b, a similar trend can be clearly observed, as in case of GO:NMP ratio. The current response of redox solution tends to increase with an increase of GO printing layers. In contrast, the response slightly reduced over 2 printing layers. It is obvious that the aggregation of excess graphene stack on the modified electrode which can cause a decrease in current response¹⁹⁴.

จุฬาลงกรณ์มหาวิทยาลัย

3.3.3.4.2.2 The effect of drop spacing

Drop spacing was evaluated to provide the homogenous pattern of GO on the electrode surface. Drop spacing is spot size of solution or fluid on the substrate. The range of drop spacing was examined from 10 to 100 μm (Fig. 48c). If the drop spacing is too low, the GO ink droplets are connected with each other and affect to a spread in a large amount of GO on the electrode surface. On the other hand, if the drop spacing is too large, the dot of GO ink was printed on the electrode surface,

leading to a low amount of GO and provide a low current response. Therefore, the 25 μm of drop spacing was used to print the GO from the cartridge.

3.3.3.4.2.3 Apply voltage of inkjet printing

The voltage of piezoelectric inkjet was further studied. The voltage was applied in the range from 20 to 40 V (Fig. 48d). If the voltage is too low, the drop of GO was applied at a low amount on the substrate surface. However, if the voltage is high, a splashing of ink will occur when the drops print on the electrode surface. Therefore, the suitable voltage is 40 V, cause them provides high sensitivity.



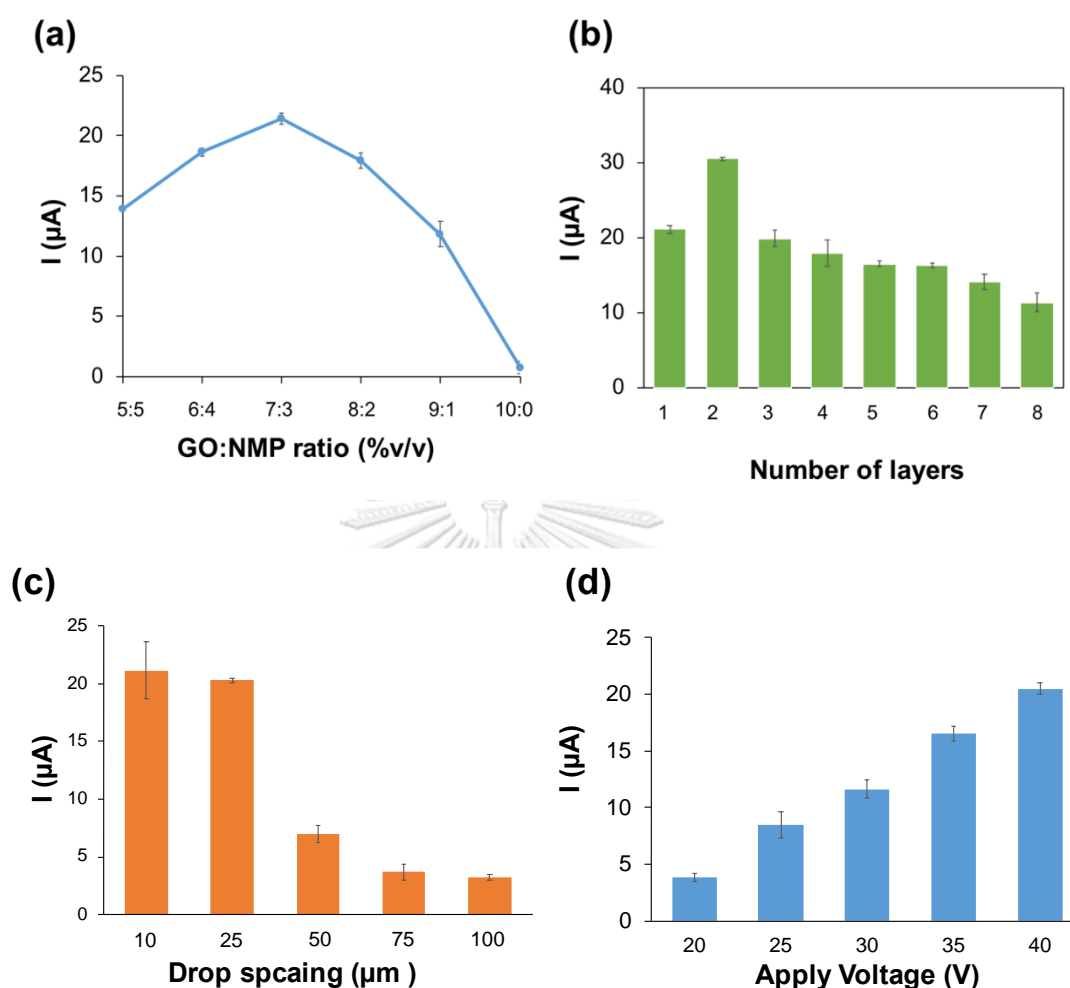


Figure 48. Optimization of the variable parameters: (a) The effect of GO:NMP ratio, (b) number of GO layer modified on the SPGE, (c) the effect of drop spacing, (d) and applied voltage of inkjet printing, using DPV technique in 5.0 mM $[\text{Fe}(\text{CN})_6]^{3-/4-}$ as a redox probe.

3.3.3.4.3 Influence of antibody concentration

To achieve the best ferritin detection, the influence of antibody concentration was first optimized. The effect of antibody concentration on the current

response was studied in the range from 10 to 250 ng mL⁻¹ using the condition as follows: 100 ng mL⁻¹ of ferritin, and 60 min for incubation time. As shown in Fig. 49a, the current responses slightly decreased with increasing antibody concentrations. This signal then reached a plateau when 100 ng mL⁻¹ of antibody concentration was applied. The result obtained is described by saturation of binding between anti-FTH and the ferritin target on the electrode surface. Thus, 100 ng mL⁻¹ for the antibody concentration was determined as the optimal condition for this parameter and was selected for the next experiments.

3.3.3.4.4 Influence of incubation time

The incubation times were evaluated in the range of 10 to 90 min. As shown in Fig. 49b, the current response slightly increased with increasing time; however, the signal reached a plateau after 40 min. These results indicated that a longer incubation time above 40 min did not provide a significantly higher efficiency for immunocomplex formation; hence, 40 min was chosen as a suitable condition for this parameter.

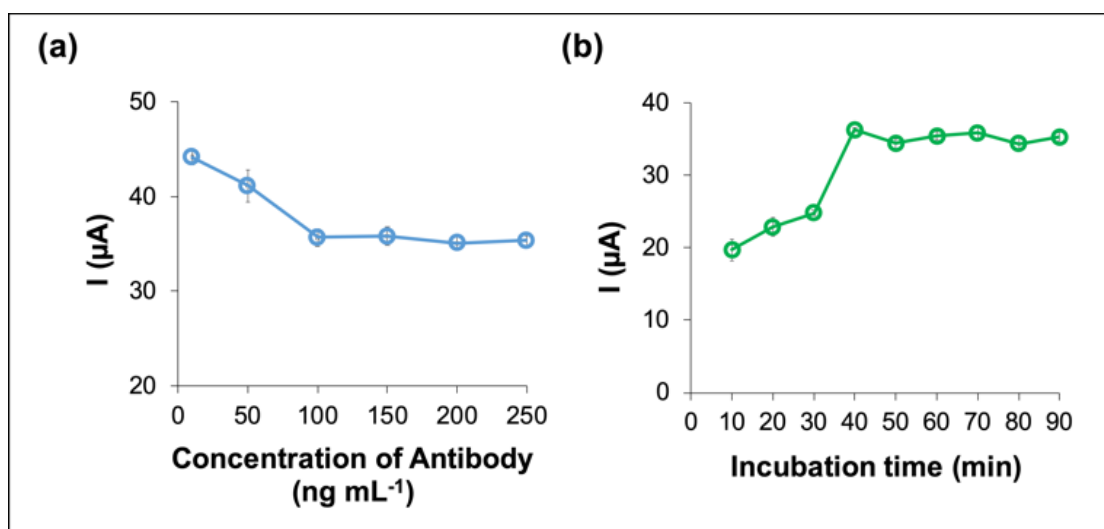


Figure 49. The effect of concentration of ferritin antibodies (from 25 to 250 ng mL^{-1}) with 100 ng mL^{-1} of ferritin (a) and incubation time between 100 ng mL^{-1} of antibodies and 100 ng mL^{-1} of ferritin (from 10 to 90 min) (b), using DPV technique and 5 mM of $[\text{Fe}(\text{CN})_6]^{3-/4-}$ as a redox solution.

3.3.3.5 Analytical performance

Under optimal conditions, the analytical performance of the fabricated immunosensor was evaluated. As shown in Fig. 50a, the current of 5 mM $[\text{Fe}(\text{CN})_6]^{3-/4-}$ decreased linearly with increasing ferritin concentration. A linear calibration was plotted between the ΔI and ferritin concentration (1–1000 ng mL^{-1}), which demonstrated the equation of $y = 0.0325x + 10.434$ with a correlation coefficient (R^2) of 0.9932 (Fig. 50b). All measurements were a mean of three replicates ($n = 3$). The limit of detection ($3\text{SD}/\text{slope}$) and a limit of quantification ($10\text{SD}/\text{slope}$) from the calculation were found to be 0.19 ng mL^{-1} and 0.63 ng mL^{-1} , respectively. A comparison of the analytical performance of this proposed assay with other previously

reported methods is provided in Table 5. As shown in Table 5, among the methods, our proposed approach provided the highest sensitivity, disposability, ease of operation, and the lowest cost. In addition, the performance of this proposed immunosensor was successfully used to detect ferritin in a real sample, thereby making it very attractive for rapid point-of-care applications.

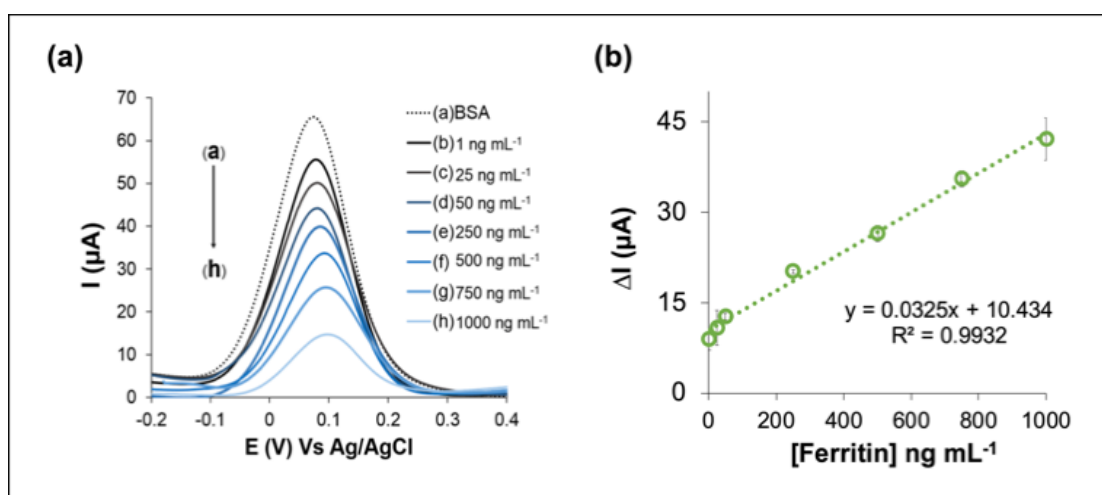


Figure 50. (a) a current response of ferritin concentration in the range from 1 to 1000 ng mL⁻¹, (b) A linear calibration plot between a ΔI and ferritin concentration (1-1000 ng mL⁻¹) is following to the equation $y = 0.0325x + 10.434$ with a correlation coefficient (R^2) of 0.9932. All measurements were a mean of three replicates ($n = 3$).

Table 5. The comparison of different analytical performance for detecting ferritin using different immunoassay methods.

Modified electrode	Labelling approach	Substrates	Technique	LOD (ng mL ⁻¹)	Ref.
AuNPs ^a	labeling	PAD	Fluorescence spectroscopy	-	196
AuNR-CTAB ^b	labeling	Thread	ASV ^d	1.58	168
AuNPs	labeling	Thread	colorimetric	10	197
Agarose hydrogel	Label-free	GCE ^c	DPV	15	163
GO/SPGE	Label-free	PAD	DPV	0.19	This work

^a Gold nanoparticles

^b Gold nanorod stabilized with cetyltrimethylammonium bromide

^c Glassy carbon electrode

^d Anodic stripping voltammetry

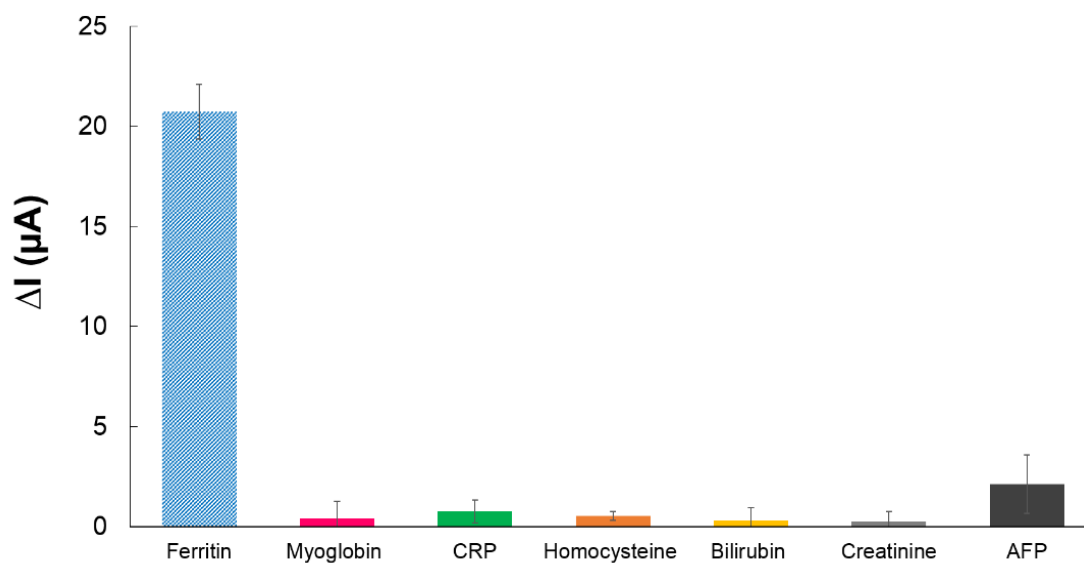


Figure 51. The change of current response in DPV after immobilization with 10000 ng mL^{-1} of myoglobin, C-reactive protein, homocysteine, bilirubin, creatinine, and 100 ng mL^{-1} using 100 ng mL^{-1} of anti-FTH, and in the presence of $5 \text{ mM } [\text{Fe}(\text{CN})_6]^{3-/4-}$

3.3.3.6 Reproducibility, selectivity, and stability of the electrochemical paper-based immunosensor

To access electrode-to-electrode reproducibility of the constructed immunosensor, five electrodes were verified using three different concentrations of ferritin (50 , 100 , and 250 ng mL^{-1}). Percent relative standard deviations (%RSDs) in the range of 2.18% to 4.06% were obtained. These attained %RSDs were less than 5% , implying a significantly low sensor-to-sensor deviation with excellent fabrication reproducibility.

To examine the selectivity of this proposed system, the immunosensor was tested with various interferences that can be possibly found in a practical sample.

Concentrations of $10,000 \text{ ng mL}^{-1}$ of myoglobin, C-reactive protein (CRP), homocysteine, bilirubin, creatinine, and alpha-fetoprotein (AFP) were prepared and examined using the differential pulse voltammetry technique. As shown in Fig. 51, the changes in current response (ΔI) of other tested interferences were less than 10%¹⁹⁸. Even though the concentrations of these examined interferences were 100-times higher than that of ferritin, the current response was only observed in the presence of ferritin. These results confirmed the good selectivity and specificity of the developed sensor for ferritin determination.

In addition, the storage stability of the immunosensor was investigated. BSA/anti-FTH/EDC-NHS/GO/SPGE was prepared using the same procedure and stored at $4 \text{ }^{\circ}\text{C}$ for 4 weeks. As shown in Fig. 52, the current response was stable for 3 weeks and retained a percentage of ΔI of 96.09% from the initial current value and a %RSD of the decreased current response of less than 5% (4.34%). Nonetheless, the current response was gradually decreased compared with the initial current response after 21 days. The results indicated that this immunosensor has an exceptional stability for up to 3 weeks.

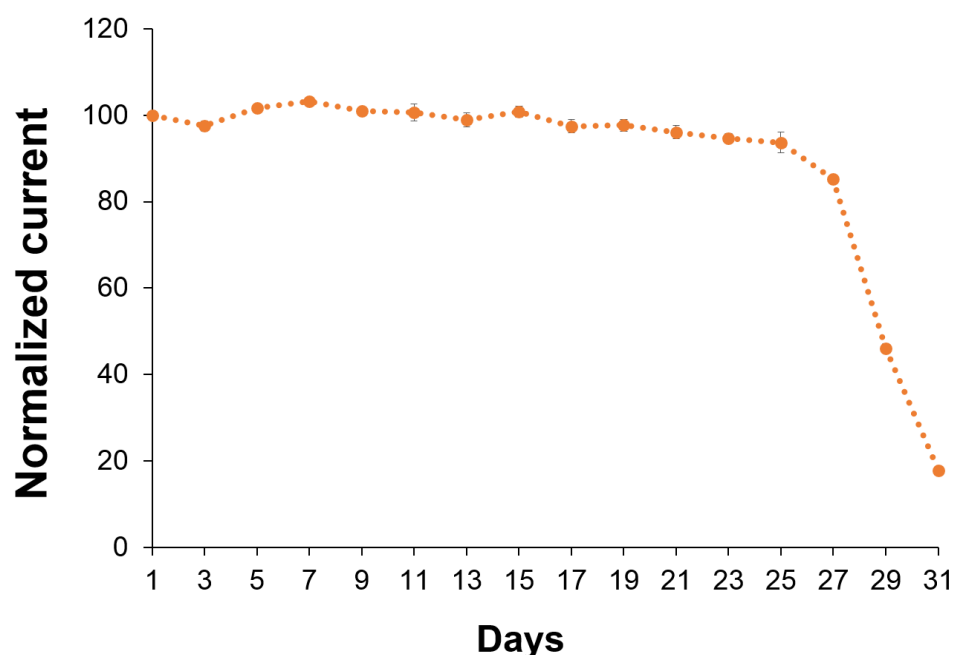


Figure 52. The storage stability of the electrochemical paper-based immunosensor.

3.3.3.7 Detection of ferritin in a human serum sample

For the detection of ferritin in a practical sample, human serum with known amounts of spiked ferritin concentrations were employed as a reference material. These samples were kept at 4 °C until use. As summarized in Table. 6, the % recoveries and %RSDs were determined to be in the ranges of 103.4% to 103.9% and of 0.1% to 2.5%, respectively. The results confirmed the acceptable performance of this developed method for real sample analysis.

Furthermore, to demonstrate the reliability and accuracy, the chemiluminescent immunoassay (CLIA) method was employed as a standard method for validation. The comparison of %recovery between the proposed and CLIA method is tabulated in Table 6. The calculated t-values obtained for this novel sensor are in

the range of 0.31 to 1.78 and are significantly lower than the critical t-value (2.77). According to the paired t-test at the 95% confidence interval, the mean values achieved were indifferent, indicating there was no significant difference between the proposed method and the CLIA. Therefore, this proposed method has no major limitation since it can be applied with other biomarkers. Thereby, this approach could be an alternative tool for point of care testing of ferritin in the early state of iron deficiency anemia.

Table 6. The comparison of determination results for ferritin in spiked serum samples obtained by the developed system (ePAD) and CLIA as a reference method. All measurements were a mean of three replicates (n=3).

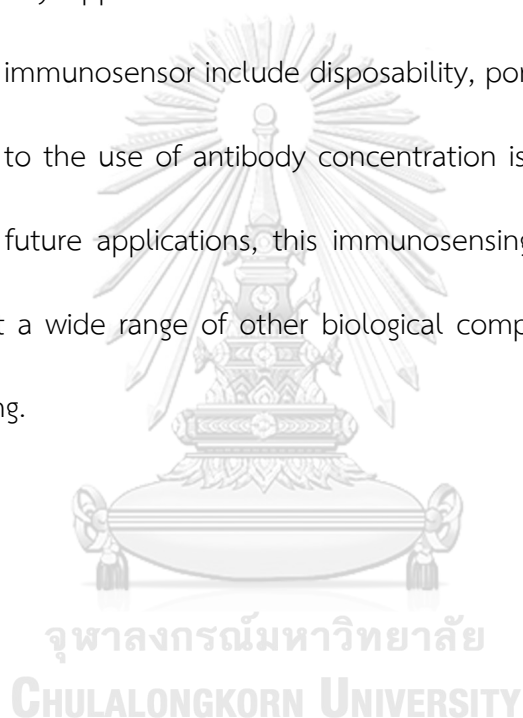
Added (ng mL ⁻¹)	Human serum		% Recovery		%RSD	
	Found (mean \pm SD, ng mL ⁻¹)		ePAD	CLIA	ePAD	CLIA
	ePAD	CLIA				
0	ND	ND	-	-	-	-
10	10.3 \pm 0.2	9.8 \pm 0.1	103.4	98.0	2.5	1.4
100	103.6 \pm 0.1	100.9 \pm 1.7	103.6	100.9	0.1	1.7
1000	1039.7 \pm 0.7	1018.5 \pm 0.4	103.9	101.9	0.1	0.1

*ND = not detectable

3.3.4 Conclusion

A label-free electrochemical immunosensor based on a paper-based analytical device for ferritin detection was successfully hand-fabricated for the first time. The

current response clearly decreased in the presence of the target, ferritin. The electrochemical paper-based immunosensor can successfully detect a wide range of ferritin concentrations (1–1000 ng mL⁻¹) with a limit of detection in the ng mL⁻¹ range (0.19 ng mL⁻¹). Additionally, this immunosensor exhibited a good selectivity, reproducibility, and long-term storage stability for up to 3 weeks. This immunosensor has been successfully applied to determine ferritin in a serum sample. The main advantages of this immunosensor include disposability, portability, ease of operation, and low-cost due to the use of antibody concentration is much lower than that of ELISA method. In future applications, this immunosensing platform can be readily adopted to detect a wide range of other biological compounds for healthcare and point-of-care testing.



PART IV

3.4 Dual flow-controlled behaviors on microfluidic fast-flow/delayed channels for an automated and simultaneous electrochemical detection of Hepatitis B virus and Hepatitis C virus core antigen

(Submitted)

Suchanat Boonkaew¹, Abdulhadee Yakoh², Nattaya Chuaypen³, Pisit Tangkijvanich³,
Sirirat Rengpipat⁴, Weena Siangproh⁵, and Orawon Chailapakul^{1,6*}

¹*Electrochemistry and Optical Spectroscopy Center of Excellence (EOSCE), Department of Chemistry, Chulalongkorn University, Pathumwan, Bangkok, 10330, Thailand*

²*Institute of Biotechnology and Genetic Engineering, Chulalongkorn University, Bangkok 10330, Thailand*

³*Center of Excellence in Hepatitis and Liver cancer, Department of Biochemistry, Faculty of Medicine, Chulalongkorn University, Pathumwan, Bangkok, 10330, Thailand*

⁴*Department of Microbiology, Faculty of Science, Chulalongkorn University, Pathumwan, Bangkok, 10330, Thailand*

⁵*Department of Chemistry, Faculty of Science, Srinakharinwirot University, Wattana, Bangkok, 10110, Thailand*

⁶*Center of Excellence on Petrochemical and Materials Technology, Chulalongkorn University, Pathumwan, Bangkok, 10330, Thailand*

*Corresponding author at: Electrochemistry and Optical Spectroscopy Center of Excellence (EOSCE), Department of Chemistry, Chulalongkorn University, Pathumwan, Bangkok, 10330, Thailand. E-mail: corawon@chula.ac.th

Abstract

Electrochemical paper-based analytical devices (ePAD) are the powerful analytical device tool which is attracting attention to serve as point-of-care testing (POCT) device owing to their require a simple, portable, easy to use, pump-free, and reagent storage. However, the multistep delivery of the chemical solution is necessary to obtain a good performance of the POCT device. Herein, we developed a novel ePAD for sequential fluid delivery by integrating the fast-flow velocity with a paper-based platform for simultaneous detection of hepatitis B (HBV) and hepatitis C core antigen (HCV). The components of ePAD consist of sample and buffer inlet, fast-flow channel, delay channel, electrode layer, and fan-shape waste reservoir. In this present work, we take advantage of the fast-flow velocity to create a fast-flow channel for the washing steps of the immunoassay process. While the delay channel was created to hold the redox reagent for the detection step. Once loading buffer, the buffer will automatically flow through a fast-flow channel, delay channel, electrode layer, and fan-shape reservoir, respectively, without no need of an external pump. To investigate the performance of sensor, the quantity of HBV and HCV was measured using chronoamperometry. Eventually, this proposed ePAD was applied for the simultaneous detection of HBV and HCV in a serum sample to verify the biological applicability. The ePAD sensor provides a great promise as easy to use, portable, capable to perform multiplex detection, and can be applied in wide applications.

Keyword: Microfluidic paper-based analytical device, Hepatitis B virus, Hepatitis C virus core antigen, Dual electrochemical detection, label-free detection

3.4.1 Introduction

Presently, the use of point-of-care testing (POCT) devices at the testing sites of the hospital care units has continued to increase in number since the first exemplification of blood glucose sensor¹⁹⁹⁻²⁰². This substantial expansion is due to the characteristic features of POCT devices such as their simplicity, compact setup, rapid response and low-cost measurement relative to the central laboratory measurement²⁰³⁻²⁰⁵. Since Whiteside's group firstly introduced the microfluidic paper-based analytical device (μ PAD) in 2007⁶⁶, myriad POCT applications for a range of clinical indicators have been later demonstrated²⁰⁶⁻²⁰⁹. Paper itself offers distinguishing characteristics (affordable price, lightweight, compatibility, disposability by incineration, simple fabrication and operation, and liquid transport through capillary force without no need for external pump^{120, 210, 211}), which synergistically amplify the exploitation of POCT device. Although the μ PAD has been extensively employed, it was primarily used in a straightforward analysis. While the assays with high complexity (especially in the complexed biological assay) are still an issue limiting the general use of the μ PAD. By contrast with a single step analysis, a multistep procedure is usually involved in most bioassay (e.g., sample and reagent(s) loading, repetitive washing steps, and detecting step), requiring manual user's interventions during the assay, thus resulting in an imprecision result and lengthening total analysis time. Previously published works attempted to implement those multistep procedures in a single device by tuning the paper-based configurations^{147, 212, 213}. While these reports offer excellent compatibility

with complex bioassays, most of them relied on the colorimetric assay in which the sensitivity is still somewhat limited and not yet reached trace level detection.

To resolve these issues, an electrochemical technique has been integrated with μ PADs (so-called “electrochemical paper-based analytical device” (ePAD))^{20, 214, 215} to enhance the analytical performance of μ PADs for complexed biosensing applications. For example, our group has reported a combination of a three-dimensional paper-based device and a sequential injection format for electrochemical detection of α -fetoprotein¹⁴⁷. Using such a device, the electro-immunoassay, which involves timed order steps, was integrated within a device using a single introduction of running buffer, thus minimizing the reagents manipulation by the user. However, this sensing device still demands a manual user operation to introduce each reagent or switch off the fluid flow. In addition, as the flow in the paper channel followed Lucas-Washburn's theory, the sluggish fluid flow over time (governing by the capillary-driven force) is a crucial factor in lessening the performance of this device.

In 2020, Jang et al.²¹⁶ have demonstrated a fast-flow microfluidic device fabricated from paper, double-sided adhesive, and transparent film for viscosity measurement. This μ PAD possessed two types of fluid flow interconnecting and synergy inside the channel, thus achieving much faster flow rates than the traditional μ PADs. For this purpose, we envisioned that the conceptual idea of a fast-flow format

could be broadened for a paper-based biosensor device to improve the analysis period and facilitate the slow fluid flow in the porous network of ePAD.

Herein, we engineered an automated and fast flow-through ePAD combining multiple steps (washing step, reagent delivery, and detection step) in one-shot analysis using a single running buffer loading. To be highlighted, the proposed platform was elaborately designed for a simultaneous determination of the hepatitis B virus (HBV) and hepatitis C virus (HCV) core antigen, leading causes of death worldwide^{32, 217-219}. Indeed, concurrent infection with both HBV and HCV is growingly recognized in patients with acute and chronic hepatitis²²⁰⁻²²³. It has been reported that 22% of patients with HBV infection are tested positive with HCV²²⁴⁻²²⁸. According to the reports published, the HCV core antigen can also be used as a direct indicator of viral replication in the chronic phase of infection²²⁹ and a related indicator for monitoring the treatment response^{230, 231}. Besides, the HCV core antigen assays provide a comparable sensitivity to NAT (nucleic acid testing), allowing early detection within a few days of window period^{232, 233}. Hence, the immunosensing device capable of detecting HBV and HCV infections occurring either alone or in combination will play a decisive role in diagnosing and evaluating the treatment.

In this present study, the first ePAD for simultaneous quantification of HBV and HCV core antigen based on a label-free immunoassay will be reported. The device integrated two different strategies: a fast flow geometry adapted

from a previous report by Jang et al.²¹⁶ and a time-delayed strategy to achieve full electrochemical detection automation. By merely stacking layers of wax-printed paper, transparency film and double-sided adhesive tape, an automated and time-sequenced electrochemical assay can be accomplished. As illustrated in Fig. 53, the ePAD consists of three main channels: inlet channel (for sample and buffer introduction), fast-flow channel (for washing step), and delayed channel (for electrochemical detection step). In this simultaneous ePAD, a serum sample will wick down towards two discrete electrochemical detection zones that were primarily immobilized with specific antibodies of HBV and HCV. These two electrochemical zones feature separated working electrode (WE) while sharing the same counter electrode (CE) and reference electrode (RE), thus facilitating the multiplexed detection of HBV and HCV. Once a running buffer is introduced to the system, an automated washing of unbound antigens and transferring of the redox indicator in a time-sequenced manner are achieved. As the immunocomplex between antibody and antigen is formed, a decreased current response (correlated with HBV and HCV concentration) is observed, which could be ascribed to the blocking effect from the immunostructures. This ePAD provides several advantages in terms of its easiness, portability, and broad sensing applicability. Finally, this proposed sensor was tested with real patient sera to evaluate the potential applicability of the sensor.

3.4.2 Experimental

3.4.2.1 Material and reagent

All reagents used are analytical reagent grade and used as received. Hepatitis B antigen (ab193473), anti-hepatitis B antibody (ab8636), Hepatitis C core antigen (ab49015), and anti-hepatitis C antibody (ab252694) were purchased from Abcam (Cambridge, United Kingdom). The standard stock solutions of hepatitis B (HBV) and hepatitis C core antigen (HCV) were prepared with phosphate buffer saline (PBS, pH 7.4) and then stored at 2 °C until use. Albumin from human serum was purchased from Sigma-Aldrich (St. Louis, USA). Myoglobin, bilirubin, bovine serum albumin (BSA), creatinine, potassium hexacyanoferrate (III) ($K_3[Fe(CN)_6]$), 1-ethyl-3-(3-dimethylaminopropyl) carbodiimide hydrochloride (EDC), N-hydroxysulfosuccinimide (sulfo-NHS), and N-methyl-2-pyrrolidone (NMP) were purchased from Sigma-Aldrich (St. Louis, USA).

Graphene and silver/silver chloride (Ag/AgCl) inks were obtained from Gwent Group (New Jersey, United States). Nano graphene Oxide platelets (GO) were purchased from Angstrommaterials (Dayton, USA). Filter paper grade no.1 was purchased from Whatman international Ltd. (St. Louis, USA, www.sigmaaldrich.com). The screen-printed templates were designed using Adobe Illustrator and made by Chaiyaboon Co. Ltd., (Bangkok, Thailand, <http://www.chaiyaboon.com>). All aqueous solutions were

prepared in ultra-purified Milli-Q water (MQ) ($R \geq 18.2 \text{ M}\Omega \text{ cm}$) obtained from a water purification system of Merck Millipore (USA).

3.4.2.3 Apparatus

A Xerox Color Qube 8570 series wax printer was used to create the hydrophobic and hydrophilic areas on the PAD. All electrochemical measurements were carried out by a CHI 1223a bipotentiostat (Metrohm Siam Company Ltd., Switzerland). In all cases, chronoamperometry and cyclic voltammetry (CV) were performed at room temperature ($25 \pm 2 \text{ }^\circ\text{C}$) with the adjusted experiments: potential at $-0.1 \text{ V vs. Ag/AgCl}$. For the CV experiment, the potential range was scanned from -0.5 to $+0.7 \text{ V vs. Ag/AgCl}$. All of the experiments were performed in three replications using $5 \text{ mM } [\text{Fe}(\text{CN})_6]^{3-}$ in 0.1 M KCl as a redox solution.

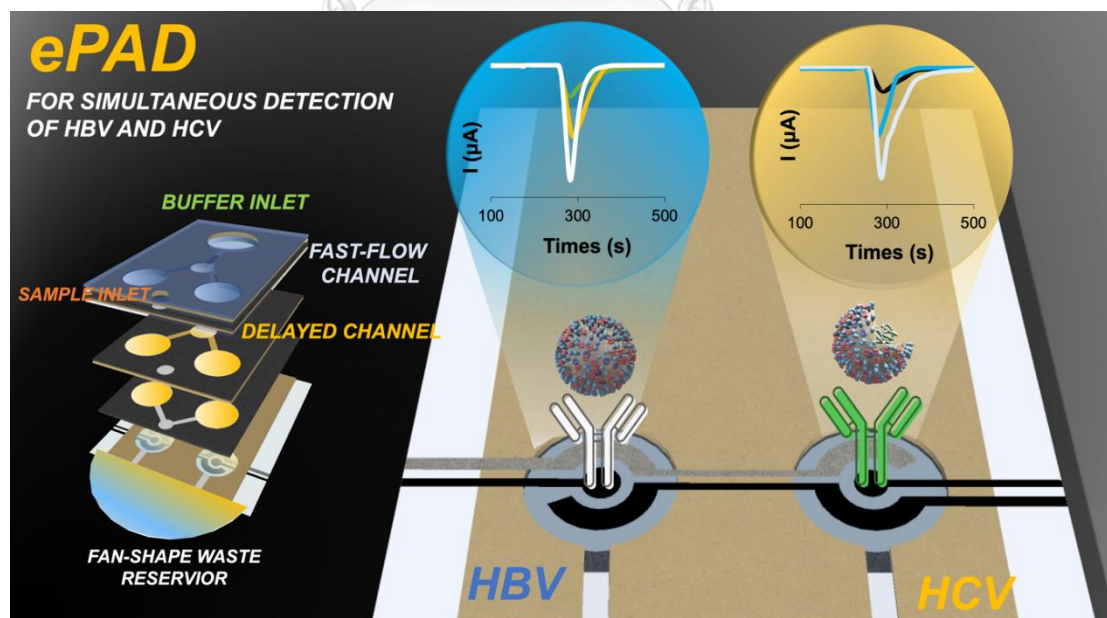


Figure 53. Schematic illustration of components and ePAD device assembly for the simultaneous determination of HBV and HCV.

3.4.2.3 ePAD fabrication

ePAD pattern was fabricated according to a previously described procedure²³⁴. In short, the ePAD pattern was designed by the CorelDRAW X4 software and fabricated by wax printing method on filter paper using a wax printer (Xerox ColorQube, Japan). The printed wax paper was cured in an oven at 160°C for 2 min to create the hydrophobic and hydrophilic area. The double-sided adhesive tape (467MP, 3M) and transparency film were then individually cut using a CO₂ laser engraving machine to create a flow channel. The gap height of the fast-flow channel was adjusted by stacking the double-sided adhesive tape with transparency film along the channel. Each increment layer has an average height of 150 µm. The effect of the device geometries was further studied and described in section 3.4.3.3. For electrodes fabrication, a carbon-based ink (as a working electrode (WE) and counter electrode (CE) and Ag/AgCl ink (as a reference electrode (RE)) were printed on transparency film. The three-electrode system was constructed using an in-house screening method. After that, the printed electrode was baked in an oven at 55°C for 1 h to remove the organic solvent in the ink composition. Lastly, the electrode was assembled with other components and connected with an alligator clip to perform the electrochemical measurement.

3.4.2.4 Electrode modifications

The drop-casting method was used to fabricate the GO-modified electrode, following our previous report²³⁵. Briefly, GO was prepared with N-methyl-2-pyrrolidone

(NMP) at the ratio of 7:3 %v/v or 0.35 mg mL⁻¹. Next, 1.5 μL of 0.35 mg mL⁻¹ GO was casted on the surface of the WE (GO-SPGE) and allowed to dry at 60° C for 10 min. Then, GO-SPGE was anodized with 20 μL of 0.5 M NaOH at +1.4 V vs. Ag/AgCl for 30 s to increase the amount of carboxylic group on the GO sheets, followed by washing step with milli-q water. This anodized electrode was further activated with 1 μL solution including 10 mM of EDC and 30 mM of NHS at 4° C for 1 h, followed by washing step (2X) with 10 μL of PBS buffer pH 7.4. A 1 μL of monoclonal anti-hepatitis B (1 μL of anti-hepatitis B : 75 μL of PBS buffer) and monoclonal anti-hepatitis C (1 μg mL⁻¹) were covalently attached on the modified electrode surface through a direct conjugation of amine groups (-NH₂) on the antibodies and amine-reactive sulfo-NHS group on the modified electrode and incubated at 4° C for 1 h. Then, the antibodies/GO-SPGE was washed twice with 10 μL of PBS buffer pH 7.4. The unreacted carboxyl group on the WE was treated with PBS buffer at -1.4 V vs. Ag/AgCl for 30 s, followed by washing with 20 μL of milli-q water. Next, 3 mg mL⁻¹ of 1 μL bovine serum albumin (BSA) was applied on the electrode surface for 1 h to prevent the non-specific adsorption, then followed by washing twice with 10 μL of PBS buffer pH 7.4. The modified electrodes were stored at -20 ° C when not immediately used. The step-by-step preparations of the electrode are shown in Fig. 54.

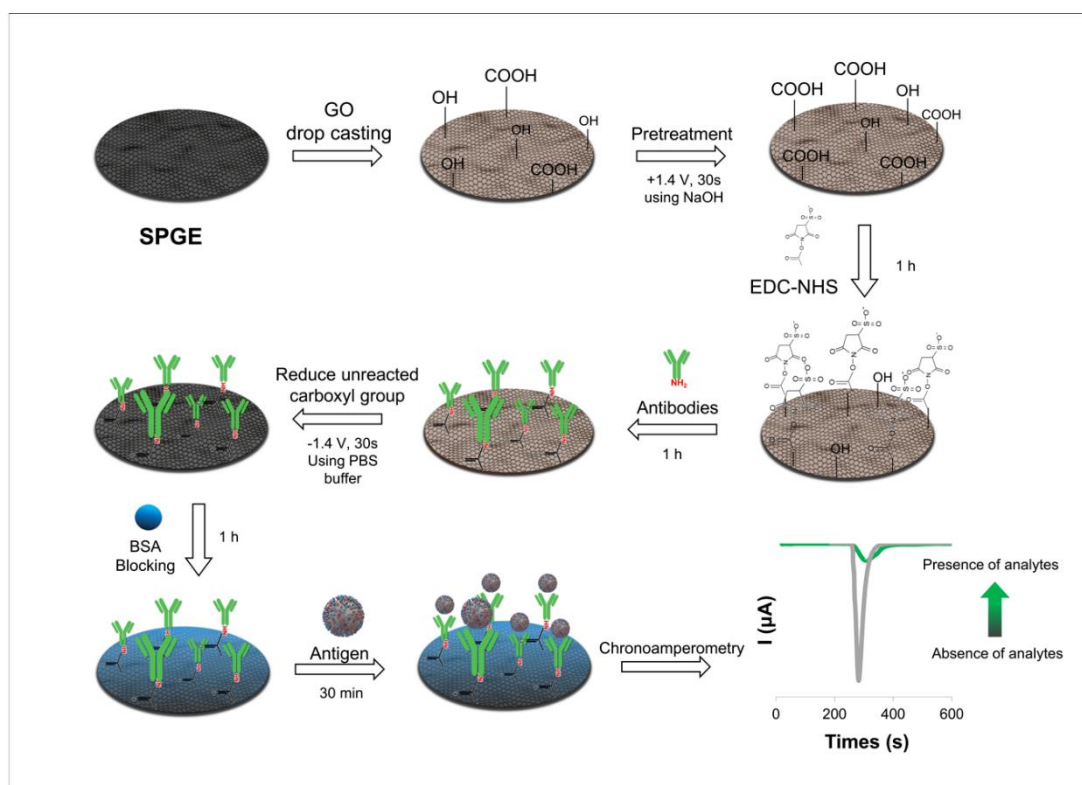


Figure 54. The step-by-step modification on the modified electrode.

3.4.2.5 Sample preparation

Serum samples were obtained from the Faculty of Medicine, Chulalongkorn University. The samples were prepared following the protocol from our previous study²³. Briefly, the blood samples were collected from the patient. The clot was then removed by centrifugation at 1500 rpm for 15 min. Lastly, the supernatant (or serum) was kept in the refrigerator at -80°C when not in use.

3.4.2.6 Detection procedure

For simultaneous detection of HBV and HCV, 15 μL of sample solution was first introduced to the sample inlet. After the reaction is completed, 300 μL of a carrier buffer was loaded onto the buffer inlet. A chronoamperometry (potential of -0.1 V vs Ag/AgCl , sample interval of 250-400s, and run time of 600s) was then monitored.

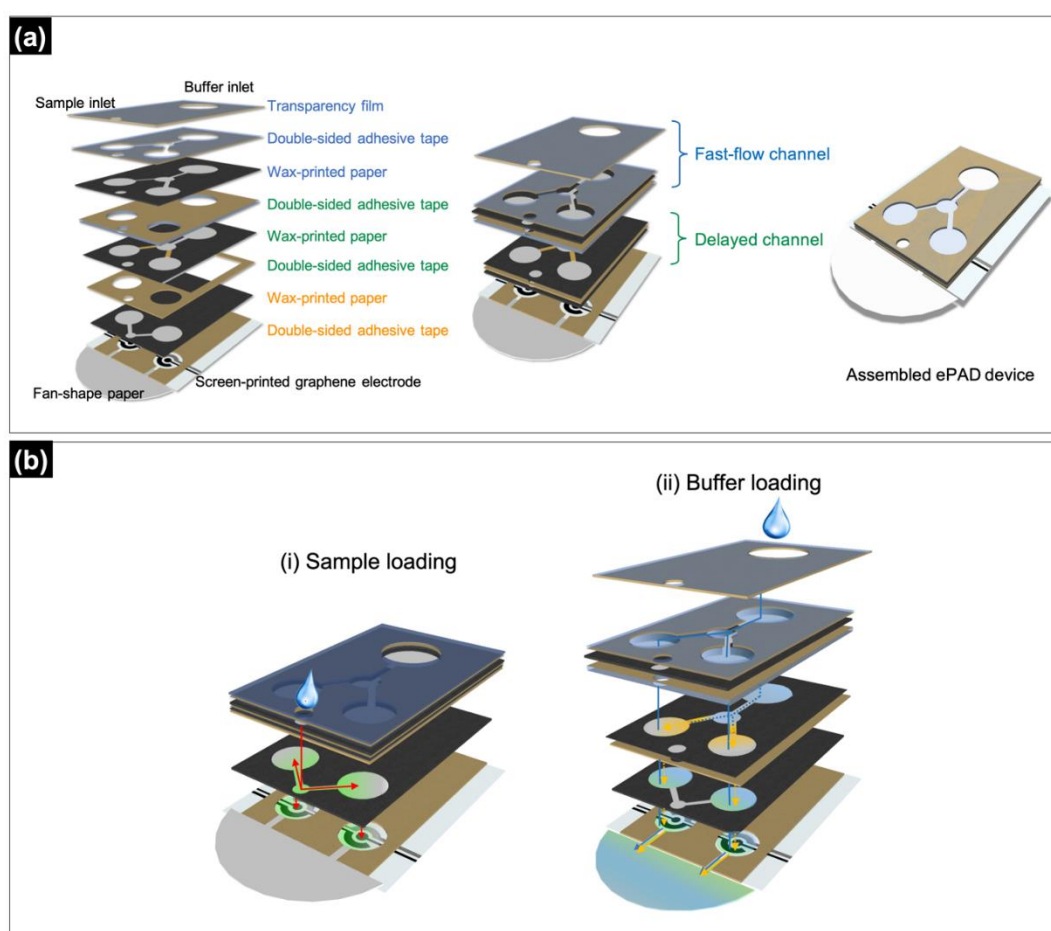


Figure 55. (a) ePAD components and assembly and (b) operation of ePAD: (i) sample loading via a sample inlet, (ii) running buffer loading through the buffer inlet to perform the automated assay, and simultaneous electrochemical measurements.

3.4.3 Results and discussion

3.4.3.1 Design and operation of the immunosensing ePAD

To integrate advanced functionality of the fluid handling using an ePAD device, here, we united the two different microfluidic strategies; fast-flow platform and sequential fluid delivery, within the 3D multilayers ePAD for automated electrochemical detection. An ePAD device was fabricated by laminating filter papers with transparency films, and double-sided adhesive tapes (DSA), thus forming a sandwiched paper device (Fig. 55). The ePAD device consists of five major components: the electrode layer, fan-shaped waste reservoir, layers of delayed channel, layers of fast-flow channel, and inlet zone (Fig. 55a). Starting from the top component, the inlet zone is where the sample and running buffer will be loaded. The loading sample will move across each layer and directly terminate at two electrochemical detection zones. Likewise, a running buffer coming from the buffer inlet will pass through each zone (fast-flow zone, detection zone and delayed zone, respectively) in a time-sequenced manner, thus resulting in a continued washing of unbound antigens and subsequent eluting the stored redox indicator from the delayed zones. Next, the fast-flow paper zone containing a hollow channel served as an external pump to facilitate rapid fluid transport, enabling continued and rapid washing of preloaded unbound samples without the need for user intervention. By contrast, the running buffer moving through the delayed zone will be slowed down compared to that of moving through the fast-flow channel due to an absence of the fast-flow hollow channel. Also, the paper layer

in the delayed zone was used to store the redox indicator solution. This deposited solution will be subsequently introduced to the microfluidic mainstream, thus facilitating a label-free electrochemical measurement. Lastly, electrochemical detection zones connected with the fan-shaped waste reservoir were designed for simultaneous electrochemical detection. Interestingly, it has been reported in the literature that the fan-shaped waste reservoir can compensate the decay in flow rate within the analysis channel and provide a quasi-steady flow behavior²³⁶.

The overall operation of the proposed ePAD is presented in Fig 55b. In brief, after the sample solution is loaded (i), the targeted antigens will transport from a single sample inlet to two detection zones, which were prior immobilized with each specific antibody. Once the reaction is completed, the buffer solution will be loaded via a buffer inlet (ii). This running buffer is quickly transported through a fast-flow channel to wash the excess antigens/interferences to the fan-shape waste reservoir and gradually released the spotted redox indicator to the detection zones. Finally, the label-free electrochemical measurements were performed via chronoamperometry to quantify the amount of HBV and HCV (iii).

To demonstrate an automated sequential delivery of the redox indicator of the proposed ePAD, red color dye representing a redox solution was spotted on the delayed channel to monitor the flow behavior (Fig. 56). After loading the carrier solution (300 μ L), a solution flows through the fast-flow channel and reaches the

detection zone within 16 s (Fig. 56a). In the meantime, the buffer solution traversed across the delayed channel will gradually elute the red-spotted dye to waste reservoirs within 300s (Fig. 56a). From this result, the velocity (over 3.7 cm of ePAD device) is approximately calculated to be 0.0136 cm s^{-1} . Likewise, we further verified the fast-flow functionality of the proposed ePAD by loading a green dye representing a sample and a red dye representing a redox solution and monitoring the flow behavior. It is apparent in Fig. 56b and 57 that the green dye (representing a sample) was visibly eluted from the discrete sample zone and washed out to the waste reservoir while the red dye (representing a redox solution) from the delayed channel will consecutively reach the detection zone and rinse off in a time-sequence step (as illustrated in fan-shaped waste reservoir). Also, this result clearly justifies the effective washing and reagent transferring step by the fast-flow channel. A similar experiment was conducted with a redox solution for electrochemical measurement. A solution $\text{K}_3\text{Fe}[\text{CN}_6]^{3-}$ was spotted on a delayed channel to confirm the working principle by chronoamperometry. In this study, chronoamperometry was chosen to monitor the continuous flow response due to its high sensitivity technique. Also, the chronoamperometric measurement can particularly avoid the limitations from static electrochemical techniques (e.g., voltammetry, electrochemical impedance spectroscopy), in which the electrochemical measurement can be performed after the solution flow saturated in a paper-channel or after a device was cut off by the user to prevent a convective mass transfer contribution²³⁷. 300 μL of buffer solution was

loaded to the ePAD device and measured the change of charge response after captured with 1 ng mL^{-1} of HCV target analyte. The result is presented in Fig. 58. The result showed that the redox solution initially elutes at $\sim 260\text{s}$ and the velocity (over 3.7 cm) is approximately 0.0144 cm s^{-1} . It was found that the velocity results of the redox solution were consistent with results from a dye solution measurement. Accordingly, these results evidently verify the functionality of the proposed sensor.



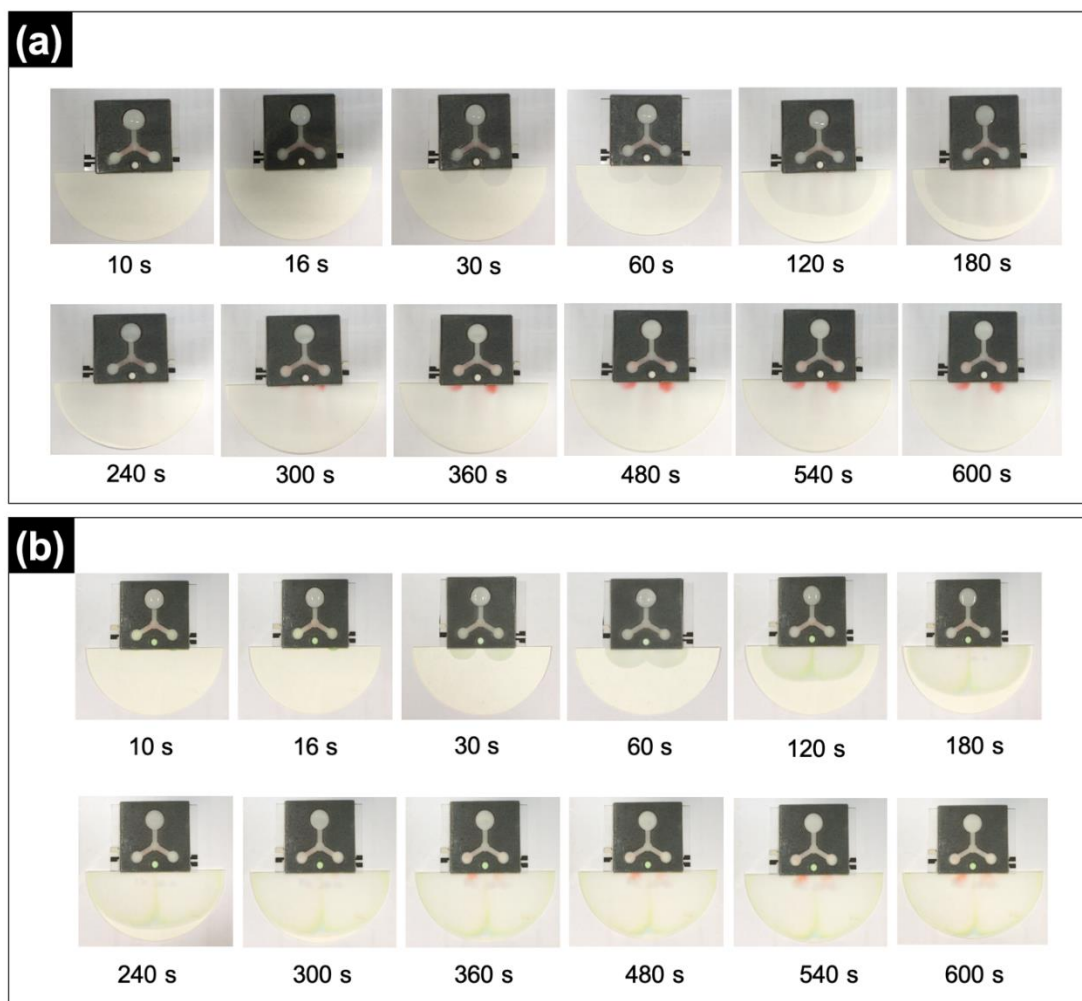


Figure 56. (a) Time-lapse images of ePAD device during flow using a red dye to represent a redox solution in a delayed channel and (b) Time-lapse images after buffer loading by using a green dye representing a sample and a red dye representing a redox solution with gap height at $150\ \mu\text{m}$ and the channel width of the delayed channel at $4.0\ \text{mm}$.

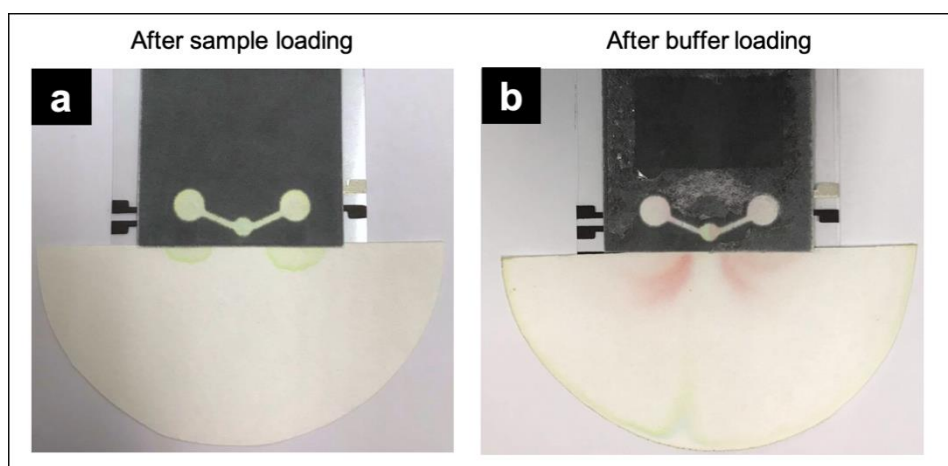


Figure 57. (a) Image showing the flow path after sample loading by using a green dye to represent a sample solution and (b) Image showing the flow path after buffer loading.

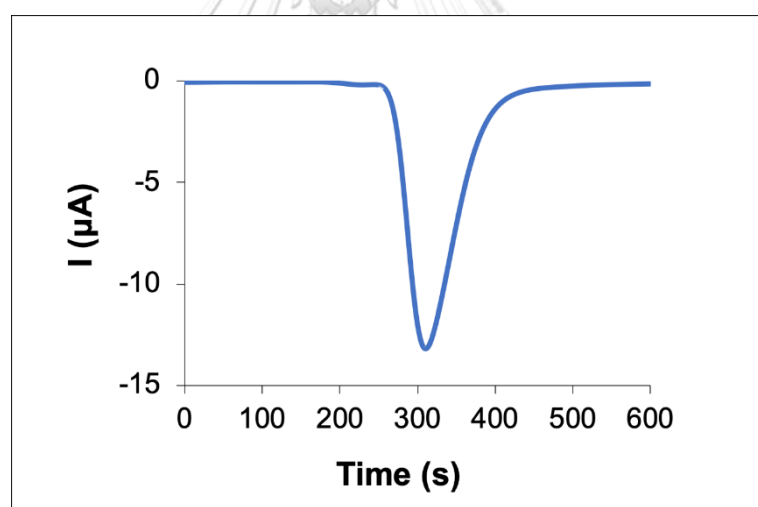


Figure 58. The flow profile of redox solution using 25 mM $\text{K}_3[\text{Fe}(\text{CN})_6]$ spot on the delayed channel.

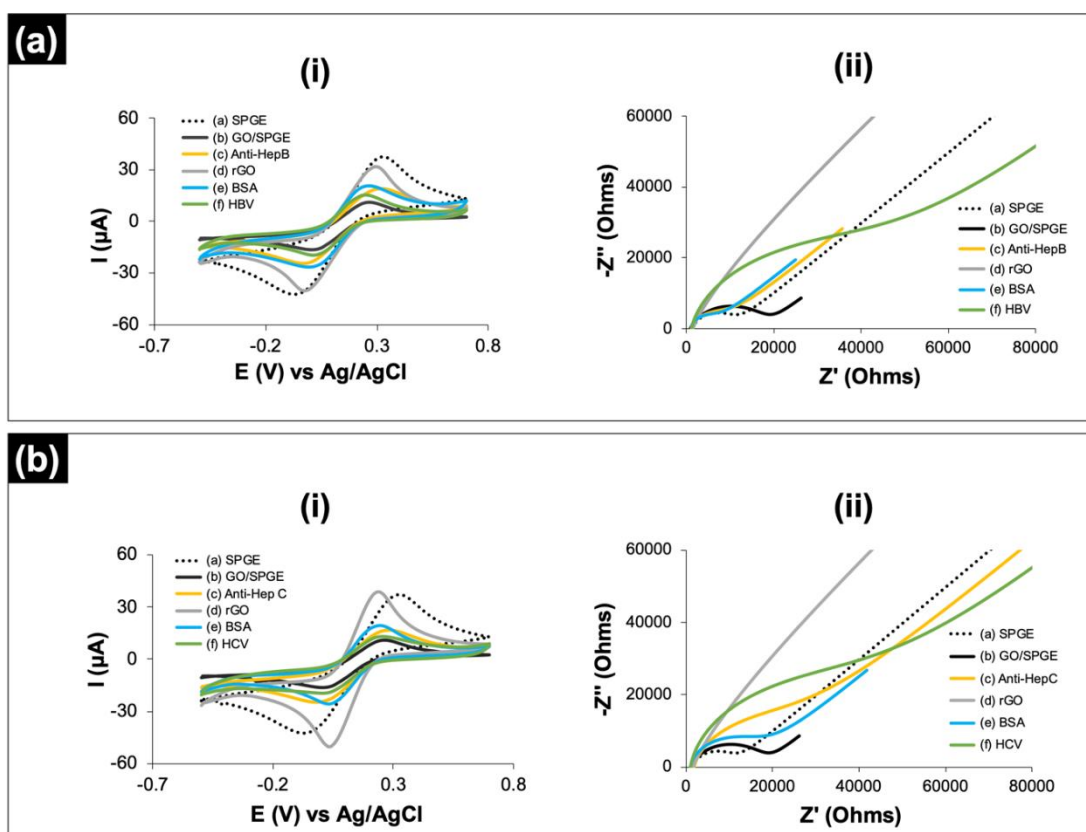


Figure 59. CV (i) and EIS (ii) characterization of step-by-step modification in a static system using 5 mM of $\text{Fe}(\text{CN})_6^{3-/4-}$ containing 0.1 M KCl for HBV (a) and HCV (b), respectively.

3.4.3.2 Electrochemical characterization of the immunosensing ePAD

The change in the interfacial properties from the step-by-step modifications can be characterized by the complementary cyclic voltammetry (CV) and electrochemical impedance spectroscopy (EIS) technique in a static system (using 5 mM of $\text{Fe}(\text{CN})_6^{3-/4-}$ in 0.1 M KCl solution). CV experiment was performed by sweeping from -0.5 to +0.7 V vs. Ag/AgCl at scan rate 75 mV s^{-1} . As shown in Fig.59a(i) and 59b (i), the current response of the bare electrode (SPGE, curve a, dash line) decreased

when GO was casted on the electrode (GO/SPGE, curve b, dash line). The decreasing in current response has been caused by the insulator properties of GO solution^{20, 147}. After the antibodies were captured on the modified electrode (curve c, yellow line), the current response continually decreased due to the presence of the protein molecules (antibodies) that hindered the redox conversion at the interface. However, the current response significantly increased after unreacted GO was electrochemically reduced (curve d, grey line) to its reduced form (rGO). The increase in current response can be explained by the increased electron transfer property of the electrochemically reduced graphene¹³⁶. Again, the electrochemical responses were further decreased after blocking with the BSA (curve e, blue line) and binding with target analytes (curve f, green line). These results indicated that the immunocomplexes acted as a barrier to block the electron transfer through the electrode surface, thus resulting in small current responses²³⁸. Therefore, we successfully immobilized the biomolecules on the electrode surface.

EIS was further used to study and to validate the immunosensor fabricated through the modification steps. The platform of EIS is present in terms of the Nyquist plot, which consists of two parts. First, at higher frequencies, the semicircle of the Nyquist plot reflects the charge transfer resistance (R_{ct}) of the electrode surface. The R_{ct} value changed when the resistance, modification, and interaction between analyte and electrolyte interface. The second part at lower frequencies is a straight line, which reflects the diffusion process on the electrode surface¹⁴. As shown in Fig. 59(ii), the

bare SPGE showed small R_{ct} , indicating that the bare SPGE (curve a, dash line) provides low electron-transfer resistance when compared with drop-casting GO on the SPGE (GO-SPGE, curve b, black line). After antibodies modification on the modified electrode (curve c, yellow line), the R_{ct} value or the semicircle increased, revealing that the antibodies/protein molecules acted as an electrode transfer barrier. The reduction process (curve d, grey line) reduced the R_{ct} value, which could be described the change of the excess of GO that provides an insulator property to the purity graphene. The blocking unreacted surface area using BSA (curve e, blue line) and target analytes (curve f, green line) induced a decrease of the R_{ct} value, which can be explained by the immunocomplexes between antigen/antibody hindered electron transfer of the redox solution through the electrode surface. All of EIS evidence confirmed the successful assembly of the ePADs immunosensor. Also, these results were consistent with CV results.

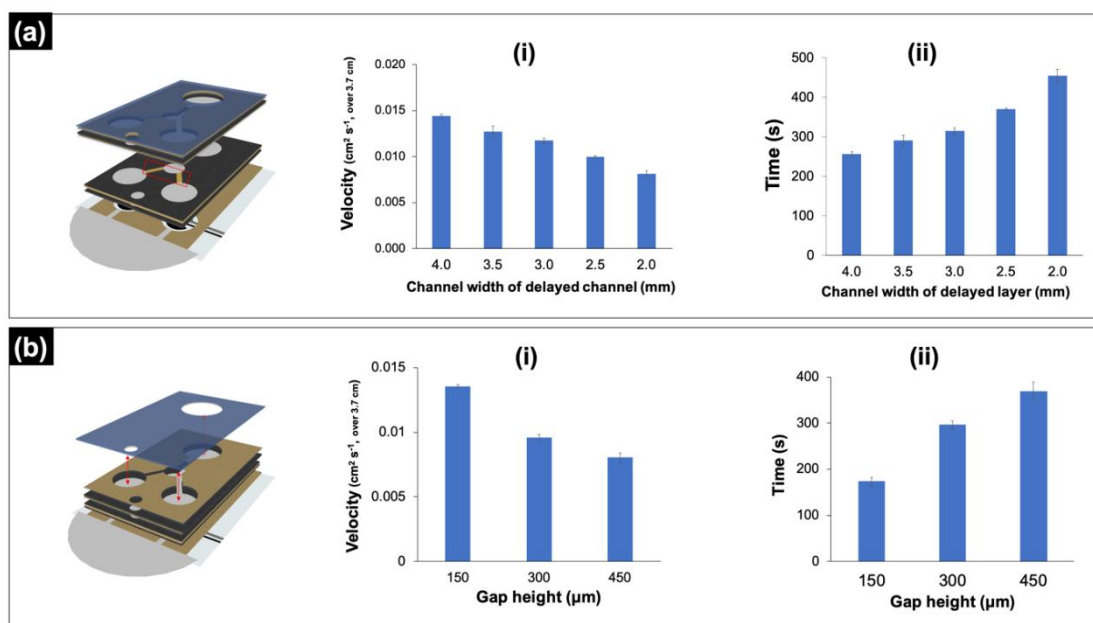


Figure 60. Optimization of device geometry for simultaneous HBV and HCV detection including (a) effect of channel width on the delayed channel and (b) effect of double-sided adhesive layers (gap height). All results were a mean of three replicated measurements ($n=3$). Note that HCV core antigen was used as a representative model analyte for the optimization (conditions: 10 $\mu\text{g mL}^{-1}$ of anti-hepatitis C concentration, 3 mg mL⁻¹ of BSA blocking, and 10 ng mL⁻¹ of HCV core antigen).

3.4.3.3 Optimization of device geometry

In this part, two geometrical factors (channel width and gap height) affecting the performance of the ePAD were investigated. Flow velocities and total times were monitored instead of the charge (peak area) since the chronoamperometric charges obtained from different device geometries are the same (%RSD: 5.1) under the

controlled assay conditions. It should be noted that the HCV antigen was used as a representative model analyte for the whole optimization of device geometry. The discussions of the optimal conditions are as follows:

3.4.3.3.1 Effect of channel width of the delayed channel

The channel width of the delay channel (4.0, 3.5, 3.0, 2.5, and 2.0 mm) was initially investigated. As can be seen in Fig. 60 (i), the flow velocity of the ePAD with channel width of 4.0 mm offers the fastest flow velocity (0.014 cm s^{-1}) among the four widths. The slow flow velocity in a smaller width can be explained by the surface tension forces at the hydrophobic boundaries of delayed channel which oppose the fluid flow²³⁹. Additionally, the total time of the redox mediator (defined as the response time (time required for a sensor to reach the maximum response) plus recovery time (time required for a sensor to return to the original baseline)) or peak width was monitored. It was observed in Fig. 60 (ii) that the total time was increased with increasing the channel width. This phenomenon could be ascribed by the small channel width which accordingly limit the amount the fluid flow in the channel, thus lengthening the total analysis time. Therefore, the channel width of 4.0 mm was selected in this study.

3.4.3.3.2 Effect of gap height of the fast-flow channel

Next, the fast flow channel with various gap heights (150 to 300 μm) were also tested by varying a DSA layer from one to three layers (noted that each increment layer has a gap height of 150 μm) (Fig. 60b). Theoretical fluidic behavior has previously

been reported by Martinez et al.²⁴⁰ using the Lucas-Washburn equation^{234, 241} (eq. 3.4.1), treated with a modified term for the effective pore radius (r) for multilayer μ PADs (eq. 3.4.2),

$$l(t) = \sqrt{\frac{\gamma r' t \cos\theta}{2\mu}} \quad (\text{equation 3.4.1})$$

$$r = \frac{2r'(hw) + R(gw)}{2hw + gw} \quad (\text{equation 3.4.2})$$

where l is the distance transversed down the channel at time t (s), γ is the interfacial tension (N m^{-1}), θ is the contact angle of the fluid on the paper substrate, and μ is the viscosity of fluid (N s m^{-1}). For eq. 3.4.2, r' is mean capillary radius of the paper, h is the paper thickness, w is the channel width, g is the channel height (distance between the paper layers) and $R = g/2$ is the half channel height, with all measurements in meters (m). It should be marked that this theoretical explanation was initially investigated by holding the μ PADs vertically (with the channel perpendicular to the workbench), and dipping them into sample wells.

According to the eq. 3.4.1 and eq. 3.4.2, the increase in the channel gap height can increase the flow velocity. In contrary, we observed that the flow velocity decreased upon increasing the channel gap height (Fig. 60b (i and ii)). A similar observation was also reported by the Channon et al.²³⁴ that the flow rate increased and reached its peak at the gap height of 234 μm , after which the flow rate decreased upon increasing the gap heights. This result could be attributed to the body force of

the sample mass which offsets the increased pore radius l , thus lowering the flow velocity at high gap height. Furthermore, a similar trend was also observed with the total analysis time due to a decreased flow velocity upon increasing the hollow gap height. For this reason, we therefore selected gap height of 150 μm (single layer of DSA tape) for the whole device fabrication.

3.4.3.4 Optimization of assay conditions

3.4.3.4.1 Effect of the $\text{K}_3[\text{FeCN}_6]$ concentration

The concentration of redox solution spotted on the delayed zone was initially studied in the range of 0.5 to 100 mM. As shown in Fig. 61a (i), the change of charge increased with increasing concentration of the redox solution up to 25 mM. Afterwards, insignificant changes in the charge difference were observed, which possibly be due to the saturation of the redox solution on the electrode surface¹⁵². Additionally, the total time of each redox concentration was monitored (Fig. 61a (ii)). Upon increasing a redox concentration, the total time is also increased, in which lengthened time is undesirable. Therefore, we chosen 25 mM $\text{K}_3[\text{FeCN}_6]$ for the label-free electrochemical detection of both HBV and HCV as it presents a clear trade-off between the sensitivity and analysis time.

3.4.3.4.2 Concentration of antibodies

Next, the optimal concentration of anti-hepatitis B and anti-hepatitis C were investigated. Optimal dilutions of anti-hepatitis B were studied in the range of 1:25 to 1:200 (antibody solution : buffer solution) while optimal concentrations of anti-

hepatitis C were investigated in the range of 0.5 to 50 $\mu\text{g mL}^{-1}$. The changes in charge as a function of the antibody concentration are shown in Fig. 61b. As observed in panel (i) and (ii), the maximum responses were obtained at the dilution/concentration of 1:75 and 1 $\mu\text{g mL}^{-1}$ for anti-hepatitis B and anti-hepatitis C, respectively. The results also suggest that excessive concentrations of antibodies can negatively cause the steric hindrance by the high density of the biomolecule on the electrode surface, which lowering the electrochemical charge response²⁴². Therefore, a dilution of 1:75 for anti-hepatitis B ratio and concentration of 1 $\mu\text{g mL}^{-1}$ for anti-hepatitis C were chosen as the optimal concentration for further assays.

3.4.3.4.3 Incubation time

Lastly, the incubation time for the immunoreaction between anti-hepatitis B and HBV, and anti-hepatitis C and HCV, were studied in the range of 10 to 70 min. As can be seen in Fig. 61c, the optimum incubation periods for HBV and HCV detection were at 30 min and 40 min, respectively, as the charge reached the plateau state beyond this period. Thus, the incubation time of 40 min was used in this study to enable the simultaneous detection of HBV and HCV.

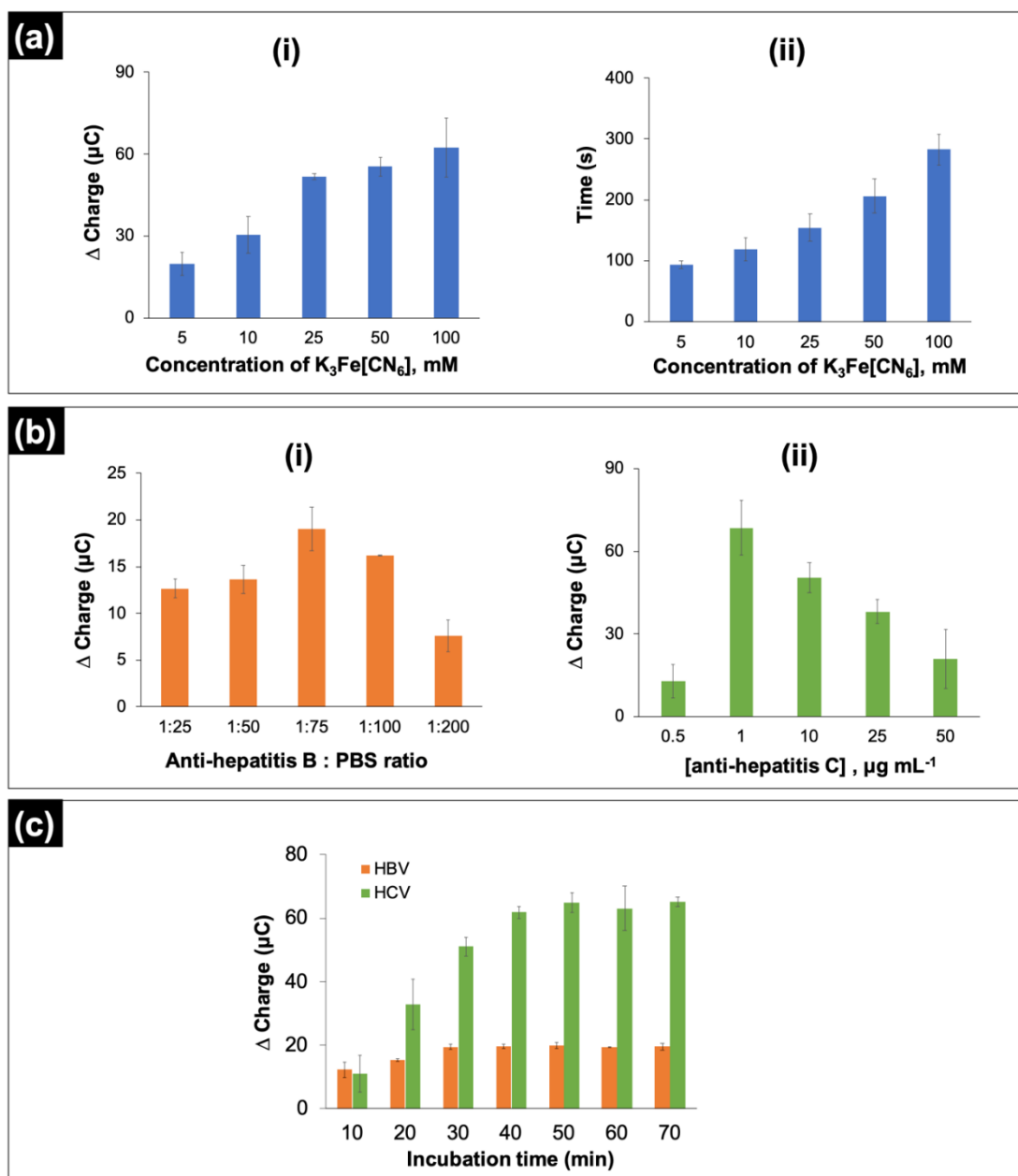


Figure 61. The optimization of assay condition; (a) effect of the $K_3[Fe(CN)_6]$ concentration to the velocity (i) and the total time (ii), (b) antibodies concentration of anti-hepatitis b (i), anti-hepatitis c (ii), and (c) the suitable incubation time between antibody and antigen.

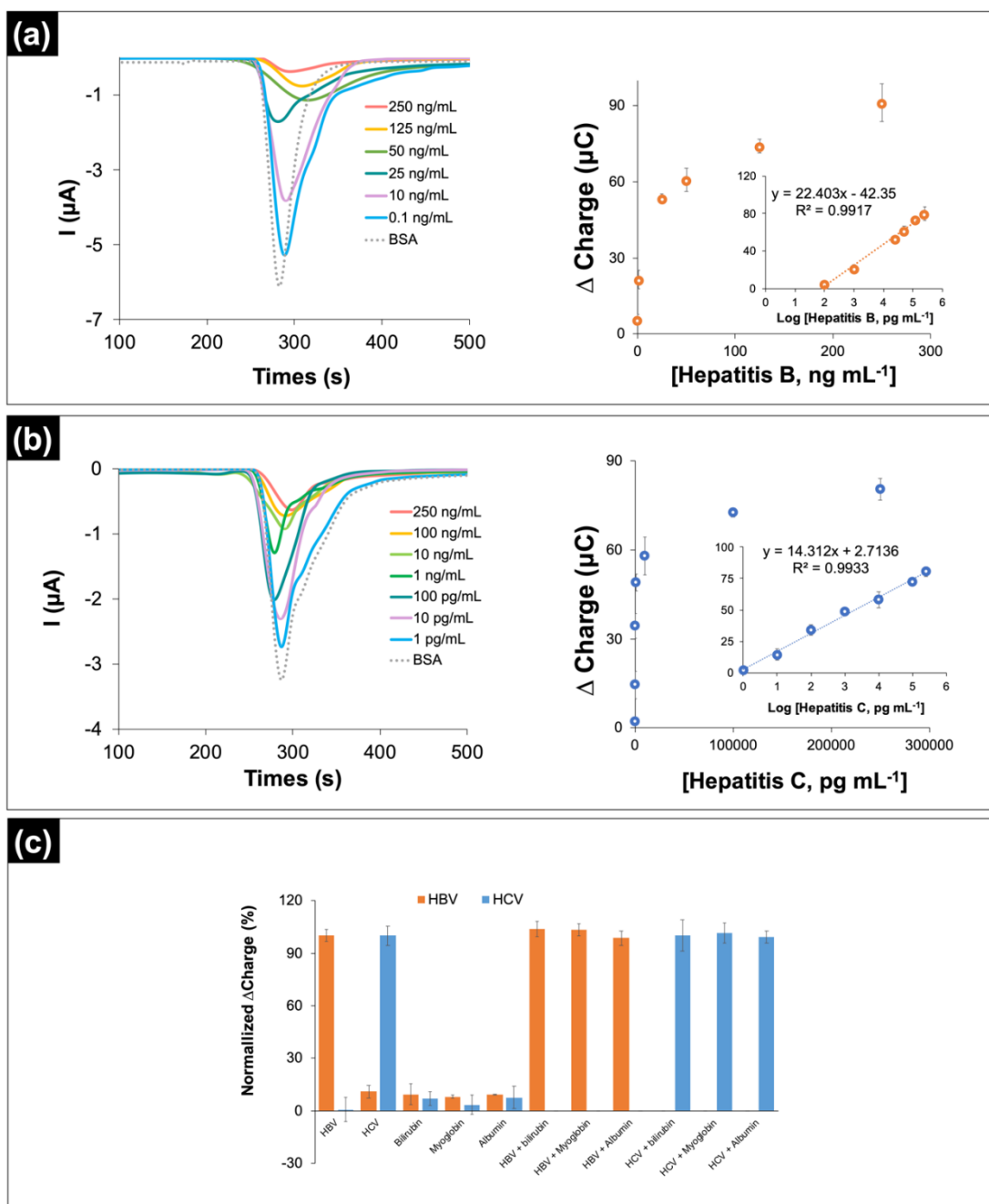


Figure 62. The quantitative calibration plot between the change in charge (Δ charge) and logarithmic concentration of HBV (a) and HCV (b), and its corresponding chronoamperograms (left). Study of the specificity of the ePAD in the presence of

common proteins (c). The error bar represents the standard deviation calculated from three replicated measurements (n=3).

3.4.3.5 Analytical performance of ePAD device for detection of HBV and HCV

The analytical performance of the ePAD immunosensor was concisely evaluated. As illustrated in Fig. 62a and 62b, the charge difference (Δ charge) is proportionally increased to the increasing concentration of HBV and HCV. Under the optimal condition, the Δ charge was linearly related to the logarithm of HBV concentration (Fig. 62a) in the range of 0.1 to 250 ng mL⁻¹ (Δ charge = 22.403 log C_{HBV} (pg mL⁻¹) - 42.35, R²= 0.9917) with a limit of detection of 0.018 ng mL⁻¹ (LOD = 3SD/slope). For HCV (Fig. 62b), the calibration plot showed a linear response in the range of 0.001 to 250 ng mL⁻¹ (Δ charge = 14.312 log C_{HCV} (pg mL⁻¹) + 2.71, R²= 0.9933) with a limit of detection of 1.19 pg mL⁻¹ (LOD = 3SD/slope). A comparison of the analytical performance between this ePAD and other label-free electrochemical immunosensor for HBV and HCV determination was also presented in Table 7. Here, a comparable analytical performance for both HBV and HCV is achieved. Although some reports may present a superior performance, most of them require tedious modification steps and expensive electrode materials. Also, none of these reports was developed for simultaneous detection of both HBV and HCV, making our developed platform an excellent PoC device for routine testing.

To assess the reproducibility, five μ PADs immunosensors were simultaneously detected different concentrations of HBV and HCV. It was found that the relative standard deviations (RSDs) of the signal response were less than 9.7%, indicating a good reproducibility for the developed sensor.

We further examined the specificity of the proposed ePAD. Myoglobin, bilirubin, and albumin were used as interferences in this study. $1 \mu\text{g mL}^{-1}$ of all interferences were prepared in PBS buffer and measured with the developed ePAD. The results were exhibited in Fig. 62c. The significant changes in charge were only observed in the presence of 10 ng mL^{-1} HBV and HCV. On the other hand, no significant change (larger than 10%) was observed from these common interferences. Therefore, it can be concluded that the proposed immunosensor showed good selectivity toward targeted HBV and HCV

The storage stability was also explored in this study. The prepared immunosensor was kept at $-20 \text{ }^{\circ}\text{C}$ until used. As shown in Fig.63, the result revealed that the device could preserve its activity for 30 days while causing the signal change less than 10% (the signal response were retained in the range of 95.3 – 106.6%) with %RSD less than 10s.

Table 7. The comparison of analytical performance of label-free immunosensors for HBV and HCV assays.

Analyte	Modified electrode	Substrates	Detection method	Limit of detection (ng mL ⁻¹)	Linear range (ng mL ⁻¹)	Ref.	
HBV	HCV						
✓	-	PtPd NCs@MoS ₂	GCE	DPV	0.00001	0.000032-100	243
✓	-	AuNPs/CS-Fc	GCE	DPV	0.016	0.05 - 305	244
✓	-	CD/AuNPs/SPGE	PADs	Amperometry	170	10000-200000	23
✓	-	GO-Fc-CS/AuNPs	GE	DPV	0.01	0.05 - 150	245
✓	-	Nafion-L-Cys/AuNPs	CPE	DPV	0.01	0.5-200	246
✓	-	PAA-Fc/AuNPs	GCE	DPV	0.04	0.1-150	247
-	✓	GQD	GCE	DPV	0.0033	0.01-0.07, 0.07-0.4	248
-	✓	Aptamer/MWCNTs-CS	GCE	DPV	0.00000167	0.000005-0.001	249
-	✓	AuNPs/ZrO ₂ -CS	GCE	DPV	0.17	2-512	250
-	✓	V ₂ O ₅ nanobelts	GCE	DPV	0.00000125	0.0001 - 0.1	251
✓	✓	GO/G-SPCE	PADs	Chronoamp- erometry	0.018 0.0012	0.1 - 250 0.001 - 250	This work

PtPd NCs@MoS₂: platinum palladium nano cubes on molybdenum disulfide nanosheet, GCE: glassy carbon electrode, DPV: differential pulse voltammetry, CS-Fc/AuNPs: gold nanoparticles modified on ferrocene-branched chitosan, GO-Fc-CS/AuNPs: graphene oxide-ferrocene-chitosan modified on gold nanoparticles, GE: gold electrode, Nafion-L-Cys/AuNPs: Gold nanoparticles modified on nafion L-cysteine film composite, CPE: carbon paste electrode, PAA-Fc: poly(allylamine)-branched ferrocene on gold nanoparticles, GQD: graphene quantum dot, Aptamer/MWCNTs-CS: Aptamer modified on the Multi-walled carbon nanotubes-chitosan composited, AuNPs/ZrO₂-CS: gold nanoparticle modified on zirconia nanoparticle-chitosan composite, V₂O₅ nanobelts: vanadium oxide nanobelts

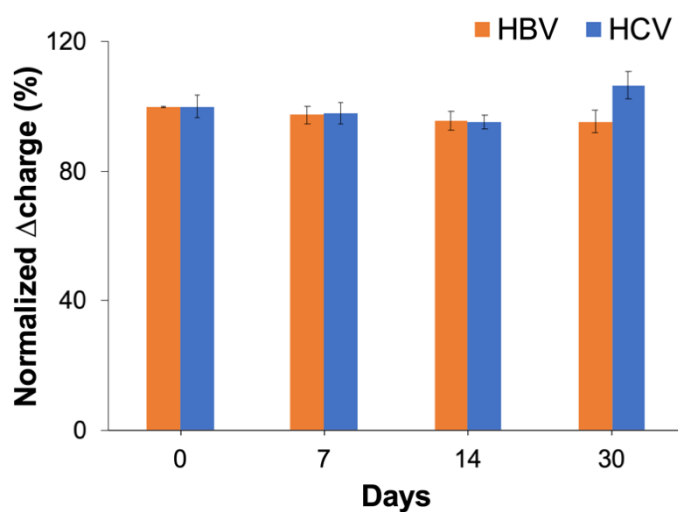


Figure 63. The storage stability of ePAD device. All measurements were calculated from three replicates (n=3)

Table 8. The comparison of the determination results by the proposed ePAD and CLIA reference method for HBV and HCV detection in real clinical sera from patients.

sample	CLIA pg mL ⁻¹		Proposed sensor pg mL ⁻¹		% Relative error	
	HBV	HCV	HBV	HCV	HBV	HCV
1	ND	420	ND	408.73 ± 0.23	-	-2.68
2	ND	104.25	ND	107.14 ± 1.17	-	+2.77
3	ND	44.61	ND	46.63 ± 1.77	-	+4.54
4	305.85	ND	314.50 ± 1.94	ND	+2.83	-
5	84.84	ND	91.57 ± 2.63	ND	+7.93	-

ND = non detectable, CLIA = chemiluminescent immunoassay

% relative error = measured value – real value / real value x 100%

3.4.3.6 Real sample analysis

To evaluate the feasibility of this system, the ePAD was utilized to verify the amount of HBV and HCV in a serum sample. The amount of HBV and HCV in serum from patients was verified and compared with the chemiluminescent immunoassay (CLIA) technique. The quantity of HBV and HCV in the sample could be determined by calculations according to the linear equation of the standard calibration curve (Fig. 62). The results are presented in Table 8. It revealed that our ePAD device could be simultaneously detected and quantified the amount of HBV and HCV in a real serum sample. The results obtained from the ePAD device provide similar concentration values to the standard CLIA method with percentage relative error less than 10% for all concentrations. These results clearly demonstrated that this sensing platform could be an alternative POCT device for simultaneous detection of HBV and HCV in clinical samples with reliability and accuracy.

3.4.4 Conclusion

To sum up, a paper-based electrochemical platform for simultaneous detection of HBV and HCV was proposed, where straightforward, automated, and ready-to-use format are primary concerned. Herein, two microfluidic strategies, fast-flow microfluidic and delayed microfluidic, were specifically designed to enable an automated function in a time-sequenced manner. Notably, the fast-flow channel was used for an automated washing of unbound antigens while the delayed channel was

created to store a redox reagent for further electrochemical analysis. The device was constructed by stacking layers of the wax-printed paper with layers of laser-engraved double-sided adhesive tapes, thus forming a sandwiched device. Once a human serum is loading, a sample solution will wick down to the discrete sample zone that is selective each antigen. Next, the buffer was then added to begin an automated electrochemical assay without requiring additional manipulation by a user. This simultaneous assay exhibited a sensitive quantification over a broad range (0.1 to 250 ng mL⁻¹ for HBV, and 0.001 to 250 ng mL⁻¹ for HCV) with a detection limit of 18.2 pg mL⁻¹ for HBV and 1.19 pg mL⁻¹ for HCV, which are sufficient for real sample analysis. Although the obtained LODs of this electrochemical approach may be inferior compared to some of label-free sensors utilized advanced and complicated electrode materials, none of these sensors was reported for a simultaneous determination of HBV and HCV. Benefitting from this device architecture, it can be further expanded for the analysis of other clinical compounds, which typically requires a detection of two or more markers for an accurate diagnosis. We believed that the developed ePAD can eliminate the complexity of the assay which end-users must carry out. Also, this sensor also offers high sensitivity, and portability, yet maintains simplicity.

CHAPTER 4

CONCLUSIONS AND FUTURE PERSPECTIVE

4.1 Conclusion

The conclusions were divided into four parts as follows;

PART I:

“An origami paper-based electrochemical immunoassay for C-reactive protein detection using a screen-printed carbon electrode modified with graphene and gold nanoparticles”

An oPAD was specifically designed to integrate the immunosensing preparation and detection step into a single device for CRP detection. The graphene and gold nanoparticles were modified to improve the sensitivity of the electrode, followed by a self-assembled monolayer of L-Cysteine. A specific antibody was captured on the modified electrode via a covalent bond. The linear range of 0.05-100 $\mu\text{g mL}^{-1}$ with a limit of detection (3S/N) of 15 ng mL^{-1} was achieved. An oPAD was successfully applied for CRP detection in a certified serum sample with satisfactory results.

PART II:

“Electrochemical paper-based analytical device for multiplexed, point-of-care detection of cardiovascular disease biomarkers”

An ePAD for multiplexed, point-of-care detection of cardiovascular disease based on a label-free immunoassay was demonstrated. An ePAD was designed for the simultaneous determination of three important CVD biomarkers, including CRP, cTnI, and PCT. The fluidic channel on ePAD was created to hold the redox reagent for the detection step. The analytical performances, such as sensitivity, selectivity, and reproducibility, were investigated. The limits of detection ($LOD = 3SD/slope$) were found to be 0.38 ng mL^{-1} for CRP, 0.16 pg mL^{-1} for cTnI, and 0.27 pg mL^{-1} for PCT, respectively. Finally, this proposed sensor was applied to determine CRP, cTnI, and PCT in a certified serum sample.

PART III:

“Cost-effective paper-based electrochemical immunosensor using a label-free assay for sensitive detection of ferritin”

A cost-effective ePAD immunosensor based on a label-free assay for the detection of ferritin was reported. The ePAD device was custom designed on the filter paper to successfully fabricate an immunosensor. To improve the reproducibility of electrode, the SPGE was first modified with GO using an inkjet-printing technique. Then, anti-ferritin antibodies were assigned to covalently immobilized onto the surface of the modified electrode. The linear range was obtained in the range of $1\text{-}1000 \text{ ng mL}^{-1}$ with a limit of detection ($3SD/slope$) of 0.19 ng mL^{-1} . The ePAD was applied in a serum

sample with remarkable performance in terms of high sensitivity, specificity, portability, and reproducibility.

PART IV:

“Dual flow-controlled behaviors on microfluidic fast-flow/delayed channels for an automated and simultaneous electrochemical detection of Hepatitis B virus and Hepatitis C virus core antigen”

An ePAD platform for simultaneous detection of HBV and HCV was reported, where automated and ready-to-use format are primarily concerned. The two microfluidic strategies, fast-flow microfluidic and delayed microfluidic, were designed to enable an automated function in a time-sequenced manner. The fast-flow channel was used for an automated washing of unbound target analytes while the delayed channel was generated to store a redox reagent for further electrochemical analysis. An ePAD exhibited a sensitive quantification over a wide range (0.1 to 250 ng mL⁻¹ for HBV, and 0.001 to 250 ng mL⁻¹ for HCV) with a detection limit of 18.2 pg mL⁻¹ for HBV and 1.19 pg mL⁻¹ for HCV, which are adequate for real sample analysis. This proposed device can be developed for the analysis of other biomarkers, which requires at least two biomarkers for an accurate diagnosis.

To be highlighted, all ePAD platforms were integrated with label-free immunoassay but using in different electrochemical technique for biomarkers

detection. Based on our experiment, an appropriate electrochemical technique was considered from three main points including the electrochemical condition which is a static and hydrodynamic conditions, high sensitivity, and the electrochemical technique that can distinguish in a concentration-dependent manner. Moreover, the size of protein can be affected by the electrochemical current response. For example, a high scan rate (such as SWV) used with large protein molecule might not be able to quantify amount of biomarkers because a dense protein between antigen and antibody formed on the modified electrode will block the electron transfer of redox solution from electrode surface and the redox solution will take time to transfer through the electrode surface. Therefore, a slow scan rate (such as DPV) was performed.

4.2 Future perspective

The paper-based analytical device (PAD) is clearly demonstrated as a miniaturized and portable sensor for point-of-care testing (POCT). Because it offers disposability and self-pumping ability through capillary force without no need of an external pump, and it is easy to operate and fabricate using various printing and patterning techniques. Therefore, it is a great promising to extend the use of PAD platform with various applications. Nowadays, wireless communication technology such as near-field communication (NFC) has been attention to integrating with PAD for real-time monitoring and quantification of a variety of analytes. Therefore, this system

could be further coupled with the proposed PAD to be the next generation technology of portable and versatile POCT in the near future.



REFERENCES

1. Dai, Y.; Liu, C. C., Recent Advances on Electrochemical Biosensing Strategies toward Universal Point-of-Care Systems. *Angewandte Chemie International Edition* **2019**, *58* (36), 12355-12368.
2. Noviana, E.; Henry, C. S., Simultaneous electrochemical detection in paper-based analytical devices. *Current Opinion in Electrochemistry* **2020**, *23*, 1-6.
3. Fu, L.-M.; Wang, Y.-N., Detection methods and applications of microfluidic paper-based analytical devices. *TrAC Trends in Analytical Chemistry* **2018**, *107*, 196-211.
4. Nie, Z.; Deiss, F.; Liu, X.; Akbulut, O.; Whitesides, G. M., Integration of paper-based microfluidic devices with commercial electrochemical readers. *Lab on a Chip* **2010**, *10* (22), 3163-3169.
5. Cardoso, R. M.; Kalinke, C.; Rocha, R. G.; dos Santos, P. L.; Rocha, D. P.; Oliveira, P. R.; Janegitz, B. C.; Bonacin, J. A.; Richter, E. M.; Munoz, R. A. A., Additive-manufactured (3D-printed) electrochemical sensors: A critical review. *Analytica Chimica Acta* **2020**, *1118*, 73-91.
6. Wang, Z.; Dai, Z., Carbon nanomaterial-based electrochemical biosensors: an overview. *Nanoscale* **2015**, *7* (15), 6420-6431.
7. Tiwari, J. N.; Vij, V.; Kemp, K. C.; Kim, K. S., Engineered Carbon-Nanomaterial-Based Electrochemical Sensors for Biomolecules. *ACS Nano* **2016**, *10* (1), 46-80.
8. Rende, D.; Baysal, N.; Kirdar, B., A novel integrative network approach to understand the interplay between cardiovascular disease and other complex disorders. *Molecular BioSystems* **2011**, *7* (7), 2205-2219.
9. Ikonomidis, I.; Lekakis, J.; Vamvakou, G.; Andreotti, F.; Nihoyannopoulos, P., Cigarette smoking is associated with increased circulating proinflammatory and procoagulant markers in patients with chronic coronary artery disease: Effects of aspirin treatment. *American Heart Journal* **2005**, *149* (5), 832-839.
10. McRae, M. P.; Simmons, G. W.; Christodoulides, N. J.; Lu, Z.; Kang, S. K.; Fenyó, D.; Alcorn, T.; Dapkins, I. P.; Sharif, I.; Vurmaz, D.; Modak, S. S.; Srinivasan, K.; Warhadpande, S.; Shrivastav, R.; McDevitt, J. T., Clinical decision support tool and rapid

point-of-care platform for determining disease severity in patients with COVID-19. *Lab on a Chip* **2020**, *20* (12), 2075-2085.

11. Goldhammer, E.; Tanchilevitch, A.; Maor, I.; Beniamini, Y.; Rosenschein, U.; Sagiv, M., Exercise training modulates cytokines activity in coronary heart disease patients. *International Journal of Cardiology* **2005**, *100* (1), 93-99.

12. Yáñez-Sedeño, P.; Campuzano, S.; Pingarrón, J. M., Pushing the limits of electrochemistry toward challenging applications in clinical diagnosis, prognosis, and therapeutic action. *Chemical Communications* **2019**, *55* (18), 2563-2592.

13. Yakoh, A.; Siangproh, W.; Chailapakul, O.; Ngamrojanavanich, N., Optical Bioelectronic Device Based on a Screen-Printed Electroluminescent Transducer. *ACS Applied Materials & Interfaces* **2020**, *12* (20), 22543-22551.

14. Boonkaew, S.; Chaiyo, S.; Jampasa, S.; Rengpipat, S.; Siangproh, W.; Chailapakul, O., An origami paper-based electrochemical immunoassay for the C-reactive protein using a screen-printed carbon electrode modified with graphene and gold nanoparticles. *Microchimica Acta* **2019**, *186* (3), 153.

15. Wang, S.; Luo, J.; He, Y.; Chai, Y.; Yuan, R.; Yang, X., Combining Porous Magnetic Ni@C Nanospheres and CaCO₃ Microcapsule as Surface-Enhanced Raman Spectroscopy Sensing Platform for Hypersensitive C-Reactive Protein Detection. *ACS Applied Materials & Interfaces* **2018**, *10* (39), 33707-33712.

16. Koralewski, M.; Balejíčková, L.; Mitróová, Z.; Pochylski, M.; Baranowski, M.; Kopčanský, P., Morphology and Magnetic Structure of the Ferritin Core during Iron Loading and Release by Magneto-optical and NMR Methods. *ACS Applied Materials & Interfaces* **2018**, *10* (9), 7777-7787.

17. Sarangi, R.; Pathak, M.; Padhi, S.; Mahapatra, S., Ferritin in hemophagocytic lymphohistiocytosis (HLH): current concepts and controversies. *Clinica Chimica Acta* **2020**, *510*, 408-415.

18. DiSilvestro, R. A.; Joseph, E.; Diehl, J.; Swain, C. B., Ferritin readings in young adult, female university student recreational runners. *Journal of Trace Elements in Medicine and Biology* **2020**, *62*, 126617.

19. Garg, M.; Chatterjee, M.; Sharma, A. L.; Singh, S., Label-free approach for electrochemical ferritin sensing using biosurfactant stabilized tungsten disulfide quantum dots. *Biosensors and Bioelectronics* **2020**, *151*, 111979.
20. Boonkaew, S.; Teengam, P.; Jampasa, S.; Rengpipat, S.; Siangproh, W.; Chailapakul, O., Cost-effective paper-based electrochemical immunosensor using a label-free assay for sensitive detection of ferritin. *Analyst* **2020**, *145* (14), 5019-5026.
21. Khan, M. Z. H.; Hasan, M. R.; Hossain, S. I.; Ahommed, M. S.; Daizy, M., Ultrasensitive detection of pathogenic viruses with electrochemical biosensor: State of the art. *Biosensors and Bioelectronics* **2020**, *166*, 112431.
22. Li, X.; Scida, K.; Crooks, R. M., Detection of Hepatitis B Virus DNA with a Paper Electrochemical Sensor. *Analytical Chemistry* **2015**, *87* (17), 9009-9015.
23. Teengam, P.; Siangproh, W.; Tontisirin, S.; Jiraseree-amornkun, A.; Chuaypen, N.; Tangkijvanich, P.; Henry, C. S.; Ngamrojanavanich, N.; Chailapakul, O., NFC-enabling smartphone-based portable amperometric immunosensor for hepatitis B virus detection. *Sensors and Actuators B: Chemical* **2021**, *326*, 128825.
24. Srisomwat, C.; Teengam, P.; Chuaypen, N.; Tangkijvanich, P.; Vilaivan, T.; Chailapakul, O., Pop-up paper electrochemical device for label-free hepatitis B virus DNA detection. *Sensors and Actuators B: Chemical* **2020**, *316*, 128077.
25. de Eguilaz, M. R.; Cumba, L. R.; Forster, R. J., Electrochemical detection of viruses and antibodies: A mini review. *Electrochemistry Communications* **2020**, *116*, 106762.
26. Almeida, M. I. G. S.; Jayawardane, B. M.; Kolev, S. D.; McKelvie, I. D., Developments of microfluidic paper-based analytical devices (μ PADs) for water analysis: A review. *Talanta* **2018**, *177*, 176-190.
27. Martinez, A. W., Microfluidic paper-based analytical devices: from POCKET to paper-based ELISA. *Bioanalysis* **2011**, *3* (23), 2589-2592.
28. Han, T.; Jin, Y.; Geng, C.; Aziz, A. u. R.; Zhang, Y.; Deng, S.; Ren, H.; Liu, B., Microfluidic Paper-based Analytical Devices in Clinical Applications. *Chromatographia* **2020**, *83* (6), 693-701.
29. Schilling, K. M.; Lepore, A. L.; Kurian, J. A.; Martinez, A. W., Fully Enclosed Microfluidic Paper-Based Analytical Devices. *Analytical Chemistry* **2012**, *84* (3), 1579-1585.

30. Ozer, T.; McMahon, C.; Henry, C. S., Advances in Paper-Based Analytical Devices. *Annual Review of Analytical Chemistry* **2020**, *13* (1), 85-109.
31. Rashiku, M.; Bhattacharya, S., Fabrication Techniques for Paper-Based Microfluidic Devices. In *Paper Microfluidics: Theory and Applications*, Bhattacharya, S.; Kumar, S.; Agarwal, A. K., Eds. Springer Singapore: Singapore, 2019; pp 29-45.
32. Martinez, A. W.; Phillips, S. T.; Butte, M. J.; Whitesides, G. M., Patterned Paper as a Platform for Inexpensive, Low-Volume, Portable Bioassays. *Angewandte Chemie International Edition* **2007**, *46* (8), 1318-1320.
33. Carrilho, E.; Martinez, A. W.; Whitesides, G. M., Understanding Wax Printing: A Simple Micropatterning Process for Paper-Based Microfluidics. *Analytical Chemistry* **2009**, *81* (16), 7091-7095.
34. Sempionatto, J. R.; Khorshed, A. A.; Ahmed, A.; De Loyola e Silva, A. N.; Barfidokht, A.; Yin, L.; Goud, K. Y.; Mohamed, M. A.; Bailey, E.; May, J.; Aebischer, C.; Chatelle, C.; Wang, J., Epidermal Enzymatic Biosensors for Sweat Vitamin C: Toward Personalized Nutrition. *ACS Sensors* **2020**, *5* (6), 1804-1813.
35. Mehrotra, P., Biosensors and their applications - A review. *J Oral Biol Craniofac Res* **2016**, *6* (2), 153-159.
36. Xiang, Q. In *The Development and Application of Electrochemical Biosensor*, Information and Management Engineering, Berlin, Heidelberg, 2011//; Zhu, M., Ed. Springer Berlin Heidelberg: Berlin, Heidelberg, 2011; pp 215-220.
37. Hasan, A.; Nurunnabi, M.; Morshed, M.; Paul, A.; Polini, A.; Kuila, T.; Al Hariri, M.; Lee, Y.-k.; Jaffa, A. A., Recent Advances in Application of Biosensors in Tissue Engineering. *BioMed Research International* **2014**, *2014*, 307519.
38. Grieshaber, D.; MacKenzie, R.; Vörös, J.; Reimhult, E., Electrochemical Biosensors - Sensor Principles and Architectures. *Sensors* **2008**, *8* (3), 1400-1458.
39. Cho, I.-H.; Kim, D. H.; Park, S., Electrochemical biosensors: perspective on functional nanomaterials for on-site analysis. *Biomaterials Research* **2020**, *24* (1), 6.
40. Kang, W.; Pei, X.; Rusinek, C. A.; Bange, A.; Haynes, E. N.; Heineman, W. R.; Papautsky, I., Determination of Lead with a Copper-Based Electrochemical Sensor. *Analytical Chemistry* **2017**, *89* (6), 3345-3352.

41. Thevenot, D. R.; Tóth, K.; Durst, R. A.; Wilson, G. S., Electrochemical Biosensors: Recommended Definitions and Classification. *Pure and Applied Chemistry* **1999**, *71* (12), 2333-2348.
42. Abdulbari, H. A.; Basheer, E. A. M., Electrochemical Biosensors: Electrode Development, Materials, Design, and Fabrication. *ChemBioEng Reviews* **2017**, *4* (2), 92-105.
43. da Silva, E. T. S. G.; Souto, D. E. P.; Barragan, J. T. C.; de F. Giarola, J.; de Moraes, A. C. M.; Kubota, L. T., Electrochemical Biosensors in Point-of-Care Devices: Recent Advances and Future Trends. *ChemElectroChem* **2017**, *4* (4), 778-794.
44. Darwish, I. A., Immunoassay Methods and their Applications in Pharmaceutical Analysis: Basic Methodology and Recent Advances. *Int J Biomed Sci* **2006**, *2* (3), 217-235.
45. Varma, M., Limitations of Label-Free Sensors in Serum Based Molecular Diagnostics. *arXiv: Biological Physics* **2015**.
46. Perez, N., Mass Transport by Diffusion and Migration. In *Electrochemistry and Corrosion Science*, Perez, N., Ed. Springer International Publishing: Cham, 2016; pp 151-197.
47. Oberacher, H.; Pitterl, F.; Erb, R.; Plattner, S., Mass spectrometric methods for monitoring redox processes in electrochemical cells. *Mass Spectrometry Reviews* **2015**, *34* (1), 64-92.
48. Mirceski, V.; Skrzypek, S.; Stojanov, L., Square-wave voltammetry. *ChemTexts* **2018**, *4* (4), 17.
49. Miles, D. T., Run-D.M.C.: A Mnemonic Aid for Explaining Mass Transfer in Electrochemical Systems. *Journal of Chemical Education* **2013**, *90* (12), 1649-1653.
50. Allen J. Bard and Larry R. Faulkner, *Electrochemical Methods: Fundamentals and Applications*, New York: Wiley, 2001, 2nd ed. *Russian Journal of Electrochemistry* **2002**, *38* (12), 1364-1365.
51. Byun, J. Y.; Shin, Y. B.; Kim, D. M.; Kim, M. G., A colorimetric homogeneous immunoassay system for the C-reactive protein. *Analyst* **2013**, *138* (5), 1538-43.
52. Hennessey, H.; Afara, N.; Omanovic, S.; Padjen, A. L., Electrochemical investigations of the interaction of C-reactive protein (CRP) with a CRP antibody chemically immobilized on a gold surface. *Anal Chim Acta* **2009**, *643* (1-2), 45-53.

53. Choi, H. W.; Sakata, Y.; Kurihara, Y.; Ooya, T.; Takeuchi, T., Label-free detection of C-reactive protein using reflectometric interference spectroscopy-based sensing system. *Anal Chim Acta* **2012**, *728*, 64-8.
54. Bryan, T.; Luo, X.; Bueno, P. R.; Davis, J. J., An optimised electrochemical biosensor for the label-free detection of C-reactive protein in blood. *Biosens Bioelectron* **2013**, *39* (1), 94-8.
55. Fakanya, W. M.; Tothill, I. E., Detection of the inflammation biomarker C-reactive protein in serum samples: towards an optimal biosensor formula. *Biosensors (Basel)* **2014**, *4* (4), 340-57.
56. Kokkinos, C.; Prodromidis, M.; Economou, A.; Petrou, P.; Kakabakos, S., Disposable integrated bismuth citrate-modified screen-printed immunosensor for ultrasensitive quantum dot-based electrochemical assay of C-reactive protein in human serum. *Anal Chim Acta* **2015**, *886*, 29-36.
57. Thangamuthu, M.; Santschi, C.; J. F. Martin, O., Label-Free Electrochemical Immunoassay for C-Reactive Protein. *Biosensors* **2018**, *8* (2), 34.
58. Srisa-Art, M.; Boehle, K. E.; Geiss, B. J.; Henry, C. S., Highly Sensitive Detection of Salmonella typhimurium Using a Colorimetric Paper-Based Analytical Device Coupled with Immunomagnetic Separation. *Analytical Chemistry* **2018**, *90* (1), 1035-1043.
59. Apilux, A.; Dungchai, W.; Siangproh, W.; Praphairaksit, N.; Henry, C. S.; Chailapakul, O., Lab-on-paper with dual electrochemical/ colorimetric detection for simultaneous determination of gold and iron. *Analytical Chemistry* **2010**, *82* (5), 1727-1732.
60. Charoenkitamorn, K.; Chaiyo, S.; Chailapakul, O.; Siangproh, W., Low-cost and disposable sensors for the simultaneous determination of coenzyme Q10 and α -lipoic acid using manganese (IV) oxide-modified screen-printed graphene electrodes. *Analytica Chimica Acta* **2018**, *1004*, 22-31.
61. Shen, W.; Tian, D.; Cui, H.; Yang, D.; Bian, Z., Nanoparticle-based electrochemiluminescence immunosensor with enhanced sensitivity for cardiac troponin I using N-(aminobutyl)-N-(ethylisoluminol)-functionalized gold nanoparticles as labels. *Biosensors and Bioelectronics* **2011**, *27* (1), 18-24.

62. Byzova, N. A.; Zherdev, A. V.; Vengerov, Y. Y.; Starovoitova, T. A.; Dzantiev, B. B., A triple immunochromatographic test for simultaneous determination of cardiac troponin I, fatty acid binding protein, and C-reactive protein biomarkers. *Microchimica Acta* **2017**, *184* (2), 463-471.
63. Zhang, J.; Zhang, W.; Guo, J.; Wang, J.; Zhang, Y., Electrochemical detection of C-reactive protein using Copper nanoparticles and hybridization chain reaction amplifying signal. *Analytical Biochemistry* **2017**, *539*, 1-7.
64. Yan, Q.; Yang, Y.; Tan, Z.; Liu, Q.; Liu, H.; Wang, P.; Chen, L.; Zhang, D.; Li, Y.; Dong, Y., A label-free electrochemical immunosensor based on the novel signal amplification system of AuPdCu ternary nanoparticles functionalized polymer nanospheres. *Biosensors and Bioelectronics* **2018**, *103*, 151-157.
65. Jampasa, S.; Siangproh, W.; Laocharoensuk, R.; Vilaivan, T.; Chailapakul, O., Electrochemical detection of c-reactive protein based on anthraquinone-labeled antibody using a screen-printed graphene electrode. *Talanta* **2018**, *183*, 311-319.
66. Martinez, A. W.; Phillips, S. T.; Whitesides, G. M.; Carrilho, E., Diagnostics for the developing world: Microfluidic paper-based analytical devices. *Analytical Chemistry* **2010**, *82* (1), 3-10.
67. Glavan, A. C.; Niu, J.; Chen, Z.; Güder, F.; Cheng, C.-M.; Liu, D.; Whitesides, G. M., Analytical Devices Based on Direct Synthesis of DNA on Paper. *Analytical Chemistry* **2016**, *88* (1), 725-731.
68. Martinez, A. W.; Phillips, S. T.; Carrilho, E.; Thomas, S. W.; Sindi, H.; Whitesides, G. M., Simple Telemedicine for Developing Regions: Camera Phones and Paper-Based Microfluidic Devices for Real-Time, Off-Site Diagnosis. *Analytical Chemistry* **2008**, *80* (10), 3699-3707.
69. Liu, H.; Crooks, R. M., Three-Dimensional Paper Microfluidic Devices Assembled Using the Principles of Origami. *Journal of the American Chemical Society* **2011**, *133* (44), 17564-17566.
70. Renault, C.; Anderson, M. J.; Crooks, R. M., Electrochemistry in hollow-channel paper analytical devices. *J Am Chem Soc* **2014**, *136* (12), 4616-23.

71. Li, L.; Li, W.; Yang, H.; Ma, C.; Yu, J.; Yan, M.; Song, X., Sensitive origami dual-analyte electrochemical immunodevice based on polyaniline/Au-paper electrode and multi-labeled 3D graphene sheets. *Electrochimica Acta* **2014**, *120*, 102-109.
72. Ma, C.; Li, W.; Kong, Q.; Yang, H.; Bian, Z.; Song, X.; Yu, J.; Yan, M., 3D origami electrochemical immunodevice for sensitive point-of-care testing based on dual-signal amplification strategy. *Biosensors and Bioelectronics* **2015**, *63*, 7-13.
73. Wang, X.; Yang, C.; Zhu, S.; Yan, M.; Ge, S.; Yu, J., 3D origami electrochemical device for sensitive Pb²⁺ testing based on DNA functionalized iron-porphyrinic metal-organic framework. *Biosensors and Bioelectronics* **2017**, *87*, 108-115.
74. Pungjunun, K.; Chaiyo, S.; Jantrahong, I.; Nantaphol, S.; Siangproh, W.; Chailapakul, O., Anodic stripping voltammetric determination of total arsenic using a gold nanoparticle-modified boron-doped diamond electrode on a paper-based device. *Microchimica Acta* **2018**, *185* (7), 324.
75. Jampasa, S.; Siangproh, W.; Duangmal, K.; Chailapakul, O., Electrochemically reduced graphene oxide-modified screen-printed carbon electrodes for a simple and highly sensitive electrochemical detection of synthetic colorants in beverages. *Talanta* **2016**, *160*, 113-124.
76. Wang, L.; Hua, E.; Liang, M.; Ma, C.; Liu, Z.; Sheng, S.; Liu, M.; Xie, G.; Feng, W., Graphene sheets, polyaniline and AuNPs based DNA sensor for electrochemical determination of BCR/ABL fusion gene with functional hairpin probe. *Biosensors and Bioelectronics* **2014**, *51*, 201-207.
77. Nantaphol, S.; Channon, R. B.; Kondo, T.; Siangproh, W.; Chailapakul, O.; Henry, C. S., Boron Doped Diamond Paste Electrodes for Microfluidic Paper-Based Analytical Devices. *Analytical Chemistry* **2017**, *89* (7), 4100-4107.
78. Songjaroen, T.; Feeny, R. M.; Mensack, M. M.; Laiwattanapaisal, W.; Henry, C. S., Label-free detection of C-reactive protein using an electrochemical DNA immunoassay. *Sensing and Bio-Sensing Research* **2016**, *8*, 14-19.
79. Özcan, B.; Sezgintürk, M. K., A novel label free immunosensor based on single-use ITO-PET electrodes for detection MAGE1 protein. *Journal of Electroanalytical Chemistry* **2017**, *792*, 31-38.

80. Zou, Y.; He, L.; Dou, K.; Wang, S.; Ke, P.; Wang, A., Amperometric glucose sensor based on boron doped microcrystalline diamond film electrode with different boron doping levels. *RSC Adv.* **2014**, *4* (102), 58349-58356.
81. Feng, D.; Lu, X.; Dong, X.; Ling, Y.; Zhang, Y., Label-free electrochemical immunosensor for the carcinoembryonic antigen using a glassy carbon electrode modified with electrodeposited Prussian Blue, a graphene and carbon nanotube assembly and an antibody immobilized on gold nanoparticles. *Microchimica Acta* **2013**, *180* (9), 767-774.
82. Rodthongkum, N.; Ruecha, N.; Rangkupan, R.; Vachet, R. W.; Chailapakul, O., Graphene-loaded nanofiber-modified electrodes for the ultrasensitive determination of dopamine. *Analytica Chimica Acta* **2013**, *804*, 84-91.
83. Preecharueangrit, S.; Thavarungkul, P.; Kanatharana, P.; Numnuam, A., Amperometric sensing of sulfite using a gold electrode coated with ordered mesoporous carbon modified with nickel hexacyanoferrate. *Journal of Electroanalytical Chemistry* **2018**, *808*, 150-159.
84. Chen, X.; Wang, Y.; Zhou, J.; Yan, W.; Li, X.; Zhu, J.-J., Electrochemical Impedance Immunosensor Based on Three-Dimensionally Ordered Macroporous Gold Film. *Analytical Chemistry* **2008**, *80* (6), 2133-2140.
85. Li, Y.-W.; Xia, K.; Wang, R.-Z.; Jiang, J.-H.; Xiao, L.-T., An impedance immunosensor for the detection of the phytohormone abscisic acid. *Analytical and Bioanalytical Chemistry* **2008**, *391* (8), 2869.
86. Liu, G.; Lin, Y.-Y.; Wang, J.; Wu, H.; Wai, C. M.; Lin, Y., Disposable Electrochemical Immunosensor Diagnosis Device Based on Nanoparticle Probe and Immunochromatographic Strip. *Analytical Chemistry* **2007**, *79* (20), 7644-7653.
87. Gupta, R. K.; Periyakaruppan, A.; Meyyappan, M.; Koehne, J. E., Label-free detection of C-reactive protein using a carbon nanofiber based biosensor. *Biosens Bioelectron* **2014**, *59*, 112-9.
88. Yagati, A. K.; Pyun, J. C.; Min, J.; Cho, S., Label-free and direct detection of C-reactive protein using reduced graphene oxide-nanoparticle hybrid impedimetric sensor. *Bioelectrochemistry* **2016**, *107*, 37-44.

89. Cozlea, D. L.; Farcas, D. M.; Nagy, A.; Keresztesi, A. A.; Tifrea, R.; Cozlea, L.; Caraşca, E., The impact of C reactive protein on global cardiovascular risk on patients with coronary artery disease. *Current health sciences journal* **2013**, *39* (4), 225-231.
90. Yagati, A. K.; Pyun, J.-C.; Min, J.; Cho, S., Label-free and direct detection of C-reactive protein using reduced graphene oxide-nanoparticle hybrid impedimetric sensor. *Bioelectrochemistry* **2016**, *107*, 37-44.
91. Arques, S., Human serum albumin in cardiovascular diseases. *European Journal of Internal Medicine* **2018**, *52*, 8-12.
92. Tamosiunas, A.; Luksiene, D.; Baceviciene, M.; Bernotiene, G.; Radisauskas, R.; Malinauskiene, V.; Kranciukaite-Butylkiniene, D.; Virviciute, D.; Peasey, A.; Bobak, M., Health Factors and Risk of All-Cause, Cardiovascular, and Coronary Heart Disease Mortality: Findings from the MONICA and HAPIEE Studies in Lithuania. *PLOS ONE* **2014**, *9* (12), e114283.
93. Keto, J.; Ventola, H.; Jokelainen, J.; Linden, K.; Keinänen-Kiukaanniemi, S.; Timonen, M.; Ylisaukko-Oja, T.; Auvinen, J., Cardiovascular disease risk factors in relation to smoking behaviour and history: a population-based cohort study. *Open Heart* **2016**, *3* (2), e000358-e000358.
94. Kaptoge, S.; Pennells, L.; De Bacquer, D.; Cooney, M. T.; Kavousi, M.; Stevens, G.; Riley, L. M.; Savin, S.; Khan, T.; Altay, S.; Amouyel, P.; Assmann, G.; Bell, S.; Ben-Shlomo, Y.; Berkman, L.; Beulens, J. W.; Björkelund, C.; Blaha, M.; Blazer, D. G.; Bolton, T.; Bonita Beaglehole, R.; Brenner, H.; Brunner, E. J.; Casiglia, E.; Chamnan, P.; Choi, Y.-H.; Chowdry, R.; Coady, S.; Crespo, C. J.; Cushman, M.; Dagenais, G. R.; D'Agostino Sr, R. B.; Daimon, M.; Davidson, K. W.; Engström, G.; Ford, I.; Gallacher, J.; Gansevoort, R. T.; Gaziano, T. A.; Giampaoli, S.; Grandits, G.; Grimsgaard, S.; Grobbee, D. E.; Gudnason, V.; Guo, Q.; Tolonen, H.; Humphries, S.; Iso, H.; Jukema, J. W.; Kauhanen, J.; Kengne, A. P.; Khalili, D.; Koenig, W.; Kromhout, D.; Krumholz, H.; Lam, T. H.; Laughlin, G.; Marín Ibañez, A.; Meade, T. W.; Moons, K. G. M.; Nietert, P. J.; Ninomiya, T.; Nordestgaard, B. G.; O'Donnell, C.; Palmieri, L.; Patel, A.; Perel, P.; Price, J. F.; Providencia, R.; Ridker, P. M.; Rodriguez, B.; Rosengren, A.; Rousset, R.; Sakurai, M.; Salomaa, V.; Sato, S.; Schöttker, B.; Shara, N.; Shaw, J. E.; Shin, H.-C.; Simons, L. A.;

Sofianopoulou, E.; Sundström, J.; Völzke, H.; Wallace, R. B.; Wareham, N. J.; Willeit, P.; Wood, D.; Wood, A.; Zhao, D.; Woodward, M.; Danaei, G.; Roth, G.; Mendis, S.; Onuma, O.; Varghese, C.; Ezzati, M.; Graham, I.; Jackson, R.; Danesh, J.; Di Angelantonio, E., World Health Organization cardiovascular disease risk charts: revised models to estimate risk in 21 global regions. *The Lancet Global Health* **2019**, *7* (10), e1332-e1345.

95. Arnett, D. K.; Blumenthal, R. S.; Albert, M. A.; Buroker, A. B.; Goldberger, Z. D.; Hahn, E. J.; Himmelfarb, C. D.; Khera, A.; Lloyd-Jones, D.; McEvoy, J. W.; Michos, E. D.; Miedema, M. D.; Muñoz, D.; Smith, S. C., Jr.; Virani, S. S.; Williams, K. A., Sr.; Yeboah, J.; Ziaeian, B., 2019 ACC/AHA Guideline on the Primary Prevention of Cardiovascular Disease: A Report of the American College of Cardiology/American Heart Association Task Force on Clinical Practice Guidelines. *J Am Coll Cardiol* **2019**, *74* (10), e177-e232.

96. Mayeux, R., Biomarkers: potential uses and limitations. *NeuroRx* **2004**, *1* (2), 182-188.

97. Oyejide, L.; Mendes, O. R.; Mikaelian, I., Chapter 16 - Molecular Pathology: Applications in Nonclinical Drug Development. In *A Comprehensive Guide to Toxicology in Nonclinical Drug Development (Second Edition)*, Faqi, A. S., Ed. Academic Press: Boston, 2017; pp 407-445.

98. Strimbu, K.; Tavel, J. A., What are biomarkers? *Curr Opin HIV AIDS* **2010**, *5* (6), 463-466.

99. Lu, W.; Tao, L.; Wang, Y.; Cao, X.; Ge, J.; Dong, J.; Qian, W., An electrochemical immunosensor for simultaneous multiplexed detection of two lung cancer biomarkers using Au nanoparticles coated resin microspheres composed of L-tryptophan and caffeic acid. *Ionics* **2015**, *21* (4), 1141-1152.

100. Jones, A.; Dhanapala, L.; Kankanamage, R. N. T.; Kumar, C. V.; Rusling, J. F., Multiplexed Immunosensors and Immunoarrays. *Analytical Chemistry* **2020**, *92* (1), 345-362.

101. Yáñez-Sedeño, P.; Campuzano, S.; Pingarrón, J. M., Multiplexed Electrochemical Immunosensors for Clinical Biomarkers. *Sensors (Basel)* **2017**, *17* (5), 965.

102. Han, X.; Li, S.; Peng, Z.; Othman, A. M.; Leblanc, R., Recent Development of Cardiac Troponin I Detection. *ACS Sensors* **2016**, *1* (2), 106-114.

103. Molinero-Fernández, Á.; Moreno-Guzmán, M.; Arruza, L.; López, M. Á.; Escarpa, A., Toward Early Diagnosis of Late-Onset Sepsis in Preterm Neonates: Dual Magnetoimmunosensor for Simultaneous Procalcitonin and C-Reactive Protein Determination in Diagnosed Clinical Samples. *ACS Sensors* **2019**, *4* (8), 2117-2123.
104. Phurimsak, C.; Tarn, M. D.; Peyman, S. A.; Greenman, J.; Pamme, N., On-Chip Determination of C-Reactive Protein Using Magnetic Particles in Continuous Flow. *Analytical Chemistry* **2014**, *86* (21), 10552-10559.
105. Lv, H.; Zhang, X.; Li, Y.; Ren, Y.; Zhang, C.; Wang, P.; Xu, Z.; Li, X.; Chen, Z.; Dong, Y., An electrochemical sandwich immunosensor for cardiac troponin I by using nitrogen/sulfur co-doped graphene oxide modified with Au@Ag nanocubes as amplifiers. *Microchimica Acta* **2019**, *186* (7), 416.
106. Ghrera, A. S., Quantum dot modified interface for electrochemical immunosensing of procalcitonin for the detection of urinary tract infection. *Analytica Chimica Acta* **2019**, *1056*, 26-33.
107. Chinnadayala, R. S.; Park, J.; Kim, H. Y.; Choi, H. S.; Lee, S.-M.; Cho, W. W.; Lee, G.-Y.; Pyun, J.-C.; Cho, S., Electrochemical Detection of C-Reactive Protein in Human Serum Based on Self-Assembled Monolayer-Modified Interdigitated Wave-Shaped Electrode. *Sensors* **2019**, *19* (24).
108. Shen, W.-J.; Zhuo, Y.; Chai, Y.-Q.; Yang, Z.-H.; Han, J.; Yuan, R., Enzyme-Free Electrochemical Immunosensor Based on Host-Guest Nanonets Catalyzing Amplification for Procalcitonin Detection. *ACS Applied Materials & Interfaces* **2015**, *7* (7), 4127-4134.
109. Akter, R.; Jeong, B.; Lee, Y.-M.; Choi, J.-S.; Rahman, M. A., Femtomolar detection of cardiac troponin I using a novel label-free and reagent-free dendrimer enhanced impedimetric immunosensor. *Biosensors and Bioelectronics* **2017**, *91*, 637-643.
110. Sener, G.; Ozgur, E.; Rad, A. Y.; Uzun, L.; Say, R.; Denizli, A., Rapid real-time detection of procalcitonin using a microcontact imprinted surface plasmon resonance biosensor. *Analyst* **2013**, *138* (21), 6422-6428.
111. Wang, W.; Mai, Z.; Chen, Y.; Wang, J.; Li, L.; Su, Q.; Li, X.; Hong, X., A label-free fiber optic SPR biosensor for specific detection of C-reactive protein. *Scientific Reports* **2017**, *7* (1), 16904.

112. Koya, J.; Nannya, Y.; Kurokawa, M., Evaluation of procalcitonin with liquid-phase binding assay in hematological malignancy. *Clinica Chimica Acta* **2012**, *413* (19), 1633-1636.
113. Tang, M.; Zhou, Z.; Shanguan, L.; Zhao, F.; Liu, S., Electrochemiluminescent detection of cardiac troponin I by using soybean peroxidase labeled-antibody as signal amplifier. *Talanta* **2018**, *180*, 47-53.
114. Wang, M.; Liu, J.; Qin, X.; Nie, X.; Dong, Y.; Liang, X.; Zhu, Z.; Yang, D.; Shao, Y., Electrochemiluminescence detection of cardiac troponin I based on Au-Ag alloy nanourchins. *Analyst* **2020**, *145* (3), 873-879.
115. Park, J. P.; Park, C. Y.; Park, A. Y.; Ryu, M. Y., Evolutionary identification of affinity peptides for the detection of sepsis biomarker procalcitonin. *RSC Advances* **2015**, *5* (110), 90531-90533.
116. Liao, T.; Yuan, F.; Yu, H.; Li, Z., An ultrasensitive ELISA method for the detection of procalcitonin based on magnetic beads and enzyme-antibody labeled gold nanoparticles. *Analytical Methods* **2016**, *8* (7), 1577-1585.
117. Meyer, K.; Ueland, P. M., Targeted Quantification of C-Reactive Protein and Cystatin C and Its Variants by Immuno-MALDI-MS. *Analytical Chemistry* **2014**, *86* (12), 5807-5814.
118. de Oliveira, T. R.; Fonseca, W. T.; de Oliveira Setti, G.; Faria, R. C., Fast and flexible strategy to produce electrochemical paper-based analytical devices using a craft cutter printer to create wax barrier and screen-printed electrodes. *Talanta* **2019**, *195*, 480-489.
119. Pradela-Filho, L. A.; Noviana, E.; Araújo, D. A. G.; Takeuchi, R. M.; Santos, A. L.; Henry, C. S., Rapid Analysis in Continuous-Flow Electrochemical Paper-Based Analytical Devices. *ACS Sensors* **2020**, *5* (1), 274-281.
120. Noviana, E.; McCord, C. P.; Clark, K. M.; Jang, I.; Henry, C. S., Electrochemical paper-based devices: sensing approaches and progress toward practical applications. *Lab on a Chip* **2020**, *20* (1), 9-34.
121. Trieu, P. T.; Lee, N. Y., Paper-Based All-in-One Origami Microdevice for Nucleic Acid Amplification Testing for Rapid Colorimetric Identification of Live Cells for Point-of-Care Testing. *Analytical Chemistry* **2019**, *91* (17), 11013-11022.

122. Zhang, Y.; Xu, J.; Zhou, S.; Zhu, L.; Lv, X.; Zhang, J.; Zhang, L.; Zhu, P.; Yu, J., DNAzyme-Triggered Visual and Ratiometric Electrochemiluminescence Dual-Readout Assay for Pb(II) Based on an Assembled Paper Device. *Analytical Chemistry* **2020**, *92* (5), 3874-3881.
123. Liu, F.; Xiang, G.; Yuan, R.; Chen, X.; Luo, F.; Jiang, D.; Huang, S.; Li, Y.; Pu, X., Procalcitonin sensitive detection based on graphene-gold nanocomposite film sensor platform and single-walled carbon nanohorns/hollow Pt chains complex as signal tags. *Biosensors and Bioelectronics* **2014**, *60*, 210-217.
124. Kokkinos, C.; Prodromidis, M.; Economou, A.; Petrou, P.; Kakabakos, S., Disposable integrated bismuth citrate-modified screen-printed immunosensor for ultrasensitive quantum dot-based electrochemical assay of C-reactive protein in human serum. *Analytica Chimica Acta* **2015**, *886*, 29-36.
125. de Ávila, B. E.-F.; Escamilla-Gómez, V.; Lanzone, V.; Campuzano, S.; Pedrero, M.; Compagnone, D.; Pingarrón, J. M., Multiplexed Determination of Amino-Terminal Pro-B-Type Natriuretic Peptide and C-Reactive Protein Cardiac Biomarkers in Human Serum at a Disposable Electrochemical Magnetoimmunosensor. *Electroanalysis* **2014**, *26* (2), 254-261.
126. Liu, P.; Li, C.; Zhang, R.; Tang, Q.; Wei, J.; Lu, Y.; Shen, P., An ultrasensitive electrochemical immunosensor for procalcitonin detection based on the gold nanoparticles-enhanced tyramide signal amplification strategy. *Biosensors and Bioelectronics* **2019**, *126*, 543-550.
127. Zhang, T.; Ma, N.; Ali, A.; Wei, Q.; Wu, D.; Ren, X., Electrochemical ultrasensitive detection of cardiac troponin I using covalent organic frameworks for signal amplification. *Biosensors and Bioelectronics* **2018**, *119*, 176-181.
128. António, M.; Nogueira, J.; Vitorino, R.; Daniel-da-Silva, L. A., Functionalized Gold Nanoparticles for the Detection of C-Reactive Protein. *Nanomaterials* **2018**, *8* (4).
129. Islam, M. S.; Kang, S. H., Chemiluminescence detection of label-free C-reactive protein based on catalytic activity of gold nanoparticles. *Talanta* **2011**, *84* (3), 752-758.
130. Lee, T.; Lee, Y.; Park, S. Y.; Hong, K.; Kim, Y.; Park, C.; Chung, Y.-H.; Lee, M.-H.; Min, J., Fabrication of electrochemical biosensor composed of multi-functional DNA

- structure/Au nanospikes on micro-gap/PCB system for detecting troponin I in human serum. *Colloids and Surfaces B: Biointerfaces* **2019**, *175*, 343-350.
131. Dutta, G.; Lillehoj, P. B., Wash-free, label-free immunoassay for rapid electrochemical detection of PfHRP2 in whole blood samples. *Scientific Reports* **2018**, *8* (1), 17129.
132. Giavazzi, F.; Salina, M.; Ceccarello, E.; Ilacqua, A.; Damin, F.; Sola, L.; Chiari, M.; Chini, B.; Cerbino, R.; Bellini, T.; Buscaglia, M., A fast and simple label-free immunoassay based on a smartphone. *Biosensors and Bioelectronics* **2014**, *58*, 395-402.
133. Channon, R. B.; Nguyen, M. P.; Henry, C. S.; Dandy, D. S., Multilayered Microfluidic Paper-Based Devices: Characterization, Modeling, and Perspectives. *Analytical Chemistry* **2019**, *91* (14), 8966-8972.
134. Kava, A. A.; Beardsley, C.; Hofstetter, J.; Henry, C. S., Disposable glassy carbon stencil printed electrodes for trace detection of cadmium and lead. *Analytica Chimica Acta* **2019**.
135. Mettakoonpitak, J.; Volckens, J.; Henry, C. S., Janus Electrochemical Paper-Based Analytical Devices for Metals Detection in Aerosol Samples. *Analytical Chemistry* **2020**, *92* (1), 1439-1446.
136. Jampasa, S.; Lae-ngee, P.; Patarakul, K.; Ngamrojanavanich, N.; Chailapakul, O.; Rodthongkum, N., Electrochemical immunosensor based on gold-labeled monoclonal anti-LipL32 for leptospirosis diagnosis. *Biosensors and Bioelectronics* **2019**, *142*, 111539.
137. Randviir, E. P.; Brownson, D. A. C.; Metters, J. P.; Kadara, R. O.; Banks, C. E., The fabrication, characterisation and electrochemical investigation of screen-printed graphene electrodes. *Physical Chemistry Chemical Physics* **2014**, *16* (10), 4598-4611.
138. Jabbar, A.; Yasin, G.; Khan, W. Q.; Anwar, M. Y.; Korai, R. M.; Nizam, M. N.; Muhyodin, G., Electrochemical deposition of nickel graphene composite coatings: effect of deposition temperature on its surface morphology and corrosion resistance. *RSC Advances* **2017**, *7* (49), 31100-31109.
139. Ibáñez-Redín, G.; Wilson, D.; Gonçalves, D.; Oliveira, O. N., Low-cost screen-printed electrodes based on electrochemically reduced graphene oxide-carbon black nanocomposites for dopamine, epinephrine and paracetamol detection. *Journal of Colloid and Interface Science* **2018**, *515*, 101-108.

140. Stankovich, S.; Dikin, D. A.; Piner, R. D.; Kohlhaas, K. A.; Kleinhammes, A.; Jia, Y.; Wu, Y.; Nguyen, S. T.; Ruoff, R. S., Synthesis of graphene-based nanosheets via chemical reduction of exfoliated graphite oxide. *Carbon* **2007**, *45* (7), 1558-1565.
141. Wei, H.; Sun, J.-J.; Xie, Y.; Lin, C.-G.; Wang, Y.-M.; Yin, W.-H.; Chen, G.-N., Enhanced electrochemical performance at screen-printed carbon electrodes by a new pretreating procedure. *Analytica Chimica Acta* **2007**, *588* (2), 297-303.
142. Demirbakan, B.; Kemal Sezgintürk, M., A novel ultrasensitive immunosensor based on disposable graphite paper electrodes for troponin T detection in cardiovascular disease. *Talanta* **2020**, *213*, 120779.
143. Wang, W.; Liu, Y.; Shi, T.; Sun, J.; Mo, F.; Liu, X., Biosynthesized Quantum Dot for Facile and Ultrasensitive Electrochemical and Electrochemiluminescence Immunoassay. *Analytical Chemistry* **2020**, *92* (1), 1598-1604.
144. Engstrom, R. C.; Strasser, V. A., Characterization of electrochemically pretreated glassy carbon electrodes. *Analytical Chemistry* **1984**, *56* (2), 136-141.
145. Toh, S. Y.; Loh, K. S.; Kamarudin, S. K.; Daud, W. R. W., Graphene production via electrochemical reduction of graphene oxide: Synthesis and characterisation. *Chemical Engineering Journal* **2014**, *251*, 422-434.
146. El-Moghazy, A. Y.; Zhao, C.; Istamboulie, G.; Amaly, N.; Si, Y.; Noguier, T.; Sun, G., Ultrasensitive label-free electrochemical immunosensor based on PVA-co-PE nanofibrous membrane for the detection of chloramphenicol residues in milk. *Biosensors and Bioelectronics* **2018**, *117*, 838-844.
147. Yakoh, A.; Chaiyo, S.; Siangproh, W.; Chailapakul, O., 3D Capillary-Driven Paper-Based Sequential Microfluidic Device for Electrochemical Sensing Applications. *ACS Sensors* **2019**, *4* (5), 1211-1221.
148. Yang, Z.-H.; Ren, S.; Zhuo, Y.; Yuan, R.; Chai, Y.-Q., Cu/Mn Double-Doped CeO₂ Nanocomposites as Signal Tags and Signal Amplifiers for Sensitive Electrochemical Detection of Procalcitonin. *Analytical Chemistry* **2017**, *89* (24), 13349-13356.
149. Li, F.; Yu, Y.; Cui, H.; Yang, D.; Bian, Z., Label-free electrochemiluminescence immunosensor for cardiac troponin I using luminol functionalized gold nanoparticles as a sensing platform. *Analyst* **2013**, *138* (6), 1844-1850.

150. Bhalla, V.; Carrara, S.; Sharma, P.; Nangia, Y.; Raman Suri, C., Gold nanoparticles mediated label-free capacitance detection of cardiac troponin I. *Sensors and Actuators B: Chemical* **2012**, *161* (1), 761-768.
151. Lopa, N. S.; Rahman, M. M.; Ahmed, F.; Ryu, T.; Sutradhar, S. C.; Lei, J.; Kim, J.; Kim, D. H.; Lee, Y. H.; Kim, W., Simple, low-cost, sensitive and label-free aptasensor for the detection of cardiac troponin I based on a gold nanoparticles modified titanium foil. *Biosensors and Bioelectronics* **2019**, *126*, 381-388.
152. Pinyorosphatum, C.; Chaiyo, S.; Sae-ung, P.; Hoven, V. P.; Damsongsang, P.; Siangproh, W.; Chailapakul, O., Disposable paper-based electrochemical sensor using thiol-terminated poly(2-methacryloyloxyethyl phosphorylcholine) for the label-free detection of C-reactive protein. *Microchimica Acta* **2019**, *186* (7), 472.
153. Psarouli, A.; Botsialas, A.; Salapatias, A.; Stefanitsis, G.; Nikita, D.; Jobst, G.; Chaniotakis, N.; Goustouridis, D.; Makarona, E.; Petrou, P. S.; Raptis, I.; Misiakos, K.; Kakabakos, S. E., Fast label-free detection of C-reactive protein using broad-band Mach-Zehnder interferometers integrated on silicon chips. *Talanta* **2017**, *165*, 458-465.
154. Soppi, E. T., Iron deficiency without anemia - a clinical challenge. *Clin Case Rep* **2018**, *6* (6), 1082-1086.
155. Amreen, K.; Kumar, A. S., Electrochemical redox signaling of hemoglobin in human whole blood and its relevance to anemia and thalassemia diagnosis. *Analyst* **2016**, *141* (7), 2145-2149.
156. Amayreh, M.; Hourani, M., Direct Electrochemical Determination of Hemoglobin in Blood Using Iodine-Coated Platinum Polycrystalline Electrode. *Analytical and Bioanalytical Chemistry Research* **2019**, *6* (1), 59-68.
157. Johnson-Wimbley, T. D.; Graham, D. Y., Diagnosis and management of iron deficiency anemia in the 21st century. *Therap Adv Gastroenterol* **2011**, *4* (3), 177-184.
158. Knovich, M. A.; Storey, J. A.; Coffman, L. G.; Torti, S. V.; Torti, F. M., Ferritin for the clinician. *Blood Rev* **2009**, *23* (3), 95-104.
159. Carmona, F.; Palacios, Ò.; Gálvez, N.; Cuesta, R.; Atrian, S.; Capdevila, M.; Domínguez-Vera, J. M., Ferritin iron uptake and release in the presence of metals and metalloproteins: Chemical implications in the brain. *Coordination Chemistry Reviews* **2013**, *257* (19), 2752-2764.

160. Dutta, P.; Meher, N.; Malik, A. H.; Choudhury, B.; Iyer, P. K., Polyfluorene-Based Bioconjugates for Selective Detection of Ferritin in Normal and Cancer Human Blood Serums. *ACS Applied Polymer Materials* **2019**, *1* (1), 18-26.
161. Dignass, A.; Farrag, K.; Stein, J., Limitations of Serum Ferritin in Diagnosing Iron Deficiency in Inflammatory Conditions. *Int J Chronic Dis* **2018**, *2018*, 9394060-9394060.
162. Yoon, H. C.; Yang, H.; Byun, S. Y., Ferritin Immunosensing on Microfabricated Electrodes Based on the Integration of Immunoprecipitation and Electrochemical Signaling Reactions. *Analytical Sciences* **2004**, *20* (9), 1249-1253.
163. Zhang, X.; Wang, S.; Hu, M.; Xiao, Y., An immunosensor for ferritin based on agarose hydrogel. *Biosensors and Bioelectronics* **2006**, *21* (11), 2180-2183.
164. Ren, Y.; Walczyk, T., Quantification of ferritin bound iron in human serum using species-specific isotope dilution mass spectrometry. *Metallomics* **2014**, *6* (9), 1709-1717.
165. Szunerits, S.; Mishyn, V.; Grabowska, I.; Boukherroub, R., Electrochemical cardiovascular platforms: Current state of the art and beyond. *Biosensors and Bioelectronics* **2019**, *131*, 287-298.
166. Lv, H.; Li, Y.; Zhang, X.; Li, X.; Xu, Z.; Chen, L.; Li, D.; Dong, Y., Thionin functionalized signal amplification label derived dual-mode electrochemical immunoassay for sensitive detection of cardiac troponin I. *Biosensors and Bioelectronics* **2019**, *133*, 72-78.
167. Zhang, C.; Zhang, S.; Jia, Y.; Li, Y.; Wang, P.; Liu, Q.; Xu, Z.; Li, X.; Dong, Y., Sandwich-type electrochemical immunosensor for sensitive detection of CEA based on the enhanced effects of Ag NPs@CS spaced Hemin/rGO. *Biosensors and Bioelectronics* **2019**, *126*, 785-791.
168. Song, T.-T.; Wang, W.; Meng, L.-L.; Liu, Y.; Jia, X.-B.; Mao, X., Electrochemical detection of human ferritin based on gold nanorod reporter probe and cotton thread immunoassay device. *Chinese Chemical Letters* **2017**, *28* (2), 226-230.
169. Yang, R.; Miao, D.; Liang, Y.; Qu, L.; Li, J.; Harrington, P. d. B., Ultrasensitive electrochemical sensor based on CdTe quantum dots-decorated poly(diallyldimethylammonium chloride)-functionalized graphene nanocomposite modified glassy carbon electrode for the determination of puerarin in biological samples. *Electrochimica Acta* **2015**, *173*, 839-846.

170. Sun, H.; Wu, L.; Wei, W.; Qu, X., Recent advances in graphene quantum dots for sensing. *Materials Today* **2013**, *16* (11), 433-442.
171. Singh, A.; Park, S.; Yang, H., Glucose-Oxidase Label-Based Redox Cycling for an Incubation Period-Free Electrochemical Immunosensor. *Analytical Chemistry* **2013**, *85* (10), 4863-4868.
172. Li, L.; Xu, J.; Zheng, X.; Ma, C.; Song, X.; Ge, S.; Yu, J.; Yan, M., Growth of gold-manganese oxide nanostructures on a 3D origami device for glucose-oxidase label based electrochemical immunosensor. *Biosensors and Bioelectronics* **2014**, *61*, 76-82.
173. Hu, J.; Wang, S.; Wang, L.; Li, F.; Pingguan-Murphy, B.; Lu, T. J.; Xu, F., Advances in paper-based point-of-care diagnostics. *Biosensors and Bioelectronics* **2014**, *54*, 585-597.
174. Chinnadayala, S. R.; Park, J.; Le, H. T. N.; Santhosh, M.; Kadam, A. N.; Cho, S., Recent advances in microfluidic paper-based electrochemiluminescence analytical devices for point-of-care testing applications. *Biosensors and Bioelectronics* **2019**, *126*, 68-81.
175. Yamamoto, S.; Uno, S., Redox Cycling Realized in Paper-Based Biochemical Sensor for Selective Detection of Reversible Redox Molecules Without Micro/Nano Fabrication Process. *Sensors (Basel)* **2018**, *18* (3), 730.
176. Ravgiala, R. R.; Weisburd, S.; Sleeper, R.; Martinez, A.; Rozkiewicz, D.; Whitesides, G. M.; Hollar, K. A., Using Paper-Based Diagnostics with High School Students To Model Forensic Investigation and Colorimetric Analysis. *Journal of Chemical Education* **2014**, *91* (1), 107-111.
177. Zhu, G.; Yin, X.; Jin, D.; Zhang, B.; Gu, Y.; An, Y., Paper-based immunosensors: Current trends in the types and applied detection techniques. *TrAC Trends in Analytical Chemistry* **2019**, *111*, 100-117.
178. Taprab, N.; Sameenoi, Y., Rapid screening of formaldehyde in food using paper-based titration. *Analytica Chimica Acta* **2019**, *1069*, 66-72.
179. Liu, C.-C.; Wang, Y.-N.; Fu, L.-M.; Chen, K.-L., Microfluidic paper-based chip platform for benzoic acid detection in food. *Food Chemistry* **2018**, *249*, 162-167.

180. Wu, Y.; Gao, Q.; Nie, J.; Fu, J.-z.; He, Y., From Microfluidic Paper-Based Analytical Devices to Paper-Based Biofluidics with Integrated Continuous Perfusion. *ACS Biomaterials Science & Engineering* **2017**, *3* (4), 601-607.
181. Dungchai, W.; Chailapakul, O.; Henry, C. S., Electrochemical Detection for Paper-Based Microfluidics. *Analytical Chemistry* **2009**, *81* (14), 5821-5826.
182. Mettakoonpitak, J.; Boehle, K.; Nantaphol, S.; Teengam, P.; Adkins, J. A.; Srisa-Art, M.; Henry, C. S., Electrochemistry on Paper-based Analytical Devices: A Review. *Electroanalysis* **2016**, *28* (7), 1420-1436.
183. Gomes, T. C.; Constantino, C. J. L.; Lopes, E. M.; Job, A. E.; Alves, N., Thermal inkjet printing of polyaniline on paper. *Thin Solid Films* **2012**, *520* (24), 7200-7204.
184. Bardpho, C.; Rattanarat, P.; Siangproh, W.; Chailapakul, O., Ultra-high performance liquid chromatographic determination of antioxidants in teas using inkjet-printed graphene-polyaniline electrode. *Talanta* **2016**, *148*, 673-679.
185. Karuwan, C.; Sriprachuabwong, C.; Wisitsoraat, A.; Phokharatkul, D.; Sritongkham, P.; Tuantranont, A., Inkjet-printed graphene-poly(3,4-ethylenedioxythiophene):poly(styrene-sulfonate) modified on screen printed carbon electrode for electrochemical sensing of salbutamol. *Sensors and Actuators B: Chemical* **2012**, *161* (1), 549-555.
186. Zhang, H.; Sun, Y.; Gao, S.; Zhang, J.; Zhang, H.; Song, D., A Novel Graphene Oxide-Based Surface Plasmon Resonance Biosensor for Immunoassay. *Small* **2013**, *9* (15), 2537-2540.
187. Chiu, N.-F.; Huang, T.-Y.; Lai, H.-C.; Liu, K.-C., Graphene oxide-based SPR biosensor chip for immunoassay applications. *Nanoscale Research Letters* **2014**, *9* (1), 445.
188. Rattana; Chaiyakun, S.; Witit-anun, N.; Nuntawong, N.; Chindaudom, P.; Oaew, S.; Kedkeaw, C.; Limsuwan, P., Preparation and characterization of graphene oxide nanosheets. *Procedia Engineering* **2012**, *32*, 759-764.
189. Yang, Z.; Jian, Z.; Chen, X.; Li, J.; Qin, P.; Zhao, J.; Jiao, X. a.; Hu, X., Electrochemical impedance immunosensor for sub-picogram level detection of bovine interferon gamma based on cylinder-shaped TiO₂ nanorods. *Biosensors and Bioelectronics* **2015**, *63*, 190-195.

190. Haji-Hashemi, H.; Safarnejad, M. R.; Norouzi, P.; Ebrahimi, M.; Shahmirzaie, M.; Ganjali, M. R., Simple and effective label free electrochemical immunosensor for Fig mosaic virus detection. *Analytical Biochemistry* **2019**, *566*, 102-106.
191. Bradbury, C. R.; Kuster, L.; Fermín, D. J., Electrochemical reactivity of HOPG electrodes modified by ultrathin films and two-dimensional arrays of metal nanoparticles. *Journal of Electroanalytical Chemistry* **2010**, *646* (1), 114-123.
192. Nkosi, D.; Pillay, J.; Ozoemena, K. I.; Nouneh, K.; Oyama, M., Heterogeneous electron transfer kinetics and electrocatalytic behaviour of mixed self-assembled ferrocenes and SWCNT layers. *Physical Chemistry Chemical Physics* **2010**, *12* (3), 604-613.
193. Dubin, S.; Gilje, S.; Wang, K.; Tung, V. C.; Cha, K.; Hall, A. S.; Farrar, J.; Varshneya, R.; Yang, Y.; Kaner, R. B., A one-step, solvothermal reduction method for producing reduced graphene oxide dispersions in organic solvents. *ACS nano* **2010**, *4* (7), 3845-3852.
194. Teengam, P.; Siangproh, W.; Tuantranont, A.; Henry, C. S.; Vilaivan, T.; Chailapakul, O., Electrochemical paper-based peptide nucleic acid biosensor for detecting human papillomavirus. *Analytica Chimica Acta* **2017**, *952*, 32-40.
195. Roy, S.; Soin, N.; Bajpai, R.; Misra, D. S.; McLaughlin, J. A.; Roy, S. S., Graphene oxide for electrochemical sensing applications. *Journal of Materials Chemistry* **2011**, *21* (38), 14725-14731.
196. Hu, S.-W.; Qiao, S.; Xu, B.-Y.; Peng, X.; Xu, J.-J.; Chen, H.-Y., Dual-Functional Carbon Dots Pattern on Paper Chips for Fe³⁺ and Ferritin Analysis in Whole Blood. *Analytical Chemistry* **2017**, *89* (3), 2131-2137.
197. Mao, X.; Du, T.-E.; Meng, L.; Song, T., Novel gold nanoparticle trimer reporter probe combined with dry-reagent cotton thread immunoassay device for rapid human ferritin test. *Analytica Chimica Acta* **2015**, *889*, 172-178.
198. Chen, L.; Zhao, S.; Liu, M.; Wu, P.; Chen, C., A novel label-free electrochemical immunosensor modified by glutathione and hyaluronic acid for the ultrasensitive and ultrasensitive detection of brucellosis in dilute serum. *Sensors and Actuators B: Chemical* **2019**, *287*, 510-516.
199. St John, A.; Price, C. P., Existing and Emerging Technologies for Point-of-Care Testing. *Clin Biochem Rev* **2014**, *35* (3), 155-167.

200. Silva, E. T. S. G.; Santhiago, M.; Barragan, J. T. C.; Kubota, L. T., Construction of a new versatile point-of-care testing device with electrochemical detection employing paper as a microfluidic platform. *Analytical Methods* **2014**, *6* (15), 6133-6136.
201. Paschoalino, W. J.; Kogikoski Jr., S.; Barragan, J. T. C.; Giarola, J. F.; Cantelli, L.; Rabelo, T. M.; Pessanha, T. M.; Kubota, L. T., Emerging Considerations for the Future Development of Electrochemical Paper-Based Analytical Devices. *ChemElectroChem* **2019**, *6* (1), 10-30.
202. Gubala, V.; Harris, L. F.; Ricco, A. J.; Tan, M. X.; Williams, D. E., Point of Care Diagnostics: Status and Future. *Analytical Chemistry* **2012**, *84* (2), 487-515.
203. Ballard, Z. S.; Joung, H.-A.; Goncharov, A.; Liang, J.; Nugroho, K.; Di Carlo, D.; Garner, O. B.; Ozcan, A., Deep learning-enabled point-of-care sensing using multiplexed paper-based sensors. *npj Digital Medicine* **2020**, *3* (1), 66.
204. Mondal, S.; Zehra, N.; Choudhury, A.; Iyer, P. K., Wearable Sensing Devices for Point of Care Diagnostics. *ACS Applied Bio Materials* **2020**.
205. Pashchenko, O.; Shelby, T.; Banerjee, T.; Santra, S., A Comparison of Optical, Electrochemical, Magnetic, and Colorimetric Point-of-Care Biosensors for Infectious Disease Diagnosis. *ACS Infectious Diseases* **2018**, *4* (8), 1162-1178.
206. Nilghaz, A.; Guan, L.; Tan, W.; Shen, W., Advances of Paper-Based Microfluidics for Diagnostics—The Original Motivation and Current Status. *ACS Sensors* **2016**, *1* (12), 1382-1393.
207. Gong, M. M.; Sinton, D., Turning the Page: Advancing Paper-Based Microfluidics for Broad Diagnostic Application. *Chemical Reviews* **2017**, *117* (12), 8447-8480.
208. Yang, T.; Pan, S.-C.; Cheng, C.-M., Paper-based human neutrophil elastase detection device for clinical wound monitoring. *Lab on a Chip* **2020**, *20* (15), 2709-2716.
209. Kasetsirikul, S.; Umer, M.; Soda, N.; Sreejith, K. R.; Shiddiky, M. J. A.; Nguyen, N.-T., Detection of the SARS-CoV-2 humanized antibody with paper-based ELISA. *Analyst* **2020**, *145* (23), 7680-7686.
210. Cate, D. M.; Adkins, J. A.; Mettakoonpitak, J.; Henry, C. S., Recent Developments in Paper-Based Microfluidic Devices. *Analytical Chemistry* **2015**, *87* (1), 19-41.
211. Yetisen, A. K.; Akram, M. S.; Lowe, C. R., Paper-based microfluidic point-of-care diagnostic devices. *Lab on a Chip* **2013**, *13* (12), 2210-2251.

212. Jang, I.; Song, S., Facile and precise flow control for a paper-based microfluidic device through varying paper permeability. *Lab on a Chip* **2015**, *15* (16), 3405-3412.
213. Sun, X.; Wang, H.; Jian, Y.; Lan, F.; Zhang, L.; Liu, H.; Ge, S.; Yu, J., Ultrasensitive microfluidic paper-based electrochemical/visual biosensor based on spherical-like cerium dioxide catalyst for miR-21 detection. *Biosensors and Bioelectronics* **2018**, *105*, 218-225.
214. Fava, E. L.; Martimiano do Prado, T.; Almeida Silva, T.; Cruz de Moraes, F.; Censi Faria, R.; Fatibello-Filho, O., New Disposable Electrochemical Paper-based Microfluidic Device with Multiplexed Electrodes for Biomarkers Determination in Urine Sample. *Electroanalysis* **2020**, *32* (5), 1075-1083.
215. Ataide, V. N.; Mendes, L. F.; Gama, L. I. L. M.; de Araujo, W. R.; Paixão, T. R. L. C., Electrochemical paper-based analytical devices: ten years of development. *Analytical Methods* **2020**, *12* (8), 1030-1054.
216. Jang, I.; Berg, K. E.; Henry, C. S., Viscosity measurements utilizing a fast-flow microfluidic paper-based device. *Sensors and Actuators B: Chemical* **2020**, *319*, 128240.
217. Chen, S. L.; Morgan, T. R., The Natural History of Hepatitis C Virus (HCV) Infection. *International Journal of Medical Sciences* **2006**, *3* (2), 47-52.
218. Aronoff-Spencer, E.; Venkatesh, A. G.; Sun, A.; Brickner, H.; Looney, D.; Hall, D. A., Detection of Hepatitis C core antibody by dual-affinity yeast chimera and smartphone-based electrochemical sensing. *Biosensors and Bioelectronics* **2016**, *86*, 690-696.
219. Akkapinyo, C.; Khownarumit, P.; Waraho-Zhmayev, D.; Poo-arporn, R. P., Development of a multiplex immunochromatographic strip test and ultrasensitive electrochemical immunosensor for hepatitis B virus screening. *Analytica Chimica Acta* **2020**, *1095*, 162-171.
220. Rodríguez, M.; Navascués, C. A.; Suárez, A.; Sotorrio, N. G.; Linares, A.; Pérez, R.; Rodrigo, L.; Martínez, A.; Cimadevilla, R., Hepatitis C virus infection in patients with acute hepatitis B. *Infection* **1992**, *20* (6), 316-319.
221. Hu, K.-Q.; Yu, C.-H.; Lee, S.; Villamil, F. G.; Vierling, J. M., Simultaneous detection of both hepatitis B virus DNA and hepatitis C virus RNA using a combined one-step polymerase chain reaction technique. *Hepatology* **1995**, *21* (4), 901-907.

222. Rodríguez, M.; Navascues, C. A.; Martínez, A.; Suárez, A.; Riestra, S.; Sala, P.; González, M.; Rodrigo, L. In *Prevalence of antibody to hepatitis C virus in chronic HBsAg carriers*, Chronically Evolving Viral Hepatitis, Vienna, 1992//; De Bac, C.; Taliani, G.; Gerlich, W. H., Eds. Springer Vienna: Vienna, 1992; pp 327-328.
223. Botti, P.; Pistelli, A.; Gambassi, F.; Zorn, A. M.; Caramelli, L.; Peruzzi, S.; Smorlesi, C.; Masini, E.; Mannaioni, P. F. In *HBV and HCV infection in i.v. drug addicts; coinfection with HIV*, Chronically Evolving Viral Hepatitis, Vienna, 1992//; De Bac, C.; Taliani, G.; Gerlich, W. H., Eds. Springer Vienna: Vienna, 1992; pp 329-332.
224. Villamil, F. G.; Hu, K.-Q.; Yu, C.-H.; Lee, C.-H.; Rojter, S. E.; Podesta, L. G.; Makowka, L.; Geller, S. A.; Vierling, J. M., Detection of hepatitis C virus with RNA polymerase chain reaction in fulminant hepatic failure. *Hepatology* **1995**, *22* (5), 1379-1386.
225. Féray, C.; Gigou, M.; Samuel, D.; Reyes, G.; Bernuau, J.; Reynes, M.; Bismuth, H.; Bréchot, C., Hepatitis C virus RNA and hepatitis B virus DNA in serum and liver of patients with fulminant hepatitis. *Gastroenterology* **1993**, *104* (2), 549-555.
226. Wright, T. L.; Mamish, D.; Combs, C.; Kim, M.; Wright, T. L.; Mamish, D.; Combs, C.; Kim, M.; Lake, J.; Donegan, E.; Ferrell, L.; Roberts, J.; Ascher, N. L., Hepatitis B virus and apparent fulminant non-A, non-B hepatitis. *The Lancet* **1992**, *339* (8799), 952-955.
227. THEILMANN, L.; SOLBACH, C.; TOEX, U.; MÜLLER, H. M.; PFAFF, E.; OTTO, G.; GOESER, T., Role of hepatitis C virus infection in German patients with fulminant and subacute hepatic failure. *European Journal of Clinical Investigation* **1992**, *22* (8), 569-571.
228. Farci, P.; Alter, H. J.; Shimoda, A.; Govindarajan, S.; Cheung, L. C.; Melpolder, J. C.; Sacher, R. A.; Shih, J. W.; Purcell, R. H., Hepatitis C Virus-Associated Fulminant Hepatic Failure. *New England Journal of Medicine* **1996**, *335* (9), 631-634.
229. Bouvier-Alias, M.; Patel, K.; Dahari, H.; Beaucourt, S.; Larderie, P.; Blatt, L.; Hezode, C.; Picchio, G.; Dhumeaux, D.; Neumann, A. U.; McHutchison, J. G.; Pawlotsky, J.-M., Clinical utility of total HCV core antigen quantification: A new indirect marker of HCV replication. *Hepatology* **2002**, *36* (1), 211-218.
230. Buti, M.; Mendez, C.; Schaper, M.; Sauleda, S.; Valdes, A.; Rodriguez-Frias, F.; Jordi, R.; Esteban, R., Hepatitis C virus Core Antigen as a predictor of non-response in

genotype 1 chronic hepatitis C patients treated with peginterferon α -2b plus ribavirin. *Journal of Hepatology* **2004**, *40* (3), 527-532.

231. Maynard, M.; Pradat, P.; Berthillon, P.; Picchio, G.; Voirin, N.; Martinot, M.; Marcellin, P.; Trepo, C., Clinical relevance of total HCV Core antigen testing for hepatitis C monitoring and for predicting patients' response to therapy. *Journal of Viral Hepatitis* **2003**, *10* (4), 318-323.

232. Laperche, S.; Marrec, N. L.; Simon, N.; Bouchardeau, F.; Defer, C.; Maniez-Montreuil, M.; Levayer, T.; Zappitelli, J.-P.; Lefrère, J.-J., A new HCV core antigen assay based on disassociation of immune complexes: an alternative to molecular biology in the diagnosis of early HCV infection. *Transfusion* **2003**, *43* (7), 958-962.

233. Laperche, S.; Le Marrec, N.; Girault, A.; Bouchardeau, F.; Servant-Delmas, A.; Maniez-Montreuil, M.; Gallian, P.; Levayer, T.; Morel, P.; Simon, N., Simultaneous detection of hepatitis C virus (HCV) core antigen and anti-HCV antibodies improves the early detection of HCV infection. *J Clin Microbiol* **2005**, *43* (8), 3877-3883.

234. Channon, R. B.; Nguyen, M. P.; Scorzelli, A. G.; Henry, E. M.; Volckens, J.; Dandy, D. S.; Henry, C. S., Rapid flow in multilayer microfluidic paper-based analytical devices. *Lab on a Chip* **2018**, *18* (5), 793-802.

235. Boonkaew, S.; Jang, I.; Noviana, E.; Siangproh, W.; Chailapakul, O.; Henry, C. S., Electrochemical paper-based analytical device for multiplexed, point-of-care detection of cardiovascular disease biomarkers. *Sensors and Actuators B: Chemical* **2021**, *330*, 129336.

236. Adkins, J. A.; Noviana, E.; Henry, C. S., Development of a Quasi-Steady Flow Electrochemical Paper-Based Analytical Device. *Analytical Chemistry* **2016**, *88* (21), 10639-10647.

237. Amatore, C.; Pebay, C.; Sella, C.; Thouin, L., Mass Transport at Microband Electrodes: Transient, Quasi-Steady-State, and Convective Regimes. *ChemPhysChem* **2012**, *13* (6), 1562-1568.

238. Tancharoen, C.; Sukjee, W.; Thepparit, C.; Jaimipuk, T.; Auewarakul, P.; Thithithanyanont, A.; Sangma, C., Electrochemical Biosensor Based on Surface Imprinting for Zika Virus Detection in Serum. *ACS Sensors* **2019**, *4* (1), 69-75.

239. Walji, N.; MacDonald, B. D., Influence of Geometry and Surrounding Conditions on Fluid Flow in Paper-Based Devices. *Micromachines (Basel)* **2016**, *7* (5), 73.
240. Camplisson, C. K.; Schilling, K. M.; Pedrotti, W. L.; Stone, H. A.; Martinez, A. W., Two-ply channels for faster wicking in paper-based microfluidic devices. *Lab on a Chip* **2015**, *15* (23), 4461-4466.
241. Jahanshahi-Anbuhi, S.; Chavan, P.; Sicard, C.; Leung, V.; Hossain, S. M. Z.; Pelton, R.; Brennan, J. D.; Filipe, C. D. M., Creating fast flow channels in paper fluidic devices to control timing of sequential reactions. *Lab on a Chip* **2012**, *12* (23), 5079-5085.
242. Shen, G.; Shen, Y.; Zhang, X.; Zhang, C., The Fabrication of Electrochemical Impedance Immunosensor Based on Aldehyde-containing Self-assembled Monolayers for Hepatitis B Surface Antigen Detection. *Electrochemistry* **2016**, *84* (4), 224-227.
243. Tan, Z.; Dong, H.; Liu, Q.; Liu, H.; Zhao, P.; Wang, P.; Li, Y.; Zhang, D.; Zhao, Z.; Dong, Y., A label-free immunosensor based on PtPd NCs@MoS₂ nanoenzymes for hepatitis B surface antigen detection. *Biosensors and Bioelectronics* **2019**, *142*, 111556.
244. Qiu, J.-D.; Liang, R.-P.; Wang, R.; Fan, L.-X.; Chen, Y.-W.; Xia, X.-H., A label-free amperometric immunosensor based on biocompatible conductive redox chitosan-ferrocene/gold nanoparticles matrix. *Biosensors and Bioelectronics* **2009**, *25* (4), 852-857.
245. Zhao, F.; Bai, Y.; Zeng, R.; Cao, L.; Zhu, J.; Han, G.; Chen, Z., An Electrochemical Immunosensor with Graphene-Oxide-Ferrocene-based Nanocomposites for Hepatitis B Surface Antigen Detection. *Electroanalysis* **2018**, *30* (11), 2774-2780.
246. Huang, K.-J.; Li, J.; Liu, Y.-M.; Cao, X.; Yu, S.; Yu, M., Disposable immunoassay for hepatitis B surface antigen based on a graphene paste electrode functionalized with gold nanoparticles and a Nafion-cysteine conjugate. *Microchimica Acta* **2012**, *177* (3), 419-426.
247. Qiu, J.-D.; Huang, H.; Liang, R.-P., Biocompatible and label-free amperometric immunosensor for hepatitis B surface antigen using a sensing film composed of poly(allylamine)-branched ferrocene and gold nanoparticles. *Microchimica Acta* **2011**, *174* (1), 97.
248. Ghanbari, K.; Roushani, M.; Azadbakht, A., Ultra-sensitive aptasensor based on a GQD nanocomposite for detection of hepatitis C virus core antigen. *Analytical Biochemistry* **2017**, *534*, 64-69.

249. Ghanbari, K.; Roushani, M., A nanohybrid probe based on double recognition of an aptamer MIP grafted onto a MWCNTs-Chit nanocomposite for sensing hepatitis C virus core antigen. *Sensors and Actuators B: Chemical* **2018**, *258*, 1066-1071.
250. Ma, C.; Xie, G.; Zhang, W.; Liang, M.; Liu, B.; Xiang, H., Label-free sandwich type of immunosensor for hepatitis C virus core antigen based on the use of gold nanoparticles on a nanostructured metal oxide surface. *Microchimica Acta* **2012**, *178* (3), 331-340.
251. Valipour, A.; Roushani, M., A glassy carbon immunoelectrode modified with vanadium oxide nanobelts for ultrasensitive voltammetric determination of the core antigen of hepatitis C virus. *Microchimica Acta* **2017**, *184* (11), 4477-4483.



VITA

NAME	Suchanat Boonkaew
DATE OF BIRTH	6 March 1993
PLACE OF BIRTH	Suratthani
INSTITUTIONS ATTENDED	Chulalongkorn University
HOME ADDRESS	83 Village 2, Lamphun, Bannasan, Suratthani 84120
PUBLICATION	<ol style="list-style-type: none">Suchanat Boonkaew, Sudkate Chaiyo, Sakda Jampasa, Sirirat Rengpipat, Weena Siangproh, Orawon Chialapakul “An origami paper-based electrochemical immunoassay for the C-reactive protein using a screen-printed carbon electrode modified with graphene and gold nanoparticles” <i>Microchimica Acta</i>, 2019, 186, 153.Suchanat Boonkaew, Prinjaporn Teengam, Sakda Jampasa, Sirirat Rengpipat, Weena Siangproh, Orawon Chialapakul “Cost effective paper-based electrochemical immunosensor using a label-free assay for sensitive detection of ferritin” <i>Analyst</i>, 2020, 145, 5019.Suchanat Boonkaew, Ilhoon Jang, Eka Noviana, Weena Siangproh, Orawon Chialapakul, Charles S. Henry “Electrochemical paper-based analytical device for multiplexed, point-of-care detection of cardiovascular disease biomarkers” <i>Sensor and Actuator B</i>, 2021, 330, 129336.
AWARD RECEIVED	<ol style="list-style-type: none">รางวัลเหรียญเงิน จากงานนวัตกรรมนานาชาติ Seoul International Invention Fair (SIIF) 2018 ณ กรุงโซล ประเทศเกาหลีใต้รางวัลผลประดิษฐ์คิดค้นระดับดี จากรางวัลสภาวิจัยแห่งชาติ:

รางวัลผลงานประดิษฐ์คิดค้นประจำปีงบประมาณ 2562 จัดโดย
สำนักงานคณะกรรมการการวิจัยแห่งชาติ (วช.)



จุฬาลงกรณ์มหาวิทยาลัย
CHULALONGKORN UNIVERSITY